D 2024

U.PORTO
FEUP FACULDADE DE ENGENHARIA
UNIVERSIDADE DO PORTO

THE ESTIMATION OF DIFFERENTIAL SETTLEMENT OF BUILDINGS ON LIQUEFIABLE SOIL DEPOSITS FOR VULNERABILITY ASSESSMENT

JULIETH PAOLA QUINTERO BANOS

TESE DE DOUTORAMENTO APRESENTADA
À FACULDADE DE ENGENHARIA DA UNIVERSIDADE DO PORTO EM
ENGENHARIA CIVIL

U.PORTO

FEUP FACULDADE DE ENGENHARIA
UNIVERSIDADE DO PORTO

The estimation of differential settlement of buildings on liquefiable soil deposits for vulnerability assessment

JULIETH PAOLA QUINTERO BAÑOS

Dissertation submitted to the Faculty of Engineering of the University of Porto in accordance with the requirements of the degree of Doctor in Civil Engineering

---

Supervisors: Antonio Viana da Fonseca, Ph.D.
Maxim Millen, Ph.D.

fct Fundação para a Ciência e a Tecnologia

CONSTRUCT

September 2024

PROGRAMA DOUTORAL EM ENGENHARIA CIVIL

DEPARTAMENTO DE ENGENHARIA CIVIL

Tel. +351 22 508 1901

Fax +351 22 508 2139

✉prodec@fe.up.pt

Editado por

FACULDADE DE ENGENHARIA DA UNIVERSIDADE DO PORTO

Rua Dr. Roberto Frias

4200-465 PORTO

Portugal

Tel. +351 22 508 1400

Fax +351 22-508 1440

✉feup@fe.up.pt

http://www.fe.up.pt

Reproduções parciais deste documento serão autorizadas na condição que seja mencionado o Autor e feita referência a Programa Doutoral em Engenharia Civil - Departamento de Engenharia Civil, Faculdade de Engenharia da Universidade do Porto, Porto, Portugal, 2024.

As opiniões e informações incluídas neste documento representam unicamente o ponto de vista do respetivo Autor, não podendo o Editor aceitar qualquer responsabilidade legal ou outra em relação a erros ou omissões que possam existir.

Este documento foi produzido a partir de versão eletrónica fornecida pelo respetivo Autor.

© Julieth Quintero, 2024

À minha pessoa favorita,

por não soltar minha mão durante toda essa jornada

Abstract

Differential settlement is one of the key causes of damage to buildings on liquefiable soil deposits. Although important technical developments in geotechnical earthquake engineering have provided significant insights into the performance of buildings on liquefiable soil, current approaches have focused on the settlement of buildings with strong and expensive mat foundations. While buildings with isolated footings are less expensive, they are more susceptible to differential settlements, which can not only make a building unusable and irreparable, but also introduce large stresses into a building that can result in damage and collapse for the superstructure.

The main objective of the research work is to extend current approaches by investigating the key parameters that influence differential settlements and tilting of reinforced concrete frame structures with isolated footings through the analysis of previous earthquakes and nonlinear effective stress fully-coupled dynamic numerical simulations in commercial software programs, namely FLAC and PLAXIS 2D. These insights provide the basis for the development of new equations for evaluating the potential settlement, residual tilt and angular distortion of structures with isolated footings. In addition to thickness, and depth of the layer of liquefiable sand, it was found that others parameters are also strongly correlated to residual tilt and angular distortion, in particular, the footings width, the bays length and the bearing pressure. It was also explored how the influence of these parameters is affected by ground shaking intensity.

First, this document presents a literature review covering the phenomena of liquefaction, how it develops in the free-field condition, what a constitutive model to simulate liquefaction behavior should account for, how the sand plasticity model PM4Sand works and why soil-structure interaction needs to be considered. Additionally, existing numerical techniques for model liquefaction effects, in particular for the modeling of foundation settlements and analytical methods to estimate settlements and tilt were discussed. Then, the efficacy of the numerical modeling and the constitutive model in the software was validated against results from centrifuge experiments involving soil-structure systems. The primary damage to buildings during earthquakes is shaking damage, therefore the modification to ground shaking due to liquefaction is extremely important in the context of quantifying building performance. Thus, the ability of the software to get the surface ground motion was demonstrated by validating the fundamental frequencies of the numerical analyses in the linear elastic domain against HVSR curves obtained of a well-document pilot site in the Greater Lisbon region. Additionally, the boundary conditions of the numerical models were validated by solving a common geotechnical problem of the ultimate bearing capacity and non-linear static moment-rotation response of a rough strip footing over both homogeneous and layered soil. Finally, a sensitivity analysis to investigate the influence of different soil conditions and building configurations on liquefaction-induced differential settlements was performed and a well

documented case study in Turkey was numerically modeled to analyze the differential settlements and tilt considering the soil-liquefaction-structure interaction of a real building.

Keywords: Earthquake induced liquefaction, seismic site response, effective stress numerical analysis, soil-structure interaction, liquefaction induced differential settlements

Resumo

Assentamentos diferenciais são uma das principais causas de danos a edifícios em maciços liquidificáveis. Embora importantes desenvolvimentos técnicos em engenharia sísmica geotécnica tenham proporcionado conhecimentos significativos sobre o desempenho de edifícios em solo liquidificável, as abordagens atuais têm-se concentrado nos assentamentos de edifícios com fundações em ensoleiramentos (radier), rígidos mas dispendiosos. Se os edifícios com sapatas isoladas são menos dispendiosos, são em contrapartida mais suscetíveis a assentamentos diferenciais, que podem não apenas tornar um edifício inutilizável e irreparável, mas mais do que isso introduzir esforços tais que podem resultar em danos ou mesmo no colapso da superestrutura.

O principal objetivo do trabalho de investigação é de ampliar as abordagens atuais investigando os parâmetros-chave que influenciam os assentamentos diferenciais e consequentemente distorções de estruturas porticadas de betão armado com sapatas isoladas através da análise de sismos anteriores e simulações numéricas dinâmicas, acopladas, não lineares e em tensões efetivas em códigos numéricos, nomeadamente FLAC e PLAXIS 2D. Esses entendimentos fornecerão a base para o desenvolvimento de novas equações para avaliar os potenciais assentamentos, e distorção angular de estruturas com sapatas isoladas. Além da espessura e profundidade da camada de areia liquidificável, constatou-se que outros parâmetros também estão fortemente correlacionados com a distorção angular, em particular, a largura das sapatas, o comprimento dos vãos e a tensão de contacto entre as sapatas e o solo. Também foi explorado como a influência desses parâmetros é afetada pela intensidade do sismo.

Em primeiro lugar, este documento faz uma revisão da literatura cobrindo o fenómeno de liquefação, como este se expressa em situação de campo livre, o que um modelo constitutivo para simular o comportamento de liquefação deve considerar, como o modelo constitutivo para areias PM4Sand funciona e por que razão a interação solo-estrutura precisa de ser considerada. Além disso, foram discutidas técnicas numéricas existentes para modelar os efeitos da liquefação, em particular para a modelação de assentamentos de fundações e métodos analíticos para estimar os assentamentos e distorções. Em seguida, a eficácia da modelação numérica e do modelo constitutivo no software foi validada em comparação com resultados de experimentos em centrifugadora geotécnica envolvendo sistemas solo-estrutura. Os principais danos a edifícios durante um evento sísmico são danos causados pela ação transmitida à superfície, portanto, a alteração da ação devido à liquefação é extremamente importante no contexto da quantificação do desempenho de edifícios. Assim, a capacidade do software de obter o movimento superficial do solo foi demonstrada através da validação das frequências fundamentais das análises numéricas no domínio elástico linear comparando-as com curvas HVSR obtidas de um campo experimental bem documentado na região da Grande Lisboa. Além disso, as condições de contorno dos modelos numéricos foram validadas resolvendo um prob-

lema geotécnico comum da capacidade de carga final e da resposta de momento-rotação estática não linear de uma sapata sobre um maciço homogêneo e também um maciço estratificado. Por fim, uma análise de sensibilidade foi realizada para investigar a influência de diferentes condições do solo e tipologia dos edifícios nos assentamentos diferenciais induzidos por liquefação. Um estudo de caso bem documentado na Turquia foi modelado numericamente para analisar os assentamentos diferenciais e distorções considerando a interação solo-estrutura de um edifício real.

Palavras chave: Liquefação induzida por sismos, resposta sísmica local, análise numérica em tensões efetivas, interação solo-estrutura, assentamentos diferenciais induzidos por liquefação.

Acknowledgments

Este trabalho teve o apoio financeiro da Fundação para a ciência e a tecnologia (FCT), através da bolsa de doutoramento SFRH/BD/143817/2019, que é reconhecido com gratidão. Este trabalho foi também apoiado pelo: Financiamento Base UIDB/04708/2020 e Financiamento Programático UIDP/ 04708/2020 da unidade de investigação CONSTRUCT—Instituto de I&D em Estruturas e Construções – financiada por fundos nacionais através da FCT/ MCTES (PIDDAC). Este trabalho foi inspirado no projeto LIQUEFACT ("Assessment and mitigation of liquefaction potential across Europe: a holistic approach to protect structures/infrastructures for improved resilience to earthquake-induced liquefaction disasters"), que recebeu financiamento do programa marco de investigación e innovación de la unión europea (Horizonte 2020) ao abrigo do acordo de subvenção Nº GAP-700748.

Primeiramente agradeço a Deus, por me trazer a este maravilhoso país para cumprir satisfatoriamente mais uma etapa na minha vida, onde não só ganhei conhecimentos se não pessoas valiosíssimas que com certeza ajudaram a concluir esta importante fase.

Ao Professor António Viana da Fonseca, que supervisionou este trabalho, por me receber inicialmente como investigadora e pela oportunidade que me deu de trabalhar numa área, até então, nova para mim. Agradeço a disponibilidade que sempre teve para orientar o meu trabalho de doutoramento, pela confiança, pelo constante apoio, pelos ensinamentos e pela motivação. Muito obrigada!

To Maxim, who co-supervised this work, for teaching me so many things, for giving me this love for programming, for your immense availability despite the time difference, for the many late-night meetings and above all for your patience when I didn't always understand the first time. Thank you very much!

À Sara Rios, por sempre estar disponível para me ajudar e pelas muitas palavras amigas. Com certeza agradeço ter te conhecido e trabalhado em conjunto tantas vezes.

Aos colegas e amigos da secção de Geotecnia, pela camaradagem dentro e fora da faculdade, foi muito bom partilhar com vocês: Fausto, Fabrizio, Davide, Rubens, Jesse.

Aos meus grandes amigos, Zorany e Anderson, que sempre tem acompanhado a minha caminhada apoiando as minhas decisões e motivando os meus dias. Obrigada porque mesmo a distância sempre consegui sentir o vosso apoio.

Ao Porto's Gang pelos tantos momentos de descontração e amizade. Um obrigada as minhas moças, Deisy e Kaori, pelas conversas, danças, treinos, corridas e aqueles abraços que só nos sabemos. E

ao Miguel por estar sempre atento dia após dia e pelas muitas ajudas cada vez que foi preciso. Dod na bzot!

A mis hermanas, Carolina y Laura, y a mis padres, Nancy y German, por el amor y apoyo incondicional. Gracias porque desde la distancia, hicieron parte de cada pequeño paso en este largo camino.

Aos meus mais recentes e pequenos amores, o meu sobrinho Emiliano e o meu afilhado Rafael, por fazer meus dias mais divertidos com esses vídeos cheios de sorrisos e autenticidade.

Por último, ao Danilo, meu esposo, pela companhia de vida, pela paciência, por saber sempre quando é que precisava de uma palavra de apoio, por me motivar cada dia a ser uma melhor pessoa, pelas muitas ajudas e pelo amor incondicional. Sou imensamente grata por ter você comigo.

Obrigada a todos.

Summary

1 Introduction **27**

1.1 Prologue and research motivation 27

1.2 Objectives 29

1.3 Thesis organization 29

2 Literature review **31**

2.1 Liquefaction soil behavior 31

2.1.1 Phenomena 31

2.1.2 Undrained monotonic loading 33

2.1.3 State parameters 34

2.1.4 Undrained cyclic loading 36

2.1.5 Liquefaction susceptibility in free-field conditions 37

2.1.6 Soil constitutive models 42

2.2 Soil-structure interaction 52

2.3 Liquefaction-induced settlements 58

2.3.1 Introduction 58

2.3.2 Approach by Karamitros et al. (2013a) 63

2.3.3 Approach by Bray and Macedo (2017) 65

2.3.4 Approach by Lu (2017) 67

2.3.5 Approach by Bullock et al. (2019a) 68

2.3.6 Approach by Bullock et al. (2019b) 72

3 Numerical models validation against centrifuge tests **77**

3.1 Overview of numerical model 77

3.2 Results and validation 80

3.3 Conclusions 87

4 Validation of liquefaction-induced ground motion modification **89**

4.1 Introduction 90

4.2 Geological setting and geotechnical model 91
4.3 Input motion selection 95
4.4 Liquefaction assessment methods based on field CPT tests 97
4.5 Site response analysis 98
4.5.1 Equivalent linear analyses 98
4.5.2 1D and 2D numerical models 99
4.6 Results and discussion 105
4.6.1 1D analysis at certain profiles along A10 cross-section 105
4.6.2 2D analysis of A10 cross-section to evaluate the valley effect 112
4.6.3 North of Benavente SI110 profile 117
4.7 Main findings 119

5 Boundary condition validation of the numerical models 121
5.1 Vertical loading 121
5.1.1 Sandy soil 122
5.1.2 Clayey soil 129
5.1.3 Layered soil profile with a liquefiable layer under a crust 131
5.1.4 Conclusions 137
5.2 Moment loading 138
5.2.1 Sandy soil 138
5.2.2 Clayey soil 141
5.2.3 Layered soil profile 142
5.2.4 Conclusions 147

6 Procedure to estimate differential settlements of buildings with isolated footings 149
6.1 Model construction 149
6.2 Results 153
6.3 Conclusions 166

7 Key parameters controlling liquefaction-induced differential settlements for buildings with isolated footings 167
7.1 Overview 167
7.2 Results 169
7.2.1 Soil parameters 169
7.2.2 Building parameters 181
7.2.3 Summary 207
7.3 Conclusions 211

8 Case Study of a real building on a liquefiable deposit 213

8.1 Soil conditions and input motion 214
8.2 Building and load 215
8.3 Overview of numerical model 217
8.4 Results and discussion 221
8.5 Main findings 225

9 Conclusions **227**
9.1 Final remarks 227
9.2 Future Works 229

Bibliography **231**

List of Figures

2.1 Liquefaction behavior in the free-field: a) soil is subject to confining stress and shaking induces shear stress; b) the soil particles rearrange under shear strain and the soil tries to contract, but undrained behavior results in reduce effective stress; c) critical state and phase transformation line; d) softening of the low strain stiffness (Viana da Fonseca et al., 2017). 32

2.2 Monotonic undrained behavior of sand: a) behavior in void ratio versus mean effective stress space ($e - p'$); b) pore pressure ratio (r_u) versus shear strain (γ); c) deviatoric stress ($q = 2\dot{\tau}$) versus p'; d) q versus γ (Viana da Fonseca et al., 2017). . 34

2.3 Definition of state parameter (Jefferies and Been, 2015). 35

2.4 Behavior of Toyoura sand in cyclic torsional tests: a) stress-strain curve; b) stress-path; c) excess pore pressure generation (adapted from Ishihara, 1985) 37

2.5 Simplified method for evaluating earthquake induced shear stresses: a) soil column scheme; b) change with depth of the shear stress in horizontal planes for the rigid and deformable body hypotheses; c) typical change with depth of the r_d coefficient, relating the previous stresses (Fernandes, 2020) 38

2.6 Correlations for cyclic resistance ratio (CRR) from SPT data (adapted from Boulanger and Ziotopolou, 2017) 40

2.7 Definition of the relative state parameter index (ε_R) (Boulanger and Ziotopolou, 2017) 44

2.8 Effects of varying Q and R (Boulanger and Ziotopolou, 2017) 45

2.9 Schematic of yield, critical, dilatancy and bounding lines in $q - p$ space. Relative location of dilatancy and bounding lines corresponds to dense-of-critical state of stress (Boulanger and Ziotopolou, 2017) 46

2.10 Correlation between overburden-corrected shear wave velocity and SPT penetration resistances in clean sands (Boulanger and Ziotopolou, 2017) 48

2.11 Logic tree of inputs and modeling decisions for h_{po} study 49

2.12 Cyclic stress ratios versus number of equivalent uniform loading cycles in undrained DSS loading to cause r_u=98% for D_R=40%. 49

2.13 Cyclic stress ratios corresponding to 15 uniform loading cycles (CRR_{15}) versus h_{po} values from element test results 50
2.14 Conceptual natural seismic isolation due to liquefaction (Viana da Fonseca et al., 2017) 54
2.15 Different modeling approaches for SSI in liquefiable soils (Viana da Fonseca et al., 2023) 55
2.16 Macro-mechanism approach (Viana da Fonseca et al., 2023) 57
2.17 Liquefaction-induced building displacement mechanisms: a) volumetric-induced settlement from post-liquefaction reconsolidation; b) shear-induced settlement from punching failure; c) shear-induced settlement from soil-structure-interaction (SSI) ratcheting; d) volumetric-induced settlement from sedimentation; e) ground loss due to soil ejecta (adapted from Bray and Macedo, 2017) 59
2.18 Comparison between analytical predictions and experimental measurements of ρ_{dyn} (Karamitros et al., 2013a) 65
2.19 Comparison of liquefaction-induced model building settlements measured during centrifuge tests with estimated liquefaction-induced settlements with the proposed procedure (Bray and Macedo, 2017) 67
2.20 Chart to estimate N_{LR} (Lu, 2017) 68
2.21 Comparison of estimated settlement and observed settlement from literature using the proposed calculation method: a) predictions on field observation; b) predictions on experimental studies; c) predictions on numerical studies (Lu, 2017) 69
2.22 Predicted settlement plotted against observed settlement for the mat case histories in the database (Bullock et al., 2019a) 72
2.23 Adjusted residuals for the case history data using the semi-empirical model for residual tilt (Bullock et al., 2019b) 74

3.1 Numerical model of centrifuge test (T6-40) performed by Dashti et al. (2010a) . . 78
3.2 Motions applied in the numerical model of centrifuge experiments (Dashti et al., 2010a) 80
3.3 Comparison between numerical and centrifuge models for T3-30 scenario and moderate ground motion: (a) settlements; (b) pore pressure build up under the building; (c) pore pressure build up in free-field; and (d) input motion (FLAC results were sourced from Viana da Fonseca et al., 2018) 81
3.4 Comparison between numerical and centrifuge models for T3-30 scenario and large ground motion: (a) settlements; (b) pore pressure build up under the building; (c) pore pressure build up in free-field; and (d) input motion (FLAC results were sourced from Viana da Fonseca et al., 2018) 82

3.5 Comparison between numerical and centrifuge models for T6-40 scenario and moderate ground motion: (a) settlements; (b) pore pressure build up under the building; (c) pore pressure build up in free-field; and (d) input motion (FLAC results were sourced from Viana da Fonseca et al., 2018) 83
3.6 Comparison between numerical and centrifuge models for T6-40 scenario and large ground motion: (a) settlements; (b) pore pressure build up under the building; (c) pore pressure build up in free-field; and (d) input motion (FLAC results were sourced from Viana da Fonseca et al., 2018) 84
3.7 Settlements comparison between numerical and centrifuge experimental results (FLAC results were sourced from Viana da Fonseca et al., 2018) 85
3.8 Maximum pore pressure comparison between numerical and centrifuge experimental results (FLAC results were sourced from Viana da Fonseca et al., 2018) 85
3.9 Maximum pore pressure comparison between numerical and centrifuge experimental results (FLAC results were sourced from Viana da Fonseca et al., 2018) 86
3.10 Maximum pore pressure comparison between numerical and centrifuge experimental results (FLAC results were sourced from Viana da Fonseca et al., 2018) 86
3.11 Maximum pore pressure comparison between numerical and centrifuge experimental results (FLAC results were sourced from Viana da Fonseca et al., 2018) 87
3.12 Maximum pore pressure comparison between numerical and centrifuge experimental results (FLAC results were sourced from Viana da Fonseca et al., 2018) 87

4.1 A 3-D view of: a) the stratigraphic model; b) the lithological model (Quintero et al., 2023) 92
4.2 Pilot site area, including the location of the in-situ tests (Quintero et al., 2023) . . 93
4.3 A 3D-model of the normalized clean sand equivalent cone tip resistance ($q_{c1N,cs}$). N/A in legend corresponds to non-liquefiable soils (Quintero et al., 2023) 93
4.4 Map contains $v_{s,30}$ values (Quintero et al., 2023) 94
4.5 v_s profiles for the selected sites (Quintero et al., 2023) 95
4.6 Acceleration response spectra of the ground motions recorded in soil type C (adapted from Quintero et al., 2023) 97
4.7 Cross-section of the Low Tagus Valley basin along A10: a) stratigraphic and lithological units; b) 2D numerical model geometry (Quintero et al., 2023) 100
4.8 Fundamental frequency values from HVSR curves and elastic numerical models results - Northridge-01 ground motion (Quintero et al., 2023) 101
4.9 Cyclic resistance curve for NB1 tests (Quintero et al., 2023) 104
4.10 Maximum acceleration (a_{max}) profiles (Quintero et al., 2023) 107
4.11 Shear strain (γ) profiles (Quintero et al., 2023) 108

4.12 Maximum excess pore pressure ratio r_u profile from 1D effective stress analysis (Flac-1D-Liq) considering liquefaction (Quintero et al., 2023) 109
4.13 Shear stress (τ) profiles (Quintero et al., 2023) 110
4.14 Factor of safety (FS) from B&I compared with FS from the other methods (Quintero et al., 2023) 111
4.15 Acceleration response spectra of the surface ground motions (adapted from Quintero et al., 2023) 112
4.16 Maximum acceleration (a_{max}) profiles - Northridge-01 ground motion (Quintero et al., 2023) 113
4.17 Shear strain profiles - Northridge-01 ground motion (Quintero et al., 2023) 114
4.18 Maximum excess pore pressure ratio r_u profile from 1D and 2D effective stress analysis considering liquefaction (Flac-1D-Liq and Flac-2D-Liq respectively) - Northridge-01 ground motion (Quintero et al., 2023) 114
4.19 Shear stress profiles - Northridge-01 ground motion (Quintero et al., 2023) 115
4.20 Factor of safety (FS) from B&I compared with FS from the other methods - Northridge-01 ground motion (Quintero et al., 2023) 115
4.21 Acceleration response spectra of the surface ground motions - Northridge-01 input ground motion (adapted from Quintero et al., 2023) 116
4.22 Profile SI110 of a) maximum acceleration (a_{max}); b) maximum shear strain (γ); c) maximum shear stress (τ) and d) factor of safety against liquefaction (red:0-1.0; orange:1.0-1.25; yellow: 1.25-1.5; green: 1.5-2.0) and e) maximum excess pore pressure ratio (ru_{max}) - Northridge-01 ground motion (Quintero et al., 2023) . . . 118
4.23 Results from 1D non-linear numerical model SI110: a) Surface spectral acceleration and b) r_u in different depths of liquefiable layer - Northridge-01 ground motion (Quintero et al., 2023) 118

5.1 Numerical model of sandy soil profile to estimate bearing capacity 122
5.2 PLAXIS 2D bearing capacity results for different model depths (W = 11 m) 124
5.3 PLAXIS 2D bearing capacity results for different model widths (D = 5 m) 125
5.4 PLAXIS 2D bearing capacity for different model a) depths; b) widths 126
5.5 PLAXIS 2D vertical stiffness for different model a) depths; b) widths 126
5.6 Numerical model of sandy soil profile to estimate bearing capacity (B = 2 m) . . . 127
5.7 PLAXIS 2D bearing capacity results for different model depths (B=2 m) 128
5.8 PLAXIS 2D bearing capacity results for different model widths (B=2 m) 128
5.9 PLAXIS 2D bearing capacity for different model a) depths; b) widths 129
5.10 PLAXIS 2D bearing capacity results for clayey homogeneous profile 131
5.11 PLAXIS 2D total stress for clayey homogeneous profile 131
5.12 Numerical model of layered soil profile (Crust thickness of 1.5 meters) 133

5.13 Numerical model of layered soil profile (Crust thickness of 3 meters) 133
5.14 PLAXIS 2D bearing capacity results for different layered profiles 134
5.15 Rough continuous foundation on layered soil - stronger over weaker (Das, 2014) . . 135
5.16 PLAXIS 2D total stress for layered profile ($H_c = 1.5$ and $r_u = 0.8$) 136
5.17 PLAXIS 2D total stress for layered profile ($H_c = 1.5$ and $r_u = 0.95$) 136
5.18 PLAXIS 2D total stress for layered profile ($H_c = 3.0$ and $r_u = 0.8$) 137
5.19 PLAXIS 2D total stress for layered profile ($H_c = 3.0$ and $r_u = 0.95$) 137
5.20 Numerical model of sandy soil profile for moment capacity analyses 139
5.21 Moment-rotation response of a strip footing on a sandy homogeneous profile. . . . 140
5.22 Moment-rotation response of a strip footing on a clayey homogeneous profile . . . 142
5.23 Numerical model to estimate moment capacity of a layered soil profile (Crust thickness of 1.5 meters) 143
5.24 Numerical model to estimate moment capacity of layered soil profile (Crust thickness of 3 meters) 143
5.25 Moment-rotation response of a strip footing on a layered profile ($H_c = 1.5$ and $r_u = 0.8$) 144
5.26 Moment-rotation response of a strip footing on a layered profile ($H_c = 1.5$ and $r_u = 0.95$) 145
5.27 Moment-rotation response of a strip footing on a layered profile ($H_c = 3.0$ and $r_u = 0.8$) 145
5.28 Moment-rotation response of a strip footing on a layered profile ($H_c = 3.0$ and $r_u = 0.95$) 146
5.29 M/N vs Factor of safety for the different profiles configuration from PLAXIS 2D analysis 147

6.1 Numerical model with isolated footings for 1-bays, 2-bays and 4-bays buildings . . 150
6.2 Stresses state before the ground motion 152
6.3 Stresses state before the ground motion for the same contact pressure in all the footings 152
6.4 Ground motions used in the parametric analysis: a) Acceleration time series; b) Cumulative absolute velocity (CAV) 153
6.5 Settlements after the ground motion GM1 for benchmark models NF5 154
6.6 Definition of angular distortion 154
6.7 a) Initial stresses state for benchmark model NF5; b)Equivalent building with mat foundation 155
6.8 Numerical maximum and average settlements compared with Bray and Macedo (2017) approach for the benchmark models 156
6.9 Numerical maximum tilt for the benchmark models 157

6.10 Numerical maximum angular distortion for the benchmark models 158
6.11 Time series for GM1 for the benchmark models 159
6.12 Time series for GM2 for the benchmark models 160
6.13 Time series for GM3 for the benchmark models 161
6.14 Numerical maximum and average settlements compared with Bray and Macedo (2017) approach for the same contact pressure in all the footings 162
6.15 Numerical maximum tilt for the same contact pressure in all the footings 163
6.16 Numerical maximum angular distortion for the same contact pressure in all the footings 163
6.17 Time series for GM1 for the same contact pressure in all the footings 164
6.18 Time series for GM2 for the same contact pressure in all the footings 165
6.19 Time series for GM3 for the same contact pressure in all the footings 166

7.1 Building parameters in sensitivity analysis 168
7.2 Numerical maximum and average settlements compared with Bray and Macedo (2017) approach for H_C variation 170
7.3 Numerical maximum angular distortion for H_C variation 170
7.4 Numerical maximum tilt for H_C variation 170
7.5 Time series for GM1 for H_C variation 171
7.6 Time series for GM2 for H_C variation 172
7.7 Time series for GM3 for H_C variation 173
7.8 Numerical maximum and average settlements compared with Bray and Macedo (2017) approach for D_R variation 174
7.9 Numerical maximum angular distortion for D_R variation 174
7.10 Numerical maximum tilt for D_R variation 175
7.11 Time series for GM1 for D_R variation 175
7.12 Time series for GM2 for D_R variation 176
7.13 Time series for GM3 for D_R variation 177
7.14 Numerical maximum and average settlements compared with Bray and Macedo (2017) approach for H_L variation 178
7.15 Numerical maximum angular distortion for H_L variation 178
7.16 Numerical maximum tilt for H_L variation 178
7.17 Time series for GM1 for H_L variation 179
7.18 Time series for GM2 for H_L variation 180
7.19 Time series for GM3 for H_L variation 181
7.20 Numerical maximum and average settlements compared with Bray and Macedo (2017) approach for w_{top} variation 182
7.21 Numerical maximum angular distortion for w_{top} variation 182

7.22 Numerical maximum tilt for w_{top} variation 183
7.23 Time series for GM1 for w_{top} variation 183
7.24 Time series for GM2 for w_{top} variation 184
7.25 Time series for GM3 for w_{top} variation 185
7.26 Numerical maximum and average settlements compared with Bray and Macedo (2017) approach for b_{foot} variation 186
7.27 Numerical maximum angular distortion for b_{foot} variation 186
7.28 Numerical maximum tilt for b_{foot} variation 187
7.29 Beam load w_{top} for models with different b_{foot} 187
7.30 Time series for GM1 for b_{foot} variation 188
7.31 Time series for GM2 for b_{foot} variation 189
7.32 Time series for GM3 for b_{foot} variation 190
7.33 Numerical maximum and average settlements compared with Bray and Macedo (2017) approach for H variation 191
7.34 Numerical maximum angular distortion for H variation 191
7.35 Numerical maximum tilt for H variation 192
7.36 Time series for GM1 for H variation 192
7.37 Time series for GM 2for H variation 193
7.38 Time series for GM3 for H variation 194
7.39 Numerical maximum and average settlements compared with Bray and Macedo (2017) approach for d_f variation 195
7.40 Numerical maximum angular distortion for d_f variation 195
7.41 Numerical maximum tilt for d_f variation 196
7.42 Time series for GM1 for d_f variation 196
7.43 Time series for GM2 for d_f variation 197
7.44 Time series for GM3 for d_f variation 198
7.45 Numerical maximum and average settlements compared with Bray and Macedo (2017) approach for b_{bay} variation 199
7.46 Numerical maximum angular distortion for b_{bay} variation 199
7.47 Numerical maximum tilt for b_{bay} variation 200
7.48 Beam load w_{top} for models with different b_{bay} 200
7.49 Time series for GM1 for b_{bay} variation 201
7.50 Time series for GM2 for b_{bay} variation 202
7.51 Time series for GM13 for b_{bay} variation 203
7.52 Numerical maximum and average settlements compared with Bray and Macedo (2017) approach for EI_{ratio} variation 204
7.53 Numerical maximum angular distortion for EI_{ratio} variation 204

7.54 Numerical maximum tilt for EI_{ratio} variation 205
7.55 Time series for GM1 for EI_{ratio} variation 205
7.56 Time series for GM2 for EI_{ratio} variation 206
7.57 Time series for GM3 for EI_{ratio} variation 207
7.58 Comparison between numerical average settlements and analytical results considering isolated footings 208
7.59 Comparison between numerical maximum settlements and analytical results considering isolated footings 208
7.60 Comparison between numerical average settlements and analytical results considering mat foundation 209
7.61 Tornado diagram for the sensitivity of average settlement for NF2, NF3 and NF5 (left to right) 210
7.62 Tornado diagram for the sensitivity of maximum settlement for NF2, NF3 and NF5 (left to right) 210
7.63 Tornado diagram for the sensitivity of residual tilt for NF2, NF3 and NF5 (left to right) 211
7.64 Tornado diagram for the sensitivity of maximum angular distortion for NF2, NF3 and NF5 (left to right) 211

8.1 PEC building after earthquake (Images courtesy of NISEE-PEER Library, UC Berkeley) 214
8.2 CPT data and idealized soil profile at the PEC site (Viana da Fonseca et al., 2023) 215
8.3 Vs profile at PEC site and considered depths (Viana da Fonseca et al., 2023) . . . 216
8.4 Input motion (at 55 m depth) time series (Viana da Fonseca et al., 2023) 217
8.5 a) Plan view of the structural system; b) Frame corresponding to section AA' (Viana da Fonseca et al., 2023) 217
8.6 Full approach numerical model in FLAC (Viana da Fonseca et al., 2023) 218
8.7 Calibration of Layer 2 PM4Sand parameters through a comparison of real and simulated CDSS test results in terms of shear stress - shear strain for a test with a CSR of: a) 0.41; b) 0.33. c) Calibration of Layer 6 PM4Sand parameters through a comparison with B&I curve (Viana da Fonseca et al., 2023) 220
8.8 (a) Surface acceleration time series and (b) corresponding spectral acceleration (adapted from Viana da Fonseca et al., 2023) 221
8.9 Results from numerical model: a) excess pore pressure ratio in the middle of the liquefiable layer in free-field and under central column, b) settlements at all the columns, c) maximum angular distortion, d) tilt (adapted from Viana da Fonseca et al., 2023) 222

8.10 Comparison of maximum beams moment demand from FLAC full model approach (adapted from Viana da Fonseca et al., 2023) 223
8.11 Comparison of maximum columns moment demand from FLAC full model approach (adapted from Viana da Fonseca et al., 2023) 224

List of Tables

2.1 Number of cycles of a uniform loading of amplitude $0.65 \cdot \tau_{max}$, representative of various seismic magnitudes (Seed et al., 1975) 40
2.2 Secondary input parameters of PM4Sand constitutive model (Boulanger and Ziotopolou, 2017) 52

3.1 Mohr-Coulomb input parameters for numerical model of Dashti et al. (2010a) centrifuge experiments 79
3.2 PM4Sand input parameters for numerical model of Dashti et al. (2010a) centrifuge experiments 79

4.1 Reference Type 1 and Type 2 seismic actions for the pilot site region 95
4.2 Type 1 ground motions selected 96
4.3 Type 2 ground motions selected 97
4.4 Soil parameters for the A10 highway profiles. 103
4.5 Cyclic triaxial tests performed with undisturbed specimens to assess liquefaction potential (Ramos, 2021) 104
4.6 Soil parameters for the SI110 site 105
4.7 Liquefaction potential index (LPI) values. 116

5.1 Footing input parameters 123
5.2 Sandy soil input parameters 123
5.3 PLAXIS 2D bearing capacity results for different model depths and widths 125
5.4 PLAXIS 2D bearing capacity results for different model depths and widths (Foundation width of 2 m) 129
5.5 Clayey soil input parameters 130
5.6 Liquefiable layer parameters 132
5.7 PLAXIS 2D bearing capacity results for different model depths and widths 135
5.8 PLAXIS 2D moment capacity on sandy soil for different factors of safety (FS) . . . 141
5.9 PLAXIS 2D moment capacity on clayey soil for different factors of safety (FS) . . 142

5.10 PLAXIS 2D moment capacity results for different layered profiles and FS 146

6.1 Input parameters of the HS model used in the parametric analysis 151

7.1 Parameters for sensitivity analysis 168
7.2 Summary of the trends in the results 209

8.1 Input parameters of the Mohr-Coulomb model 219

Chapter 1

Introduction

1.1 Prologue and research motivation

Earthquake-induced liquefaction can lead to significant damage in buildings and huge economic and social costs to communities. Over the past decade, earthquakes proved to be the deadliest of all European disasters, with almost 19,000 fatalities and direct economic losses of approximately €29 billion (Viana da Fonseca et al., 2017). Despite significant advancements in liquefaction mitigation achieved over the past decades in the realm of earthquake geotechnical engineering, substantial damage continues to occur in seismic regions worldwide. Liquefaction-related damage has had greater recognition as a critical issue after recent earthquake events, e.g. 2012 Emilia, Italy; 2011 Tohoku Oki, Japan; and particularly 2010-2011 Canterbury Christchurch, New Zealand, with liquefaction induced damage of $20 billion NZD (Berger et al., 2012) and many parts of the central business district and suburban areas still remain empty after eight years because buildings had to be demolished after the earthquakes.

Specifically, the challenge of accurately estimating liquefaction-induced damage remains inadequately tackled due to its complexity. One of the main issues that hinder a simple answer to this problem is the uncertainties associated with soil behavior. Settlements and tilting of structures that are not supported by deep foundations are the main types that experience liquefaction-induced damage (Yoshimi and Tokimatsu, 1977; Acacio et al., 2001) and, due to that, several methodologies have been developed to study the performance of buildings with shallow foundations on liquefiable soil deposits (Yoshimi and Tokimatsu, 1977; Liu and Dobry, 1997; Karamitros et al., 2013a; Millen et al., 2018). These methodologies have been based on field observations, centrifuge experiments, numerical simulations, or a combination of them.

Although there are a large number of uncertainties involved in the interpretation of field observations, there have been several attempts to correlate foundation settlement with building dimensions and soil profile characteristics using field observations (Acacio et al., 2001; Ishihara et al., 1993; Sancio et al., 2002; Bertalot et al., 2013). Consequently, this allowed the emergence of the first conclusions about the effects of liquefaction on buildings with shallow foundations, such as that foundation settlements are correlated with the thickness of the liquefied layer (Yoshimi and Tokimatsu, 1977) and that the bearing pressure can both increase and/or decrease the liquefaction susceptibility and extent of foundation settlement (Sancio et al., 2002; Bray et al., 2004).

Centrifuge experiments have also been conducted to investigate liquefaction-induced settlements (Liu and Dobry, 1997; Coelho et al., 2004; Dashti et al., 2010b; Bertalot and Brennan, 2015). For instance, many of the results from these experiments showed that most of the foundation settlement occurs during the strong shaking of the earthquake compared to the settlement that occurs during the excess pore pressure dissipation (post-shaking). Further findings showed that the dominant mechanisms of building settlement are building-induced shear deformation and localized volumetric strains (Dashti et al., 2010b). Additionally, it has been proved that very heavy structures, limit the excess pore pressure generation and the resulting building settlement (Bertalot and Brennan, 2015).

The inherent challenges and expenses linked with experimental and field-based research validate the increasing necessity of numerical modeling in studying soil liquefaction and soil-structure interaction within liquefaction research. Recently, numerical modeling has been used to study the performance of buildings on shallow foundations, as well as other infrastructure such as quay walls and embankments (Millen et al., 2018; Daftari and Kudla, 2014; Bhatnagar et al., 2016; Borozan et al., 2017; Luque and Bray, 2017; Ziotopoulou and Montgomery, 2017; Souliotis and Gerolymos, 2016; Quintero et al., 2018; Bullock et al., 2019a). The ability to easily vary key parameters within a numerical simulation has led to several new approaches to estimating the settlement of raft foundation buildings (Karamitros et al., 2013a; Bray and Macedo, 2017) but none have analyzed structures with isolated footings, which represent a large part of the European building stock. These current approaches and several publicly available experimental data sets provide key benchmarks for extending the existing methods to a wider range of parameters and for investigating more complex systems such as buildings on shallow isolated footings (Gómez-Martínez et al., 2018). Therefore, a sensitivity analysis was performed to investigate the influence of different soil conditions and building configurations on liquefaction-induced differential settlements in buildings with isolated footings.

1.2 Objectives

The main objective of the research work is to extend current approaches by investigating the key parameters that influence differential settlements and tilting of isolated footings supporting low- to mid-rise reinforced concrete buildings when liquefiable layer are included in the subsoil. This investigation involves the analysis of previous earthquakes and nonlinear effective stress fully-coupled dynamic numerical simulations in commercial software programs, namely FLAC and PLAXIS 2D. These insights will provide the basis for the development of new equations for evaluating the potential settlement, residual tilt and angular distortion of structures with isolated footings. Specific tasks must be followed in order to reach this goal:

1. Validate the efficacy of the numerical modeling, namely the software programs and the constitutive model to simulate liquefaction by comparing results from numerical simulations against results from centrifuge experiments involving soil-structure systems.

2. Identify the minimum numerical model size (boundary conditions) to avoid any interference in the stress-strain response of the building.

3. Study the ground shaking modification due to liquefaction, which extremely important in the context of quantifying building performance because the primary damage to buildings during earthquakes is shaking damage.

4. Create charts to estimate the ranges within which settlements, tilt and angular distortion may vary, depending on the number of footings in the structure.

1.3 Thesis organization

The present document is organized in four parts, corresponding to the main research work phases:

(I) Introduction and Literature Review

(II) Validation and verification of numerical models

(III) Settlements and tilt evaluation

(IV) Summary and Conclusions

Each part is structured into chapters that compile the information and results of each phase of the work. A detailed description of each part of the study is provided as follows.

Part I comprises the introduction and literature review, encompassing the research motivation, scope, and objectives of the study. The literature review covers the phenomena of liquefaction,

its development in free-field conditions, the essential considerations for a constitutive model to simulate liquefaction behavior, the functioning of the sand plasticity model PM4Sand, and the importance of considering soil-structure interaction. Additionally, it discusses existing numerical techniques for modeling liquefaction effects, particularly for foundation settlements, as well as analytical methods for estimating settlements and tilt.

Part II focuses on the validation and verification of numerical models, detailing various verification processes that support the effectiveness of the numerical models used in this study. This part is divided into three chapters:

Chapter 3 provides a comprehensive description of the validation process conducted to assess the efficacy of the numerical modeling and the constitutive model in the software. This validation is performed against results obtained from centrifuge experiments involving soil-structure systems.

Chapter 4 outlines the validation of the software's ability to capture surface ground motion. This validation is conducted by comparing the fundamental frequencies of a pilot site in the Greater Lisbon region obtained through numerical analyses in the linear elastic domain against Horizontal-to-Vertical Spectral Ratio (HVSR) curves.

Finally, Chapter 5 presents the boundary conditions of the numerical model validation to identify the appropriate size of the model. This is achieved by solving a common geotechnical problem involving the ultimate bearing capacity and the non-linear static moment-rotation response of a rough strip footing.

Part III focuses on the evaluation of settlements and tilt using numerical models, and it comprises the following chapters:

Chapter 6 outlines the procedure for estimating the differential settlements of buildings with isolated footings through numerical simulations. The models presented in this chapter serve as benchmark models, providing a reference for investigating the key parameters that influence building performance.

Chapter 7 presents a sensitivity analysis to investigate the influence of different soil conditions and building configurations on liquefaction-induced differential settlements.

Finally, Chapter 8 presents the numerical model of a real building in Turkey to analyze the differential settlements and tilt considering the soil-liquefaction-structure interaction.

Lastly, Part IV (Chapter 9) presents the main conclusions and recommendations for future research work.

Chapter 2

Literature review

2.1 Liquefaction soil behavior

2.1.1 Phenomena

Soil liquefaction is a phenomenon in which the strength and stiffness of saturated, loose, frictional soils are significantly reduced by pore pressure build-up, often caused by earthquake shaking. Liquefaction phenomena is categorized into two groups, flow liquefaction and cyclic mobility. Both are triggered by the pore water pressure increase, but under static and cyclic load conditions, respectively. Flow liquefaction process can be described as the collapse of the structure of the sand during untrained shearing. Cyclic mobility is achieved at large excess pore water pressure build-up close to the initial vertical effective stress; however, some level of shear stiffness is recovered during cyclic loading as soil dilation and contraction causes a cyclic decrease and increase in pore pressure (Ramos, 2011).

Figure 2.1 illustrates some important aspects of the behavior of liquefiable soils. The development of liquefaction on flat ground in free-field conditions occurs due to cyclic shear stress (τ) and strain (γ) generated by the seismic shear waves (Figure 2.1a). The soil particles rearrange under shear strain and the soil tries to contract; however, the pore water cannot easily escape under the rapid seismic loading (Figure 2.1b). Figure 2.1c shows as the pore water compresses under each cycle and increases in pressure, thus decreasing the mean effective stress (p'). Two boundary lines result of this behavior, the critical state line and the phase transformation line. The critical state line in $\tau - p'$ space denotes the stress ratio of the soil at large shear strain where no further volume change occurs under shear strain. The phase transformation line denotes the stress ratio where the soil changes from contractive to dilative under shear strain. This dilative behavior is seen when the shear stress exceeds this boundary, and the effective stress starts to increase. As the

loading continues the behavior stabilizes and forms a butterfly shape (shown in red). Therefore, in a single cycle of loading the pore pressure increases and decreases twice. Figure 2.1d shows as the reduction in effective stress causes a reduction in the low strain stiffness, which consequently leads to increased strain and increased pore pressure build up (Viana da Fonseca et al., 2017). As seen in Figure 2.1, the dilative or contractive behavior of soil is dependent on the stress state, but it is also dependent on the soil properties and density. While loose soils, have a greater tendency for contraction, dense soils have a tendency to dilate under large shear strain. The difference between these types of soil can be explained by examining the soil under monotonic loading using the framework of critical state soil mechanics.

In liquefaction analyses, the build-up of pore pressure is often described as excess pore pressure and expressed as a pore pressure ratio (r_u), which is defined as the ratio of the excess pore pressure to the initial vertical effective stress. Furthermore, r_u indicates the proximity of triggering of soil liquefaction. Prior to cyclic loading r_u value is 0, while at the triggering of liquefaction, it is near to 1 (100%).

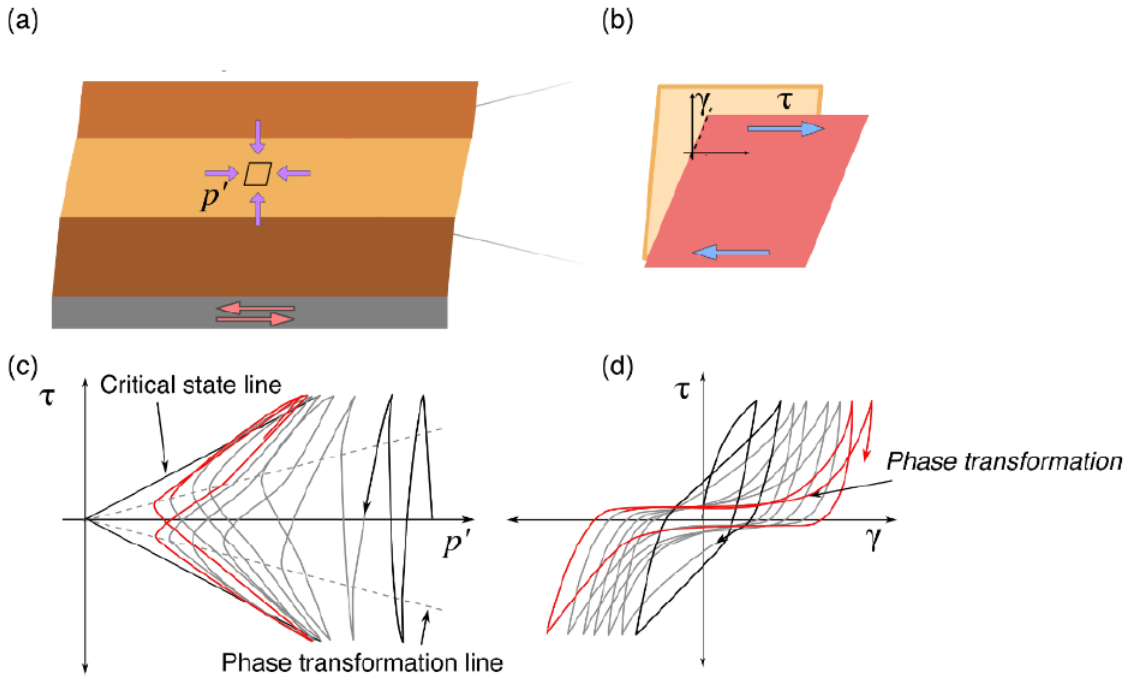


Figure 2.1: Liquefaction behavior in the free-field: a) soil is subject to confining stress and shaking induces shear stress; b) the soil particles rearrange under shear strain and the soil tries to contract, but undrained behavior results in reduce effective stress; c) critical state and phase transformation line; d) softening of the low strain stiffness (Viana da Fonseca et al., 2017).

Kramer (1996) defines that to determine whether the soil is in fact liquefiable, historical (the seismic activity of the zone involving seismic factors like magnitude, acceleration and duration), geological (such as origin, formation, fabric, structure and permeability), compositional (such as grain size distribution and the shape of the soil particles) and state (such as degree of saturation, initial stress conditions and the relative density) criterion should be analyzed.

2.1.2 Undrained monotonic loading

Figure 2.2 shows the behavior of four soil samples under a direct shear load, the initial state of these soils varies from very loose to very dense (Verdugo and Ishihara, 1996). Figure 2.2a shows the behavior in void ratio versus mean effective stress space ($e - p'$), Figure 2.2b shows the pore pressure ratio (r_u) versus shear strain (γ), Figure 2.2c shows the deviatoric stress ($q = 2\dot{\tau}$) versus p' and Figure 2.2d shows q versus γ.

Following the behavior of the "Moderately dense – high confinement" soil (orange line), Figure 2.2a shows that it starts at a state above the critical state line and contracts until it reaches the phase transformation line, at which point it dilates back to the critical state line. Figure 2.2b shows no pore pressure build up in the initial part of the loading reflecting this behavior in Figure 2.2c, where the loading is almost vertical in the $q - p'$ space, denoting that there was minimal change in pore pressure. Also in Figure 2.2c can be seen that the deviatoric stress initially increases to a maximum value, and then the build-up in pore pressure results in a softening and decrease in strength, until it crosses the phase transformation line, where it dilates and increases in strength to reach the critical state. Figure 2.2d (in $q-\gamma$ space), the behavior shows the increase in load with a softening of the response, the softening at low strain is related to the shear strain (and also occurs for drained behavior). The softening at larger strains is due to the build-up of pore pressure, and eventually limited flow can be observed before the soil state reaches the phase transformation line and hardens; the final excess pore pressure ratio being less than 1.0.

The behavior of "Moderately dense – low confinement" soil (blue line) contrasts the behavior of the previous soil. Figure 2.2a shows that the initial state is below the critical state line but above the phase transformation line. Initially, the soil contracts just like the first soil, and then dilates to the same point on the critical state line. Figure 2.2b shows that the pore pressure decreased below its initial value. Figure 2.2c and Figure 2.2d show that the behavior of this soil in the $q - p'$ and $q - \gamma$ spaces is slightly different though, it does not reach a maximum stress state until the end of loading and does not show the limited flow behavior of the first soil. Figure 2.2d also shows that overall the soil dilated.

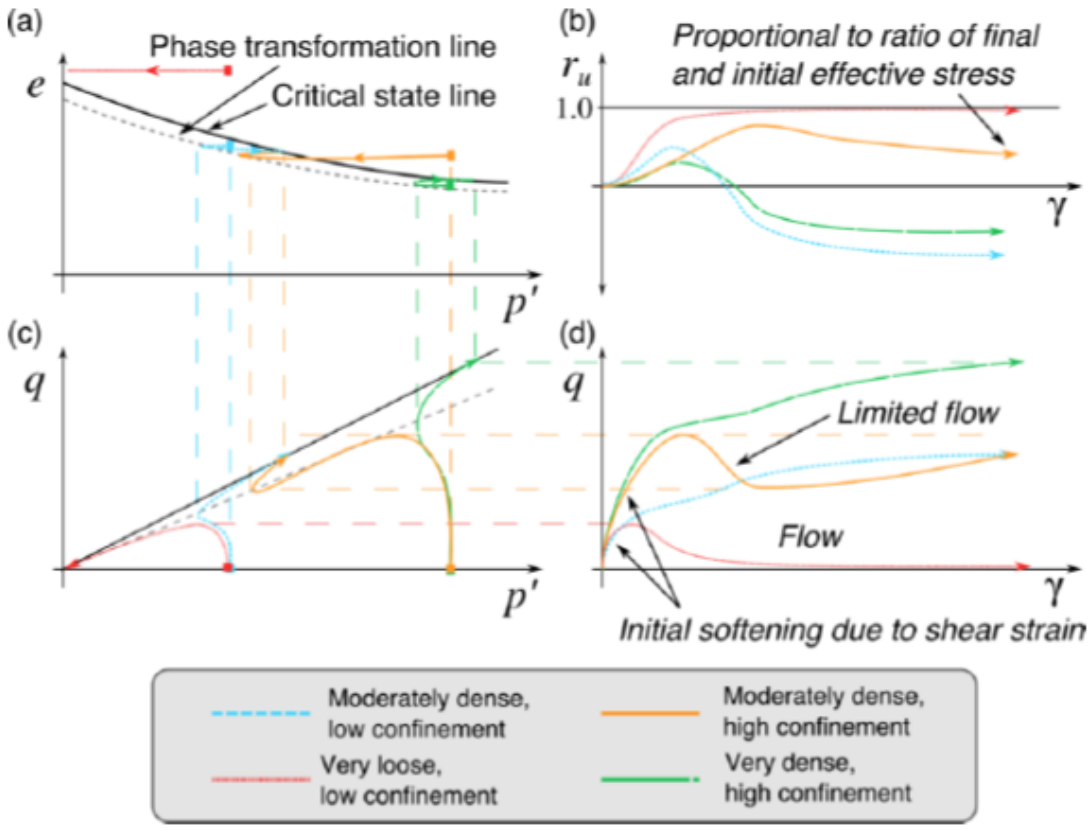


Figure 2.2: Monotonic undrained behavior of sand: a) behavior in void ratio versus mean effective stress space ($e - p'$); b) pore pressure ratio (r_u) versus shear strain (γ); c) deviatoric stress ($q = 2\hat{\tau}$) versus p'; d) q versus γ (Viana da Fonseca et al., 2017).

The behavior of the "very dense – high confinement" soil (green line), is almost identical to the second soil ("Moderately dense – low confinement"), however, the behavior is all at higher stresses. This apparent similarity in behavior provides the basis for critical state mechanics, where it can be seen that both soils are initially contractive and then dilative and do not exhibit flow. The stress state and density of the soil are intrinsically linked.

The final specimen, "very loose – low confinement" soil (red line), is an extreme case where the soil state is well above the critical state line (Figure 2.2a). In this case the soil contracts but only reaches the critical state line at very low mean effective stress, where the soil essentially loses all of its shear strength and stiffness. This behavior is called "flow" (Viana da Fonseca et al., 2017).

2.1.3 State parameters

Been and Jefferies (1985) defined the state parameter (ψ) based on critical state soil mechanics to quantify the relationship between stress and density (Figure 2.3). The state parameter (ψ) is simply the void ratio difference between the initial state of a soil and its critical-final state at the

same mean effective stress ($\psi = e - e_c$), allowing to quantify the influence of the void ratio and the stress level on the evaluation of sands behavior. This parameter is a useful reference point for understanding liquefiable soil behavior during undrained monotonic loading, where dramatic differences can be observed through the change of initial density and confining stress.

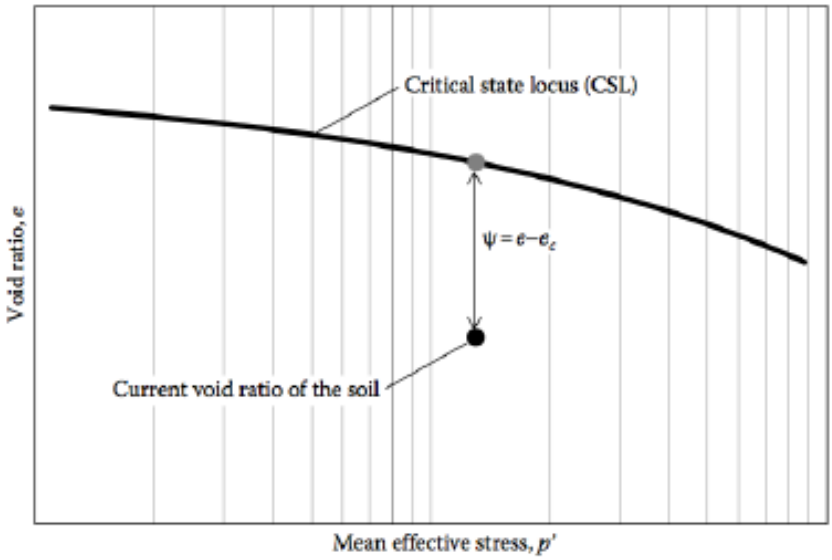


Figure 2.3: Definition of state parameter (Jefferies and Been, 2015).

Another boundary condition that is often used is the quasi-steady state (Yoshimine and Ishihara, 1998). This state exists when the soil deforms at constant volume during phase transformation and occurs for some loading conditions depending on the initial stress and density of the specimen (Alarcon-Guzman et al., 1988). Ishihara (1993) argues that the quasi-steady state is a more appropriate reference point for soil behavior as it is obtained at moderate to large strains (5-20%) compared to the critical state which is often only reached at strains of 20-30%.

Equation 2.1 was defined to quantify the behavior against the quasi-steady state through the State Index (I_S) parameter, where e_0 is the initial void ratio, e_{IC} represents the void ratio of the soil at its loosest state consolidated isotopically to the initial confining stress and e_{QSS} in the void ratio at quasi-steady state conditions (QSS).

$$IS = \frac{e_{IC} - e_0}{e_{IC} - e_{QSS}} \tag{2.1}$$

The critical state soil mechanics framework provides the basis for the majority of advanced soil constitutive models, thorough the use of the state parameter (ψ) or state index (IS). The relationship between density and confining stress allows the behavior of the soil to be described over a wide

range of stress and density states using the same set of model parameters. The major difference between the use of the quasi-steady line and the critical state line is that the critical state behavior should be independent on the initial fabric, while the quasi-steady state line is dependent on fabric (Verdugo, 1992). There are both benefits and drawbacks of this difference. Models that use the quasi-steady state as a reference tend to require further calibration of the model parameters to the specific soil specimen, compared to those that use the critical state and therefore ignore the influence of the initial fabric on the response.

2.1.4 Undrained cyclic loading

In contrast with monotonic loading, liquefaction triggering during cyclic loads is controlled not just by the density but also by the stiffness and cyclic energy dissipation. The initial contractive behavior of sand means that liquefaction or cyclic softening can occur even in dense soils. It is useful to understand the soil behavior in terms of uniform cycles of shear stress, even that in real in-situ conditions the demand is not often a uniform cyclic load and the change in soil stiffness and energy dissipation tends to modify the shear stress.

The number of cycles required to reach liquefaction is mainly controlled by the soil stress, density state and the fabric (Ishihara, 1993). This is typically quantified by liquefaction resistance curves, which quantify the number of cycles at a given uniform shear stress before liquefaction occurs. Figure 2.4 shows the results of torsional cyclic tests in Toyoura sand developed to illustrate the cyclic behavior during liquefaction process. The soil behavior after liquefaction is highly dependent on the tendency of the soil to dilate. Under large cyclic strain the soil dilates and causes a cyclic reduction in excess pore pressure and cyclic increase in the stiffness of the soil (strain hardening). The cyclic pore pressure reduction has twice the frequency of the cyclic loading, as large strains are reached twice during each cycle (Figure 2.4). The amplitude of the pore pressure reduction and subsequent strength and stiffness increase is controlled by the soil density and confining stress, among other soil parameters.

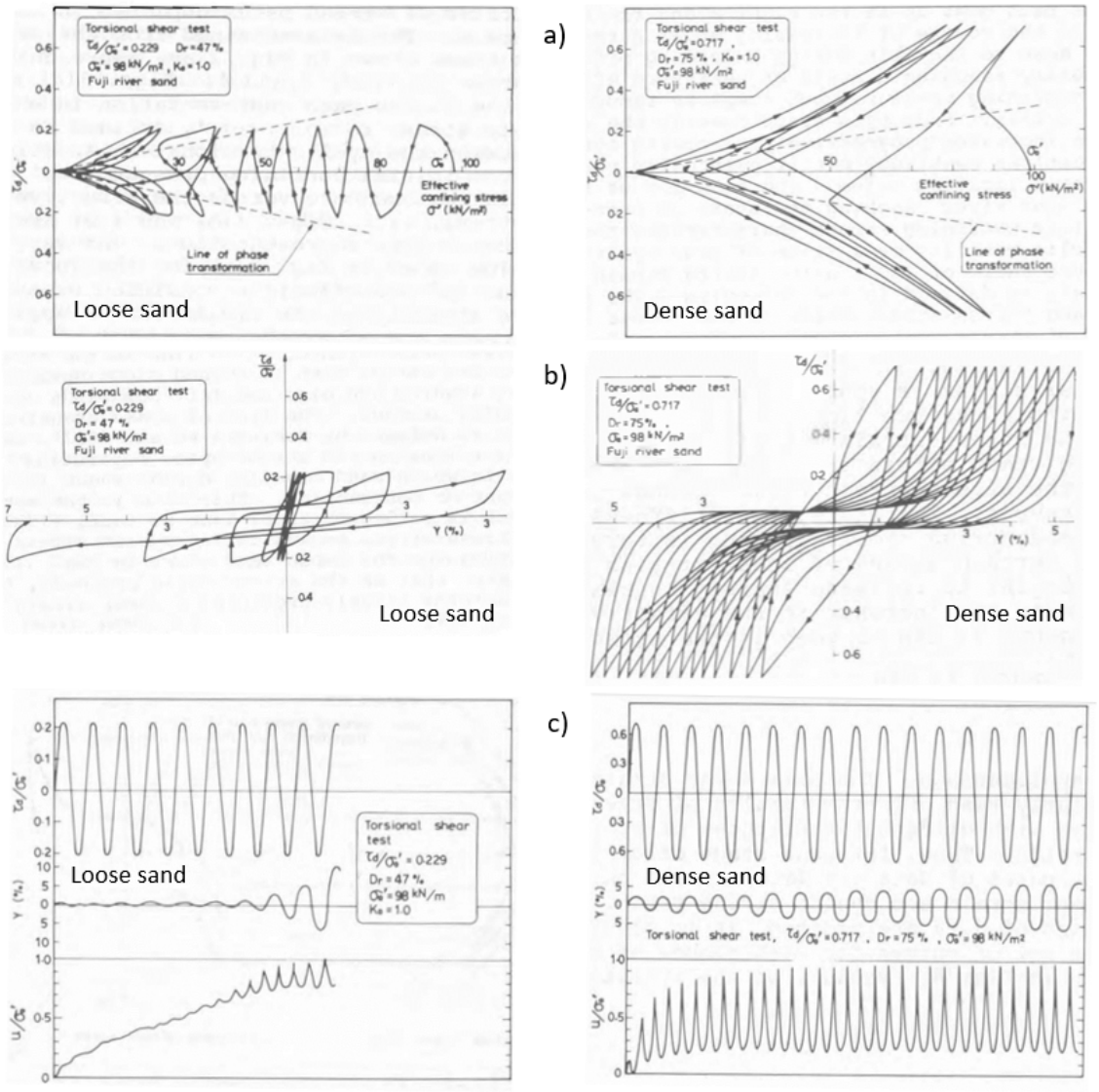


Figure 2.4: Behavior of Toyoura sand in cyclic torsional tests: a) stress-strain curve; b) stress-path; c) excess pore pressure generation (adapted from Ishihara, 1985)

2.1.5 Liquefaction susceptibility in free-field conditions

The cyclic stress procedure: general formulation

Liquefaction triggering is the critical part of most procedures for estimating liquefaction-induced damage. Occurrence of liquefaction can be estimated through simplified procedures or advanced constitutive modeling.

The best-known simplified methodology for treating the liquefaction phenomenon is the result of the work of Seed and co-workers at the University of Berkeley between the 1960s and the 1980s (Fernandes, 2020). This section presents their 'cyclic stress procedure', first formulated by Seed

and Idriss (1971).

The evaluation of safety against liquefaction for a given formation involves the calculation, at each depth, to the safety factor against liquefaction by means of the ratio between the resistance of the soil and the cyclic stress demand for the reference magnitude of 7.5 as showed in Equation 2.2.

$$F_L(z) = \frac{CRR_{M=7.5}(z)}{CSR_{M=7.5}(z)} \tag{2.2}$$

The soil mass on the surface represented in Figure 2.5a, in the at-rest-state doesn't have shear stress in the horizontal and vertical planes. But, if this soil mass is subjected to a horizontal acceleration history, at the instant in which the surface acceleration reaches its peak, a maximum shear stress along on a horizontal plane is reached.

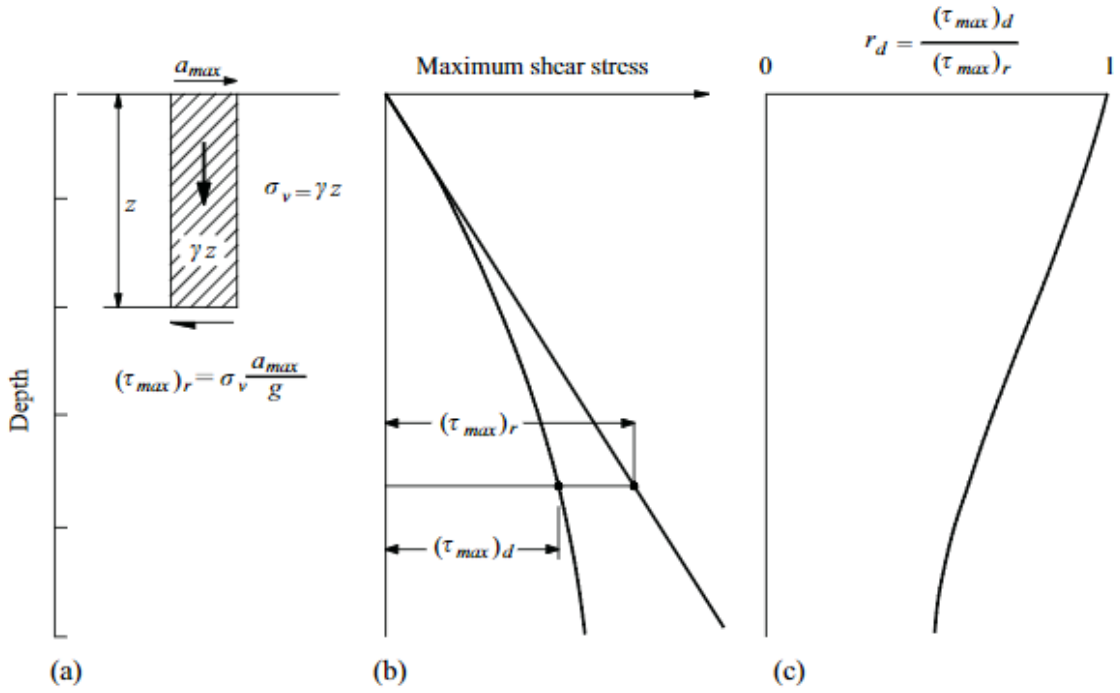


Figure 2.5: Simplified method for evaluating earthquake induced shear stresses: a) soil column scheme; b) change with depth of the shear stress in horizontal planes for the rigid and deformable body hypotheses; c) typical change with depth of the r_d coefficient, relating the previous stresses (Fernandes, 2020)

If the soil column showed in Figure 2.5a behaves as a rigid body, it would receive the horizontal inertial force (F_{ih}) in Equation 2.3, inducing in its base the shear stress in Equation 2.4, being a column of height z and unit base area.

$$F_{ih} = \frac{a_{max}}{g} \cdot \gamma \cdot z \tag{2.3}$$

$$(\tau_{max})_r = \frac{a_{max}}{g} \cdot \sigma_{v0} \tag{2.4}$$

Since the soil column is not a rigid body, the mobilized shear stress is lower than that given by the Equation 2.4 as suggested in Figure 2.5b and Equation 2.5. The $(\tau_{max})_d$ can be obtained by introducing a factor r_d lower than one and decreasing with depth as showed in Figure 2.5c. The typical trend of r_d was demonstrated through numerical simulations of the vertical propagation of earthquake-induced shear waves in sand deposits (Fernandes, 2020).

$$(\tau_{max})_d = \frac{a_{max}}{g} \cdot \sigma_{v0} \cdot r_d \tag{2.5}$$

The seismic action was defined by Seed and Idriss (1971) as an equivalent uniform cyclic loading, of constant frequency and amplitude, the latter being equal to 65% of the maximum earthquake amplitude,as represented by the cyclic shear stress in Equation2.6. If both members of this equation are divided by σ'_{v0}, the cyclic stress ratio (CSR_M), for a given seismic magnitude (M) is given by Equation 2.7.

$$\tau_{cyc} = 0.65 \cdot \frac{a_{max}}{g} \cdot \sigma_{v0} \cdot r_d \tag{2.6}$$

$$CSR_M = \frac{\tau_{cyc}}{\sigma'_{v0}} = 0.65 \cdot \frac{a_{max}}{g} \cdot \frac{\sigma_{v0}}{\sigma'_{v0}} \cdot r_d \tag{2.7}$$

Table 2.1 shows the number of uniform loading cycles as a function of earthquake magnitude (M). These results have been obtained from numerical simulation studies comparing the excess pore pressure generated in certain sand deposits, by real seismic records (with distinct magnitudes and maximum shear stress values) and by uniform cyclic loadings of amplitude equal to 65% of the maximum amplitude of the corresponding seismic record (Fernandes, 2020).

The cyclic stress ratio in Equation 2.7 has to be corrected in order to obtain the equivalent cyclic stress ratio for the reference magnitude of 7.5, $CSR_{M=7.5}$, since the liquefaction potential charts were prepared for that reference magnitude. Equation 2.8 shows the equation to estimate $CSR_{M=7.5}$, where MSF is the magnitude scaling factor. Different expressions should be used to calculate the MSF factor as a function of earthquake magnitude (e.g. Youd and Idriss (2001); CEN (2004))

$$CSR_{M=7.5} = \frac{CSR_M}{MSF} \tag{2.8}$$

Table 2.1: Number of cycles of a uniform loading of amplitude $0.65 \cdot \tau_{max}$, representative of various seismic magnitudes (Seed et al., 1975)

Magnitude (M)	Number of cycles with $0.65 \cdot \tau_{max}$
8.50	26
7.50	15
6.75	10
6.00	5-6
5.25	2-3

The resistance of the soil to liquefaction for a magnitude of 7.5 is expresses as the Cyclic Resistance Ratio ($CRR_{M=7.5}$). This resistance can be estimated through some of the liquefaction triggering correlations in Figure 2.6 as a function of the SPT result $(N_1)_{60cs}$ (normalized for an effective vertical stress of 100 kPa and for the standard energy ratio of 60%)

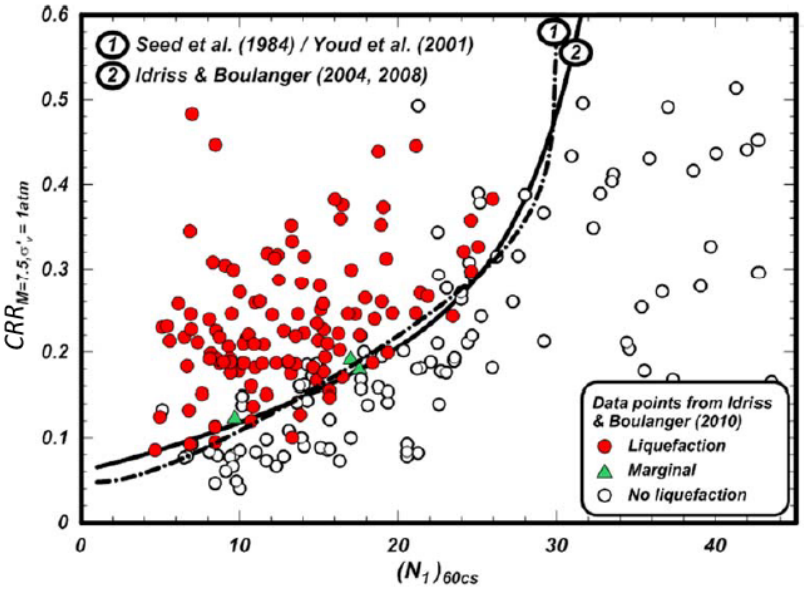


Figure 2.6: Correlations for cyclic resistance ratio (CRR) from SPT data (adapted from Boulanger and Ziotopolou, 2017)

More recent developments

The form of the simplified cyclic stress procedure has remained largely unchanged since its origin by Seed and Idriss (1971) (see previous section). However, the expressions for r_d, $CRR_{M7.5}$ and MSF have experienced several modifications and new factors (e.g. K_α, K_σ) have been created to better account for the site response, the soil type, the fines content, testing apparatus, plasticity of the soil and other factors (e.g. Seed et al., 2003; Moss et al., 2006; Cubrinovski et al., 2010; Boulanger and Idriss, 2014; Robertson, 2015).

The recent versions of the cyclic stress procedure are a very practical tool for assessing the soil susceptibility to liquefaction using easily obtainable field data. The most common simplified procedures are based on Standard Penetration Test (SPT) and Cone Penetration Test (CPT) data, while there are also methods that make use of the soil shear wave velocity and other testing instruments (Viana da Fonseca et al., 2016). Stress-based methods based on SPT and CPT tests are often used given the wide availability of these devices (e.g. Youd and Idriss, 2001; Moss et al., 2006; Boulanger and Idriss, 2014; Robertson, 2015).

The stress-based approach for evaluating the potential for liquefaction triggering proposed by Boulanger and Idriss (2014) (B&I), also compares the cyclic resistance ratio (CRR) of the soil with the earthquake-induced cyclic stress ratio (CSR) at any given depth as showed in Equation 2.2.

The cyclic stress demand (CSR_M) is also based on the peak ground surface acceleration (a_{max}) and total vertical stress (σ_{v0}), normalized by the effective vertical stress (σ'_{v0}) and corrected by the shear stress reduction coefficient (r_d), as a novelty incorporating the influence of both initial static shear stress (K_α) and overburden pressure (K_σ) as showed in Equation 2.9.

$$CSR_M = \frac{0.65 \cdot \sigma_{v0} \cdot a_{max}}{\sigma'_{v0}} \cdot r_d \cdot K_\alpha \cdot K_\sigma \tag{2.9}$$

The resistance of the soil to liquefaction, expressed as a Cyclic Resistance Ratio (CRR) is determined by means of a series of correlations from CPT and SPT results. These correlations normally estimate the CRR for cyclic loading equivalent to an earthquake event with magnitude of 7.5. Equation 2.10 shows how $CRR_{M=7.5}$ can be calculated from the normalized clean sand equivalent cone tip resistance ($q_{c1N,cs}$) obtained from $CPTu$ tests. Therefore, the CSR_M should be also adjusted to an equivalent event with magnitude 7.5 using a magnitude scaling factor (MSF) as showed Equation 2.8.

$$CRR_{M=7.5,\sigma'_v=1atm} = exp\left(\frac{q_{c1Ncs}}{113} + \left(\frac{q_{c1Ncs}}{1000}\right)^2 - \left(\frac{q_{c1Ncs}}{140}\right)^3 + \left(\frac{q_{c1Ncs}}{137}\right)^4 - 2.8\right) \tag{2.10}$$

The main disadvantage of the stress-based method is that liquefaction is ultimately a cumulative strain based phenomenon, where cyclic shear strain results in contraction of the soil skeleton causing liquefaction. To better account for the dependence on cumulative strain, several alternative methods have been proposed. The energy-based concept relies on a correlation between soil hysteretic energy dissipation and volumetric strain and typically uses Arias Intensity or Cumulative Absolute Velocity as an intensity measure (Bán et al., 2017). Energy-based methods have the advantage of using a single intensity measure and using a cumulative intensity measure gives an indication of the build-up of pore pressure throughout the motion. The main disadvantage is that the majority of seismic design standards and codes do not provide estimates of these cumulative intensity measures.

2.1.6 Soil constitutive models

Introduction

Numerical modeling of soil liquefaction is becoming an important part of liquefaction research due to the difficulties and costs associated with experimental and field based research. However, the complexity about soil fabric and the pore water pressure build up makes numerical modeling extremely demanding for the user and the software. In order to simulate the seismic response of liquefiable soils, comprehensive constitutive models with the ability to describe salient physical phenomena of the soils cyclic response have been created. According to Kramer and Elgamal (2001), a constitutive model to simulate liquefaction behavior should account for the nonlinear inelastic shear stress-strain response, the dependence of shear and volumetric stiffness on effective confining pressure, the contraction of the soil skeleton during the early stages of loading, the dilation of the soil skeleton at large strain excursions, the critical state at which shearing occurs with neither contractive nor dilative tendencies, the controlled accumulation of cyclic shear strain when cyclic loading is superimposed upon static stresses, the post-liquefaction void-ratio redistribution, the coupling response of the soil skeleton and pore water and the effect of the permeability of the soil on the rate at which volume change can occur.

The complete set of these features are beyond the capabilities of current constitutive models, but they provide a useful set of criteria for the development and validation of current and new models. It should also be noted, that the importance of various features depends on the situation and modeling goal and that one of the most important requirements of all constitutive models is the simplicity in how the model parameters can be obtained from field or laboratory tests.

Some examples of constitutive models implemented in different software for liquefaction and soil-structure interaction modeling include the PDMY02 (Yang et al., 2008), Stress-Density (Cubrinovski and Ishihara, 1998a; Cubrinovski and Ishihara, 1998b; Das, 2014), PM4Sand (Boulanger and Ziotopolou, 2017), NTUA-Sand (Andrianopoulos et al., 2010), UBCSAND (Beaty and Byrne,

1998) and UBC3D-PLM (Petalas and Galavi, 2013).

In this work the PM4Sand constitutive model will be used (Boulanger and Ziotopolou, 2017). The PM4Sand is a sand plasticity model specially developed for geotechnical earthquake engineering applications following basically the framework of the stress-ratio controlled, critical state compatible, bounding surface plasticity model for sand presented by Dafalias and Manzari (2004) but with some modifications to improve its ability to approximate stress-strain responses important for geotechnical earthquake engineering applications. The PM4Sand model has been used to successfully model case histories (Bray and Macedo, 2017)and centrifuge tests (Boulanger et al., 2017; Ziotopoulou and Montgomery, 2017; Viana da Fonseca et al., 2018).

This constitutive model has been implemented in different commercial software programs, including the FLAC software (Itasca Consulting Group, Inc., 2016) and the PLAXIS 2D software (Bentley, 2020). These software are some of the most commonly used for simulation of soil liquefaction.

FLAC, Fast Lagrangian Analysis of Continua, is a numerical modeling software for advanced geotechnical analysis of soil, rock, groundwater, and ground support, developed by Itasca Consulting Group Inc. (Itasca Consulting Group, Inc., 2016). It utilizes an explicit finite difference formulation that can model complex problems, such as problems that consist of several construction stages, large displacements and strains, non-linear material behavior or unstable systems (Itasca Consulting Group, Inc., 2016). The bulk modulus of the fluid as well as drained, undrained, or fully coupled stress-flow conditions may be specified. The software is capable of modeling the coupling response between the soil skeleton and the pore fluid, and can model the redistribution of pore pressure during shaking in either two- or three-dimensions. It also features the so called "FISH scripting", which enables the user to interact with and manipulate the numerical models, as well as Python scripting. User-defined constitutive models can be also implemented in the software. Luque and Bray (2015, 2017) and Ziotopoulou and Montgomery (2017) are some recent examples of the use of FLAC and PM4Sand constitutive model for liquefaction modeling.

PLAXIS 2D is a powerful and user-friendly finite element (FE) analysis software for 2D analysis of deformation and stability in geotechnical engineering and soil mechanics. PLAXIS 2D is used worldwide by leading engineering companies and institutions in the civil and geotechnical engineering sector. PLAXIS 2D is ideal for a range of uses from excavations, seawalls and foundations to tunnel geomechanics, mining, oil, gas and reservoirs. PLAXIS 2D includes all the essential elements to perform deformation and safety analyzes for soils and rocks that do not require consideration of creep, steady-state groundwater flow or heat flux, analysis of consolidation or any time-dependent effects. The Dynamics module of PLAXIS 2D allows the user to perform dynamic analyses of the propagation of waves through the soil and their influence on structures. Borozan et al. (2017), Vilhar et al. (2018b) and Quintero et al. (2018) are some recent examples of the use

of PLAXIS 2D and PM4Sand constitutive model for liquefaction modeling.

PM4Sand constitutive model

The PM4Sand constitutive model was presented by Boulanger (2010), later it was updated to version 2.0 by Boulanger and Ziotopolou (2012a), to version 3.0 by Boulanger and Ziotopolou (2012b) and more recently to version 3.1 by Boulanger and Ziotopolou (2017). The calibration of PM4Sand model and its implementation in the software FLAC was presented by Boulanger and Ziotopoulou (2013). More recently, its implementation in the software PLAXIS 2D was presented by Vilhar et al. (2018a).

This constitutive model uses the relative state parameter index (ξ_R) to approximate the curving of the critical state line that occurs over a broad range of confining stresses as presented in Figure 2.7. The relative state parameter (Konrad, 1988) is the state parameter normalized by the difference between the maximum void ratio (e_{max}) and minimum void ratio (e_{min}) values that are used to define relative density (D_R).

$$\xi_R = D_{R,cs} - D_R \tag{2.11}$$

$$D_{R,cs} = \frac{R}{Q - ln\left(100 \cdot \frac{p}{p_A}\right)} \tag{2.12}$$

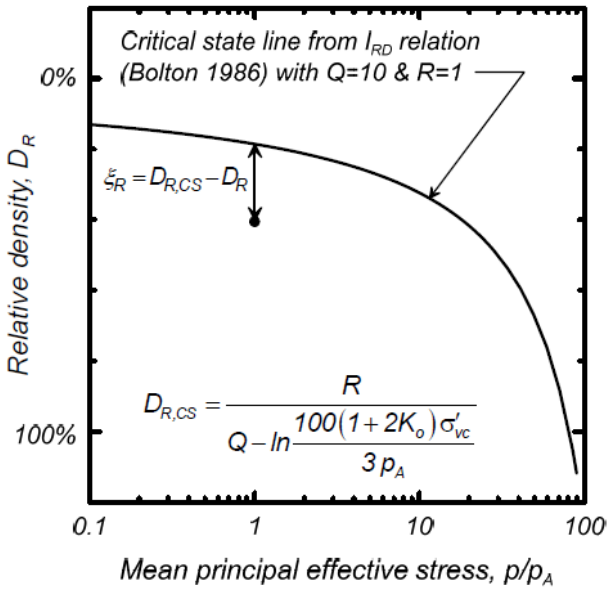


Figure 2.7: Definition of the relative state parameter index (ε_R) (Boulanger and Ziotopolou, 2017)

The relative state parameter index is just the relative state parameter defined using an empirical relationship for the critical state line. Boulanger (2003) used the dilatancy relationship proposed by Bolton (1986) to define the empirical critical state line and thus arrived at Equations 2.11 and 2.12, where $D_{R,cs}$ is the relative density at critical state for the current mean effective stress, Q is about 10 and R is about 1.0 for quartzitic sands (Bolton, 1986). Critical state lines using the above expression with Q values of 9 and 10 with R values of 1.0 and 1.5 are shown in Figure 2.8.

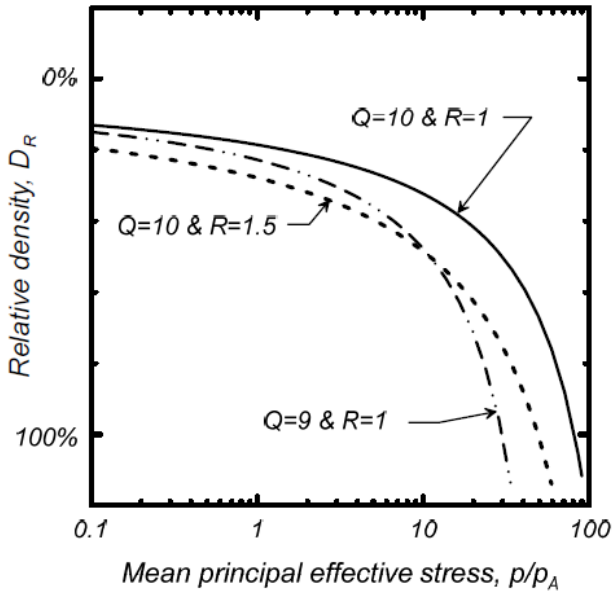


Figure 2.8: Effects of varying Q and R (Boulanger and Ziotopolou, 2017)

This model simplifies the bounding, dilatancy and critical surfaces presented by Dafalias and Manzari (2004) by removing the Lode angle dependency (since the model is only implemented in 2D and therefore there is no consideration of the out-of-plane stress) such that the bounding (M^b) and dilatancy (M^d) ratios can be related to the critical stress ratio (M) by the Equations 2.13 and 2.14, where n^b and n^d are parameters determining the values of M^b and M^d, respectively. M is represented by Equation 2.15 since for this model the mean normal stress p is taken as the average of the in-plane normal stresses, q is the difference in the major and minor principal in-plane stresses. ϕ_{cv} is the constant volume or critical state effective friction angle. The three surfaces can be visualized as linear lines on a $q-p$ plot ($q = \sigma_1 - \sigma_3$), as shown in Figure 2.9. As the model is sheared toward critical state ($\xi_R = 0$), the values of M^b and M^d will both approach the value of M. Thus, the bounding and dilatancy surfaces move together during shearing until they coincide with the critical state surface when the soil has reached critical state.

$$M^b = M \cdot exp(-n^b \cdot \xi_R) \tag{2.13}$$

$$M^d = M \cdot exp(-n^d \cdot \xi_R) \tag{2.14}$$

$$M = 2 \cdot \sin(\phi_{cv}) \tag{2.15}$$

The yield surface is a small cone in stress space, and is defined in stress terms by the Equation 2.16, where α is the back-stress ratio tensor defining the centre of the yield surface and m defines the radius of the cone in terms of stress ratio. The yield function can be related to the distance between the stress ratio r and the back-stress ratio α.

$$f = \sqrt{(r-\alpha) : (r-\alpha)} - \sqrt{\frac{1}{2} \cdot m} \tag{2.16}$$

The model parameters are grouped into two categories; a primary set of six parameters (three properties, two flags, and atmospheric pressure) that are most important for model calibration, and a secondary set of parameters that may be modified from their default values in special circumstances (Boulanger and Ziotopolou, 2017).

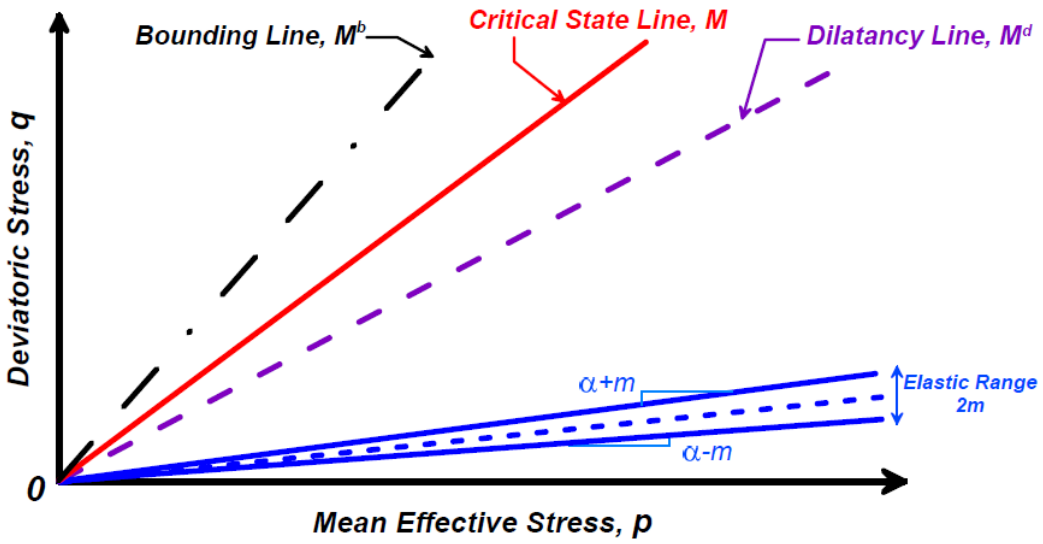


Figure 2.9: Schematic of yield, critical, dilatancy and bounding lines in $q-p$ space. Relative location of dilatancy and bounding lines corresponds to dense-of-critical state of stress (Boulanger and Ziotopolou, 2017)

Apparent relative density (D_R) is a primary variable controlling dilatancy and stress strain response characteristics. Relative density can be estimated in practice by correlation to penetration

resistances. For example, a common form for SPT correlations is Equation 2.17, where D_R is expressed as a ratio rather than a percentage and $(N_1)_{60}$ is the SPT blow count (N-value) corrected for field procedures and overburden pressure. Idriss and Boulanger (2008) adopted a value of $C_d = 46$ in the development of their liquefaction triggering correlations. For the CPT, Equation 2.18 is widely used, where q_{c1N} is the normalized cone penetration resistance corrected for overburden and and 0.9 is adopted for C_{dq} factor (Idriss and Boulanger, 2008).

$$D_R = \sqrt{\frac{(N_1)_{60}}{C_d}} \tag{2.17}$$

$$D_R = 0.465 \cdot \left(\frac{q_{c1N}}{C_{dq}}\right)^{0.264} - 1.063 \tag{2.18}$$

The input value of D_R is best considered as "apparent relative density," rather than a strict measure of relative density following conventional laboratory tests. The input value of D_R influences the response of the model (affects the peak drained and undrained strengths and the rate of strain accumulation during cyclic loading) and thus it is just another input parameter that the user can adjust as part of the calibration process. The above correlations are provided for the purpose of obtaining a reasonable estimate for the apparent D_R so that the resulting model behaviors are also reasonable. There are situations, however, where the user may choose to adjust the input D_R, up or down relative to the above relationships, to improve its calibration to some other relationship or data.

Shear modulus coefficient (G_o) is also a primary variable controlling the small strain (elastic) shear modulus, G_{max}. It should be chosen to match estimated or measured shear wave velocities (v_s) according to Equations 2.19 and 2.20, where p_A is the atmospheric pressure, p is the mean effective stress and ρ is the soil density. Shear modulus coefficient (G_o) can also be estimated based on the modified correlation between $(N_1)_{60}$ and v_{s1}, using first Figure 2.10 and then Equation 2.21.

$$G_o = \frac{G_{max}}{p_A \cdot \left(\frac{p}{p_A}\right)^{1/2}} \tag{2.19}$$

$$G_{max} = \rho \cdot v_s^2 \tag{2.20}$$

$$G_o = 167 \cdot \sqrt{(N_1)_{60} + 2.5} \tag{2.21}$$

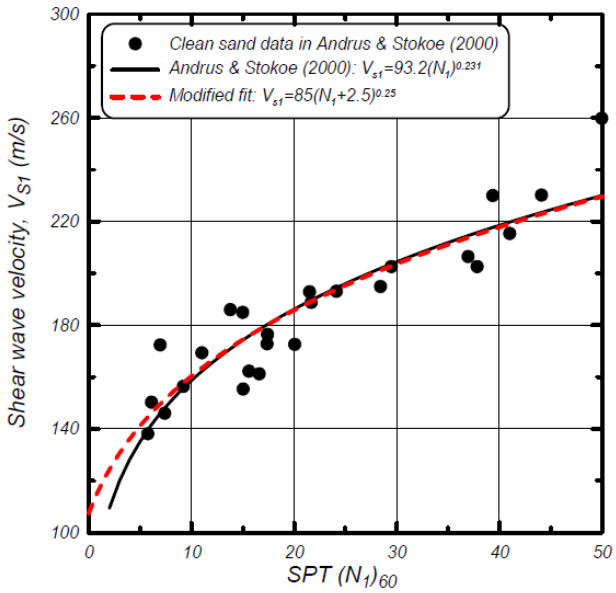


Figure 2.10: Correlation between overburden-corrected shear wave velocity and SPT penetration resistances in clean sands (Boulanger and Ziotopolou, 2017)

Contraction rate parameter (h_{po}) is the third primary variable that adjusts contraction rates and hence can be adjusted to obtain the estimated in-situ cyclic resistance ratio (CRR), as commonly estimated based on CPT or SPT penetration resistances and liquefaction correlations.

The target CRR values can be estimated on the liquefaction triggering correlation by Idriss and Boulanger (2008) in Figure 2.6. This relationship produces target CRR values for an effective overburden stress of $1atm$ and an earthquake magnitude (M) of 7.5. Calibration of h_{po} parameter should be performed last because its value can depend on the values assigned to other parameters.

Viana da Fonseca et al. (2018) performed a parametric set of over a thousand undrained cyclic direct simple shear (DSS) test simulations (element tests) to suggest an equation to estimate the contraction rate parameter (h_{po}). The apparent relative density (D_R), shear modulus coefficient (G_o) and contraction rate parameter (h_{po}) were systematically varied with a confining stress of 100 kPa, and the cyclic resistance ratio (CRR) for 15 cycles was obtained through the numerical element tests. A set of 1020 analyses were performed considering six D_R, seventeen h_{po} and ten cyclic stress ratio (CSR) values (Figure 2.11). $(N_1)_{60}$ was back calculated by using Equation 2.17 and then used in Equation 2.21 to estimate the shear modulus coefficient (G_o).

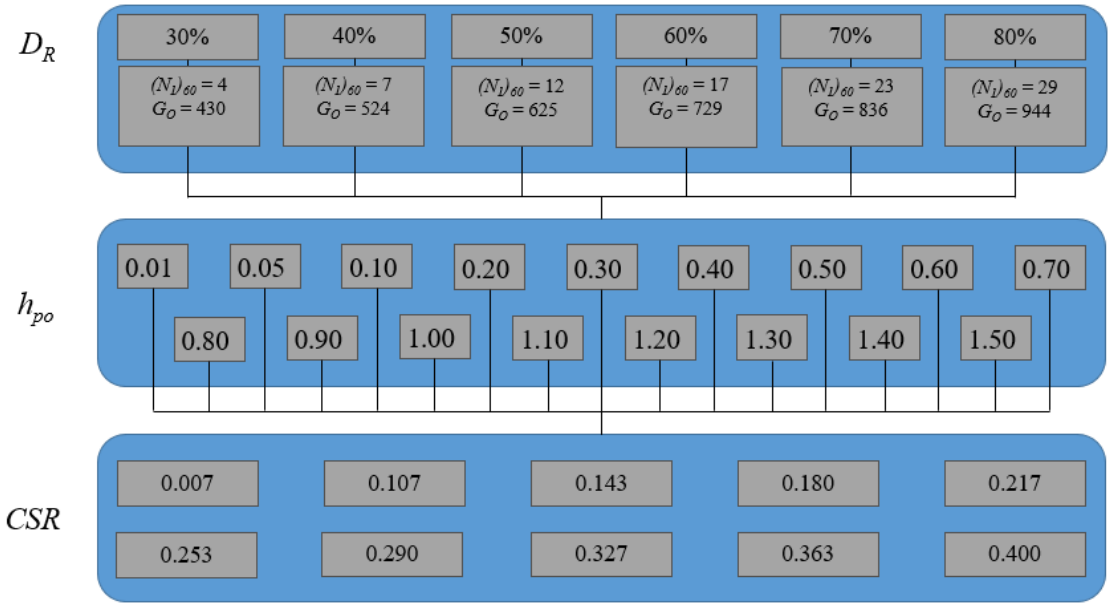


Figure 2.11: Logic tree of inputs and modeling decisions for h_{po} study

Ten element tests for each $D_R - h_{po}$ set were performed; the difference between them was just the shear stresses induced (assessed by the cyclic stress ratio – CSR). The element tests were configured to stop when a 5% of shear strain was reached. The number of cycles causing a pore pressure ratio (r_u) of 98% was estimated for each CSR induced. The number of cycles causing a r_u of 98% was plotted against the CSR induced for each $D_R - h_{po}$ set. Figure 2.12 shows the number of cycles causing a r_u of 98% applying the ten different CSR for sands having an initial D_R of 40%.

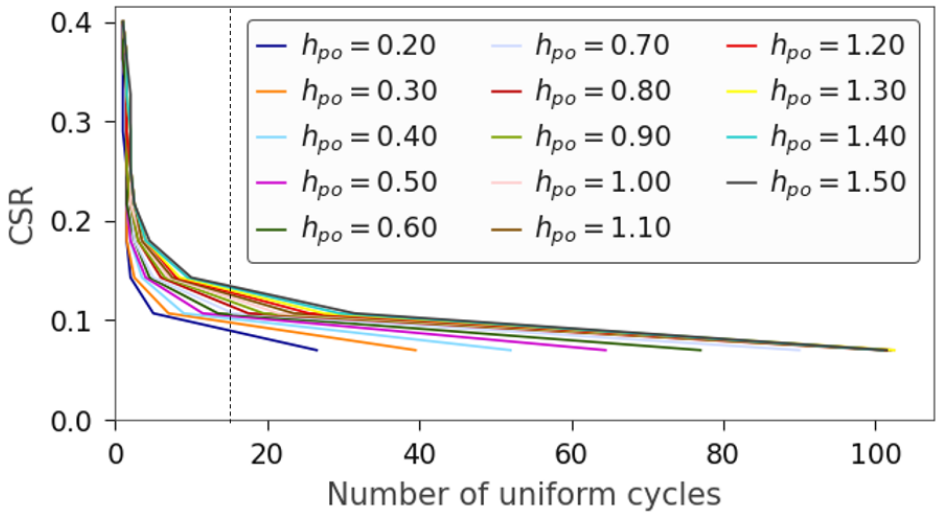


Figure 2.12: Cyclic stress ratios versus number of equivalent uniform loading cycles in undrained DSS loading to cause r_u=98% for D_R=40%.

Through interpolation, the CSR corresponding to 15 uniform loading cycles (CRR_{15}) was obtained (15 cycles represent an earthquake with a magnitude of 7.5) for each $D_R - h_{po}$ set of data. Response of the model using the three lower h_{po} values (0.01, 0.05 and 0.10) were not included because for these cases the soil liquefied before 15 cycles.

Figure 2.13 shows the CRR_{15} estimated against the respective h_{po} for each D_R analyses (straight lines). Through a regression analysis, results from parametric study simulations were used and Equation 2.22 was developed. Dashed lines in Figure 2.13 show the curves obtained from Equation 2.22 evidencing the close agreement with the curves obtained from element test results. Equation 2.23 was obtained from Equation2.22 and was proposed by Viana da Fonseca et al. (2018) to calculate the h_{po} parameter when PM4Sand constitutive model is used. Millen et al. (2020, 2021) used this equation for their numerical analyses.

$$CRR_{15} = \frac{h_{po}}{2.1 - 2.4 \cdot D_R + h_{po} \cdot (12.0 - 12.5 \cdot D_R)} \tag{2.22}$$

$$h_{po} = \frac{CRR_{target} \cdot (2.1 - 2.4 \cdot D_R)}{1 - CRR_{target} \cdot (12.0 - 12.5 \cdot D_R)} \tag{2.23}$$

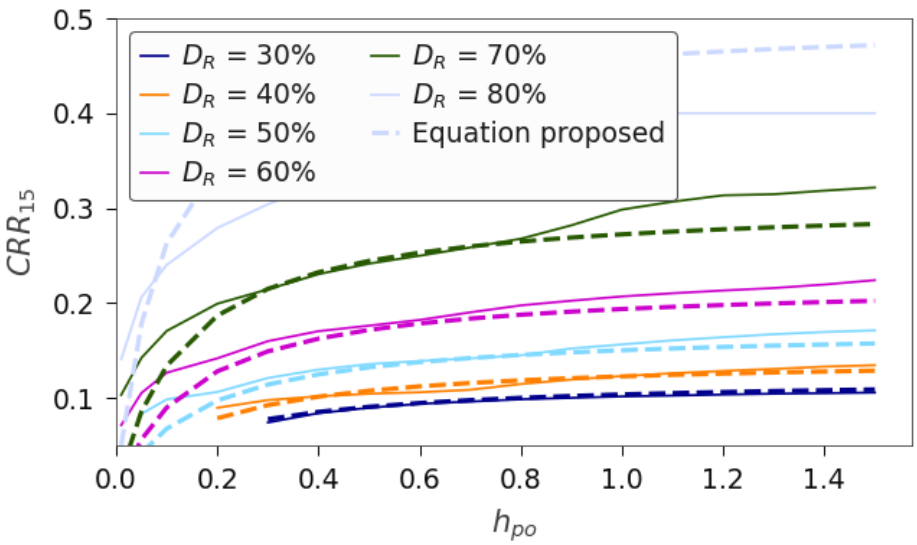


Figure 2.13: Cyclic stress ratios corresponding to 15 uniform loading cycles (CRR_{15}) versus h_{po} values from element test results

The value of atmospheric pressure, p_A, should also be specified in the unit set being used for the analysis. If not specified, it will default to $101.300 Pascal$.

The flag $FirstCall$ is used to re-set the back-stress ratio history terms equal to the current stress ratio, and to erase all fabric terms. The first time the model is called, the flag should be unspecified or have a value of zero. The model will then initiate the back-stress ratios and all pertinent history terms using the current state of stress. The flag is then set equal to one internally. If $FirstCall$ is later set equal to zero, this will cause the material to re-initiate all internal terms, thereby re-setting the back-stress and stress ratio history terms and erasing all fabric terms. $FirstCall$ should usually be set to zero just before initiating dynamic earthquake loading. Otherwise, the model will retain memory of the loading during the static initiation of the model, which may or may not be desired.

The flag $PostShake$ is used during the post-shaking portion of a simulation to improve the modeling of post-liquefaction reconsolidation strains. The flag is set to zero internally and remains zero unless the user specifies otherwise. If the flag is set to one, the elastic modulus will be reduced. $PostShake$ should only be set to one at the end of strong shaking, as the reductions in elastic modulus were not calibrated for cyclic loading behavior.

Secondary input parameters are those parameters for which default values have been developed. That will generally produce reasonable agreement with the trends in typical design correlations. The user must, however, still confirm through element loading calibrations that the default parameters are appropriate for their particular conditions. The secondary input parameters (21 in total) with the recommended default values are listed in Table 2.2.

Table 2.2: Secondary input parameters of PM4Sand constitutive model (Boulanger and Ziotopolou, 2017)

Parameter	Default value
h_o	$(0.25 + D_R)/2 \geq 0.3$
e_{max}	0.8
e_{min}	0.5
n^b	0.50
n^d	0.10
A_{do}	$1.2 \leq A_{do} \leq 1.5$
z_{max}	$0.7 \cdot exp(-6.1 \cdot \xi_R) \leq 20$
c_z	250.
c_s	5.0 if $D_R \leq 35\%$; $5.0 \geq c_s \geq 1.0$ if $35\% \leq D_R \leq 75\%$; 1.0 if $D_R \geq 75\%$
ϕ_{cv}	33
υ_o	0.30
C_{GD}	2.0
C_{DR}	$5 + 25(D_R - 0.35) \leq 10$
$C_{k\alpha f}$	$4.0 \leq 5 + 220 \cdot (D_{R0}–0.26)^3 \leq 35$
Q	10
R	1.5
m	0.01
$F_{sed,min}$	$0.03 \cdot exp(2.6 \cdot D_R) \leq 0.99$
$p'_{sed,o}$	$–P_{atm}/5$
cr_{hg}	0.005
c_{hg}	$cr_{hg} \cdot p$

2.2 Soil-structure interaction

The modeling of an infinite soil medium that is coupled, not only in terms of shear and volumetric strains, but also coupled with the water pressure and is highly non-linear and stress dependent, is an impressively challenging task, not just for the user but for the software and computer as well. The combination of the complexities of fully coupled effective stress soil modeling with the dynamic non-linear response of a structure, which is made of multiple brittle and ductile materials, has discrete and continuous joints between different elements, and can partially uplift from the soil under strong shaking, is at the limits of the abilities of numerical modeling. There are always trade-offs with numerical modeling, where some phenomena are not considered or are captured

through a series of separate numerical models (Viana da Fonseca et al., 2017).

The primary damage to buildings during earthquakes is shaking damage, therefore the modification to the ground shaking due to liquefaction is extremely important in the context of quantifying building performance.

Ishihara and Cubrinovski (2005) investigated the ground motions recorded at the Kobe Port Island Vertical Array site during the 1995 Kobe earthquake, illustrating that liquefaction caused a reduction in shaking amplitude, a loss of high frequency content and a shift to longer motion period, in comparison to the adjacent Pack House site which experienced less liquefaction. In Adapazari, the heaviest concentrations of damage in the city generally coincided with surface soils that were less sensitive to liquefaction, whereas in areas with higher susceptibility to liquefaction, the building damage was relatively reduced (Bakir et al., 2002). These perceived beneficial effects have even prompted interest in deliberately using liquefaction to isolate buildings from strong shaking (Mousavi et al., 2016).

However, liquefaction does not always result in less shaking. As matter of fact, Bouckovalas et al. (2016) demonstrated that liquefaction of the soil can cause an amplification in the seismic shaking, especially in lower frequencies, which is highly dependent on the depth of the liquefied layer. Moreover, investigations by Wotherspoon et al. (2015) of the ground motion station NNBS during the 2011 Christchurch earthquake, demonstrated post-liquefaction acceleration spikes that were double the amplitude of the pre-liquefaction acceleration values.

The current comprehension suggests that liquefaction results in a decrease in soil shear stiffness and resistance, an increase in soil shear strain, and the potential to amplify or attenuate specific frequencies of surface shaking. Consequently, the extent of surface shaking amplification or reduction, in peak values, owing to liquefaction, depends on both the frequency composition of the outcrop motion and the geotechnical characteristics unique to the site (Viana da Fonseca et al., 2017).

Conceptually, the reduction in stiffness can provide protection to buildings similar to base isolation techniques used within structural engineering, and it is often referred to as “natural seismic isolation” as illustrated in Figure 2.14.

There are many other mechanisms and phenomena as fault rupture mechanics, distance to fault, orientation of incident shear waves, influence of surface waves, topographic amplification and basin effects that contribute to the response and ground shaking of a site, but they occur independently of whether liquefaction occurs.

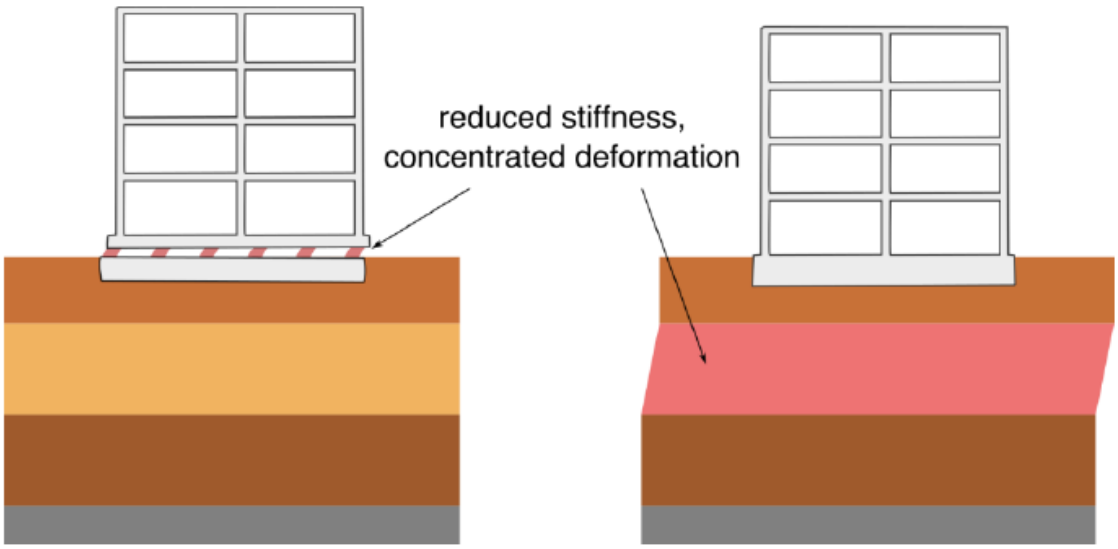


Figure 2.14: Conceptual natural seismic isolation due to liquefaction (Viana da Fonseca et al., 2017)

The vulnerability assessment of buildings on shallow foundations in liquefiable soils has been mainly focused on soil deformation and consequent damage to foundations. Since soil softening associated with liquefaction acts as a natural isolation barrier (Karatzia et al., 2019), the damage associated with strong ground shaking, in conjunction with ground deformation, is often neglected. However, several studies (e.g., Dashti et al., 2010b; Kramer et al., 2011) have demonstrated that, when liquefaction occurs later in the strong shaking, buildings exhibit both considerable shaking induced damage, as well as settlements. In fact, partial liquefaction under a building, leads to soil deformation and consequent changes in its dynamic properties, which can potentially amplify its dynamic response. In order to consider strong shaking-induced damage when liquefaction occurs, the interaction between the soil, the foundation and the structure needs to be better understood, and a framework should be established in order to account for the combined damage and loss induced by both soil-foundation deformation and by shaking (Millen et al., 2018).

While there are efforts to quantify the vulnerability of buildings to liquefaction using empirical field data sets (e.g. Paolella et al., 2021) these approaches are limited by the availability and quality of the data. Different approaches can be adopted to consider soil-structure interaction (SSI) in liquefiable soils, as indicated in Figure 2.15. The building-soil system can be assessed directly by modeling both soil and building in a single numerical or experimental model (a full model approach), e.g. see Dashti et al. (2010b), Dashti and Bray (2013) and Ramirez et al. (2018).

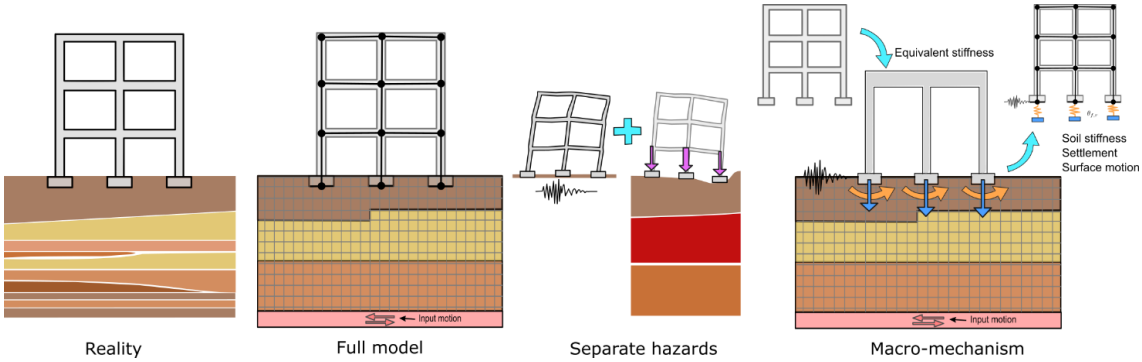


Figure 2.15: Different modeling approaches for SSI in liquefiable soils (Viana da Fonseca et al., 2023)

Alternatively, the building response and soil response can be completely decoupled. In this case, shaking and liquefaction damage are assessed independently and then combined through an interaction function (separate hazards approach), such as in the HAZUS methodology (Fema, 2003) or in the proposal of Bird et al. (2006) or imposing ground deformations directly or indirectly to a building (e.g. Fotopoulou et al., 2018, Gomez-Martinez et al., 2020).

The full model approach, where both soil and structure are modeled together with adequate constitutive laws in a single simulation, is advantageous because the interactions between all the mechanisms are implicitly accounted for. However, it is a demanding task to develop an adequate full model that accurately captures the complex effective stress-controlled soil behavior and the various nonlinear mechanisms in a building.

Notably, none of the widely used commercial software currently contain both a three-dimensional state-compatible constitutive model for the soil, and elements for modeling existing structures (e.g. reinforced concrete buildings) with a suitable array of nonlinear material constitutive models. Therefore, a trade-off must be made by reducing the accuracy for the soil or the structural modeling. In addition, the full model approach is computationally demanding as nonlinear structural models with degrading behavior often require very small time steps to achieve convergence, while in the large soil domain medium, there are many degrees-of-freedom to be assessed at each time step.

Furthermore, a full model approach is problem-specific, since advanced constitutive models need to be developed and calibrated for different soil types. Since the full model approach does not benefit from generalizing behavior, a single change in one assumption would require the numerical model to be completely re-run.

The separate hazards approach is numerically efficient and can make use of existing results for ground shaking damage (e.g. fragility functions), but it suffers from some significant drawbacks. The use of an interaction function to combine shaking and liquefaction damage is non-trivial. Es-

sentially, liquefaction modifies the shaking demand and differential settlements modify the capacity of the building, which influences the shaking damage. Meanwhile, liquefaction-induced settlement and tilt are dependent on the inertial load (shaking) of the building.

Viana da Fonseca et al. (2018) proposed an innovative modular methodology called "macro-mechanism approach" for reinforced concrete framed structures on shallow foundations in liquefiable soil deposits, where different macro-mechanisms are first quantified and then connected considering their interactions. The idea of the methodology is to capture the full system behavior through a combination of sub-models (e.g. a pore pressure model, a settlement model) that focus on a particular mechanism or system behavior, rather than at the constitutive level, for this reason, it was called the macro-mechanism approach. The procedure was applied in an extensive parametric study for the development of the fragility functions for loss assessment LIQUEFACT software (Meslem et al., 2019), and to assess liquefaction-induced loss at critical infrastructure, as described by Meslem et al. (2021).

The so-called macro-mechanism approach addresses the three liquefaction-induced macro-mechanisms of changes in ground shaking, changes in foundation impedances, and settlement, through a series of time dependent sub-models which are subsequently integrated into a time history analysis of the building using springs, dashpots and imposed displacements. The development of the model requires four steps that can either be performed separately or in combination:

1. Quantify the liquefaction potential of the soil profile in terms of depth and thickness of the liquefiable layer(s) and the resistance to liquefaction. The free-field pore pressure ratio is then quantified throughout the duration of shaking.

2. Estimate the near field ground shaking time series accounting for liquefaction, for use as acceleration input for the building time history analysis.

3. Estimate the soil-foundation stiffness using springs and dashpots, and account for the change in soil characteristics due to liquefaction and nonlinear shear deformation throughout the duration of shaking.

4. Estimate the expected load-settlement behavior of each footing accounting for the expected level of pore pressure build-up throughout the duration of shaking.

The key aspects of this approach can be seen in Figure 2.16, where the outputs of the four steps are used as inputs into a nonlinear model of the building. The input motion is the expected near-field motion from Step 2 and the expected differential settlement behavior is captured through a combination of imposed settlement (Step 4) and changes in the stiffness of the soil springs (Step 3). It is recognized that this decoupling introduces inaccuracies.

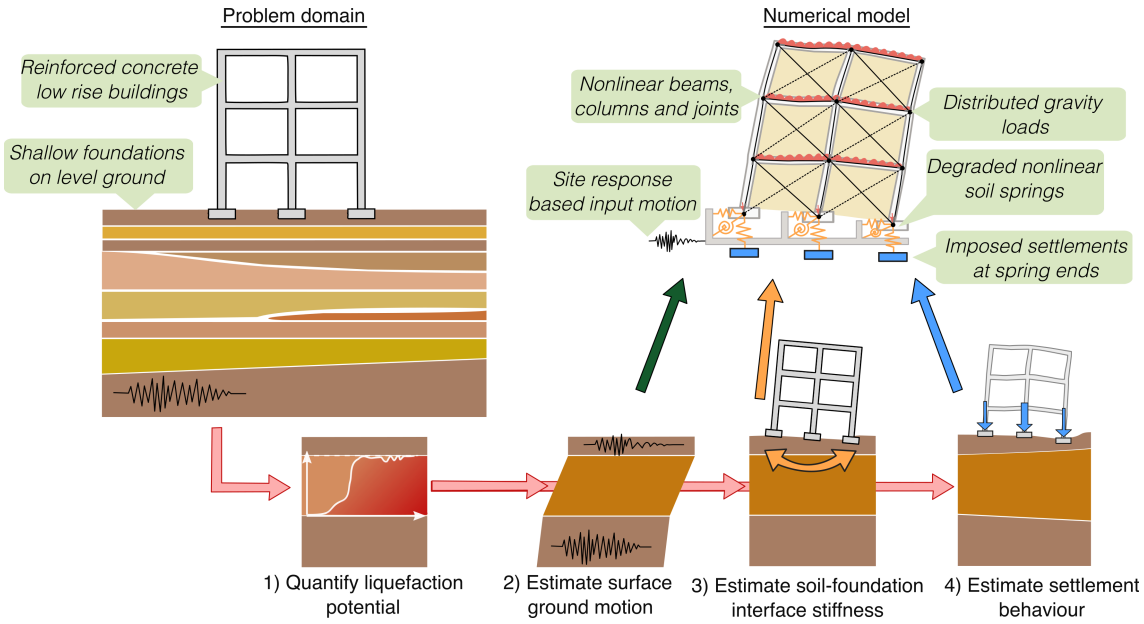


Figure 2.16: Macro-mechanism approach (Viana da Fonseca et al., 2023)

The dynamic response of the structure is influenced by the soil deformations during seismic loading which are imposed to the foundation. The compliance of the supporting soil modifies the behavior of the structure and the interplay between the soil, foundation and superstructure is called Soil-Structure Interaction (SSI) in literature.

The accurate estimation of the effects of SSI is one of the biggest challenges for geotechnical and structural engineering due to the large number of variables involved such as the soil behavior, foundation and structure geometry and ground motion characteristics. Due to these difficulties, SSI is usually neglected for the seismic design of ordinary buildings even though there are conditions in which it is important to consider.

Often, some approaches that simplify the problem are followed such as the procedure that turns the non-linearity of the problem into an equivalent linear behavior. For non-liquefiable soils nowadays there is a growing support in approaches that account for nonlinear soil-foundation deformations in order to limit the shaking energy from entering the structure (Pecker and Pender, 2000; Deng et al., 2014). This is because the behavior of the system can be predicted in terms of nonlinear stiffness, foundation moment capacity, settlements and residual tilting (Deng and Kutter, 2012).

Liquefaction phenomena also influence the structural response, changing the stiffness and strength of the supporting soil, with a consequent increase in a level of energy dissipation and deformation at the soil-foundation interface. Moreover, the reduction in stiffness in liquefied layers tends to highlight the stiffness contrast between the different materials composing the soil and making the conventional soil-foundation impedances less applicable. The possible presence of a natural or

artificial stiff crust between the foundation and the liquefied soil represents a seismic isolation system (Bouckovalas et al., 2018; Karatzia et al., 2017).

2.3 Liquefaction-induced settlements

2.3.1 Introduction

In the presence of buildings, the behavior of liquefiable deposits is more complex than in free-field conditions. A building not only modifies the initial stress field in the soil, but also alters its potential to develop excess pore pressure, its dilatancy, the gradient of water flow, the initial seismic demand, etc. On the other hand, the soil can substantially modify the ground motion at the foundation level and the dynamic properties of the structure. Hence, different strategies and methodologies are required for the assessment of the performance of buildings in liquefiable areas rather than for free-field.

Permanent deformations of buildings due to liquefaction-induced soil softening increases seismic vulnerability when compared to non-liquefiable deposits, because those deformations can significantly affect the building operability. Hence, increasing attention has been put onto this issue, especially in the last decade.

Liquefaction-induced settlements under shallow foundations have been observed to be larger than in the free-field (e.g. Yoshimi and Tokimatsu, 1977; Liu and Dobry, 1997; Hausler, 2002; Dashti et al., 2010a; Karamitros et al., 2013b; Luque and Bray, 2015; Ziotopoulou and Montgomery, 2017). Moreover, the physical phenomenon has been demonstrated to be radically different: it is primarily controlled by deviatoric strains rather than by volumetric ones (which represent only a small portion of the total settlement). However, in engineering practice it is still common to predict settlement by means of empirical-based approaches originally developed for the evaluation of free-field volumetric settlements, which only account for the mechanism of reconsolidation as showed in Figure 2.17a (e.g. Zhang et al., 2002; Ku et al., 2012).

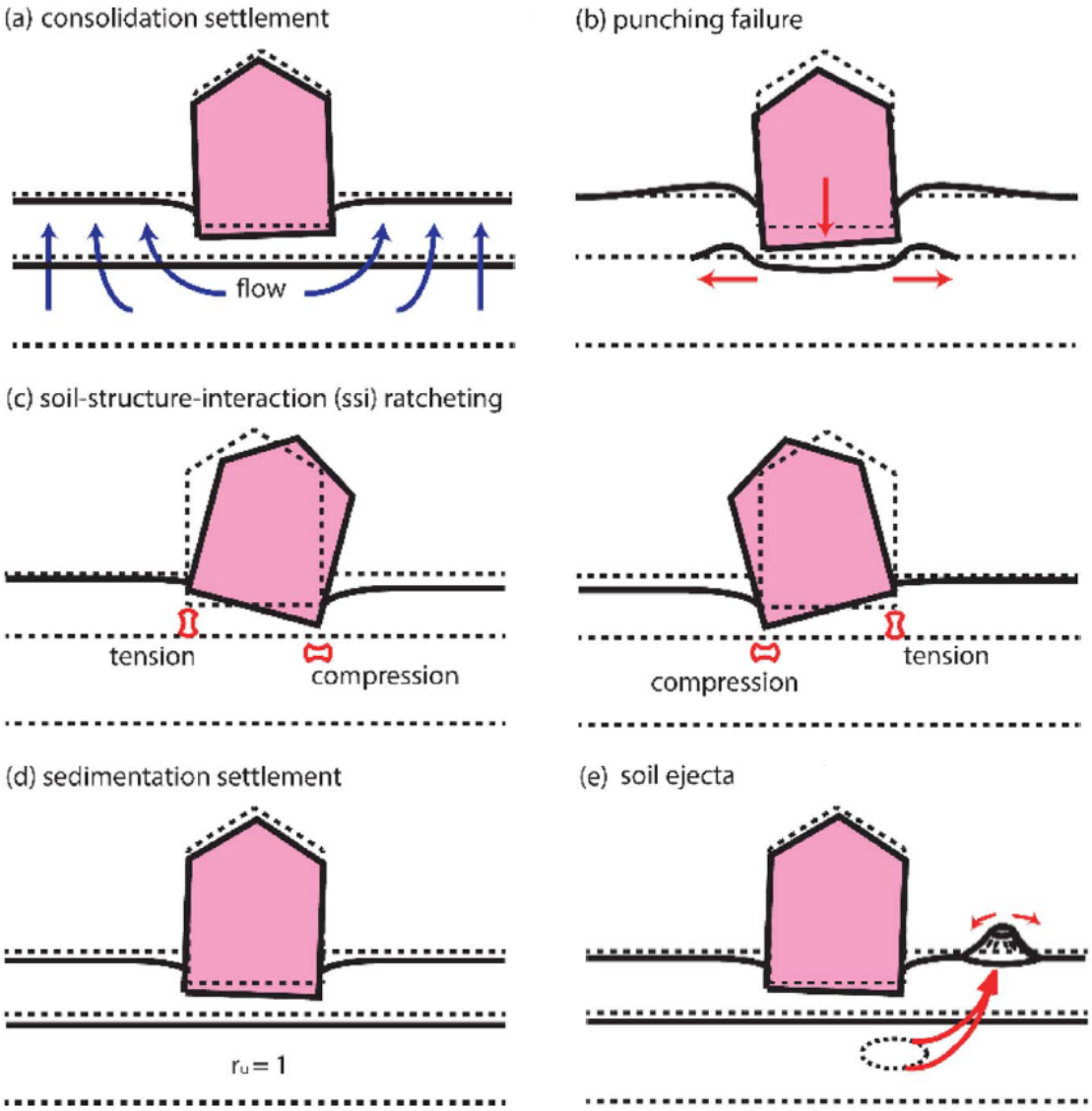


Figure 2.17: Liquefaction-induced building displacement mechanisms: a) volumetric-induced settlement from post-liquefaction reconsolidation; b) shear-induced settlement from punching failure; c) shear-induced settlement from soil-structure-interaction (SSI) ratcheting; d) volumetric-induced settlement from sedimentation; e) ground loss due to soil ejecta (adapted from Bray and Macedo, 2017)

The different mechanisms causing settlement can be categorized as being volumetric- or deviatoric-induced, depending on the ruling strain component. A major portion of the settlement takes place during the shaking, and it is mostly deviatoric-induced. Still, a part of the volumetric-induced settlement can take place during the shaking for normal ranges of soil permeability; the rest of it develops afterwards, at a minor rate. Centrifuge tests and numerical analyses show consistently a rather linear settlement evolution with time during shaking. Some authors have suggested different

intensity measures to be proportional to the settlement, e.g. Arias Intensity (Dashti et al., 2010b) or Cumulative Absolute Velocity (Karimi and Dashti, 2017; Bray and Macedo, 2017).

Deviatoric strains are induced in the soil due to the ground shaking, the static bearing pressure and the structural displacements (soil-structure interaction). Settlement is accumulating due to the development of alternate punching-shear mechanisms (Figure 2.17b) able to be modeled as a Newmark-type sliding block (Karamitros et al., 2013b). In each cycle, the relative movement of the foundation is out of phase with the bedrock, causing differential oblique forces applied to the soil surface. Also, rocking of the building causes vertical pulses of axial load in exterior footings or the edges of the mat foundation (Dashti et al., 2010a; Bray and Macedo, 2017) and, analogously, the rotation of single footings cause localized increases of vertical pressure in their edges.

At the beginning of the shaking, large inertial forces are applied to the soil, in which r_u is still not so high and thus stiffness and strength degradation in the soil is still moderate, thus lower de-amplification of the motion is attained. Consequently, the settlement at the beginning of the shaking is more prone to be ruled by the ratcheting of the superstructure (Figure 2.17c). Afterwards, if the strong shaking is sufficiently long, both the cyclic mobility of the soil and the failure mechanism act as a natural isolation which de-amplify the seismic excitation in the foundation.

Therefore, the settlement at the last phase is more prone to be ruled by static pressure, which can lead eventually to bearing capacity failure even when full liquefaction is not attained. The evaluation of soil residual strength or bearing capacity at the liquefied state is also a critical issue, because the settlement increases drastically when the factor of safety is lower than 1.0 (Shahir and Pack, 2009; Bray and Macedo, 2017). Different methodologies are proposed for the estimation of the residual strength of liquefied soil (e.g. based on equivalent degraded friction angle, ϕ_{deg} (Cascone and Bouckovalas, 1998) or assuming empirical relations (Robertson, 2009; Kramer and Wang, 2015). There is currently no consensus on the appropriate way to determine the bearing capacity of a shallow foundation on liquefied soil.

Several authors have identified the most important parameters affecting the deviatoric settlement (Dashti et al., 2010a; Karamitros et al., 2013a; Tokimatsu et al., 2017; Bray and Macedo, 2017; among others). They refer mainly to the characteristics of the soil (e.g. stratigraphic profile, thickness and depth of the liquefiable layer), the building (e.g. bearing pressure, geometry) and the ground motion.

Regarding volumetric-induced settlement, most of it is a consequence of the reconsolidation mechanism, which can be divided into sedimentation and consolidation phenomena. Consolidation corresponds to the progressive contraction associated to the increase of σ' due to the dissipation of Δu, while sedimentation only takes place when the level of r_u is high enough to cause a rearrangement of the floating particles (Figure 2.17d). Reconsolidation generally advances from the

bottom of the liquefied layer to the shallower part. Besides, hydraulic gradient with horizontal component generated during the shaking can cause localized strains and thus their contribution to the settlement can be of some importance (Dashti et al., 2010a).

When sand ejecta is present (Figure 2.17e), it can have much higher devastating potential than any other mechanism (Bray and Macedo, 2017). Localized fractures in the soil crust induce the seepage of pore water and fine soil contents to the surface, resulting in the removal of a portion of soil underneath the foundation causing settlements of footings or tilting of mat foundations.

In the case of liquefiable deposits, the definition of damage levels in buildings should account not only for the damage experienced by the structural members that typically is expressed in terms of flexural demand, but also for the loss of functionality related to rigid-body movements which do not cause structural damage (Viana da Fonseca et al., 2017).

Usually, flexural damage is related to ground shaking, while rigid-body movements are attributed to permanent ground movements. However, frames founded on pad footings instead of rigid mat foundation can experience flexural damage due to differential settlements, which are complex SSI phenomena showing high degree of uncertainty due to heterogeneity of soil, scarce field data, structural variability and intrinsic uncertainty of seismic hazard and liquefaction triggering (Viana da Fonseca et al., 2017).

The behavior of buildings in liquefiable soils regarding the time-history Δu build-up suggests that in the beginning of the ground motion both sources of flexural damage due to ground shaking and due to differential settlements may coexist. However, coupled procedures are not usually considered due to their inherent difficulty. All damage due to ground shaking occurs in the first part of the earthquake and the liquefaction-induced ground deformation occurs in the end of the earthquake (Bird et al., 2006).

In general, regardless of the liquefaction potential of the soil, the estimation of differential settlements for design purposes traditionally follows a very simple rule of thumb in which differential settlements within assumed homogeneous soil layers are equal to a fraction of the total settlement, as showed Equation 2.24, where a can range between 0.4 – 1.0 (Bjerrum, 1963; Kramer and Holtz, 1991; Viggiani, 1993; Coduto et al., 2001; Terzaghi et al., 1996). Then, those values of ΔS might be imposed alternatively to the different column bases in order to design the rest of the structural members.

$$\Delta S = a \cdot S \tag{2.24}$$

Schneider et al. (2015) suggest that a values of 0.5 may constitute a upper bound after a numerical calibration; still, only inherent heterogeneity of soil is accounted as a source of uncertainty, as most of the probabilistic studies carried out so far do (Fenton and Griffiths, 2002; Akbas and Kulhawy, 2009; Ahmed and Soubra, 2014; Schneider et al., 2015),where the inherent heterogeneity of soil, by assuming different probabilistic distributions of a chosen mechanical property (Young modulus, compressibility, SPT or CPT measures) acting as an indicator, is modeled. In most cases, they account for the distance between the footings as an input value for the probabilistic model (Kayser and Gajan, 2014).

Most of those proposals arise from empirical observation of adjacent isolated footings without any structural connection between them (e.g. D'Appolonia et al., 1968). Only Coduto et al. (2001) and Viggiani (1993) consider the structural stiffness as an input parameter. In general, it is more feasible to obtain relevant information from experimental tests rather than from field data, considering the difficulty in the measurement of S due to the lack of suitable reference points. Moreover, if any measurement of ΔS in real or simulated structures is carried out in order to obtain regression values for further linear design purposes, real movements causing nonlinear incursion in structural members should not be accounted for.

Ignoring the structural stiffness does not adequately reflect common cases (Dutta and Roy, 2002). In fact, any design methodology based on imposing sequential vertical movements to each footing, regardless of any consideration of building stiffness, does not return homogeneous safety factors for all the cases, leading to more conservative design for stiffer structures rather than for more flexible ones. Most vulnerability methodologies assume that all the potentiality of the soil to settle in a differential manner is fully becoming effective to the frame (Bird et al., 2005; Negulescu and Foerster, 2010).

Moreover, in some cases of very high seismicity and loose soil, thus large member cross-sections, the imposition of Equation 2.24 can lead to absurd, unreal flexural demands on members, because the imposed relative displacement could be eventually higher than the maximum settlement than the footing would experience if there was not any bearing capacity of the soil under it.

In liquefiable sites, ground movements are not only a consequence of the building mass, thus free-field displacements can be important. Bird et al. (2005)) suggests the use of free-field differential settlements for design or assessment purposes instead of using other probabilistic-based approaches, which may not be conservative considering that real differential settlements considering SSI could reach higher values rather than in the free-field.

The imposition of fixed differential movements to frames regardless of their stiffness may be more realistic for lateral movements rather than for settlements, although some reduction of lateral displacement demand is observed in some studies on bridges founded on piles (McGann and Arduino,

2015). When the full active pressure of the soil is mobilized on the foundation elements then no further demand is expected since the soil flows around the foundation elements (Somma, 2018).

In the case of significant post-shaking liquefaction-induced volumetric settlement (or also if sand ejecta occurs), the foundation of buildings with sufficient stiffness can experience a detachment from the ground surface due to incompatibility of deformations (Cubrinovski et al., 2011), which is not possible in the non-liquefiable case.

Conversely to the assumption of free-field displacements, other works explore the "$a - approach$" (Equation 2.24). In Stuedlein and Bong (2017), a random field model of inherent soil variability has been adopted for the analysis of settlements in free-field after shaking, for increasing seismic demand. Results show that potential a values may reduce dramatically for larger ground motions. It seems that for sufficiently high seismic demand, able to cause high excess pore pressure ratios and thus severe stiffness and strength degradation of soil, any variability of soil mechanical properties gets greatly overwhelmed, while for lower values of peak ground acceleration (PGA) the degradation is not so homogeneous and differences may exacerbate. Stuedlein and Bong (2017) suggested a maximum a value of 0.3 for PGA of 0.13g and a maximum a value of 0.15 for PGA of 0.25g, this only accounting for soil heterogeneity.

Some widely used recent methodologies to estimate the total or a fraction of the settlements are reviewed in this section. Also, the first methodology for estimating the seismically induced residual tilt of mat-founded structures that is not derived solely from settlement models on two sides of the foundation with different soil profiles is reviewed.

Numerical modeling software for advanced geotechnical analyses are also able to get liquefaction-induced settlements. Viana da Fonseca et al. (2018) obtained settlement time-series using 2D numerical models in FLAC (Itasca Consulting Group, Inc., 2016) in relatively close agreement with centrifuge experiments results.

2.3.2 Approach by Karamitros et al. (2013a)

An analytical methodology to calculate the total seismic settlement of isolated buildings during shaking was proposed by Karamitros et al. (2013a).This method, with strong physical basis has as main advantage to account for each relevant influencing parameter separately.

Following a thorough review of numerical predictions, along with observations from relevant centrifuge and large-scale experiments published in the literature,Karamitros et al. (2013a) demonstrated that the majority of liquefaction-induced settlements is not due to an accumulated sand densification, but associated to a Newmark-type "sliding block" type soil shearing mechanism.

The sliding-block settlement accumulation mechanism proposed by Karamitros et al. (2013a) al-

lows the identification of two groups of basic problem parameters, the first one, namely, loading and strength parameters, and the second one, excitation characteristics. The first ones are related to the activated failure mechanism, e.g. the average foundation bearing pressure q, the normalized thickness H/B and the undrained shear strength S_u(or c_u) of the clay crust, as well as, the normalized thickness of the liquefiable sand layer Z_{liq}/B and the relative density D_R of the underlying liquefiable sand layer. The second ones control the amount of settlement accumulated when the above failure mechanism is activated, e.g. the peak bedrock acceleration, a_{max}, the peak bedrock velocity, v_{max} (or, alternatively, the excitation period T), and the number of significant loading cycles, N.

The proposed expression for the dynamic settlement ρ_{dyn} (i.e. the settlement during shaking) is shown in Equation 2.25, being c a foundation aspect ratio correction (Equation 2.26 where $c' = 0.003$), a_{max} the peak bedrock acceleration, T the representative period of the motion, N the number of cycles of the excitation, Z_{liq} the thickness of the liquefiable sand layer, B the structure width and FS_{deg} the degraded static factor of safety of the foundation due to liquefaction. FS_{deg} can be calculated through of the static loading ratio, the degraded bearing capacity ($q_{ult,deg}$) divided by the bearing pressure (q). The variables corresponding to the input motion refer to an equivalent sinusoidal excitation but any heterogeneous seismic record can be used by relating those variables to the velocity time-history using Equation 2.27.

$$\rho_{dyn} = c \cdot a_{max} \cdot T^2 \cdot N \cdot \left(\frac{Z_{liq}}{B}\right)^{1.5} \cdot \left(\frac{1}{FS_{deg}}\right)^3 \tag{2.25}$$

$$c = c'\left(1 + 1.65\frac{L}{B}\right) \leq 11.65 \cdot c' \tag{2.26}$$

$$a_{max} \cdot T^2 \cdot N = \pi^2 \cdot \int_{t=0}^{N \cdot T} \mid v(t) \mid dt \tag{2.27}$$

The foundation bearing capacity failure mechanism is simulated by the Meyerhof and Hanna (1978) model for a crust on a weak layer using the degraded friction angle in Equation 5.4 where U is the average excess pore pressure ratio of the liquefied sand and ϕ_0 is the initial friction angle. Superficial crust is beneficial and there is an upper bound beyond where failure occurs entirely within the crust and does not get affected by the liquefiable layer.

$$\phi_{deg} = \tan^{-1}[(1 - U) \cdot \tan \phi_0] \tag{2.28}$$

Figure 2.18 shows a one-to-one comparison between all analytical predictions and experimental results, as well as, the relative error in terms of recorded settlements. There is definitely scatter

in the data points, which might be expected in view of the limitations and assumptions, regarding the application of the proposed relations.

Even though, the methodology is based on theoretical concepts and principles, it remains empirical. Hence, its application should respect the range of problem parameters considered in the numerical analyses. In this sense, this expression is strictly relevant to an infinitely extending and purely cohesive crust, as well as to an adequately thick liquefiable sand layer which will heavily modify the seismic motion at the foundation level.

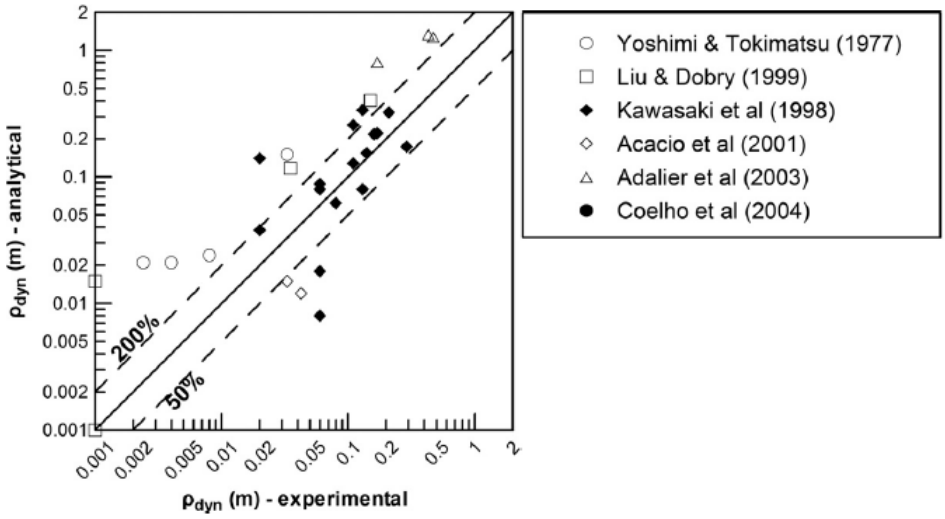


Figure 2.18: Comparison between analytical predictions and experimental measurements of ρ_{dyn} (Karamitros et al., 2013a)

Based on a parametric set of over a thousand nonlinear dynamic SSI effective stress 2D numerical analyses, Viana da Fonseca et al. (2018) proposed Equation 2.29 that improves the time-series settlement estimation from Karamitros et al. (2013a) methodology. This equation consist in multiply the total settlement calculated from the original equation by a factor that depends on the pore pressure ratio (r_u) time-series.

$$\rho_{dyn} = c \cdot \pi^2 \cdot \int_{t=0}^{N \cdot T} \mid v(t) \mid dt \cdot \left(\frac{Z_{liq}}{B}\right)^{1.5} \cdot \left(\frac{1}{FS_{deg}}\right)^{3} \cdot \frac{\sum_0^i |v_i| \cdot r_{u,i}}{\sum_0^{N \cdot T} |v_i| \cdot r_{u,i}} \tag{2.29}$$

2.3.3 Approach by Bray and Macedo (2017)

A simplified procedure from an extensive in-situ, experimental and analytical work was proposed by Bray and Macedo (2017). A numerical model was satisfactorily calibrated for the evaluation of liquefaction in soil below buildings and the intensity measures that provide a better prediction of total settlements were identified.

Consequently, a parametric set of over a thousand numerical analyses was conducted, and the influence of the different parameters on the deviatoric settlement was disaggregated, showing rather consistent trends. The influence of the degraded bearing capacity was shown to be very important: buildings near to the liquefaction-induced bearing collapse show a dramatic increment of settlement. Hence, the authors suggest that, for low bearing capacity factors of safety, the evaluation of settlements is not applicable.

A purely empirical expression for the deviatoric settlement in Equation 2.30 was obtained as a best-fitting regression of the results of the parametric analyses, where D_S is the foundation settlement, constants c_1 and c_2 depend on the liquefaction-induced building settlement index (LBS) defined by equation 2.31 and have values of -8.35 and 0.072, respectively, for $LBS \leq 16$, and -7.48 and 0.014 otherwise. Q is the foundation contact pressure, H_L is the liquefiable layer thickness, B is the building width, S_a is the spectral acceleration at a period equal to 1 second and ε is a normal random variable with zero mean and standard deviation of 0.50.

The LBS index, as defined in equation 2.31, is a weighted liquefaction-induced shear strain in the free-field. The value of the free-field shear strain, ε_{shear}, is calculated using Zhang et al. (2004), based on the estimated relative density (D_R) of the liquefied soil layer and the calculated safety factor against liquefaction triggering (FS_L). Parameter $z(m)$ in equation 2.31 is the depth measured from the ground surface (> 0) and W is a foundation-weighting factor wherein W is 0.0 for z less than D_f, which is the embedment depth of the foundation, and 1.0 otherwise. For the determination of $CAVdp$, the standardised Cumulate Absolute Velocity as defined in (Campbell and Bozorgnia, 2012), equation 2.32 was used, where N is the number of discrete 1 second time intervals and $H(x)$ is 0 if $x < 0$ or 1 otherwise. x is $(PGA_i - 0.025)$ where PGA_i is the value of the peak ground acceleration (in g) in each 1 second time interval i, inclusive of the first and last values.

$$\ln(D_S) = c_1 + 4.59 \cdot \ln(Q) - 0.42 \cdot \ln(Q)^2 + c_2 \cdot LBS + 0.58 \cdot \ln(\tanh(H_L)) - 0.02 \cdot B + 0.84 \cdot \ln(CAVdp) + 0.41 \cdot \ln(S_a) + \varepsilon \quad (2.30)$$

$$LBS = \int W \cdot \frac{\varepsilon_{shear}}{z}\, dz \quad (2.31)$$

$$CAVdp = \sum_{i=1}^{N} (H(x) \int_{i-1}^{i} |a(t)|\, dt) \quad (2.32)$$

Figure 2.19 shows the comparison between the centrifuge experiment results and the estimated settlements with Equation 2.30, including 24 cases where the settlement is lower than 11 mm.

Most of the cases are within the lines with slopes 1H:2V and 2H:1V. Thus, the proposed equation by Bray and Macedo (2017) produces reasonable results when compared to the centrifuge tests considered in that study.

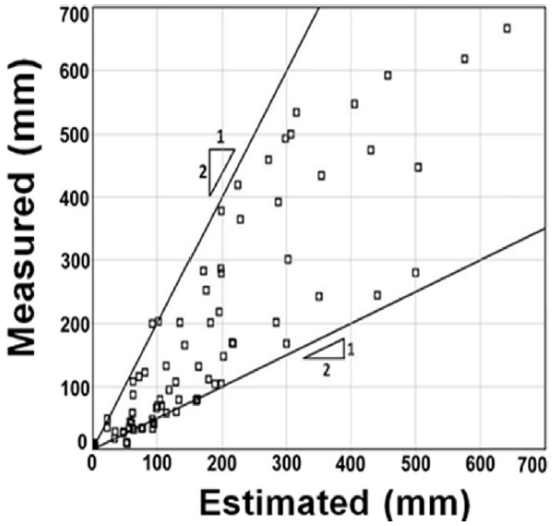


Figure 2.19: Comparison of liquefaction-induced model building settlements measured during centrifuge tests with estimated liquefaction-induced settlements with the proposed procedure (Bray and Macedo, 2017)

2.3.4 Approach by Lu (2017)

An empirical approach based on calibration from a large number of results found in literature –centrifuge tests, numerical analyses and field data was developed by Lu (2017). The agreement with the results used for calibration was rather satisfactory, but, the method does not have a strong a mechanical framework. Lu (2017) proposed the adoption of the framework of the classic Meyerhof equation for settlements, assuming superficial water table and replacing the term related to SPT ($N/0.00284$) by N_{LR} (Index of strength of liquefiable soils) as showed in Equation 2.33, where C_D is an embedment depth correction factor $(1 - (D_f/4B))$, q is the loading pressure on shallow foundation (kPa) and B is the width of shallow foundation (m).

$$S = C_D \cdot \frac{q}{N_{LR}} \cdot \left(\frac{B}{B + 0.33}\right)^2 \tag{2.33}$$

N_{LR} depends on D_R (between 30% and 60%), the level of q (low, 10-30 kPa; medium, 30-80 kPa; high, 80-120 kPa) and PGA (0.10-0.40 g), and can be obtained from the chart shown in Figure 2.20. The shortcoming lies on the lack of criteria for selecting the N_{LR} value, depending on PGA, within the corresponding boundaries for each given q-based region where higher boundary represents $0.1g$ and lower boundary corresponds to $0.4g$. Moreover, it is worth noting that the

thicknesses of the bands are so large that $N_L R$ can reach such low values that the sensitivity of settlement results with respect to different qualitative assumptions is very high.

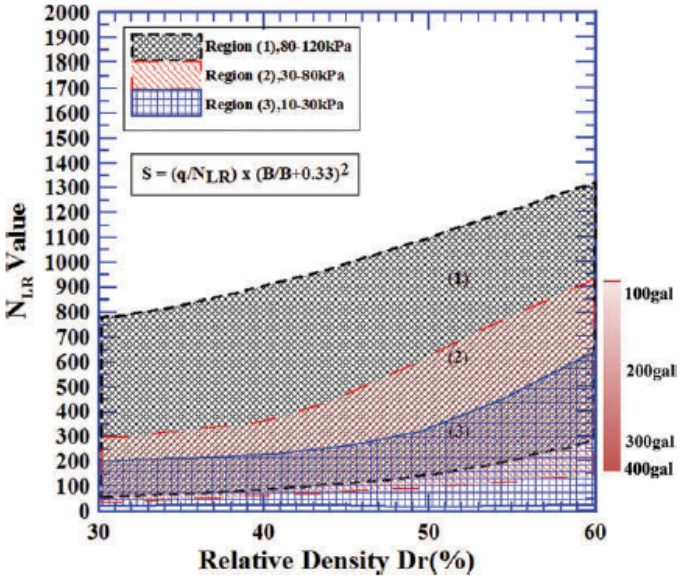


Figure 2.20: Chart to estimate N_{LR} (Lu, 2017)

Figure 2.21 shows the results obtained from Equation 2.33. In spite of the extremely simplified method and limited input parameters used in this approach, a good consistency with field observation values for all ranges of settlement was obtained. The results thus showed that the prediction method had a good capability of calculation for all the earthquake cases.

2.3.5 Approach by Bullock et al. (2019a)

A predictive model based on the results of an extensive fully coupled, three-dimensional numerical parametric study of soil–structure systems, validated with centrifuge experiments, as well as, a database of case history observations, was developed by Bullock et al. (2019a). The results of the numerical study provided insight into the relative importance and influence of each input parameter and the functional form of the predictive model for a structure's permanent settlement. The case history database helped to validate and refine the predictive model, accounting for complexities of the ground motion and site conditions in the field. Non-linear regression and latent variable analysis were used to develop model coefficients and the uncertainty around the model was modeled by a log-normal distribution.

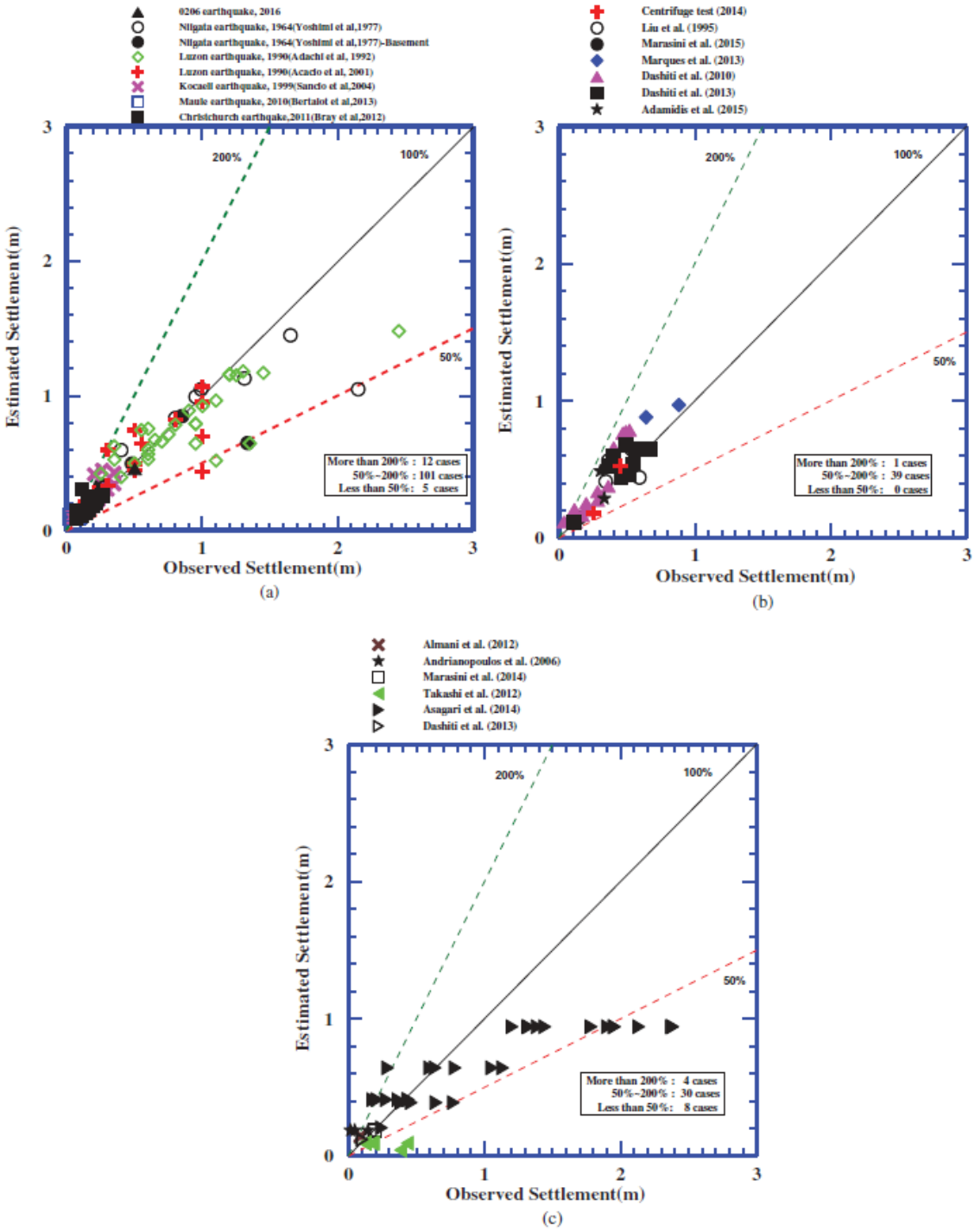


Figure 2.21: Comparison of estimated settlement and observed settlement from literature using the proposed calculation method: a) predictions on field observation; b) predictions on experimental studies; c) predictions on numerical studies (Lu, 2017)

An additional logistic model was provided to estimate the probability of insignificant settlement defined as less than 1 cm. The proposed probabilistic procedure considers variations in site con-

ditions as well as the presence and properties of a building in three dimensions. By including the case history database in its validation and adjustment, the model captures all mechanisms of settlement below the foundation, including volumetric and deviatoric strains as well as ejecta. The total uncertainty around its predictions is rigorously characterized, which is a necessary step before the benefits of performance-based seismic design can be realized in the evaluation and mitigation of the liquefaction hazard.

Equation 2.34 presents the selected functional form of the predictive equation for liquefaction-induced foundation settlement based on the numerical database, where $ln(\overline{S})_{num}$ is the natural logarithm of the median predicted numerical foundation settlement (in mm) and f_{so}, f_{fnd} and f_{st} are functions that capture effects due to the characteristics of the soil profile, foundation and the structure, respectively. The s_0 coefficient is suggested as 0.4973 and CAV is the cumulative absolute velocity.

$$ln(\overline{S})_{num} = f_{so} + f_{fnd} + f_{st} + s_0 \cdot ln(CAV) \tag{2.34}$$

Equation 2.35 describes the term that account for the effects of the soil profile characteristics, where $f_{S,i}$ is described in Equation 2.36 in terms of the corrected SPT blow count ($N_{1,60}$) and in Equation 2.37 in terms of the normalized cone tip resistance (q_{c1N}). The coefficient $f_{H,i}$ is described in Equation 2.38. Coefficients c_0, c_1, a_0, $a_{1,SPT}$, $a_{1,CPT}$, b_0 and b_1 are suggested as 1.3558, -0.1340, 1.0, -0.2174, -0.0360, 0.3026 and -0.0205, respectively.

$$f_{so} = \left[\sum_i H(H_{S,i} - 1 + \varepsilon) \cdot f_{S,i} \cdot f_{H,i}\right] + [c_0 + c_1 \cdot ln(CAV)] \cdot F_{LPC} \tag{2.35}$$

$$f_{S,i}(SPT) = \begin{cases} a_0, N_{1,60,i} < 12.6 \\ a_0 + a_{1,SPT} \cdot (N_{1,60,i} - 12.6), 12.6 \leq N_{1,60,i} < 17.2 \\ a_0 + 4.6a_{1,SPT}, 17.2 \leq N_{1,60,i} \end{cases} \tag{2.36}$$

$$f_{S,i}(CPT) = \begin{cases} a_0, q_{c1N,i} < 112.4 \\ a_0 + a_{1,CPT} \cdot (q_{c1N,i} - 112.4), 112.4 \leq q_{c1N,i} < 140.2 \\ a_0 + 27.8a_{1,CPT}, 140.2 \leq q_{c1N,i} \end{cases} \tag{2.37}$$

$$f_{H,i} = b_0 \cdot H_{S,i} \cdot exp\left[b_1\left(max(D_{S,i})^2 - 4\right)\right] \tag{2.38}$$

$H(\cdot)$ is the Heaviside step function; ε is an infinitesimal positive quantity to make $H(\cdot)$ equal to 1 for an argument of zero; F_{LPC} is a flag that is equal to 1 if a low-permeability layer is present

above the uppermost susceptible layer; $N_{1,60,i}$ is the corrected standard penetration test (SPT) blow count in the ith layer; $q_{c1N,i}$ is the corrected normalized cone penetration test (CPT) tip resistance in the ith layer; $H_{S,i}$ is the thickness of the ith susceptible layer; and $D_{S,i}$ is the depth from the bottom of the foundation to the centre of the ith susceptible layer.

Equation 2.39 represents the term that accounts for the effects of foundation characteristics, where f_q is described in Equation 2.40, being q the bearing pressure of the foundation (in kPa), B the width of a rectangular foundation (in m) and $D_{S,1}$ (in m) the depth to the center of the uppermost susceptible layer with $N_{1,60}$ less than 17.2 blows or q_{c1N} less than 140.2. Coefficients d_0, d_1 and d_2 are suggested as -1.3446, 0.2303 and 0.4189, respectively. $f_{B,L}$ is described in Equation 2.41, where D_f is the depth from the surface to the bottom of the foundation (in m) and coefficients e_0, e_1, e_2 and e_3 are suggested as -0.8727, 0.1137, -0.0947 and -0.2148, respectively.

$$f_{fnd} = f_q + f_{B,L} \tag{2.39}$$

$$f_q = \{d_0 + d_1 \cdot ln[min(CAV, 1000)]\} \cdot ln(q) \cdot exp\{d_2 \cdot min[0, B - max(D_{S,1}, 2)]\} \tag{2.40}$$

$$f_{B,L} = \{e_0 + e_1 \cdot ln[max(CAV, 1500)]\} \cdot [ln(B)]^2 + e_2 \cdot (L/B) + e_3 \cdot D_f \tag{2.41}$$

Equation 2.42 represents the term that accounts for the effects of structure characteristics, where h_{eff} is the effective height of the structure (in m) and M_{st} is the inertial mass of the structure (in kg). Coefficients f_0, f_1 and f_2 are suggested as -0.0137, 0.0021 and 0.1703, respectively.

$$f_{st} = \{f_0 + f_1 \cdot ln[min(CAV, 1000)]\} \cdot h_{eff}^2 + f_2 \cdot min[M_{st}/10^6, 1] \tag{2.42}$$

The semi-empirical prediction for settlement in Equation 2.43, results by adjusting Equation 2.34 with the case history database. $H_{S,1}$ is the thickness of the top susceptible layer (in m) and q_c is assumed as 61 kPa. Coefficients k_0, k_1, k_2 and k_3 are suggested as -1.5440, 0.0250, 0.0295 and -0.0218, respectively.

$$ln(\overline{S})_{adj} = ln(\overline{S})_{num} + k_0 + k_1 \cdot min(H_{S,1}, 12)^2 + K_2 \cdot min(q, q_c) + k_3 \cdot max(q - q_c, 0) \geq ln(\overline{S})_{num} \tag{2.43}$$

Figure 2.22 shows the model predictions for settlement plotted against the observed values for the mat-founded structures in the case history database. Although the case history database has not

been truncated at a settlement threshold of 10 mm, it includes only settlements in the range from 20 to 2000 mm. For observed settlements between 30 and 800 mm, most observations fall within 0.67 log units of the predicted value (i.e. within one standard deviation). The model is more accurate for settlements exceeding 800 mm than for settlements below 30 mm, which are generally over-predicted (Bullock et al., 2019a).

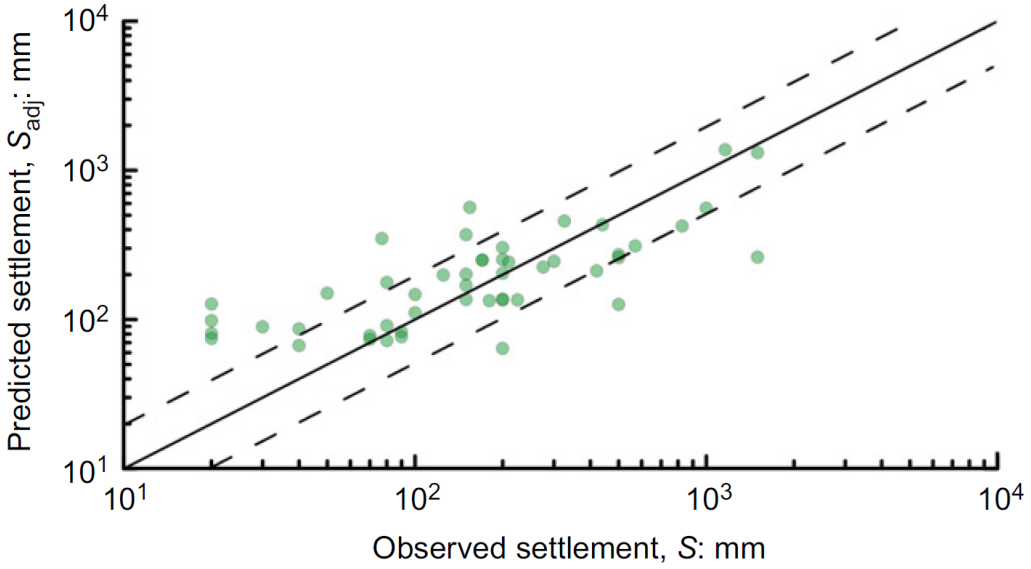


Figure 2.22: Predicted settlement plotted against observed settlement for the mat case histories in the database (Bullock et al., 2019a)

2.3.6 Approach by Bullock et al. (2019b)

Two probabilistic models for predicting the residual tilt of mat-founded structures on liquefiable ground was proposed by Bullock et al. (2019b). The first model is completely empirical, based on correlating residual tilt to settlement in case histories. The second one is semi-empirical, based on an extensive 3D numerical parametric study of soil-foundation-structure systems, centrifuge tests and case history observations.

Empirical model was proposed with three features, as showed in Equation 2.44, where S is the average settlement experienced by the foundation (in mm), B is the width of the mat foundation or the total width of the structure (in m), $D_{S,T}$ is the thickness of the non-liquefiable crust (in m) and ε_{r^e} is an error term than follows a normal distribution with zero mean and a standard deviation of 0.29. The uncertainty of the model is expressed in Equation 2.45, where B_1^* and B_2^* are threshold values of B that correspond to the values for which heteroscedasticity is observed. The parameter values suggested by Bullock et al. (2019b) are $a_1 = 0.509$, $a_2 = -0.936$, $a_3 = -0.102$, $\sigma_{r^e} = 0.287$, $B_1^* = 12$, $B_2^* = 16$, $\sigma_{r^e,1} = 0.342$, and $\sigma_{r^e,2} = 0.123$.

$$ln(\theta)_r = a_1 \cdot ln(S) + a_2 \cdot ln(B) + a_3 \cdot D_{S,T} + \varepsilon_{r^e} \tag{2.44}$$

$$\sigma^*_{r^e} = \begin{cases} \sigma_{r^e,1}, B \leq B^*_1 \\ \sigma_{r^e,1} - (\sigma_{r^e,1} - \sigma_{r^e,2}) \cdot \frac{(B-B^*_1)}{(B^*_2-B^*_1)}, B^*_1 < B \leq B^*_2 \\ \sigma_{r^e,2}, B^*_2 < B \end{cases} \tag{2.45}$$

Semi-empirical model has three features that account for the numerical database alone, centrifuge tests adjustment and case history observations adjustment. Equation 2.46 represents this model, where F_{LPC} is a flag that is 1 if the liquefiable material is below a low permeability cap and 0 otherwise, $max(H_S)_{1.0B}$ is the thickness of the largest continuous layer of susceptible material in the top B depth of the profile below the foundation (in m), $N_{NS,1.0B}/N_{S,1.0B}$ is the number of distinct non susceptible layers per susceptible layer in the top B depth of the profile below the foundation, and $\varepsilon_{r^s e}$ is an error term than follows a normal distribution with zero mean and a standard deviation of 0.548. Coefficients k_0, k_1, k_2, k_3 and k_4 are suggested as 2.383, 1.491, -0.168, -0.327 and 0.087, respectively. Figure 2.23 shows the residuals of this model as a function of several key parameters.

$$ln(\theta_{r^{se}}) = ln(\theta_r)_{adj} + k_0 + k_1 \cdot F_{LPC} + k_2 \cdot D_{S,T} + k_3 \cdot max(H_S)_{1.0B} + k_4 \cdot (N_{NS,1.0B}/N_{S,1.0B}) + \varepsilon_{r^s e} \tag{2.46}$$

$ln(\theta_r)_{adj}$ is the feature that adjusts the numerical database alone and is defined in Equation 2.47, where h_{eff} is the structure height and $\varepsilon_{r,adj}$ is the logarithmic residual of predicted residual tilt, being considered irrelevant by the authors. Coefficients γ_0 and γ_1 are suggested as 0.066 and 0.165 respectively.

$$ln(\theta_r)_{adj} = ln(\theta_r)_{num} + \gamma_0 + \gamma_1 \cdot ln(h_{eff}) + \varepsilon_{r,adj} \tag{2.47}$$

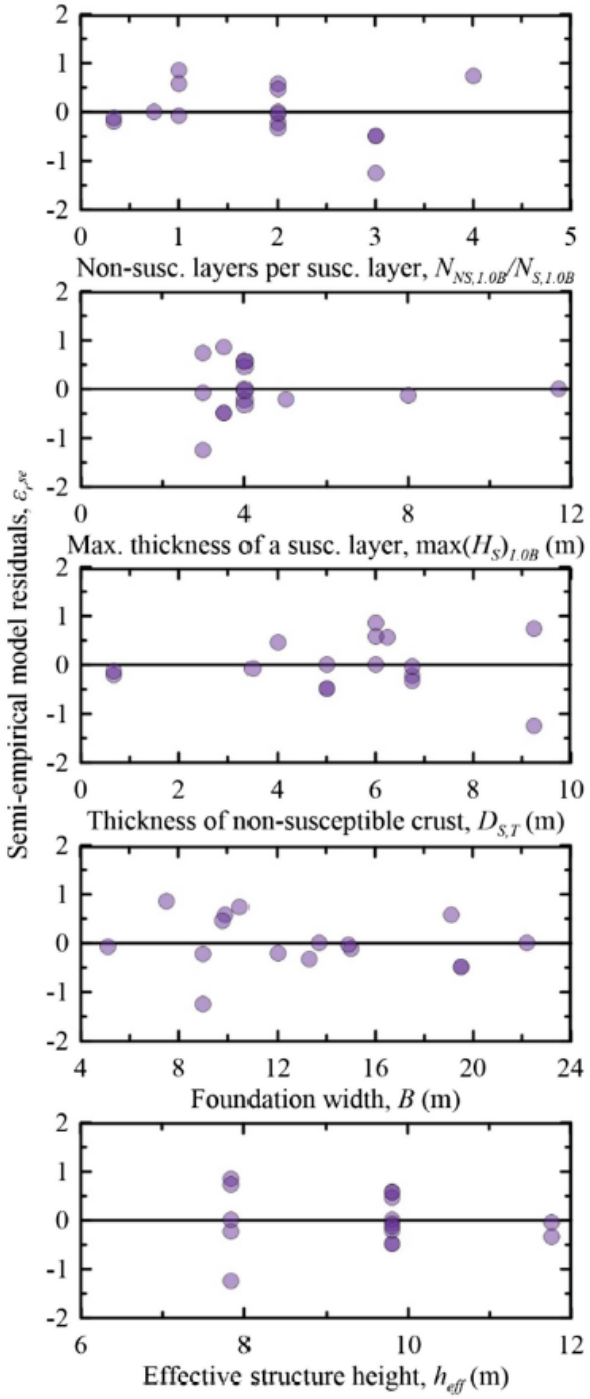


Figure 2.23: Adjusted residuals for the case history data using the semi-empirical model for residual tilt (Bullock et al., 2019b)

$ln(\theta_r)_{num}$ represents the base model using the numerical database alone and is defined in Equation 2.48, where q is the foundation bearing pressure (in kPa), L/B is the foundation length-to-width ratio, D_f is the foundation embedment depth (in m), $H_{S,1.0B}$ is the thickness of susceptible material within $1.0B$ of the bottom of the foundation (in m), H is the soil profile depth (in m), M_{st} is the

inertial mass of the structure (in kg), $N_{1,60,1}$ is the SPT blow count of the uppermost susceptible layer and $\varepsilon_{r,num}$ is the logarithmic residuals following regression on the numerical database. V_{gi} is the peak incremental ground velocity (in cm/s) and CAV is the cumulative absolute velocity of the outcropping rock motion (in cm/s). Coefficients α_0, α_1, α_2, α_3, α_4, α_5, α_6, α_7, α_8, α_9, α_{10}, α_{11}, α_{12}, and α_{13} are suggested as -4.353, -0.329, -0.252, -0.036, -0.430, -0.121, 0.003, 0.026, -0.082, 0.314, 0.472, -0.020, 0.234 and 0.404, respectively.

$$ln(\theta_r)_{num} = \alpha_0 + \alpha_1 \cdot ln(q) + \alpha_2 \cdot ln(B)^2 + \alpha_3 \cdot L/B + \alpha_4 \cdot ln\left(\frac{L}{B}\right) + \alpha_5 \cdot ln(D_f)$$
$$+ H_{S,1.0B} \cdot [\alpha_6 \cdot ln(V_{gi}) + \alpha_7 \cdot ln(CAV)] + \alpha_8 \cdot D_{S,1} + \alpha_9 \cdot H \cdot (17.2 - N_{1,60,1}) + \alpha_{10} \cdot min\left(\frac{M_{st}}{10^6}, 1\right)$$
$$+ \alpha_{11} \cdot (H/B) \cdot \left(\frac{M_{st}}{10^6}\right) + \alpha_{12} \cdot ln(V_{gi}) + \alpha_{13} \cdot ln(CAV) + \varepsilon_{r,num} \quad (2.48)$$

Chapter 3

Numerical models validation against centrifuge tests

Numerical modeling is a valuable tool for simulating the seismic response of buildings on liquefiable soils, utilizing the acceleration time series of an specific earthquake scenario. In this study, this approach has been adopted to predict the performance of structures on soil profiles with a liquefiable layer. This approach requires the utilization of an advanced constitutive model capable of accurately reproducing the stress-strain behavior and the generation of pore water pressure associated with liquefaction. The PM4Sand constitutive model (Boulanger and Ziotopolou, 2017) already implemented in FLAC and PLAXIS 2D commercial software was used in this study.

The efficacy of the numerical modeling and the constitutive model in the software FLAC was validated by Viana da Fonseca et al. (2018) using results from centrifuge experiments involving soil-structure systems. In this chapter, similar to validating the efficacy of the numerical modeling and the constitutive model in the software PLAXIS 2D, the same centrifuge experiments were replicated using this software. Two cases of the centrifuge tests (T3-30 and T6-40) performed by Dashti et al. (2010a) were selected to be simulated. The analyses were performed in prototype scale. These centrifuge experiments were already modeled numerically by Dashti and Bray (2013) and Ziotopoulou and Montgomery (2017).

3.1 Overview of numerical model

A nonlinear dynamic analysis of soil-structure interaction (SSI) using an effective stress model was performed to evaluate the response of one of the structures used in the centrifuge tests. In the centrifuge experiments, the buildings operated essentially as independent systems due to the

considerable distance between their centers, which was approximately four times their widths.

The considered soil profile has three distinct layers composed of sandy material, with a total depth of 26 m and a width of 90 m. This dimension ensures adequacy for capturing free-field conditions, minimizing wave reflections, and mitigating the influence of lateral boundaries on foundation response. In the T3-30 scenario, the thickness of the surface layer was 2.0 m and of the second layer was 3.0 m. Conversely, in the T6-40 scenario, the thickness of the surface layer remained 2.0 m and the thickness of the second layer was increased to 6.0 m. The water table was positioned at a depth of 1.1 m. Figure 3.1 illustrates the numerical model under consideration.

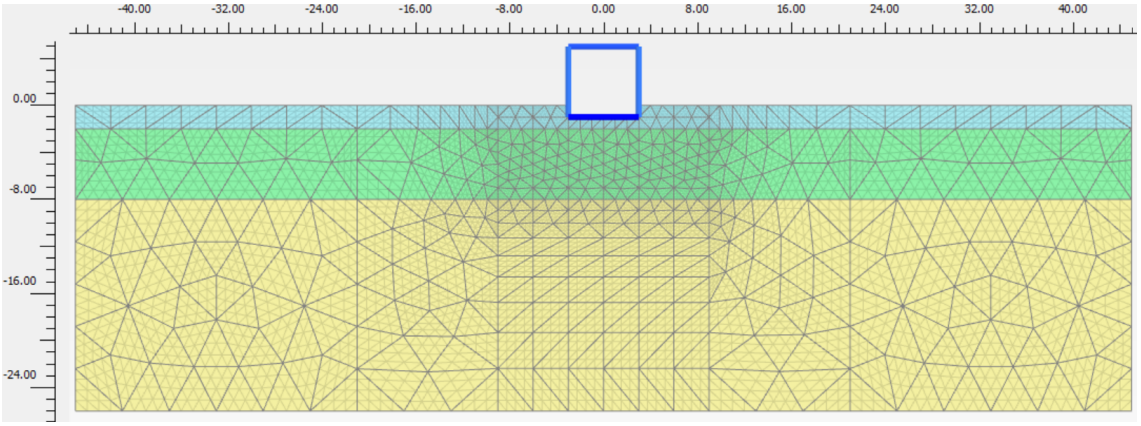


Figure 3.1: Numerical model of centrifuge test (T6-40) performed by Dashti et al. (2010a)

The Mohr-Coulomb (MC) constitutive model was applied across all three layers to determine initial stresses before applying the dynamic load and the PM4Sand constitutive model (Boulanger and Ziotopolou, 2017) was employed for the dynamic phase. Table 3.1 provides a comprehensive list of input parameters for the static phases and Table 3.2 presents the primary properties inputted for the PM4Sand constitutive model, while the secondary set of parameters remained at default values (see section 2.1.6). Parameters for the static and dynamic phases were sourced from Ziotopoulou and Montgomery (2017).

The finite element mesh underwent refinement in the vicinity of the footing, gradually transitioning to coarser resolution towards the left and right boundaries to ensure improved discretization in the critical area. Additionally, lateral boundaries were tied to undergo the exact same displacements. A rigid base was use to achieve the most accurate simulation of the base of the centrifuge box.

The numerical model adopted Structure A from Dashti et al. (2010a), with dimensions of 6.0 m in height and width. Building elements were represented using plate elements available in the software (see Figure 3.1). The building contact pressure (q=80 kPa) in the experiments was distributed in two building elements: 40% for the foundation and 50% for the top element. No self-weight or load was added to the columns but their stiffness was adjusted to achieve the experimental fundamental

period of the structure (T=0.21 sec). The stiffness of the top and bottom plates was set to be 100 times greater than that of the column elements. The interface between the base of the foundation elements and surrounding soil was fixed.

Table 3.1: Mohr-Coulomb input parameters for numerical model of Dashti et al. (2010a) centrifuge experiments

Parameter/Layer	1	2 T3-30	2 T6-40	3
γ_{unsat} $[kN/m^3]$	16.3	14.8	15.1	16.7
γ_{sat} $[kN/m^3]$	20.0	19.0	19.2	20.2
e_0	0.583	0.771	0.738	0.571
G $[MPa]$	36	28	35	167
ϕ [°]	33	33	33	33
k $[m/s]$	2E-5	2E-5	2E-5	2E-5

Table 3.2: PM4Sand input parameters for numerical model of Dashti et al. (2010a) centrifuge experiments

Parameter/Layer	1	2 T3-30	2 T6-40	3
Relative density (D_R)	0.86	0.30	0.40	0.9
Shear modulus coefficient (G_O)	1092	427	529	1162
Contraction rate parameter (h_{po})	0.56	0.05	0.48	0.06

In the centrifuge experiments, three shaking events were employed. The input motions comprised a series of scaled versions of the North-South, fault-normal component of the ground motion recorded at a depth of 83 meters in the Kobe Port Island down-hole array during the 1995 Kobe Earthquake. Specifically, the moderate and large Port Island events were utilized for this numerical investigation. The peak ground accelerations (PGAs) of the moderate and large motions were approximately 0.15 and 0.55 g, respectively Dashti et al. (2010a). Figure 3.2 shows the input acceleration-time histories.

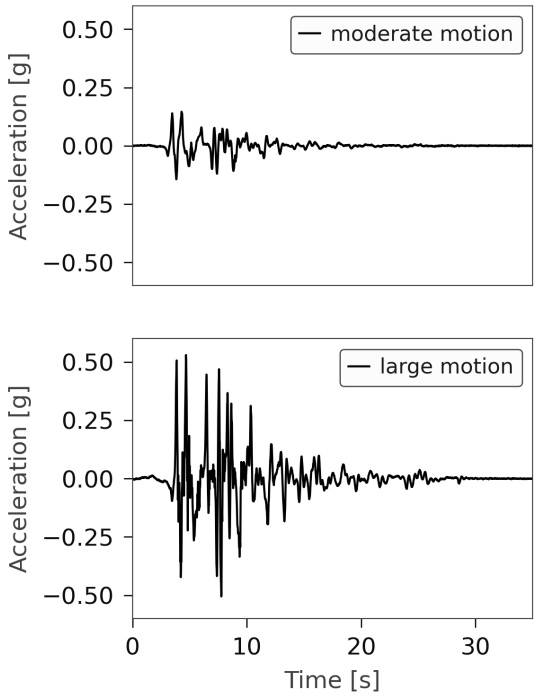


Figure 3.2: Motions applied in the numerical model of centrifuge experiments (Dashti et al., 2010a)

3.2 Results and validation

The comparison between numerical simulations and centrifuge tests was focused on settlements of the building and pore pressure generation in the bottom of the liquefiable layer beneath the building and in free-field. This comparison included the results obtained by Viana da Fonseca et al. (2018) using the software FLAC to understand if both software can provide similar results.

Figures 3.3a and 3.4a show the time history of the building settlements measured in the center of the foundation for T3-30 experiments, for the moderate and large motion, respectively. For the moderate motion, the numerical settlements were in close agreement with the centrifuge results and for the large motion the numerical settlements were slightly smaller when compared with the experimental ones but so close between them. Additionally, Figures 3.3b and 3.4b shows the pore pressure build up under the building in the bottom of the liquefiable layer (4.8 m of depth) and Figures 3.3c and 3.4c shows the pore pressure build up in free-field (18 m to the right of the structure) in the bottom of the liquefiable layer. The pore pressure build up from the numerical models looks similar to those taken from the centrifuge models in both locations and for the both motions, but in the centrifuge experiments the pore pressure decreased under the building after 15 seconds, showing the flow of water to the borders.

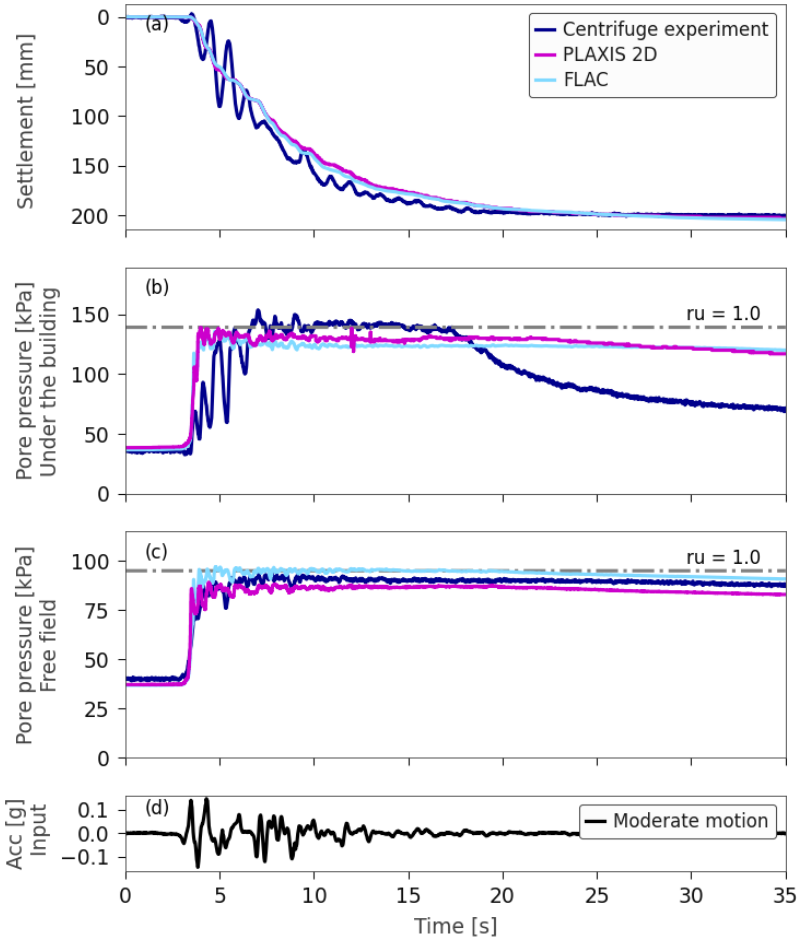


Figure 3.3: Comparison between numerical and centrifuge models for T3-30 scenario and moderate ground motion: (a) settlements; (b) pore pressure build up under the building; (c) pore pressure build up in free-field; and (d) input motion (FLAC results were sourced from Viana da Fonseca et al., 2018)

Figures 3.5a and 3.6a show the time history of the building settlements measured in the center of the foundation for T6-40 experiments, for the moderate and large motion, respectively. For the moderate motion, the numerical settlements were slightly smaller when compared with the experimental ones but so close between them and for the large motion the numerical settlements were in close agreement with the centrifuge results. Additionally, Figures 3.5b and 3.6b shows the pore pressure build up under the building in the bottom of the liquefiable layer (7.8 m of depth) and Figures 3.5c and 3.6c shows the pore pressure build up in free-field (18 m to the right of the structure) in the bottom of the liquefiable layer. For the moderate motion, the pore pressure build up under the building and in the free-field looks similar for the both numerical results but the centrifuge pore pressure build up is much lower. This appears to be a measurement error from the sensors used in these locations because such a small excess pore pressure would not generate the

presented settlements. For the large motion, the pore pressure build up from the numerical models looks similar to those taken from the centrifuge models in both locations, but in the centrifuge experiments the liquefaction is reached later.

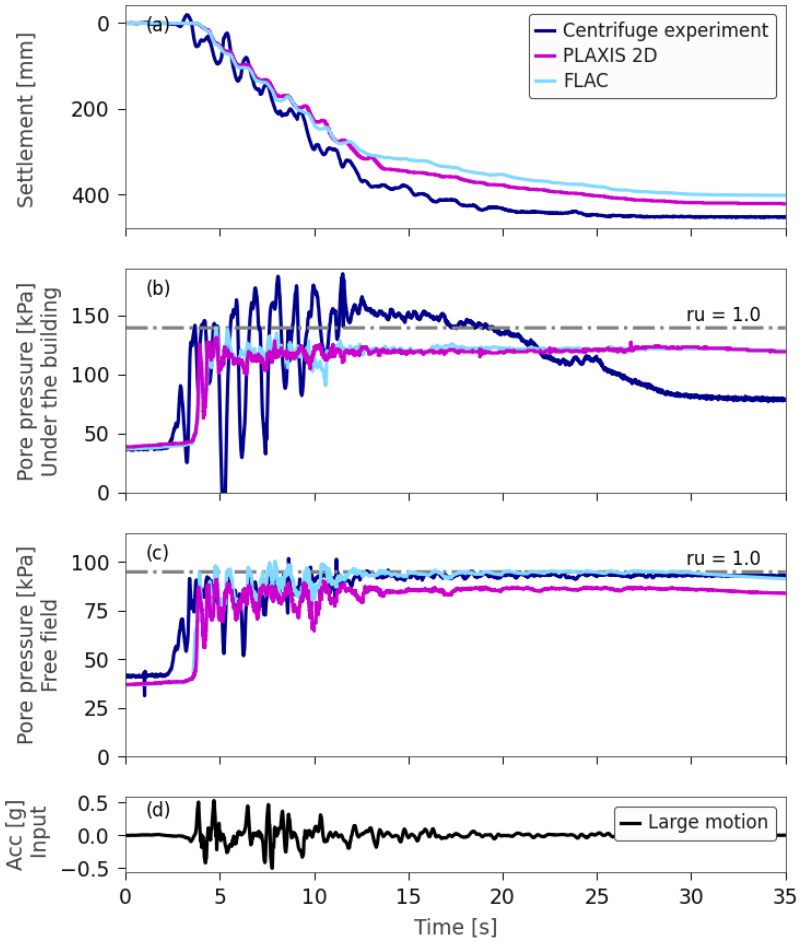


Figure 3.4: Comparison between numerical and centrifuge models for T3-30 scenario and large ground motion: (a) settlements; (b) pore pressure build up under the building; (c) pore pressure build up in free-field; and (d) input motion (FLAC results were sourced from Viana da Fonseca et al., 2018)

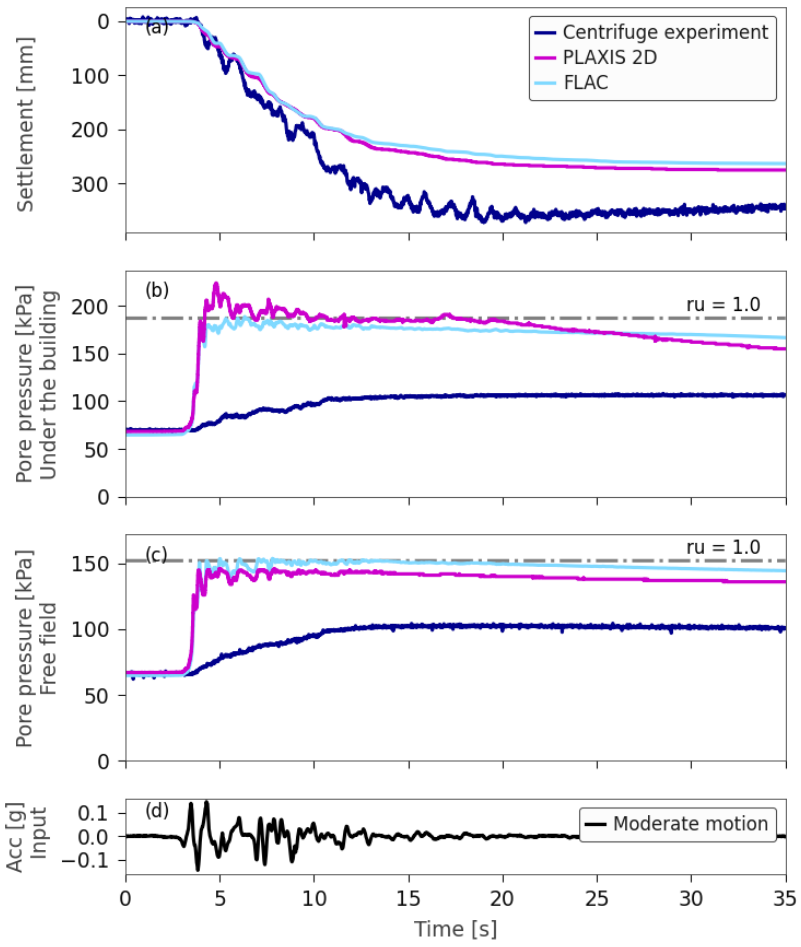


Figure 3.5: Comparison between numerical and centrifuge models for T6-40 scenario and moderate ground motion: (a) settlements; (b) pore pressure build up under the building; (c) pore pressure build up in free-field; and (d) input motion (FLAC results were sourced from Viana da Fonseca et al., 2018)

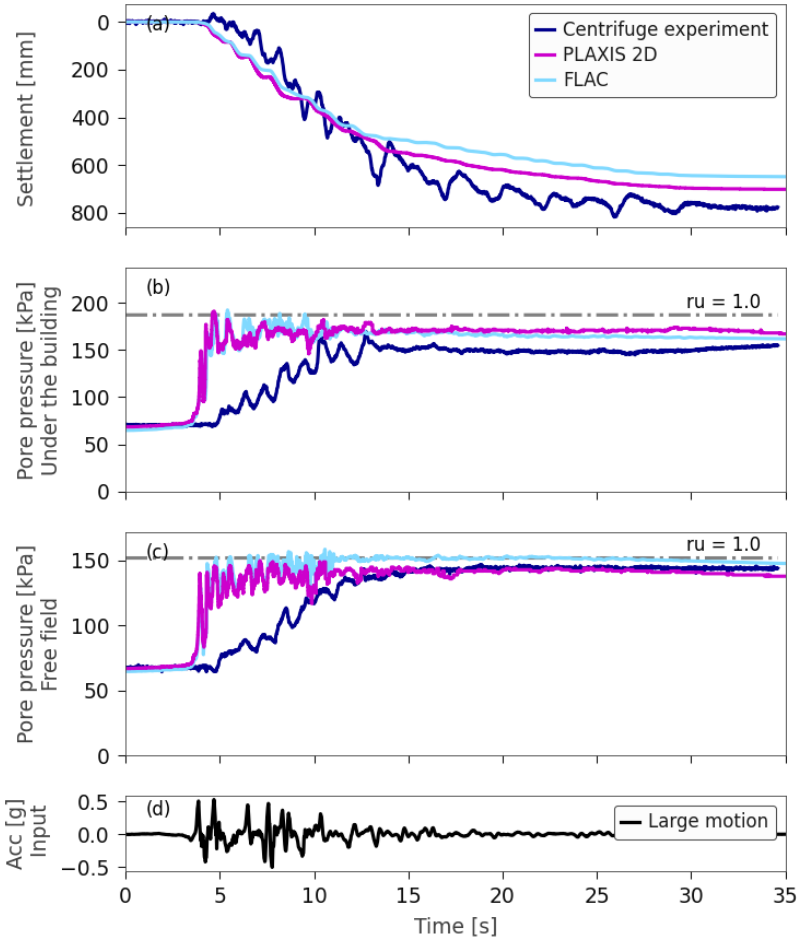


Figure 3.6: Comparison between numerical and centrifuge models for T6-40 scenario and large ground motion: (a) settlements; (b) pore pressure build up under the building; (c) pore pressure build up in free-field; and (d) input motion (FLAC results were sourced from Viana da Fonseca et al., 2018)

Maximum settlements in the center of the footing are shown in Figure 3.7 showing the close agreement between the results of both numerical models and the centrifuge experiments. Maximum pore pressure reached under the building and in free-field in the bottom of the liquefiable layer are shown in Figure 3.8 also showing a close agreement between the results.

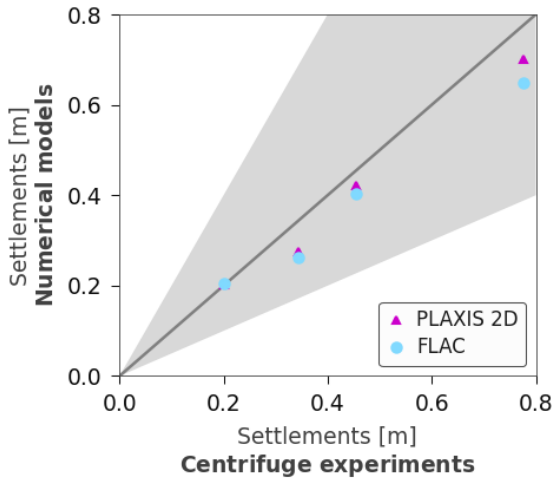


Figure 3.7: Settlements comparison between numerical and centrifuge experimental results (FLAC results were sourced from Viana da Fonseca et al., 2018)

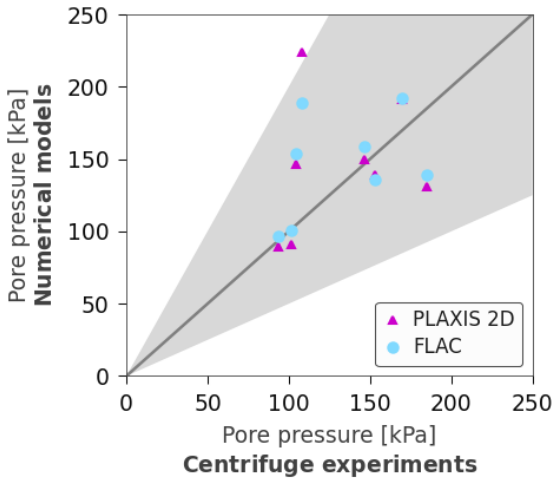


Figure 3.8: Maximum pore pressure comparison between numerical and centrifuge experimental results (FLAC results were sourced from Viana da Fonseca et al., 2018)

The surface acceleration in the free-field was also assessed through response spectra (Sa). Figures 3.9 to 3.12 illustrate the comparison between acceleration response spectra at the surface in the centrifuge experiment and those obtained in the numerical analyses. While the Moderate ground motion was reasonably well captured, the Large ground motion was significantly underestimated in the numerical simulations. A more extensive study to validate the ground motion at the surface is presented in the next chapter.

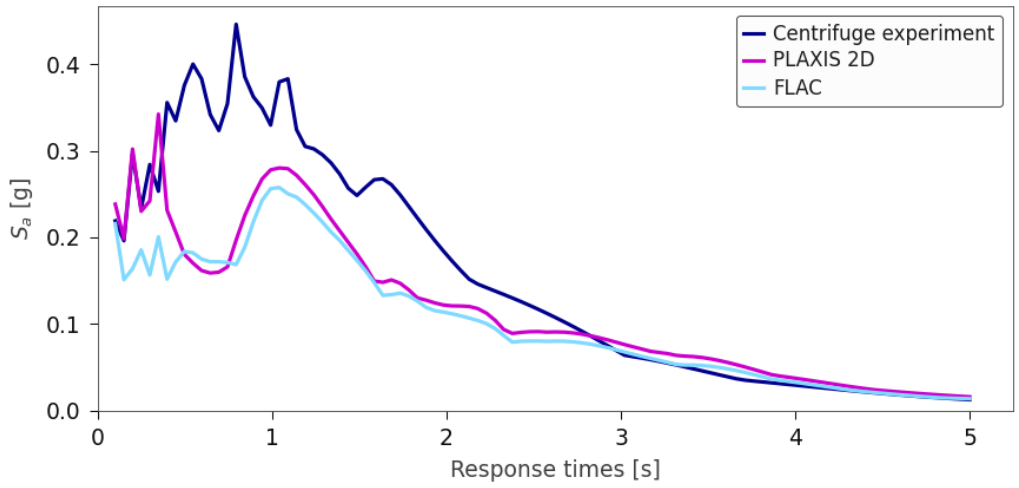


Figure 3.9: Maximum pore pressure comparison between numerical and centrifuge experimental results (FLAC results were sourced from Viana da Fonseca et al., 2018)

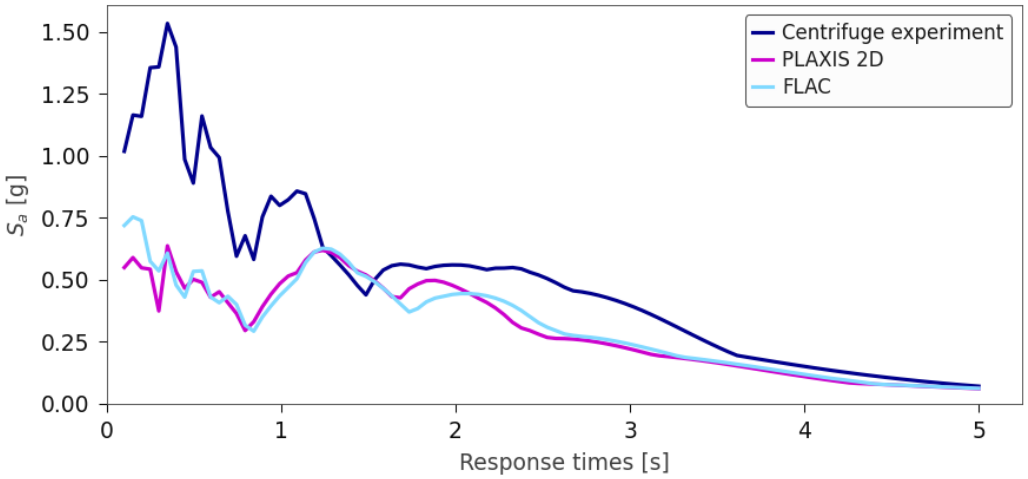


Figure 3.10: Maximum pore pressure comparison between numerical and centrifuge experimental results (FLAC results were sourced from Viana da Fonseca et al., 2018)

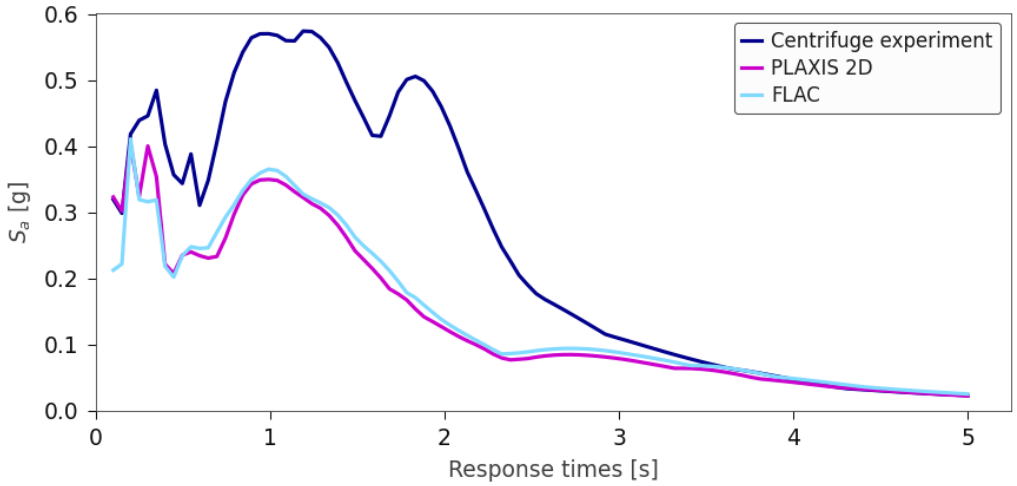


Figure 3.11: Maximum pore pressure comparison between numerical and centrifuge experimental results (FLAC results were sourced from Viana da Fonseca et al., 2018)

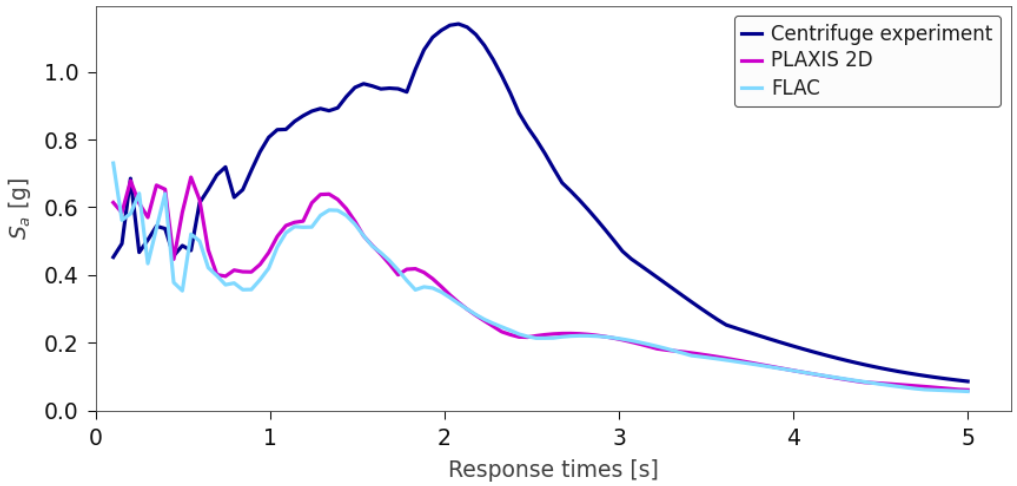


Figure 3.12: Maximum pore pressure comparison between numerical and centrifuge experimental results (FLAC results were sourced from Viana da Fonseca et al., 2018)

3.3 Conclusions

An approach for modeling pore pressure, site response, and settlement using effective stress analysis with PLAXIS 2D and PM4Sand constitutive model was introduced and validated against centrifuge tests performed by Dashti et al. (2010a) and compared with other numerical modeling validation in FLAC by Viana da Fonseca et al. (2018). The settlement results exhibited relatively close agreement with the centrifuge tests for both experiments and ground motions. The validation

indicated that pore pressures in the free-field show closer agreement compared to those under the building. Nevertheless, these validation results were considered satisfactory for the purposes of this study. Thus it was demonstrated that PLAXIS 2D (Bentley, 2020), a numerical modeling software for advanced geotechnical analysis is able to get liquefaction-induced settlements.

A more extensive study to validate the ground motion modification due to liquefaction phenomena is presented in the next chapter.

Chapter 4

Validation of liquefaction-induced ground motion modification

The primary damage to buildings during earthquakes is shaking damage, therefore the modification to the ground shaking due to liquefaction is extremely important in the context of quantifying building performance. Liquefaction impacts directly the seismic surface motion, leading to modifications in soil-foundation settlement and causing potential large settlement and tilt.

The current understanding is that liquefaction causes a reduction in soil shear stiffness, increase in soil shear strain, and can amplify and reduce particular frequencies of the surface shaking. Therefore, the amplification or reduction of the surface shaking, in terms of peak values, due to liquefaction is function of the frequency content of the outcrop motion and of the geotechnical specificity of the site (Quintero et al., 2023).

This chapter presents a well-documented pilot site where different approaches to estimate surface ground motion at surface were compared (Equivalent linear (EQL) analysis, 1D and 2D non-linear elastic and non-linear effective stress numerical model). A simplified stress-based method named as the Boulanger & Idriss (B&I) and non-linear dynamic effective stress numerical analyses in FLAC (Itasca Consulting Group, Inc., 2016) were used to identify liquefaction. $HVSR$ curves were used to validate the 1D and 2D numerical analyses and laboratory test results were employed to calibrate an advanced constitutive model capable of reproducing liquefaction stress-strain behavior and pore water pressure generation.

4.1 Introduction

Liquefaction significantly increases seismic damages, as it is associated with large settlements (including differential settlements), horizontal displacements associated with lateral spreading phenomena, and changes in the ground shaking motion arriving at the surface.

Coupled non-linear effective stress numerical analyses can provide realistic liquefaction assessment, but these approaches require the calibration of a large number of model parameters, many of them without physical meaning.

In alternative, several simplified liquefaction triggering methods have been developed (eg. Chiaradonna et al., 2018; Millen et al., 2020; Kokusho, 2021), however, these only focus on liquefaction manifestation and do not address the modification to ground motion related effects. The most widely used is the stress-based method originally proposed by Seed et al. (1975) and further updated by others (eg., Boulanger and Idriss, 2016). This methodology requires, at a given depth, the loading imposed by the ground shaking to be compared with the soil resistance to liquefaction.

Seed et al. (1975) method was calibrated using surface ground motions without considering liquefaction effects. For that reason, some seismic codes (e.g. Eurocode 8, CEN, 2004) provide conservative amplifications factors to estimate the peak ground acceleration (PGA or a_{max}) at the surface depending on the type of soil deposit, simplifying the process of estimating the complete surface ground motion. To a detailed liquefaction assessment, a complete site-specific surface ground motion is necessary.

If liquefaction is not considered, other ground response methods can be used. These can be divided into linear approaches, equivalent linear approaches (EQL) and non-linear approaches (NLA). In the simplest linear approach, a Fourier Transfer Function determines how each frequency of the bedrock motion is modified by the soil deposit. However, this transfer function depends on the dynamic parameters of the soil, namely the shear modulus (G) and damping ratio (D), which, in a simple linear analysis, are considered constant for each layer. Since the soil behavior is non-linear, the linear approach is usually modified into an EQL analysis to provide reasonable estimates of ground response. This requires an iterative process with successive linear analyses with different shear modulus and damping ratios, so that the obtained values are consistent with the level of strain induced in each layer. While an earthquake motion is highly irregular, G and D are generally obtained in laboratory tests using a simple harmonic cyclic loading. Although the EQL approach is computationally convenient and provides reasonable results for weak to moderate motions, it remains an approximation because the dynamic properties of the soil are assumed constant during the period of analysis and pore water pressure generation cannot be simulated. For instance, in strong ground motions leading to very large strain levels, the EQL may not be adequate (Pyke,

1979).

Alternatively, the actual non-linear response of a soil deposit can be simulated using direct numerical integration in the time domain (Carlton and Tokimatsu, 2016). Any elastic or inelastic stress-strain model or advanced constitutive model can be used for this purpose, such as QUIVER using the Hardin and Drnevich (1972) backbone curve (Kaynia, 2012), or the Davidenkov (1938) model for unloading-reloading that uses the General Quadratic/Hyperbolic (GQ/H) model (Groholski et al., 2015).

However, for the purpose of estimating the seismic demand for the performance assessment of surface infrastructures, the occurrence of liquefaction may render this estimate of surface PGA as irrealistic, and especially critical in terms of the estimate of ground displacements. Excess pore pressure build-up may change the natural vibration modes of the system, affecting the frequency content of the motion, as well as reducing the amplitude of high-frequency components and increasing the amplitude of longer-period components (Kramer et al., 2011). Consequently, for the purpose of evaluating earthquake-induced liquefaction damages ($EILD$), a more detailed analysis should be performed in the areas identified as potentially liquefiable (for example, based on a previous microzonation map, Lai et al., 2021). Liquefaction depends on the intensity of ground shaking, and the ground shaking felt at the surface also depends on the soil stiffness, which changes with pore pressure build-up as mentioned above.

As advanced non-linear models are not sufficiently mature to be used in practice, simplified methods are still of great practical relevance to capture the key features of liquefaction.

4.2 Geological setting and geotechnical model

The pilot site area is located in the Greater Lisbon region, involving the municipalities of Vila Franca de Xira and Benavente, on the left bank of the Tagus River. It consists of a basin that evolved as a tectonic depression, controlled by faults, resulting in an elongated rectangle oriented in the NE-SW direction. The basin rests on top of the Soco Varisco and/or Mesozoic formations and it is filled by fluvial and marine sediments, ranging from the Paleogene to the Holocene (Carvalho et al., 2006; Vis et al., 2008; Manupella et al., 2011). The sediments of the basin present vertical and lateral variations of composition and texture and, locally, stratification irregularities, with lenticular or beveled layers. The stratigraphic units were defined according to the formation process and subdivided in a set of lithological units, as explained in Lai et al. (2021).

According to geological charts and explanatory notes (Zbyszewski and Assunção, 1965; Zbyszewski and Veiga Ferreira, 1968; Manupella et al., 2011; Zbyszewski and Veiga Ferreira, 1969) the stratigraphic units in Figure 4.1a were defined. The lithological units were defined from the analysis of

the borehole information (Figure 4.1b). The study area, presented in Figure 4.1 is located between longitudes 501,550.0 m and 518,300.0 m and latitudes 4,307,650.0 m and 4,320,600.0 m.

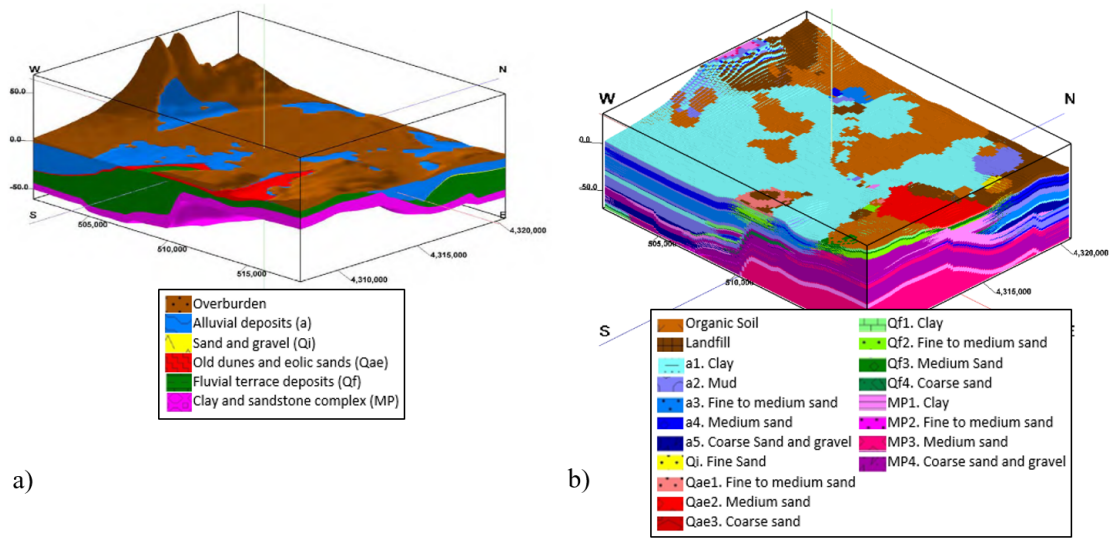


Figure 4.1: A 3-D view of: a) the stratigraphic model; b) the lithological model (Quintero et al., 2023)

The polygon that delimits the pilot site area is illustrated in Figure 4.2, covering a total area of 146.9 km2. A georeferenced database was created in SQLite with data obtained from lithological surveys and geotechnical and geophysical tests (Lai et al., 2021). This included 125 lithology boreholes, 92 Standard Penetration tests (SPT), 53 Cone Penetration Tests (including CPT, $CPTu$ and $SCPT$), 14 Cross-Hole (CH) tests, 13 Seismic Refraction (SR) tests, 9 Marchetti Flat Dilatometer tests (DMT and $SDMT$), 52 Horizontal to Vertical Spectral Ratio tests ($HVSR$), 3 Multichannel Analysis of Surface Waves tests ($MASW$) and 1 Spectral Analysis of Surface Waves tests ($SASW$).

The geotechnical information was derived mainly from $CPTu$ and DMT tests, complemented by valuable geophysical data from CH, $SCPT$ and $SDMT$ tests. Figure 4.3 presents the 3D profile of the normalized clean sand equivalent cone tip resistance ($q_{c1N,cs}$) obtained from $CPTu$ tests. The definition of the seismic bedrock resulted from an integrated analysis of geological and geophysical data, combined with the noise measurements in $HVSR$ tests. Borehole data provided by ENMC, indicate that soils with v_s higher than 800 m/s (rock) are at several hundred meters deep.Further details on the analysis and interpretation of the in-situ data are provided in Lai et al. (2019), Ferreira et al. (2020) and Lai et al. (2021).



Figure 4.2: Pilot site area, including the location of the in-situ tests (Quintero et al., 2023)

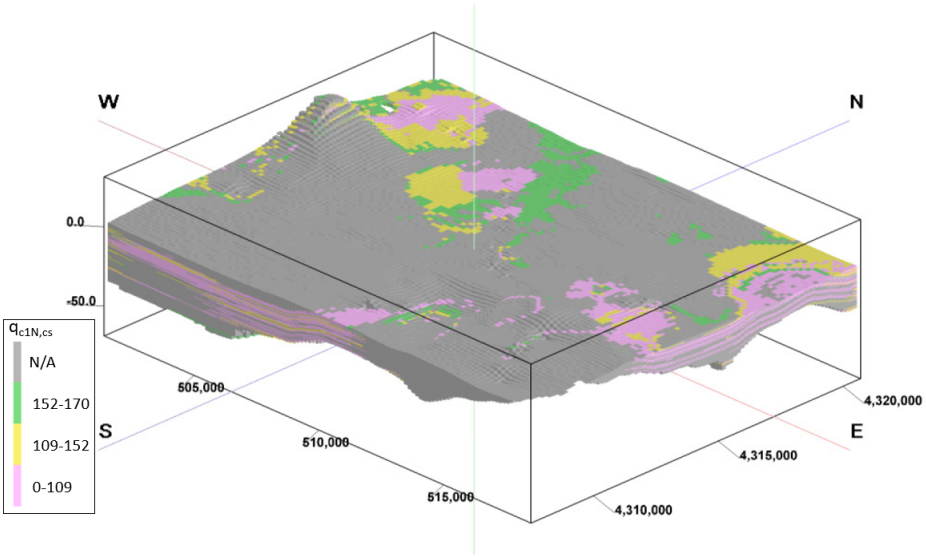


Figure 4.3: A 3D-model of the normalized clean sand equivalent cone tip resistance ($q_{c1N,cs}$). N/A in legend corresponds to non-liquefiable soils (Quintero et al., 2023)

For the purpose of illustrating the variability of the generated geotechnical model in the pilot site, a map of the distribution of the time-averaged shear wave velocity at 30 meters ($v_{s,30}$) is presented in Figure 4.4. This map clearly shows an increase of $v_{s,30}$ from West to East, predominantly in the NW-SE direction.

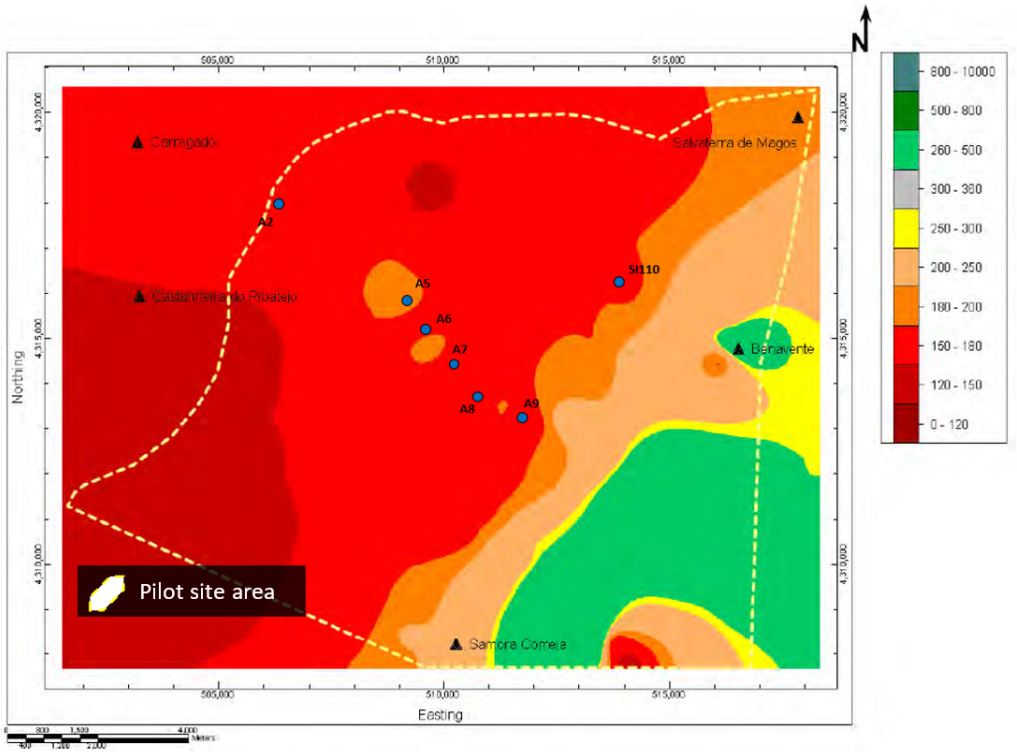


Figure 4.4: Map contains $v_{s,30}$ values (Quintero et al., 2023)

In this work, a numerical 2D analysis of a cross-section of the Lower Tagus Valley basin along the A10 highway was performed, which was characterized by a large number of field tests (see Figure 4.2). Along this cross-section, 6 profiles (A2, A5, A6, A7, A8, A9 presented in Figure 4.5) were selected to perform 1D analyses. Additionally, SI110 profile indicated in Figure 4.2 and Figure 4.4, located in the north of Benavente, corresponds to an area with historical evidence of soil liquefaction phenomena (Choffat and Bensaúde, 1912). Since cyclic triaxial tests have already been performed on undisturbed high-quality samples collected using the Gel-push sampler (Molina-Gómez et al., 2020) at this site, this profile was also analyzed. Figure 4.5 shows the shear wave velocity (v_s) profiles considered for the selected points, which will serve as the basis for the assessment of the local ground motion response.

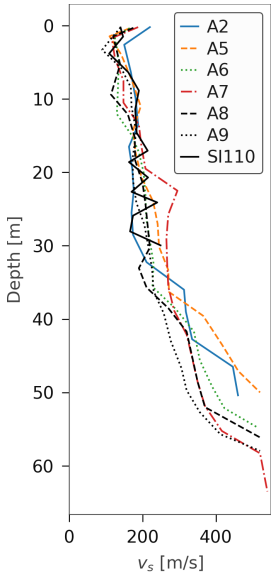


Figure 4.5: v_s profiles for the selected sites (Quintero et al., 2023)

4.3 Input motion selection

The input motions used in the numerical simulations correspond to recorded seismic events compatible with the reference seismic design action defined by the Portuguese National Annex to Eurocode 8 (PNAEC8). The values of PGA (and respective maximum magnitude) for different seismic actions were specifically computed on a seismological study carried out at LNEC (Portuguese National Laboratory of Civil Engineering). Two earthquake types and the reference return period identified in Eurocode 8 (475 years) were used to perform the analyses (Table 4.1). Type 1 seismic action corresponds to a "far" source earthquake, with epicentre in the Atlantic Ocean and Type 2 corresponds to a "near" source earthquake, with epicentre in continental Portugal.

Table 4.1: Reference Type 1 and Type 2 seismic actions for the pilot site region

Return period	Type 1		Type 2	
	Max. M_w	PGA $[m/s^2]$	Max. M_w	PGA $[m/s^2]$
RP1	7.8	1.00	6.6	1.70

Below the model depth the soil characteristics are unknown, as it is unknown the seismic bedrock depth and their material properties. In these circumstances it is common to introduce at the base of the model the seismic action compatible with the v_s at model depth. At the base level of the numerical models, the reference value of v_s is around 350 m/s, so 6 selected input motions were

recorded in soils type C for each return period (Tables 4.2 and 4.3).

For Type 1, six ground motions were selected from the Engineering Strong Motion Database (ESM) and the $NIED$ strong-motion seismograph networks.Table 4.2 shows the ground motions selected based on the information in Table 4.1. To obtain the RP1 motions, a scale factor of 1.10 was used to fit the average acceleration response spectra of the selected ground motions with the acceleration response spectra from EC8. A scale factor of 1.75 and 3.31 was used to obtain RP2 and RP3 motions, respectively. This scale factor was calculated as the ratio between the average spectral acceleration of the selected ground motions and the plateau spectral acceleration of PNAEC8 response spectrum. Figure 4.6 presents the acceleration response spectra of these ground motions.

For Type 2, six ground motions were selected from the NGAWest ground motions database. Table 4.3 shows the ground motions selected based on the information in Table 4.1. To obtain the RP1 motions, a scale factor of 1.22 was used to fit the average acceleration response spectra of the selected ground motions with the acceleration response spectra from EC8. A scale factor of 1.61 and 2.37 was used to obtain RP2 and RP3 motions respectively. Again, this scale factor was calculated as the ratio between the average spectral acceleration of the selected ground motions and the plateau spectral acceleration of PNAEC8 response spectrum. Figure 4.6 presents the acceleration response spectra of these ground motions.

The 12 ground motions for type 1 and 2 associated to the return period of 475 years were used to perform 1D numerical analysis while the Northridge-01 motion for type 2 was used for the 2D analysis to evaluate the valley effect.

Table 4.2: Type 1 ground motions selected

	Database	Earthquake	Country	E. dist $[km]$	Mw	Year	Station	PGA $[m/s^2]$
1	ESM	Izmit	Turkey	170.7	7.6	1999	TK5903	1.01
2	K-NET	Yaita	Japan	301.0	9.0	2011	TCGH09	1.47
3	KIK	Noheji	Japan	269.0	8.0	2003	AOMH05	1.33
4	K-NET	Tsu	Japan	184.0	7.4	2001	MIE006	1.17
5	K-NET	Kanonji	Japan	132.0	7.3	2000	KGW005	0.85
6	ESM	Chichi	Taiwan	136.2	7.6	1999	AE013	1.46

Table 4.3: Type 2 ground motions selected

	Earthquake	Country	E. dist $[km]$	Mw	Year	Station	PGA $[m/s^2]$
1	Imperial Valley-06	EEUU	22.4	6.5	1979	Compuertas	1.98
2	Parkfield-02, CA	EEUU	12.8	6.0	2004	Parkfield-UPSAR 01	2.09
3	N. Palm Springs	EEUU	21.1	6.1	1986	Palm Springs Airport	2.07
4	Iwate	Japan	27.1	6.9	2008	IWT011	2.16
5	Christchurch	New Zealand	16.9	6.2	2011	Canterbury Aero Club	2.22
6	Northridge-01	EEUU	28.2	6.7	1994	LA - Baldwin Hills	2.58

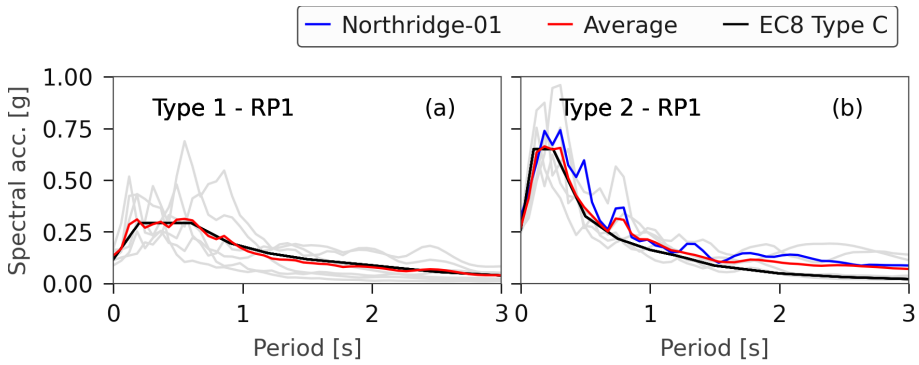


Figure 4.6: Acceleration response spectra of the ground motions recorded in soil type C (adapted from Quintero et al., 2023)

4.4 Liquefaction assessment methods based on field CPT tests

Simplified liquefaction triggering procedures based on field tests are a very practical tool for assessing the soil susceptibility to liquefaction, namely using easily obtainable and reliable CPT data.

Boulanger and Idriss (2014) (B&I) proposed a stress-based approach for evaluating the factor of safety against liquefaction triggering, which is defined as the ratio between the cyclic stress ratio (CSR) induced by the earthquake, and the cyclic resistance ratio (CRR) given by the soil resistance, through Equation 2.2 (see section 2.1.5).

Furthermore, Iwasaki (1978) proposed the liquefaction potential index (LPI) to assess the damage potential of liquefaction computed as showed in Equation 4.1, where $F_L = 1 - FS$ when FS less than 1, $F_L = 0$ when FS greater than 1 and z depth of measurement in meters.

$$LPI = \int_0^{20} (10 - 0.5 \cdot z) \cdot F_L \cdot d_z \tag{4.1}$$

In order to classify liquefaction risk, Iwasaki (1978) also proposed four categories based on ranges of values of LPI: liquefaction risk is very low when $LPI = 0$, liquefaction risk is low when $0 < LPI \leq 5$, liquefaction risk is high when $5 < LPI \leq 15$ and liquefaction risk is very high when $LPI > 15$. This was later updated by Maurer et al. (2014) for the Christchurch earthquake sequence using the following ranges: No liquefaction for $LPI < 4$, marginal liquefaction when $4 \leq LPI < 8$, moderate liquefaction when $8 \leq LPI < 15$, and severe liquefaction for $LPI \geq 15$. Ferreira et al. (2020) proposed for this pilot site another classification based on LPI associated with superficial manifestation severity, which is minor for $0 < LPI \leq 5$, moderate for $5 < LPI \leq 15$ and major to severe when $LPI > 15$.

4.5 Site response analysis

4.5.1 Equivalent linear analyses

Equivalent linear analysis (EQL) is an approach to obtain reasonable estimates of ground response where an iterative process of successive linear analyses with different shear modulus and damping ratios is required to derive values consistent with the level of strain induced in each layer.

As a result, it is common to characterize the strain level of the transient record in terms of an effective shear strain taken as an equivalent strain factor, α, (typically 65%) multiplied by the peak strain (Kramer, 1996). Idriss and Sun (1992) proposed that this shear strain ratio depends on the earthquake magnitude and can be estimated by Equation 4.5. This means that, for a magnitude of 7.5, the value of α is 0.65.

$$\alpha = \frac{M - 1}{10} \tag{4.2}$$

In this work, the analysis was performed using the open-source Python package pySRA v0.5.0 (Kottke, 2018), where the variation of the shear modulus G and damping ratio D with the strain level for a particular soil was determined using the curves proposed by Darendeli (2001), which takes into account the confining pressure (σ'_0), the plasticity index (PI), the overconsolidation ratio (OCR), the excitation frequency (f) and the number of loading cycles (N). An $OCR = 1$, Number of cycles $N = 10$, $f = 1Hz$, $PI = 0$ for sand layers, $PI = 30$ for clay layers and soil unit weight of 20 kN/m^3 were considered. The frequency was selected to be near to the fundamental frequency of the soil deposit, and the number of uniform cycles was chosen to be close to the number of cycles of the input motions.

4.5.2 1D and 2D numerical models

A 2D non-linear elastic plane-strain numerical model using a Finite Difference model in FLAC® (Itasca Consulting Group, Inc., 2016) of a cross-section of the Lower Tagus Valley basin along the A10 highway was analysed. Along the A10 cross-section, 1D non-linear elastic analyses were performed at the 6 profiles previously indicated, for validating the numerical models against the HVSR curves in the linear elastic strain range. Figure 4.7 shows the 2D numerical model including the 1D profiles (A2, A5, A6, A7, A8, A9). The soils were modeled with a linear elastic model with hysteretic damping. The default "hysteretic damping" model available in FLAC was used to provide a more realistic stress-strain response, which falls in the category of non-linear elastic models. The extreme values of logarithmic strain (the values at which the tangent slope becomes zero), L1 and L2 parameters, were estimated to fit to the modulus reduction curves from Darendeli (2001).

Additionally, a small amount of Rayleigh damping was used in the numerical model to mitigate numerical instability and material damping in the very small strain range, consistent with other uses of the PM4Sand model (e.g. Luque and Bray, 2017). The parameters for the Rayleigh damping were input by setting the damping as both stiffness and mass proportional and then defining the ξ_{min} and f_{min} parameter using Equations 4.3 and 4.4, which correspond to the minimum point in the damping versus frequency relationship. f_1 and f_2 correspond to the lowest and highest frequencies of interest in the model, and $\xi_{1,2}$ is the ratio of critical damping set at those frequencies.

$$\xi_{min} = \sqrt{\alpha \cdot \beta} \tag{4.3}$$

$$f_{min} = \frac{2 \cdot f_1 \cdot f_2}{\sqrt{4 \cdot f_1 \cdot f_2}} \tag{4.4}$$

$$\alpha = \frac{2 \cdot w_1 \cdot w_2}{w_2^2 - w_1^2}(w_2\xi_{1,2} - w_1\xi_{1,2}) \tag{4.5}$$

$$\beta = \frac{2}{w_2^2 - w_1^2}(w_2\xi_{1,2} - w_1\xi_{1,2}) \tag{4.6}$$

The lowest frequency of interest (f_1) is typically governed by the lowest natural frequency of the soil deposit or the lowest frequency of soil-structure system. The lowest frequency of the soil deposit corresponds to the first mode of the liquefied site, which was estimated by performing an elastic site response analysis $f_1 = 0.5[Hz]$ using the software Deepsoil (Hashash, Y. and Musgrove, M. and Harmon, J. and Groholski, D. and Phillips, C. and Park, D., 2016). The highest frequency

of interest was governed by the 2nd mode frequency of the soil-structure system $f_2 = 10[Hz]$. $\xi_{1,2}$ was set as 2%.

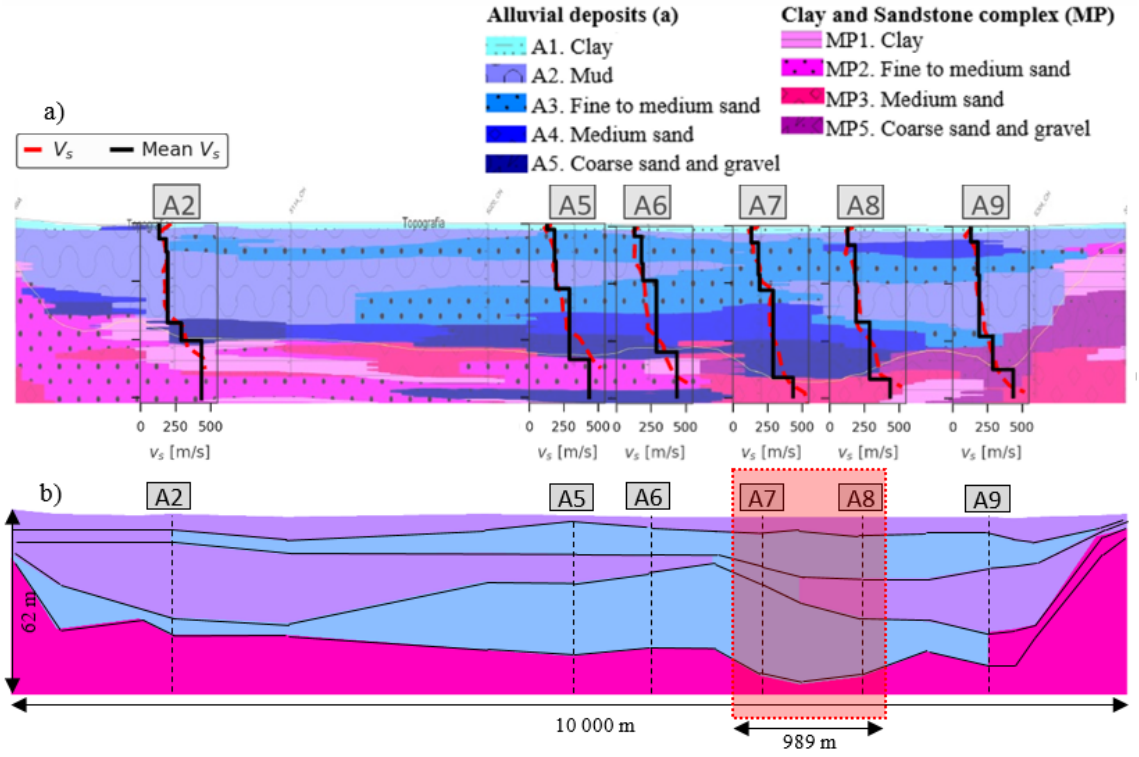


Figure 4.7: Cross-section of the Low Tagus Valley basin along A10: a) stratigraphic and lithological units; b) 2D numerical model geometry (Quintero et al., 2023)

The mesh of the 2D model is consistent with the soil profile outlined in Figure 4.7b, with element sizes of approximately 1.5 m by 2.0 m. The model was 62 m deep and 10 km wide, the lateral boundaries were tied together as recommended by Bray and Macedo (2017) and Ziotopoulou and Montgomery (2017), among many others, and the base of the soil profile was modeled as a rigid boundary, to represent the bedrock where the input motion is applied. A rigid base was incorporated into the 2D model, despite its absence from the actual soil profile. This option creates unrealistic wave reflections; however, it was deemed helpful to minimize calculation time (given that the model is 10000 m broad) and to ensure convergence.

The 1D numerical model mesh consisted of a single column of zones (equivalent to elements in the finite element method), and laterally adjacent grid points (equivalent to nodes) were attached to move together in both horizontal and vertical directions. The zones in each layer were sized to be equal or less than 0.5 m, to accurately simulate the seismic motion. In both cases, the input motion was applied at the base of the model.

HVSR curves determined from noise measurements and the transfer functions from the base to

the surface from 1D and 2D elastic numerical analysis were computed for the six profiles along A10 highway, to validate the fundamental frequencies of the numerical model in the linear elastic domain. Figure 4.8 shows the fundamental frequency values estimated from the transfer functions computed as the surface Fourier amplitude spectrum divided by the input motion Fourier amplitude spectrum. To calculate the Fourier amplitude spectrums, the Python package eqsig v1.2.10 was used (Millen, 2019). According to this validation analysis, 1D and 2D numerical models provided results that are in good agreement with the in-situ response. Comparing the fundamental frequencies from 1D and 2D numerical models, 1D analysis overestimates the values in profiles A5 and A8, while 2D numerical model overestimates the value in the profiles A6 and A8. These differences can be associated to the 1D and 2D numerical analyses are a simplification of the 3D nature of the site. Numerical fundamental frequencies in the profiles at the borders of the cross-section (A2 and A9 profiles) match very well with in-situ response. Globally, taking into account the complex geological conditions, the several models can be considered representative.

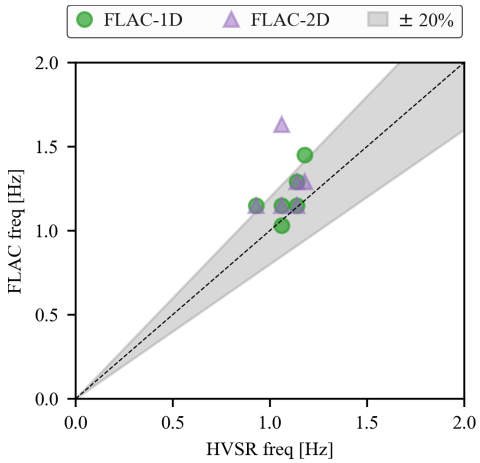


Figure 4.8: Fundamental frequency values from HVSR curves and elastic numerical models results - Northridge-01 ground motion (Quintero et al., 2023)

Numerical modeling can be employed to simulate the seismic response on liquefiable soils given a suite of acceleration time histories for a specified earthquake scenario. This procedure requires the use of an advanced constitutive model that is able to reproduce liquefaction stress-strain behavior and pore water pressure generation. In this work, besides the elastic analysis mentioned above, additional 1D and 2D effective stress numerical analyses using the PM4Sand constitutive model were performed to assess liquefaction.

For simulating liquefaction, the PM4Sand constitutive model (Boulanger and Ziotopolou, 2017) available in FLAC (Itasca Consulting Group, Inc., 2016) was used, as a user-defined material in a dynamic link library (DLL) for the liquefiable layers. The constitutive model parameters are grouped into two categories; a primary set of six parameters (three properties, two flags,

and atmospheric pressure) that are most important for model calibration, and a secondary set of parameters that may be modified from their default values in special circumstances (Boulanger and Ziotopolou, 2017). The primary model input properties of soil are the apparent relative density (D_R) affecting the peak drained and undrained strengths and the rate of strain accumulation during cyclic loading, the shear modulus coefficient (G_o) related with the maximum shear modulus ($G_{max} = \rho \cdot v_s^2$) calibrated to the estimated or measured in-situ shear wave velocity, and the contraction rate parameter (h_po) which is used to calibrate the estimated in-situ cyclic resistance ratio (CRR) after all other properties have been set. A detailed description about the constitutive model characteristics can be found in Boulanger and Ziotopoulou (Boulanger and Ziotopolou, 2017).

For the 6 profiles located along A10 highway, cyclic laboratory tests were not performed in the liquefiable soils. Therefore, PM4Sand parameters of these soils were calibrated based on the average normalized clean sand equivalent cone tip resistance ($q_{c1N,cs}$) at these depths. For this calibration, the equivalent liquefaction resistance curve adapted from (Boulanger and Idriss, 2016) and appendix A of (Boulanger and Idriss, 2014) was used considering 3% single amplitude shear strain.

Table 4.4 presents the soil parameters used in the effective stress numerical analyses for each profile, where PM4 sand was used for the liquefiable layers while the remaining layers were modeled with the elastic model with hysteretic damping. In the non-linear elastic analyses the shear modulus (G) indicated in Table 4.4 for each layer was taken. For all analyses, a soil unit weight of 20 kN/m^3 was considered.

Due to the large size of the entire 2D numerical model, it was not possible to perform the analysis with PM4Sand due to insufficient computational resources. Therefore, the red dotted zone in Figure 4.7 with about 1 km wide was simulated with a 2D effective stress numerical model and PM4Sand constitutive model in the sandy layers. This zone only contains profiles A7 and A8.

Table 4.4: Soil parameters for the A10 highway profiles.

Parameters	A2	A5	A6	A7	A8	A9
Layer 1						
Model	Elastic	Elastic	Elastic	Elastic	Elastic	Elastic
H [m]	5.5	2.0	3.5	6.0	6.5	5.5
G [MPa]	35.672	35.672	35.672	35.672	35.672	35.672
Layer 2						
Model	PM4Sand	PM4Sand	PM4Sand	PM4Sand	PM4Sand	PM4Sand
H [m]	4.5	11.0	9.5	11.0	14.0	11.5
G [MPa]	68.552	68.552	68.552	68.552	68.552	68.552
D_R	43	43	43	43	43	43
G_o	680	680	680	680	680	680
h_{po}	1.834	1.834	1.834	1.834	1.834	1.834
Layer 3						
Model	Elastic	Elastic	Elastic	PM4Sand	Elastic	Elastic
H [m]	24.5	9.5	6.0	5.5	13.0	21.5
G [MPa]	76.397	76.397	76.397	151.090	76.397	76.397
D_R	-	-	-	43	-	-
G_o	-	-	-	1084	-	-
h_{po}	-	-	-	2.270	-	-
Layer 4						
Model	Elastic	Elastic	Elastic	Elastic	Elastic	Elastic
H [m]	6.0	24.5	25.0	30.5	20.0	11.5
G [MPa]	172. 171	172. 171	172. 171	172. 171	172. 171	269.316
Layer 5						
Model	Elastic	Elastic	Elastic	Elastic	Elastic	Elastic
H [m]	20.0	13.0	15.5	6.5	6.0	9.5
G [MPa]	388. 103	388. 103	388. 103	388. 103	388. 103	388. 103

For the SI110 site, located in north Benavente area, the cyclic triaxial tests performed by Ramos (2021) were used (called NB1 in that work). The obtained samples corresponded mostly to clean to low fines content sand of recent alluvial material, which were transported along the Tagus river (Ramos, 2021). Table 4.5 presents the test identification (Test ID), the confining pressure (p'_i), the loading frequency ($Freq$), the void ratio after consolidation (e_i), the cyclic stress ratio (CSR) and the number of cycles ($Nliq$) required to develop 100% excess pore pressure ratio ($r_u = 1$) for samples collected between 3.5 and 4.5 meters depth. The pore pressure ratio is defined as the ratio

between excess pore pressure and vertical effective stress at rest.

Table 4.5: Cyclic triaxial tests performed with undisturbed specimens to assess liquefaction potential (Ramos, 2021)

Test ID	p'_i	Freq	e_i	CSR	N_{liq}
	kPa	Hz		$q/2\sigma'_c$	$r_u = 100\%$
NB1_F2_GP3.5_I1	34.9	1	0.59	0.18	378
NB1_F4_GP4_I2	39.6	1	0.70	0.12	726
NB1_F1_GP4.5_I1	45.1	1	0.70	0.21	16

The laboratory tests presented in Figure 4.9 show the soil resistance curve obtained from the cyclic triaxial tests and the following data available in Ramos (2021): $D_R = 63\%$, $G_o = 723$, $e_{max} = 0.857$ and $e_{min} = 0.548$. Although the PM4Sand sets as default values 0.8 and 0.5 for the maximum and minimum void ratio (e_{max} and e_{min}) respectively, the real values provided by Ramos (Ramos, 2021) were used as PM4Sand secondary parameters. Since cyclic simple shear tests (CDSS) resistance curves are required to calibrate the PM4Sand parameters, equation 4.7 in Ramos (Ramos, 2021) was used to transform the soil resistance curve from cyclic triaxial test to cyclic simple shear tests data.

$$CSR_{CDSS} = (0.7256 N_{liq}^{-0.052}) \cdot CSR_{CTx} \tag{4.7}$$

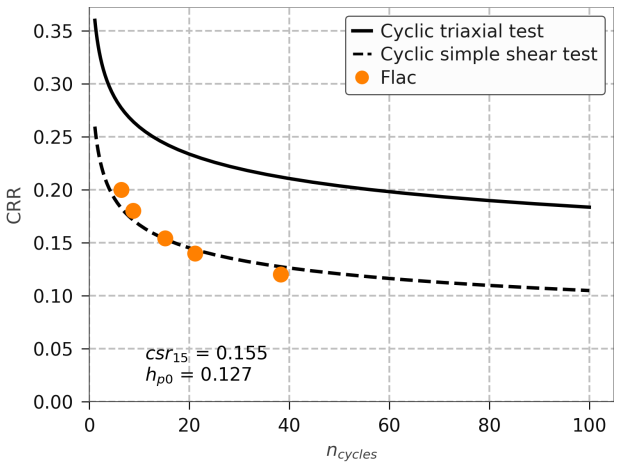


Figure 4.9: Cyclic resistance curve for NB1 tests (Quintero et al., 2023)

A contraction rate parameter (h_{po}) of 0.127 was numerically calibrated to match the model simulation results with the cyclic simple shear test resistance curve. The liquefaction failure criterion to obtain the cyclic resistance curve in Figure 4.9 was an excess pore pressure ratio of 100%. Thus,

these parameters were used in the liquefiable layer identified between 5.1 and 12.7 meters of depth at SI110 site. Other liquefiable layers were identified between 12.7-17.6 meters and 19.6-21.8 meters. For these soils, the PM4Sand parameters were calibrated as in A10 highway, based on the average normalized clean sand equivalent cone tip resistance ($q_{c1N,cs}$) in these depths. Table 4.6 presents the shear modulus (G) used for non-linear elastic analyses and the PM4Sand parameters used in effective stress numerical analysis. For this profile a soil unit weight of 20 kN/m3 was also considered.

Table 4.6: Soil parameters for the SI110 site

Parameters		SI110	
	Layer 1	Layer 2	Layer 3
H [m]	0.5	2.0	2.6
G [MPa]	40.000	44.100	24.247
	Layer 4	Layer 5	Layer 6
H [m]	7.6	3.8	1.1
G [MPa]	45.918	69.094	93.461
D_R	63	34	41
G_o	723	563	709
h_{po}	0.127	0.360	2.583
	Layer 7	Layer 8	Layer 9
H [m]	2.0	2.2	1.7
G [MPa]	54.222	94.337	58.980
D_R	-	40	-
G_o	-	653	-
h_{po}	-	2.681	-
	Layer 10	Layer 11	Layer 12
H [m]	1.2	4.3	1.9
G [MPa]	117.551	58.980	126.533

4.6 Results and discussion

4.6.1 1D analysis at certain profiles along A10 cross-section

In this section the results from B&I simplified method, EQL analyses, 1D non-linear elastic numerical analyses (Flac-1D), and 1D effective stress numerical analysis with PM4Sand (Flac-1D-Liq) performed for the 12 ground motions (for type 1 and 2) are presented for the 6 profiles along A10 highway. In the following figures the solid lines represent the median value associated to each

depth obtained for the six ground motions of each type, and the dotted lines represents the median absolute deviation.

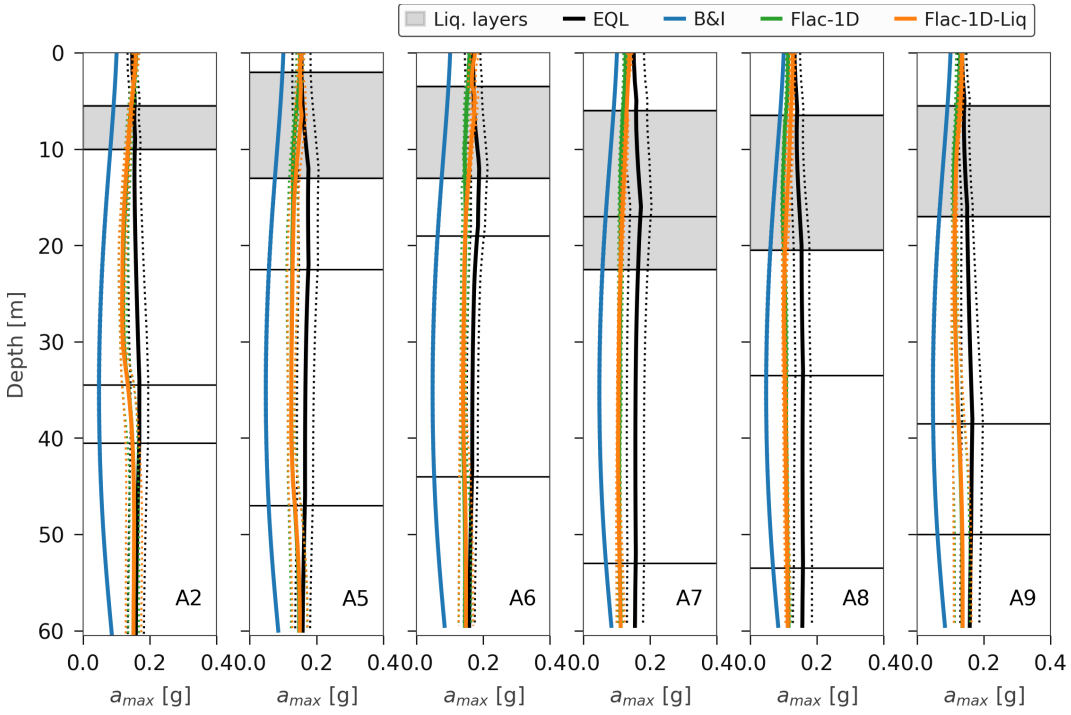
Figure 4.10 shows the maximum acceleration (a_{max}) profile where the profile for B&I method was calculated as ($a_{max} \cdot r_d$), being a_{max} the reference surface peak ground acceleration from EC8, and the profile for 1D numerical analyses was calculated as the average a_{max} value of the soil column from each depth to the ground surface. Peak ground acceleration from EC8 was used in B&I method to compare the results of a pure simplified method with 1D analyses results.

For type 1 ground motions (Figure 4.10a), B&I curves showed that the surface reference peak ground acceleration from EC8 was always lower to that calculated with the other methods, except for A8 profile where the surface B&I value was very close to Flac-1D surface a_{max}. For the remaining methods, it is clear that the median surface acceleration is quite similar in all the cases.

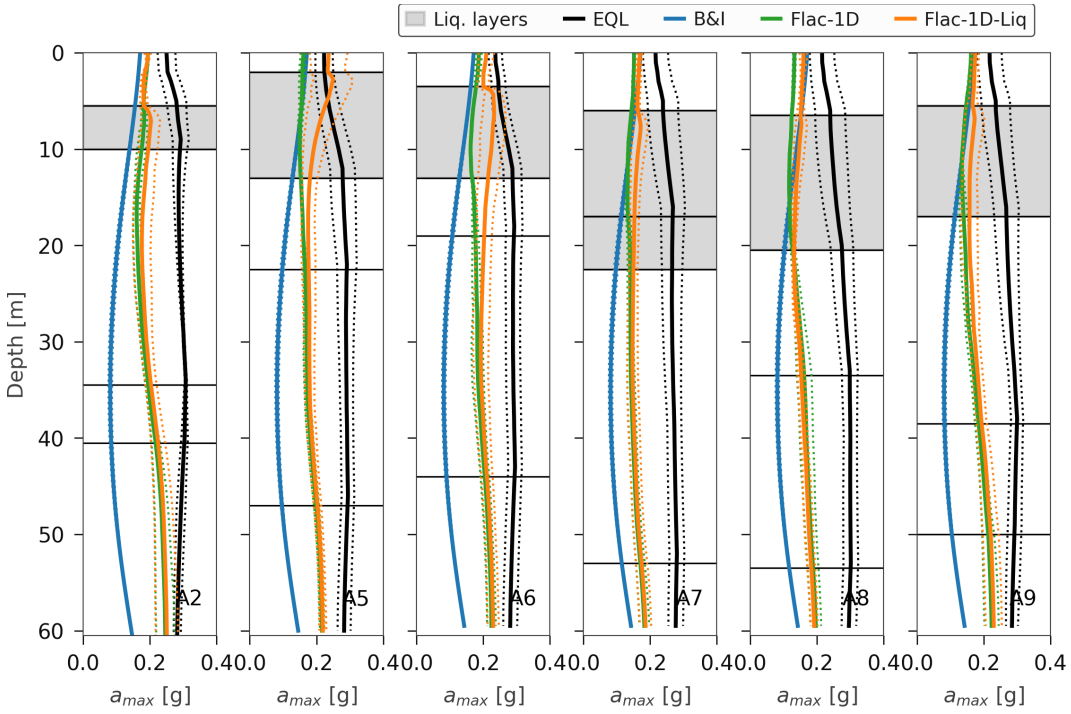
For type 2 ground motions (Figure 4.10b), B&I curves showed that the surface reference peak ground acceleration from EC8 was slightly lower to that calculated with the other methods in profiles A2 and A6, while in profiles A5 and A9 the surface B&I value was very close to Flac-1D surface a_{max} and in profiles A7, A8 and A9 to Flac-1D-Liq. Otherwise, the EQL method always estimated the highest surface acceleration values.

For B&I method calculated for both ground motions types, the a_{max} estimated at the base of the profile does not correspond to the PGA of the input motions used in the other analyses. Even when surface a_{max} from EC8 is the same of the other methods, the B&I profile is still different because the numerical analysis consider the specific soil properties of each layer which is not account for in the simplified B&I method.

Boulanger and Idriss (2014) highlight that the r_d factor can show important divergences when used in depths greater than 12 meters. Moreover, this method assumes that the soil has enough stiffness to amplify the signal up to the surface. However, the other methods (EQL, Flac-1D), using the estimated properties for each layer, have shown very low amplification due to weak soil characteristics. This highlights the importance of site-specific analysis, even using simplified approaches such as EQL.



(a) Type 1 ground motions

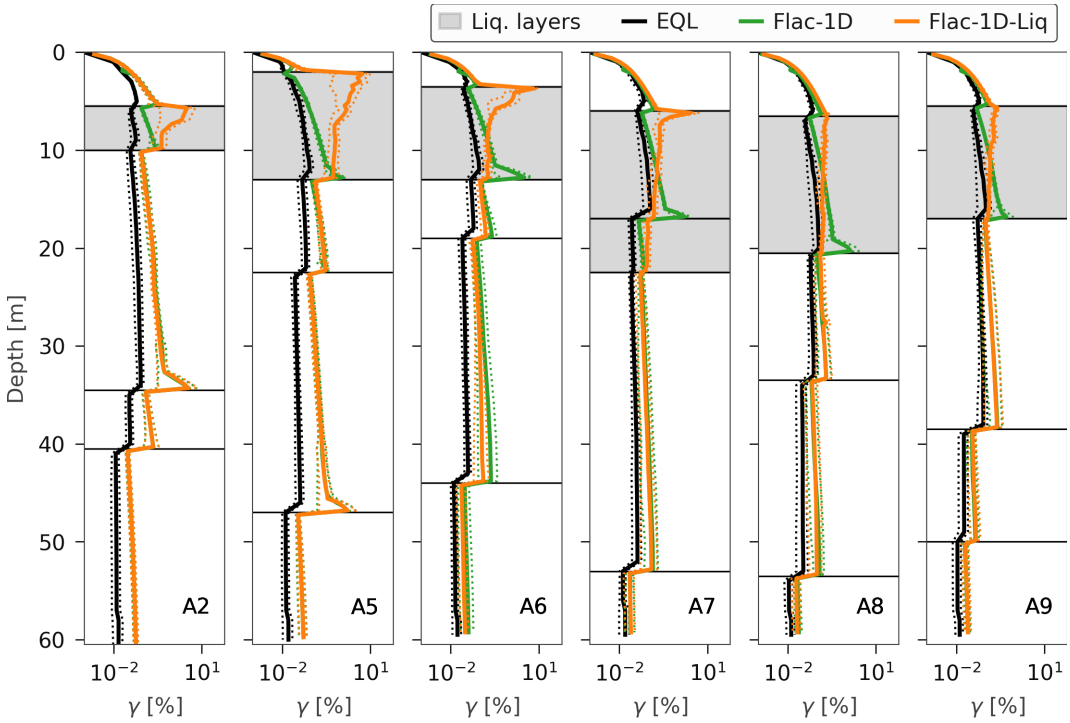


(b) Type 2 ground motions

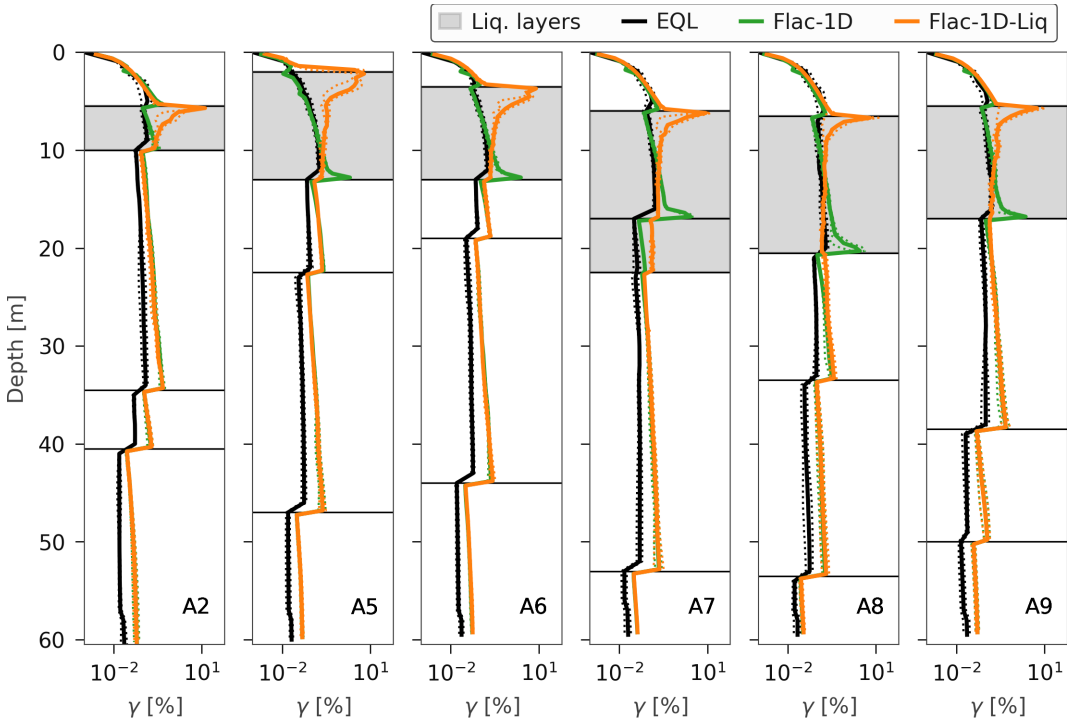
Figure 4.10: Maximum acceleration (a_{max}) profiles (Quintero et al., 2023)

Figure 4.11 presents the shear strain (γ) profiles showing that even when modeling elastic soils (Flac-1D), high deformations can be observed in all profiles, indicating the presence of weak soils.

Flac-1D estimates high deformation at the base of the liquefiable layer, while Flac-1D-Liq estimate the high deformation in the top of them. This is because Flac-1D-Liq use PM4sand for the liquefiable layer which enables excess pore pressure generation as illustrated in Figure 4.12.



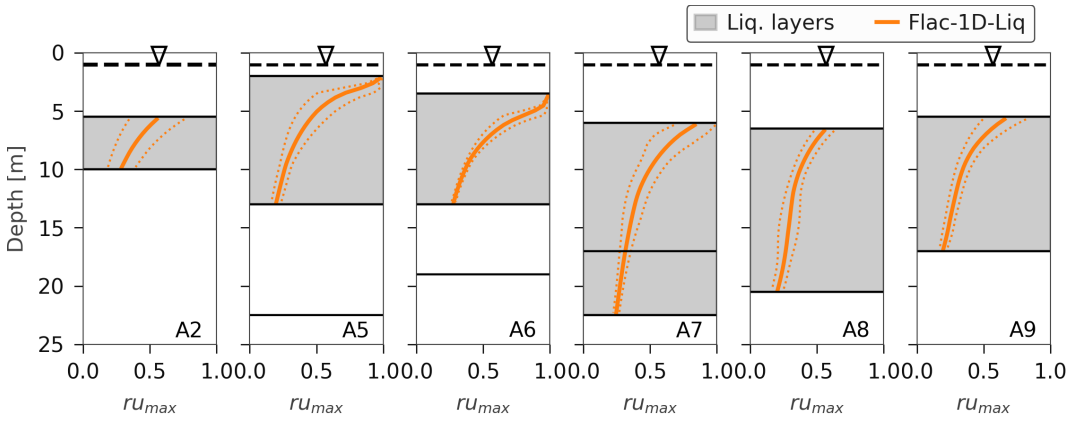
(a) Type 1 ground motions



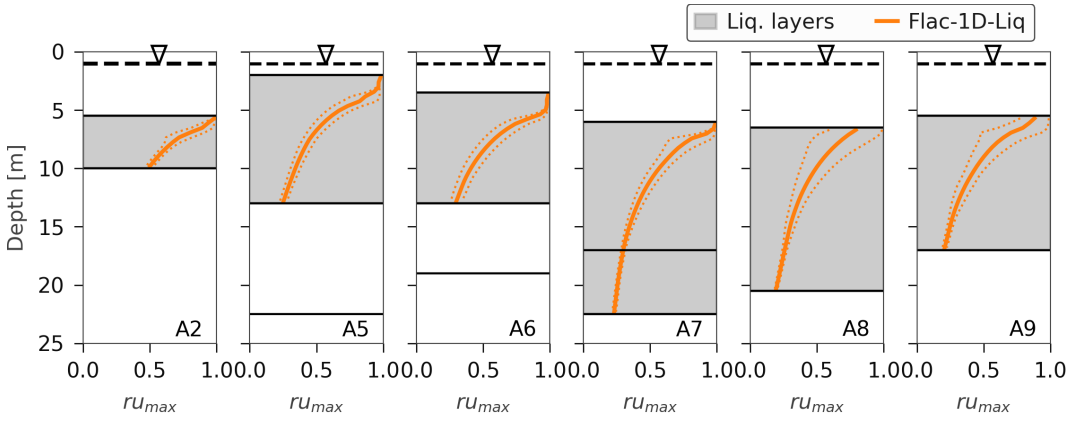
(b) Type 2 ground motions

Figure 4.11: Shear strain (γ) profiles (Quintero et al., 2023)

The high deformations observed in the Flac-1D, are probably related to the stiffness contrast between sand and clay layers. Comparing the maximum excess pore pressure ratios (ru, max) plot with the shear strain profiles, it is clear that they have the highest values at the same depth. All the profiles showed liquefaction at some depths, mostly between 2 and 6 meters depth.



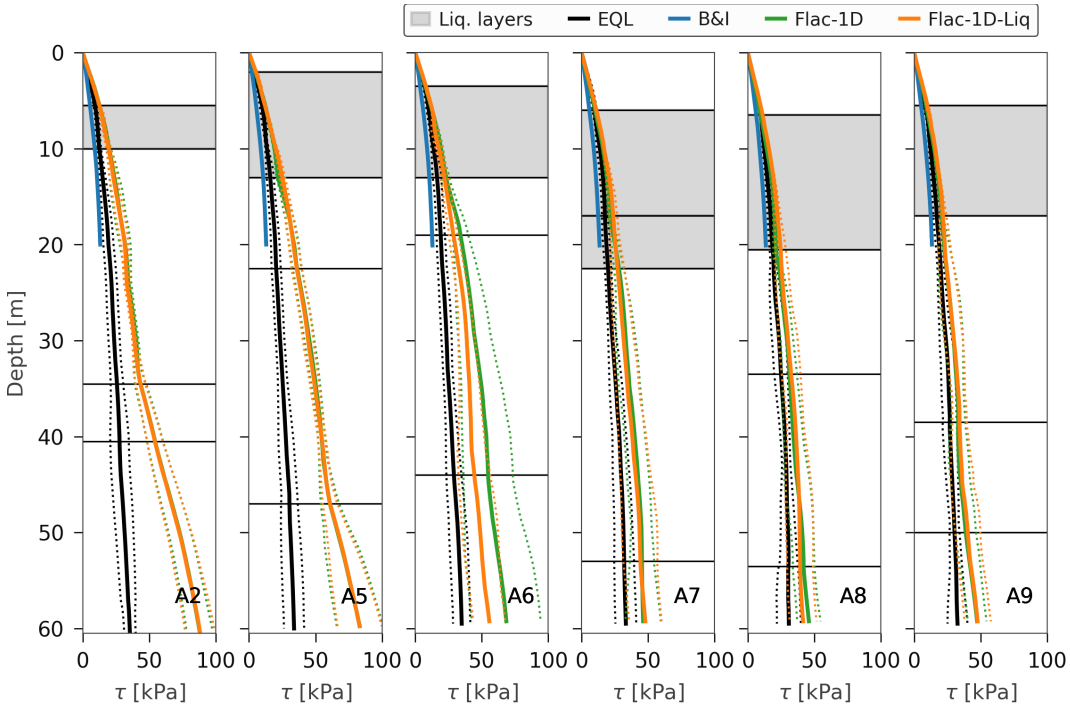
(a) Type 1 ground motions



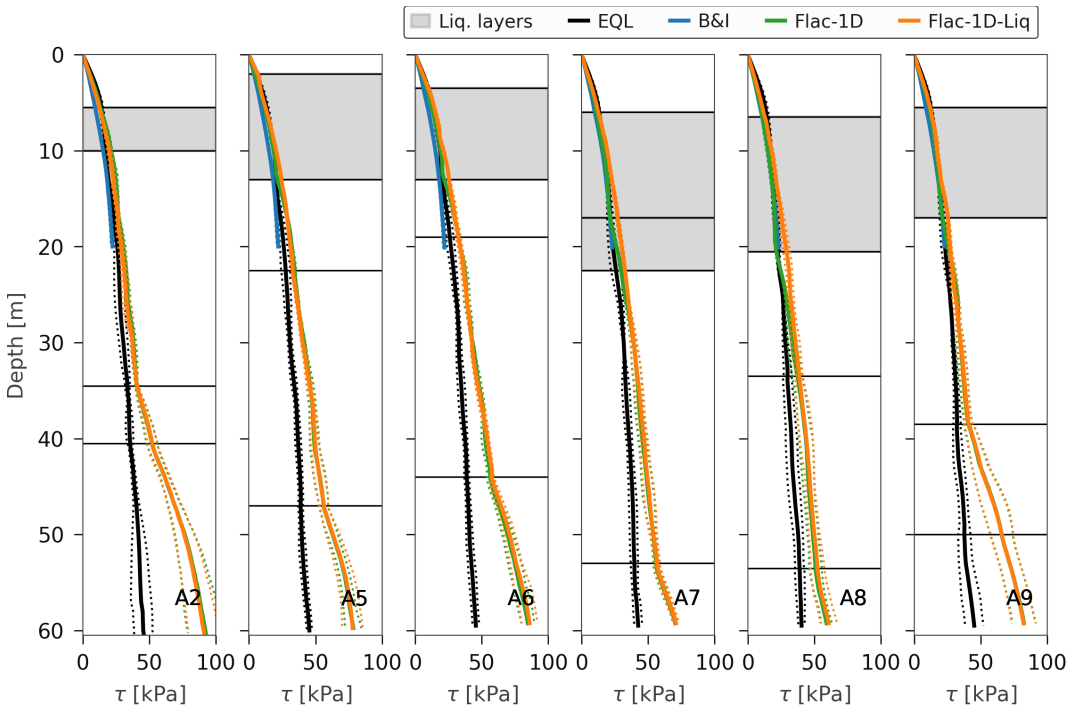
(b) Type 2 ground motions

Figure 4.12: Maximum excess pore pressure ratio r_u profile from 1D effective stress analysis (Flac-1D-Liq) considering liquefaction (Quintero et al., 2023)

Figure 4.13 presents the shear stress (τ) profiles for the 1D analysis where τ profile for B&I method was calculated as $CSR \cdot \sigma'_v$. In general, the EQL profiles were always lower when compared with the others 1D analysis results, while they were very similar to the B&I results for type 2 motions and higher for type 1 motions. In addition, comparing the elastic analysis (Flac-1D) with effective stress analysis (Flac-1D-Liq) they are coincident in all profiles with exception of profile A6 using type 1 ground motions where effective stress analysis showed lower shear stresses.



(a) Type 1 ground motions

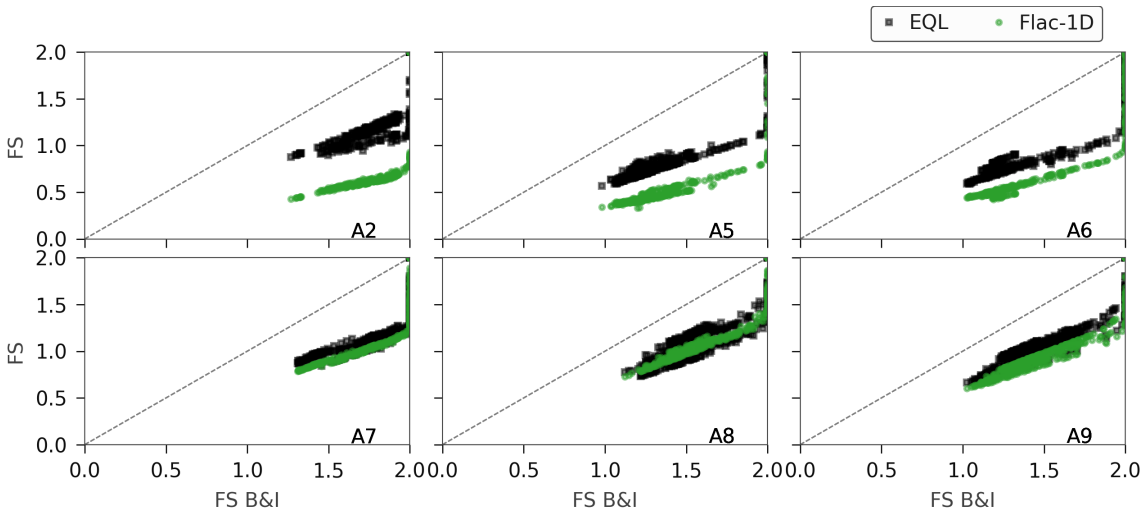


(b) Type 2 ground motions

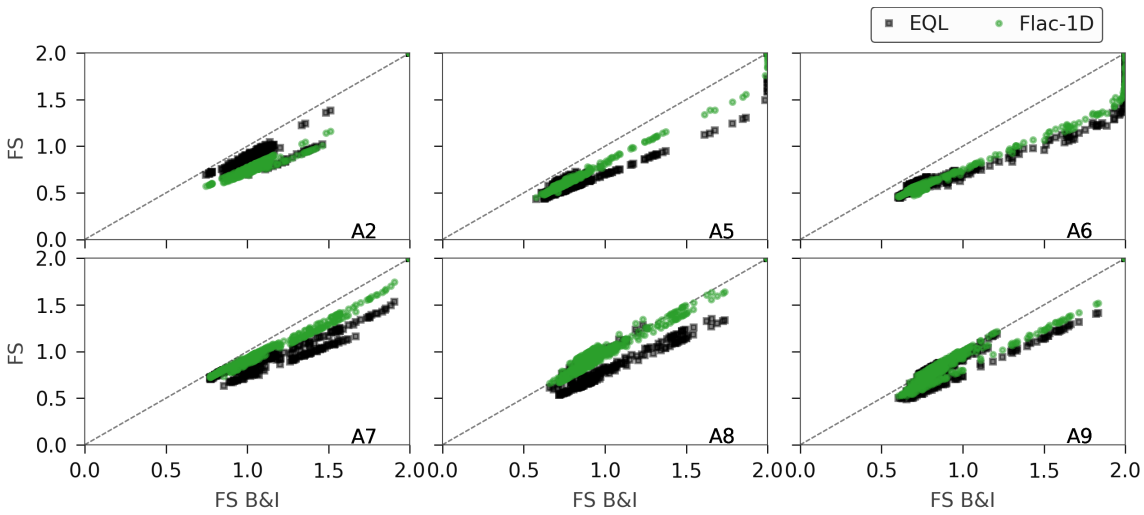
Figure 4.13: Shear stress (τ) profiles (Quintero et al., 2023)

Factor of safety against liquefaction (FS) were estimated to quantify the liquefaction potential of the profiles. Figure 4.14 shows the factor of safety estimated from B&I method (FS B&I) for all the depths compared with the FS estimated from the other methods without simulation of

liquefaction. FS B&I was calculated using the simplified method described in section 4, while for the other methods the CSR was calculated dividing the shear stress by the effective vertical stress (τ/σ'_v). For type 1 ground motions, B&I method did not predict liquefaction at depths where the other method did. For type 2 ground motions, all methods show factor of safety (FS) values lower than one at certain depths, thus indicating the presence of highly liquefiable soil layers in all profiles. B&I method appears to be less conservative estimating in most of cases higher FS values than the other methods.



(a) Type 1 ground motions



(b) Type 2 ground motions

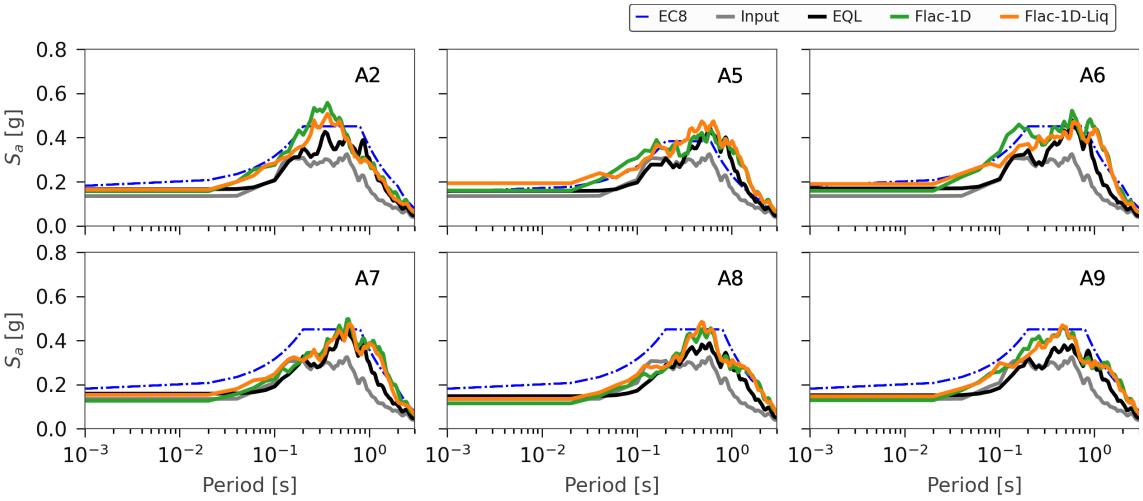
Figure 4.14: Factor of safety (FS) from B&I compared with FS from the other methods (Quintero et al., 2023)

Figure 4.15 shows the acceleration response spectra of the surface ground motions from all the methods used in the six profiles analysed above. The elastic numerical analyses (Flac-1D) show slightly higher spectral acceleration at some frequencies in comparison with the analysis with

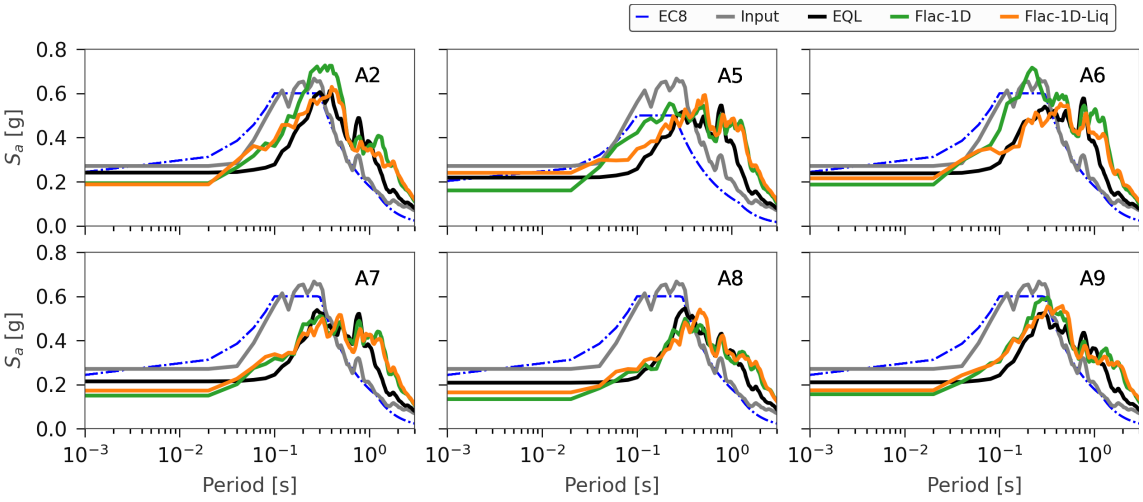
PM4Sand (Flac-1D-Liq) because of not considering liquefaction. The response spectra computed with non-linear elastic models adjust fairly well to new EC8 spectrum particularly in the plateau range.

4.6.2 2D analysis of A10 cross-section to evaluate the valley effect

2D non-linear elastic (Flac-2D) and effective stress (Flac-2D-Liq) analyses were performed for Northridge-01 ground motion to evaluate the valley effect, and to compare to the other methods and to the 1D numerical analyses presented above. As mentioned in section 4.5.2. due to the large size of the entire 2D numerical model, only a zone that contains profiles A7 and A8 was simulated for the Flac-2D-Liq analysis.



(a) Type 1 ground motions



(b) Type 2 ground motions

Figure 4.15: Acceleration response spectra of the surface ground motions (adapted from Quintero et al., 2023)

Figure 4.16 presents the maximum acceleration (a_{max}) profile for the different methods. Flac-2D maximum acceleration at the surface was always very similar to Flac-1D results, except for profile A7 where it was lower. For A7 and A8 points, the maximum acceleration (a_{max}) at the surface from Flac-2D-Liq was always slightly lower than Flac-1D-Liq models but slightly higher than Flac-2D values. In addition for profiles A2, A6 and A9, values below 20 meters depth are slightly lower in Flac-2D-Liq when compared with Flac-1D-Liq.

Figure 4.17 presents the shear strain (γ) profiles showing that Flac-2D-Liq estimates high deformation in the top of the liquefiable layers (as Flac-1D-Liq) while Flac-2D did not estimate any peak of high deformation. Once again, the high deformations in the top of the liquefiable layers are coincident with the maximum excess pore pressure ratio (ru_{max}) in Figure 4.18. Although not presented in the paper for shortness, Factor of safety profiles from Flac-1D and Flac-2D analyses show that the entire sandy layers have a high liquefaction potential while ru_{max} profiles from Flac-1D-Liq and Flac-2D-Liq analyses show full liquefaction only in the top of the sandy layers.

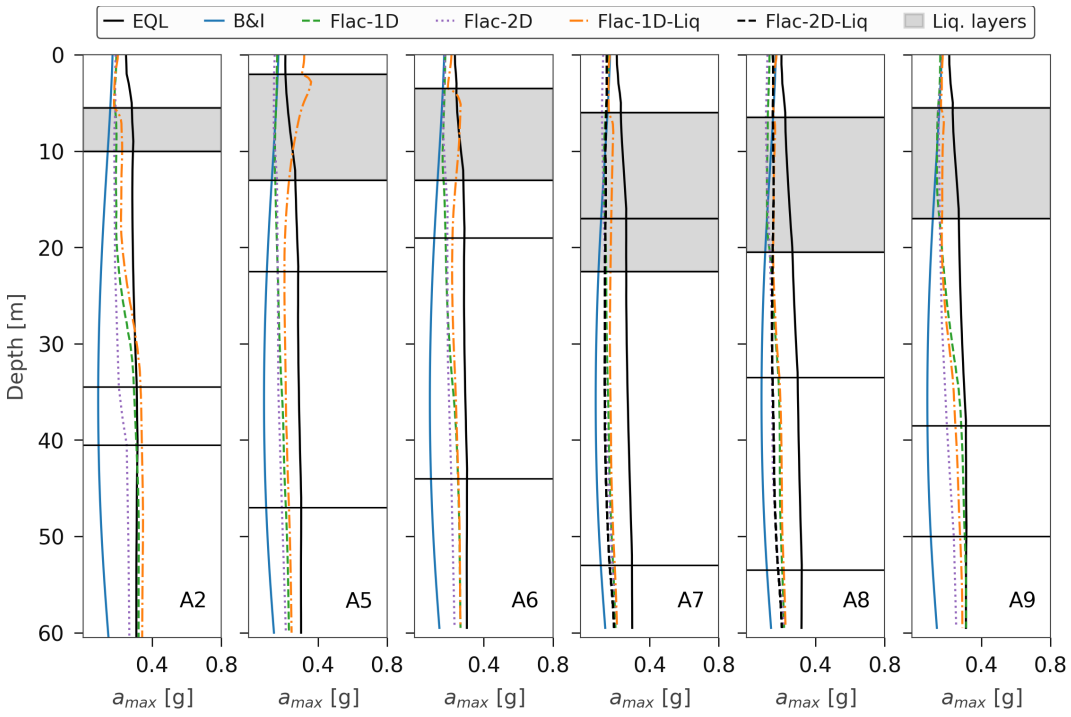


Figure 4.16: Maximum acceleration (a_{max}) profiles - Northridge-01 ground motion (Quintero et al., 2023)

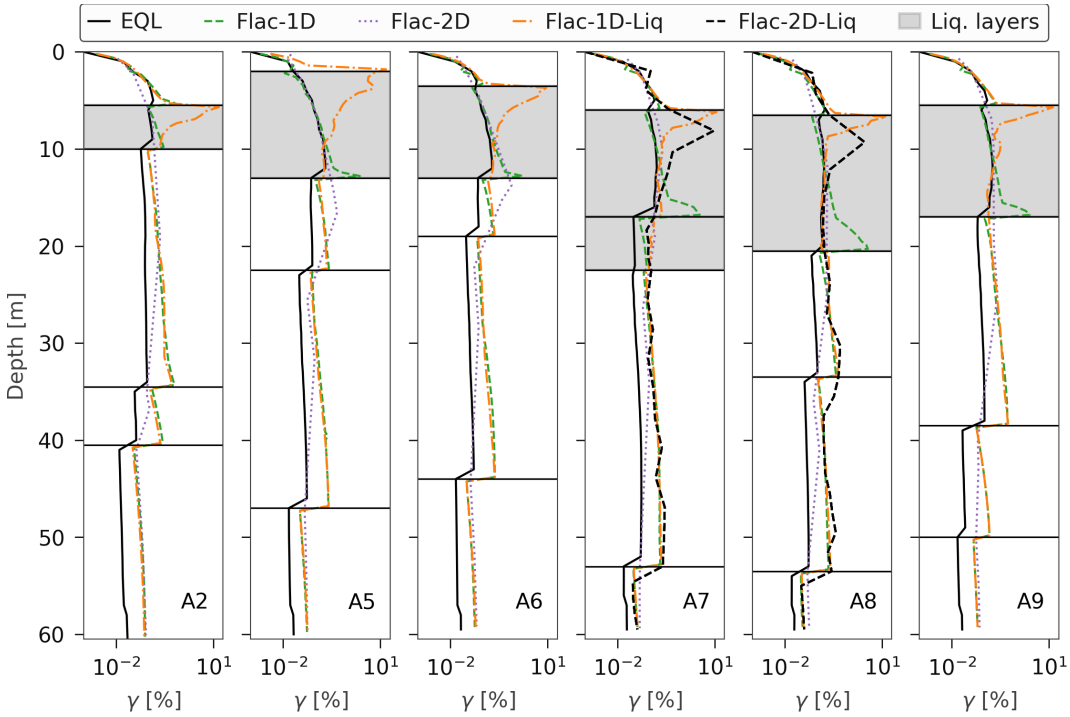


Figure 4.17: Shear strain profiles - Northridge-01 ground motion (Quintero et al., 2023)

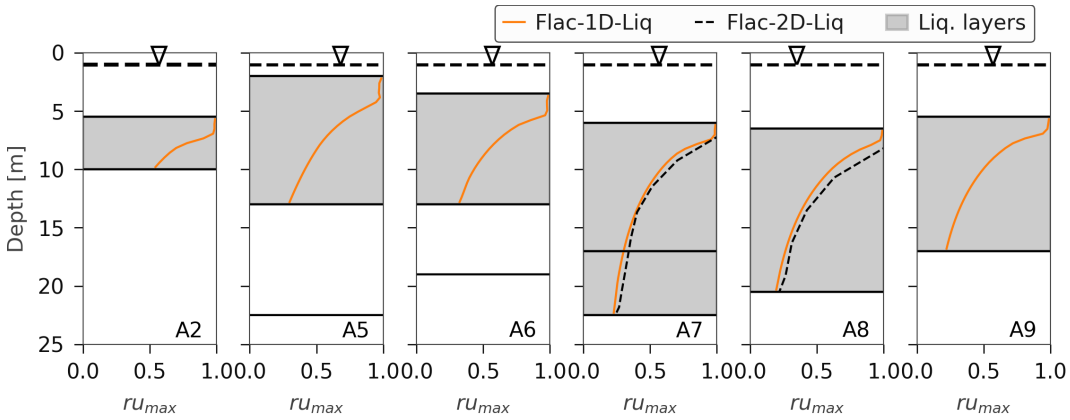


Figure 4.18: Maximum excess pore pressure ratio r_u profile from 1D and 2D effective stress analysis considering liquefaction (Flac-1D-Liq and Flac-2D-Liq respectively) - Northridge-01 ground motion (Quintero et al., 2023)

Figure 4.19 shows the shear stress (τ) profiles showing that the values estimated from 2D non-linear elastic analysis are always higher than the estimated with the other methods, and the estimated with EQL analysis are always lower than others. The profile estimated from Flac-2D-Liq model look similar with Flac-1D-Liq profile with some variations in the greatest depths.

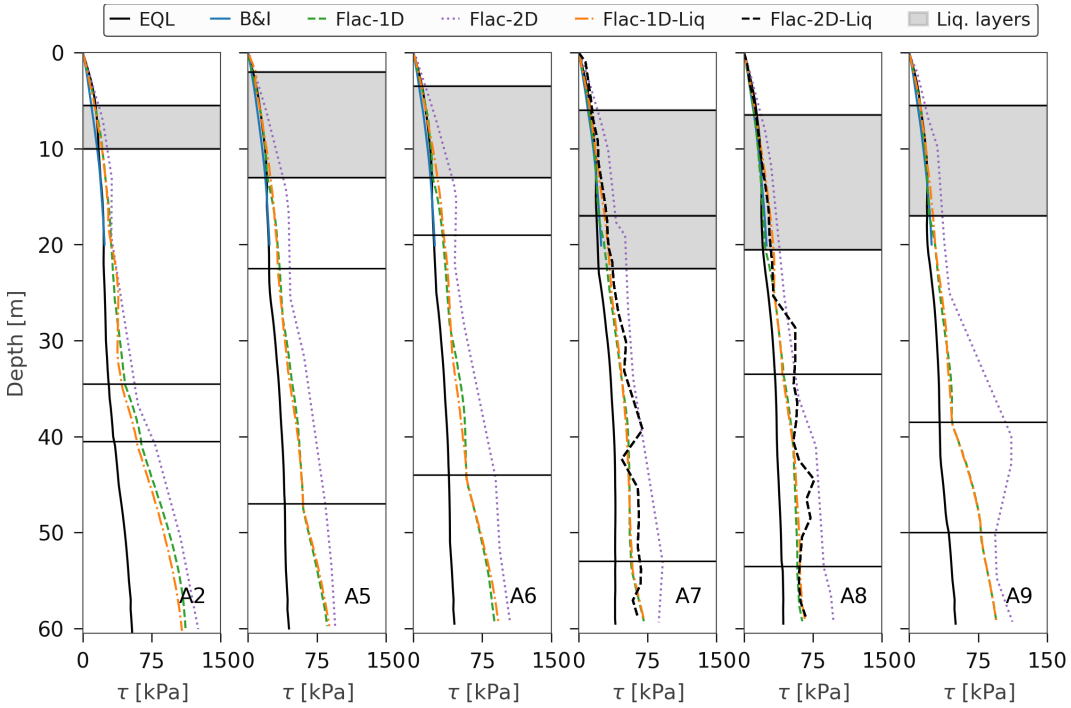


Figure 4.19: Shear stress profiles - Northridge-01 ground motion (Quintero et al., 2023)

Factor of safety against liquefaction (FS) and liquefaction potential index (LPI) were estimated to quantify the liquefaction potential of the profiles. Figure 4.20 shows the factor of safety estimated from B&I method (FS B&I) for all the depths compared with the FS estimated from non-linear 1D and 2D numerical models. Flac-2D shows factor of safety (FS) values lower than one, thus indicating the presence of highly liquefiable soil layers at different depths in all profiles.

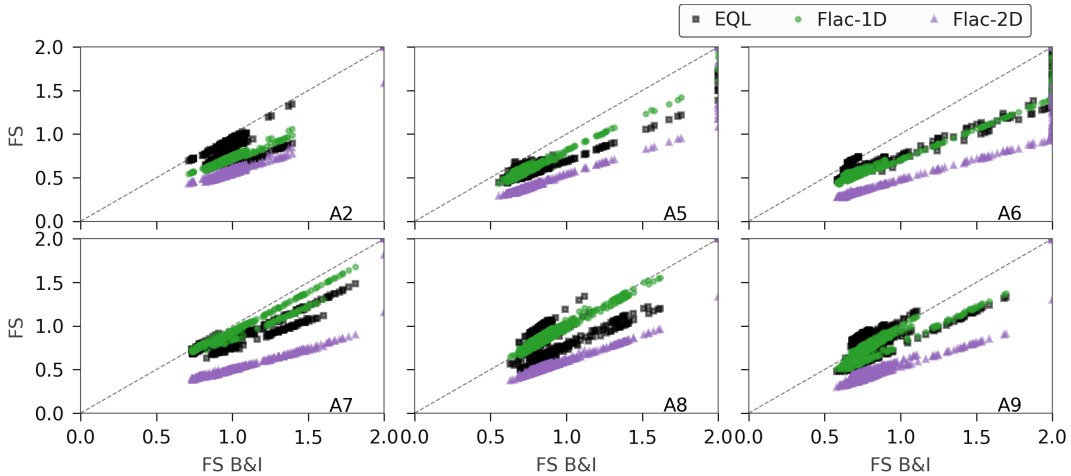


Figure 4.20: Factor of safety (FS) from B&I compared with FS from the other methods - Northridge-01 ground motion (Quintero et al., 2023)

Table 4.7 shows the LPI values calculated with Equation 4.1. Based in LPI results, from 2D analyses, all the profiles were found to have a very high liquefaction risk, except A2 profile which has a high risk. From EQL analyses, all the profiles have a high liquefaction risk, except A5 profile which has a very high risk. Flac-1D found A5 profile with a very high liquefaction risk, and A2, A6 and A9 profiles with a high risk. From B&I analyses, A5, A6 and A9 profiles have a high liquefaction risk. Similar conclusions may be taken if the criteria defined by Maurer et al. (2014) are used: from 2D analyses, all the profiles were found to have severe liquefaction, except A2 profile; from EQL analyses, A2 and A7 have marginal liquefaction, A6, A7 and A9 have moderate liquefaction and A5 has severe liquefaction; from Flac-1D, A5 profile has severe liquefaction, and A2, A6 and A9 profiles have moderate liquefaction; from B&I analyses, A6, A8 and A9 profiles have marginal liquefaction while A5 has moderate liquefaction.

Table 4.7: Liquefaction potential index (LPI) values.

	A2	A5	A6	A7	A8	A9
EQL	5.5	17.5	9.0	5.2	8.0	8.4
B&I	1.2	10.4	5.5	1.8	4.2	6.1
Flac-1D	18.0	16.6	9.8	3.1	4.1	8.1
Flac-2D	12.7	26.0	16.2	18.9	15.8	17.7

Figure 4.21 shows the acceleration response spectra of the surface ground motions from all the methods used in the six profiles analysed above. Flac-2D non-linear elastic numerical analyses show higher spectral acceleration in the central points (A5, A6 and A7) in comparison with Flac-1D results, indicating a basin effect.

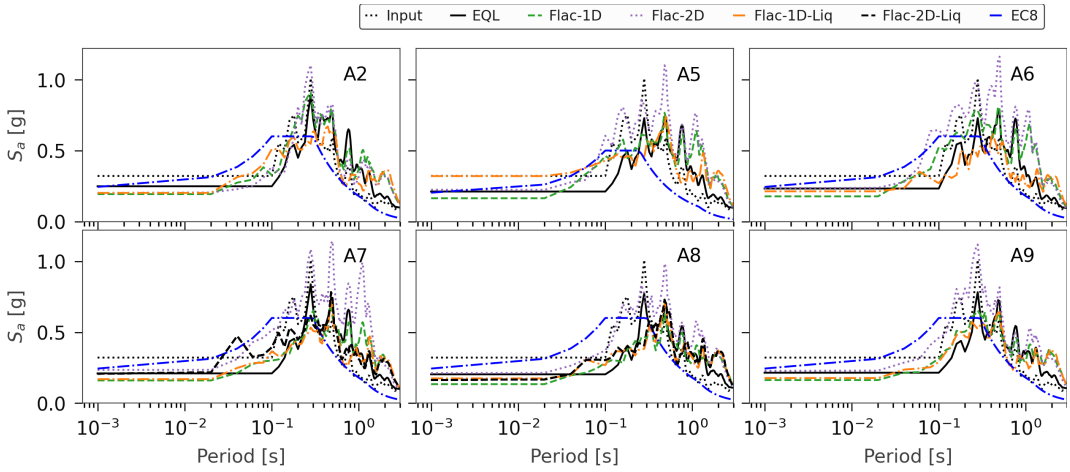


Figure 4.21: Acceleration response spectra of the surface ground motions - Northridge-01 input ground motion (adapted from Quintero et al., 2023)

4.6.3 North of Benavente SI110 profile

Due to the available results from cyclic laboratory tests in soils of the north of Benavente area, the SI110 profile was also selected for liquefaction potential analysis. 1D numerical analysis in effective stresses (Flac-1D-Liq) and elastic conditions (Flac-1D) were compared to the B&I and EQL analysis. Figure 4.22 shows the acc_{max}, γ, τ, FS and ru_{max} profiles. These results show that acc_{max} profile is similar among all the methods except for B&I where, once again, the surface reference peak ground acceleration from EC8 (0.17g) is similar to that calculated from the other methods, but the acc_{max} estimated at the base of the profile does not correspond to the PGA of the input motion used in the other analyses. Flac-1D and Flac-1D-Liq numerical models essentially provided the same response, identifying large deformation (γ) around 13-15 meters depth but the effective stress model shows more prominent peak. The shear stress (τ) profiles calculated with all the methods are similar. B&I and 1D elastic numerical analyses derived factors of safety against liquefaction (FS) less than 1.0, conversely to EQL which is less conservative in this case. Moreover, FS profile from Flac-1D analysis shows that the entire liquefiable layers have a high liquefaction potential while ru_{max} profile from Flac-1D-Liq analysis show full liquefaction only in the top of the first and second liquefiable layers, and non-liquefaction in the third and fourth liquefiable layers that are below 16 meters depth. Liquefaction potential index (LPI) was estimated resulting in values of 1.6, 5.5 and 2.3 for EQL, B&I and Flac-1D methods respectively. Only the results from the B&I method led to a LPI higher than 5, indicating high liquefaction risk. In the case of the simplified analyses (B&I), the FS results are derived directly from CPT data, where each measurement is taken at 2cm. In turn, for the modeled layers, a minimum thickness of 1 m was considered. In the case of Figure 4.22d, there is a fine layer of sand above the 5 m which was ignored given its reduced thickness. This thin layer above 5 m will likely have a minimal impact on LPI. In turn, there are also other sandy layers below 20 m, which exhibited very low FS values, which were also not considered since typically below this depth the superficial liquefaction-induced damages are negligible. This consideration is also compatible with LPI, which is computed for the first 20 m of the soil profile.

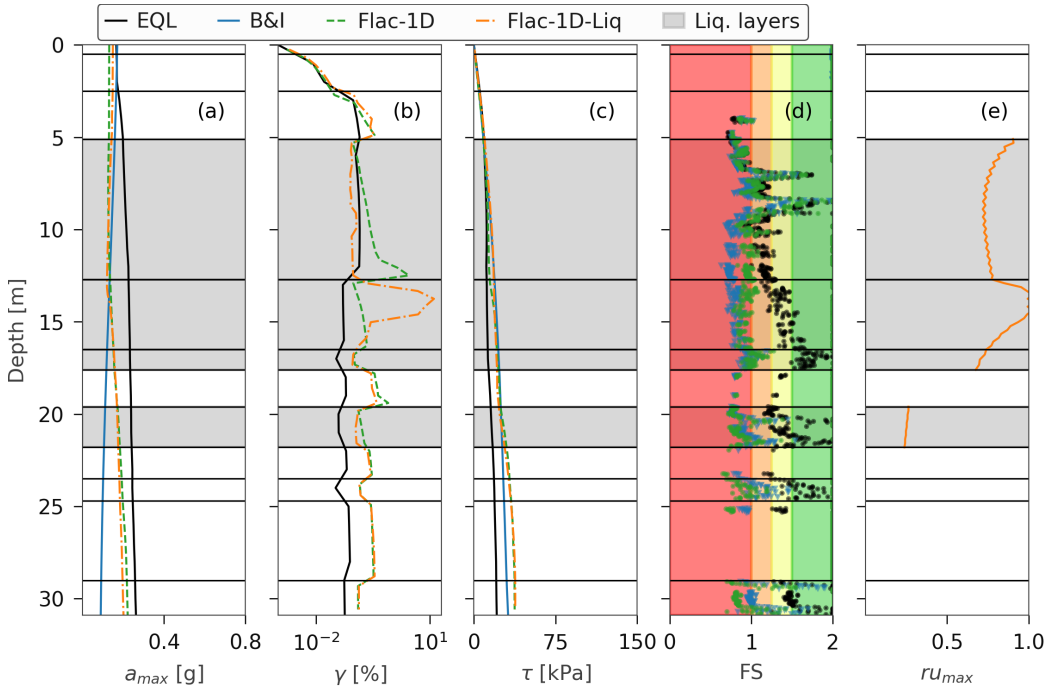


Figure 4.22: Profile SI110 of a) maximum acceleration (a_{max}); b) maximum shear strain (γ); c) maximum shear stress (τ) and d) factor of safety against liquefaction (red:0-1.0; orange:1.0-1.25; yellow: 1.25-1.5; green: 1.5-2.0) and e) maximum excess pore pressure ratio (ru_{max}) - Northridge-01 ground motion (Quintero et al., 2023)

Figure 4.23a shows again lower spectral acceleration in the numerical analysis with liquefaction in comparison to the elastic analysis, and EQL matches very well the effective-stress numerical analysis. Figure 4.23b presents excess pore pressure ratio during the earthquake showing that liquefaction was triggered around 13 meters depth.

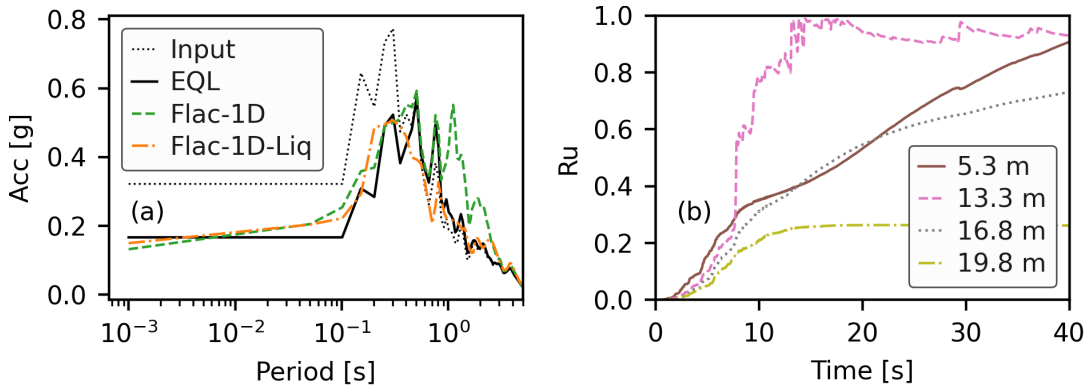


Figure 4.23: Results from 1D non-linear numerical model SI110: a) Surface spectral acceleration and b) r_u in different depths of liquefiable layer - Northridge-01 ground motion (Quintero et al., 2023)

4.7 Main findings

The well-documented pilot site located in the Greater Lisbon region was described, where 1D and 2D numerical simulations of the local ground seismic response were performed using different approaches. Simplified liquefaction assessment methods were compared with 1D and 2D effective stress numerical model.

HVSR curves were used to validate the fundamental frequencies of the numerical analyses in the linear elastic domain. The results showed good agreement with the in-situ response. Globally, taking into account the complex geological conditions, the several models can be considered representative, small differences can be associated to the 1D and 2D numerical analyses are a simplification of the 3D nature of the site. Thus it was demonstrated that FLAC (Bentley, 2020), is able to get the surface ground motion. As showed in the previous chapter FLAC and PLAXIS 2D provides really similar results, thus it is assumed that PLAXIS 2D is also capable of obtaining the ground motion at the surface.

More detailed findings in this chapter are listed as following:

- Flac-1D and Flac-1D-Liq analyses provided similar a_{max} profiles, while 2D analysis are slightly lower. Even when surface a_{max} from EC8 is the same of the other methods, the B&I profile is still different because the numerical analysis consider the specific soil properties of each layer which is not account for in the simplified B&I method which only depends on the depth and earthquake magnitude, M_w. For most profiles, the EQL method estimated the highest surface acceleration values.

- For all profiles in A10 highway, it can be observed that 1D elastic numerical analysis evidenced high shear strains in weak soils where liquefaction may occur. B&I method tended to underestimate the liquefaction risk level, justifying the need of site specific analysis. All numerical approaches classified the profiles A5, A6 and A9 with high or very high risk of liquefaction. Also, EQL and 2D non-linear elastic numerical analyses identified all profiles as having high or very high risk of liquefaction.

- The 1D and 2D models exhibit noticeable variation of the seismic motion at the surface when a non-linear elastic model is used, but when PM4sand model is used to simulate sandy layers response and liquefaction is possible, the 1D and 2D model responses become rather similar along the valley.

- Additionally, 1D effective stress numerical analysis using the PM4Sand constitutive model was performed, using three laboratory tests to calibrate the parameters of the liquefiable layer. The excess pore pressure ratio during the earthquake showed that liquefaction was

obtained around 13 m depth of the liquefiable layer. This profile was also analyzed through EQL, B&I and 1D elastic numerical analyses finding large deformation around 12-15 meters depth. B&I and 1D elastic numerical analyses found a factor of safety against liquefaction less than 1.0, but only B&I method found LPI values higher than 5 indicating high liquefaction risk. 1D elastic and 1D effective stress numerical model show similar results, but the effective stress model shows more prominent shear strain peak at that depth.

- Overall, current practice does not generally consider the occurrence of liquefaction but in this work the excess pore pressure build-up during the earthquake was evaluated to accurately estimate the surface ground motion in high liquefaction potential soil profiles. For this, an advanced constitutive model capable of reproducing liquefaction stress-strain behavior and pore water pressure generation was used.

Chapter 5

Boundary condition validation of the numerical models

The initial step in developing a numerical simulation of a building response is selecting the size of the model. These dimensions should ensure adequacy for capturing free-field conditions, minimizing wave reflections, and mitigating the influence of lateral boundaries on the stress-strain response of the building. The main objective of this chapter is to validate the boundary conditions of the numerical models in PLAXIS 2D by solving a common geotechnical problem of the ultimate bearing capacity and non-linear static moment-rotation response of a rough strip footing over both homogeneous and layered soil. This section outlines the steps followed to create the geometry of the domain, generate the finite element (FE) mesh, execute the model, interpret the results and compare them with analytical solutions.

5.1 Vertical loading

The ultimate bearing capacity of shallow foundations is a useful benchmark for verifying the correct implementation of the numerical model. First, because there are many widely accepted closed form solutions for comparison (Vesić, 1973), and secondly the bearing capacity is a key aspect of the ultimate foundation moment capacity (Chatzigogos et al., 2011; Deng and Kutter, 2012). For that, the external boundaries should be far enough to avoid any interference in the stress-strain involved and to ensure the geostatic conditions in points sufficiently distanced. A parametric study was performed changing the depth (D) and width (W) of the model separately to find the most suitable boundaries. Initially, sandy and clayey homogeneous soil profiles were used, and then some profiles with two layers were analyzed.

5.1.1 Sandy soil

Model construction

This study used a plane strain model with a homogeneous sand profile, the water table was assumed to be below the base of the model and therefore was neglected. PLAXIS 2D have five element distribution options to generate the finite element mesh, very fine, fine, medium, coarse and very coarse. For this study a 'medium' element distribution was selected. The mesh was refined in the region closer to the footing through a coarseness factor of 0.7 to provide a better discretization in the area of interest and gradually coarsened towards the left and right boundaries. The lateral boundaries were normally fixed, the base model boundary was considered as rigid in order to simulate a stiff rock below then it was fully fixed; and, the surface boundary was not fixed to simulate the free-field condition. The model depth (D) influence was studied varying this dimension between 2 m and 6 m keeping a constant model width (11 m). Also the model width (W) influence was studied varying this dimension between 5 m and 13 m keeping a constant model depth (D = 5 m). The considered numerical model is shown in Figure 5.1.

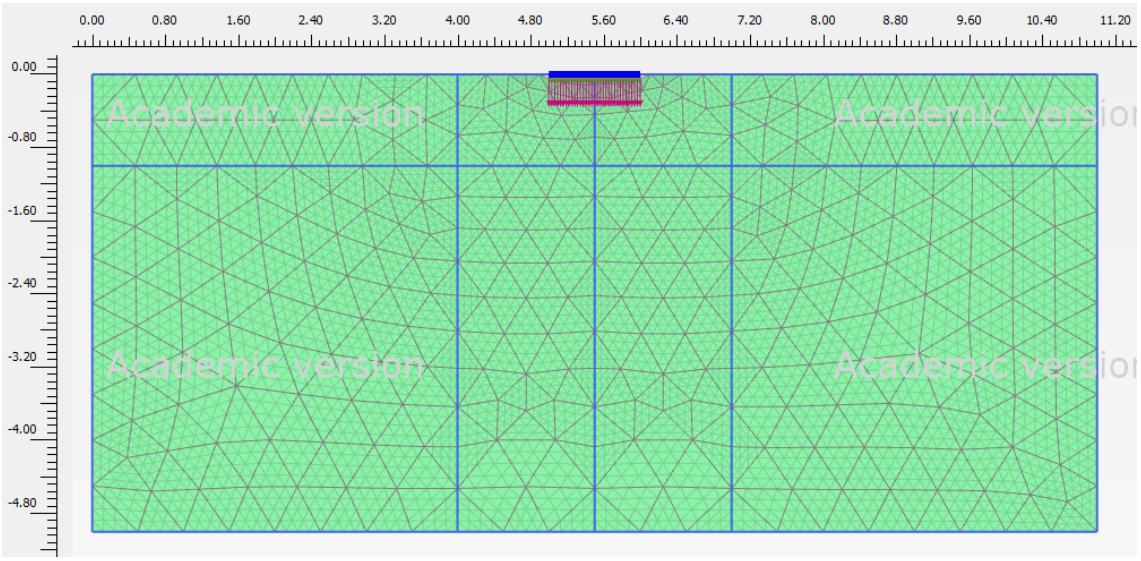


Figure 5.1: Numerical model of sandy soil profile to estimate bearing capacity

Footing and load

A strip footing with one meter width was modeled in the surface as a 'plate' element available in the software (Figure 5.1). It was considered rigid, massless and with a rough interface in order not to allow sliding. Table 5.1 gives the list of input parameters for the plate element. A strain deformation analysis was performed, so a displacement in the vertical direction was imposed until failure and the maximum load reached was considered the numerical bearing capacity.

Table 5.1: Footing input parameters

Parameter	Name	Value
Set type	-	Plates
Material type	-	Elastic isotropic
Axial stiffness	EA $[kN/m]$	5E6
Bending stiffness	EI $[kN \cdot m^2/m]$	1E6
Weight	w $[kN/m/m]$	0
Poisson's ratio	ν	0.3

Soil models

The sandy soil was modeled using the Mohr-Coulomb constitutive model in drained conditions. Table 5.2 presents the geomechanics properties of the soil, the unit weight (γ), the initial void ratio (e_{init}), the Poisson's ratio (ν'), the shear modulus (G), the cohesion (c'_{ref}) and the friction angle (ϕ'). An interface element under the foundation with the adjacent soil properties was added to model the soil-footing interaction, it was set as rigid with a corresponding unit value of the strength reduction factor R_{inter}.

Table 5.2: Sandy soil input parameters

Parameter	Name	Value
Set type	-	Soil and interfaces
Material type	-	Mohr-Coulomb
Drainage type	-	Drained
Soil unit weight	γ $[kN/m^3]$	17
Initial void ratio	e_{init}	0.8
Poisson's ratio	ν'	0.2
Shear modulus	G $[kN \cdot m^2]$	11.25E3
Cohesion	c'_{ref} $[kN/m^2]$	0
Friction angle	ϕ' [°]	34

Staged construction

The calculation was divided in two phases:

- Initial phase: The calculation type in this phase is 'K_0 procedure', where initial effective stresses, pore pressures and state parameters are generated. The plate element, interface

and line load were not activated in this phase.

- Phase 1: The calculation type in this phase is 'Plastic' where the elastoplastic drained or undrained analysis is performed. The plate element, interface and line displacement were activated in this phase and the option 'use line search' in numerical control parameters was activated. 'Line search' aims to improve the convergence of non-linear problems in a relatively inexpensive way.

Validation of results

A central point in the footing was selected to compute the vertical displacements in this point. Figure 5.2 shows the incremental values of the vertical load against the vertical displacements (S) during the analyses for variation depths study and Figure 5.3 for different width analyses.

The maximum reached load found until the soil collapse was considered the PLAXIS 2D bearing capacity, while the theoretical capacity was calculated with the theoretical relationship in Equation 5.1 proposed by Meyerhof (1963), this resulting in 265 kPa. The ultimate bearing capacity of a shallow strip . In this Equation, B is the foundation width,D is the foundation depth, c denotes the unit or apparent cohesion and γ the effective unit weight of the soil material. The theoretical bearing capacity factors for a shallow horizontal strip foundation under a vertical load (N_q, N_c and N_γ) depend mainly on the angle of internal friction or shearing resistance ϕ.

$$q_u = c \cdot N_c + \gamma \cdot D \cdot N_q + \frac{B}{2} \cdot \gamma \cdot N_\gamma \tag{5.1}$$

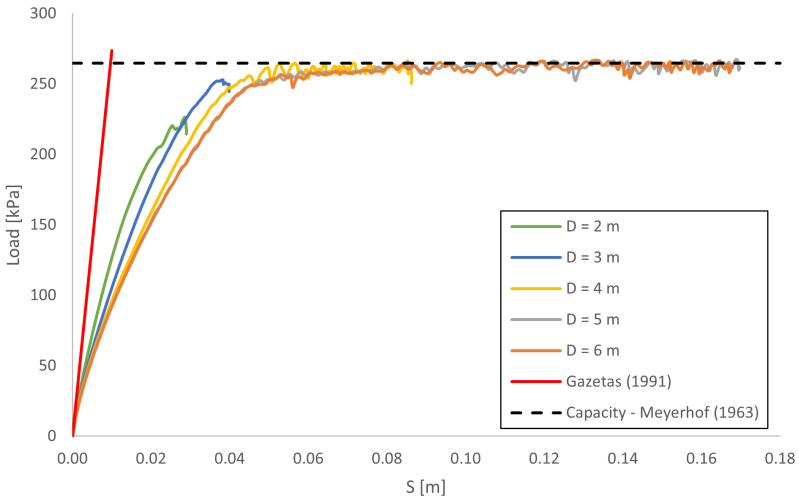


Figure 5.2: PLAXIS 2D bearing capacity results for different model depths (W = 11 m)

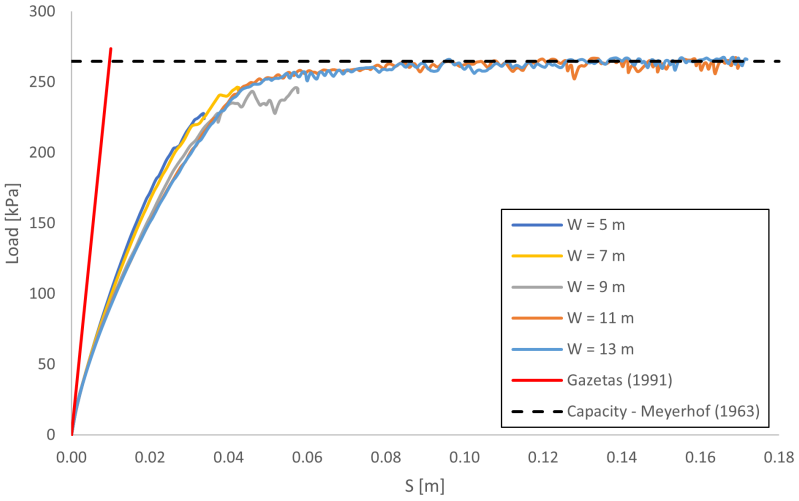


Figure 5.3: PLAXIS 2D bearing capacity results for different model widths (D = 5 m)

Table 5.3 shows the values found using PLAXIS 2D with the corresponding error when compared with the theoretical bearing capacity. When depth of the model (D) was varied, the difference between Meyerhof approach and PLAXIS 2D analyses was always less than 5%, except when the model with 2 m depth was used. Also, when the model was 2 m and 3 m depth, the curves were different compared with the rest (Figure 5.2). A depth greatest than 4 m is recommended (4 times the footing width). When width of the model (W) was varied, the difference between Meyerhof approach and PLAXIS 2D analyses was always less than 10%, except when the model with 5 m width was used. Also, when the model was 5 m, 7 m and 9 m width, the curves were different compared with the rest (Figure 5.3). A width greater than 9 m is recommended. Loukidis and Salgado (2011) found that for 2D analyses a model width (W) of 10 times the footing width (B) is suitable as it was also found in this study. Figure 5.4 shows the information in Table 5.3, bearing capacities against depths (D) and widths (W) were plotted.

Table 5.3: PLAXIS 2D bearing capacity results for different model depths and widths

Model depth (m)	PLAXIS 2D (kN/m/m)	Difference (%)	Model width (m)	PLAXIS 2D (kN/m/m)	Difference (%)
2	226	14.7	5	228	14.0
3	253	4.5	7	246	7.2
4	266	0.4	9	246	7.2
5	267	0.8	11	267	0.8
6	267	0.8	13	268	1.1

Figure 5.2 and Figure 5.3 include a red line with slope of 20531 kN/m indicating the theoretical elastic vertical stiffness estimated with Equation 5.2 (Gazetas, 1991). Figure 5.5 compares the theoretical values with the PLAXIS 2D results. The numerical elastic vertical stiffness was calculated as the slope of the linear part of the curve (three first points).

$$k_{NN,0} = \frac{2 \cdot G \cdot L}{1 - \nu}(0.73 + 1.54 \cdot \chi^{0.75}) \tag{5.2}$$

$$\chi = \frac{A_b}{4L^2} \tag{5.3}$$

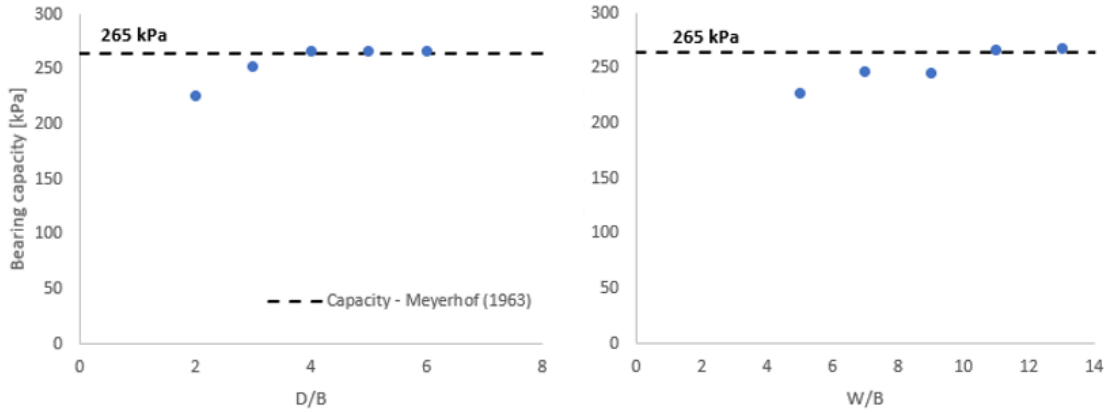


Figure 5.4: PLAXIS 2D bearing capacity for different model a) depths; b) widths

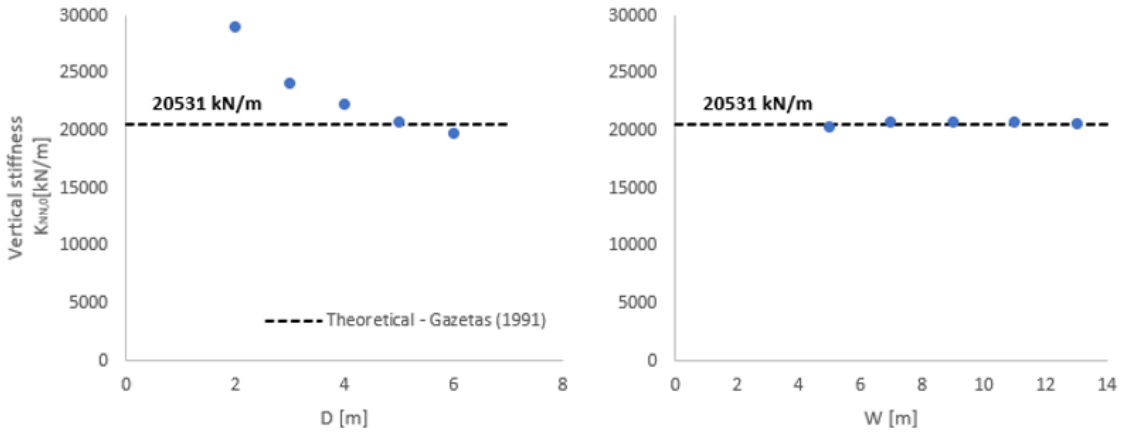


Figure 5.5: PLAXIS 2D vertical stiffness for different model a) depths; b) widths

A second parametric study was performed to evaluate the effect of doubling the foundation width (B=2). The model depth (D) influence was studied varying this dimension between 5 m and 10 m keeping a constant model width (21 m, almost 10 times the footing width (B) which is a suitable

dimension as found in B=1 study). Also the model width (W) influence was studied varying this dimension between 15 m and 25 m keeping a constant model depth (9 m). For these models the strip footing was modeled with two meters width. The footing and soil parameters are the same in tables 5.1 and 5.2, respectively. The considered numerical model is shown in Figure 5.6.The staged model construction was the same as indicated in section 5.1.1.

Once again a central point in the footing was selected to compute the vertical displacements (S) in this point. Figure 5.7 shows the incremental values of the vertical load against the vertical displacements (S) during the analyses for variation depths study and Figure 5.8 for different width analyses. The maximum load reached was considered the PLAXIS 2D bearing capacity and the theoretical bearing capacity was calculated with the relationship by Meyerhof (1963) in Equation 5.1 resulting in 530 kPa.

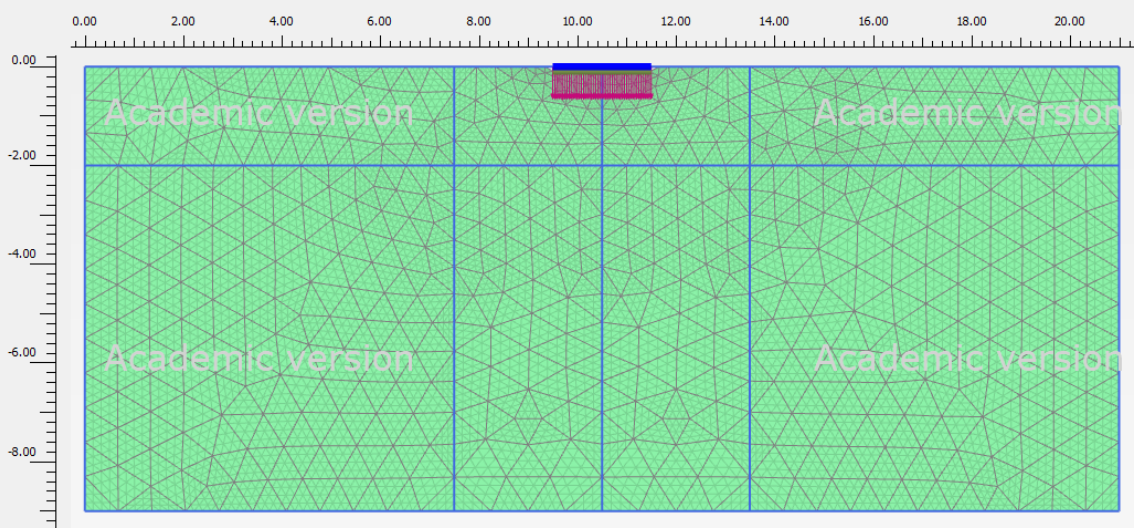


Figure 5.6: Numerical model of sandy soil profile to estimate bearing capacity (B = 2 m)

Table 5.4 shows the values found using PLAXIS 2D with the corresponding error when compared with the theoretical bearing capacity. When depth of the model (D) was varied, the difference between Meyerhof approach and PLAXIS 2D analyses was always less than 4%, however, when the model was 9 m and 10 m depth, the curves were very similar and different compared with the rest (Figure 5.7). A depth greatest than 9 m is recommended. When width of the model (W) was varied, the difference between Meyerhof approach and PLAXIS 2D analyses was always less than 9%, showing similarity between all the curves. A width greatest than 21 m is recommended. Figure 5.9 presents the information in Table 5.4, bearing capacities against depths (D/B) and widths (W/B), showing that D/B should be higher than 4 and W/B higher than 10 as the model with B=1 also indicated.

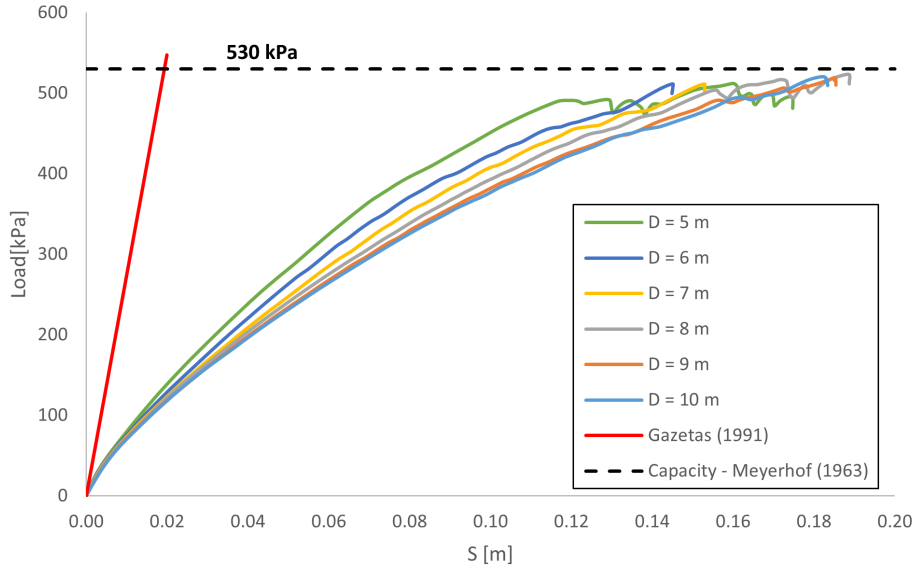


Figure 5.7: PLAXIS 2D bearing capacity results for different model depths (B=2 m)

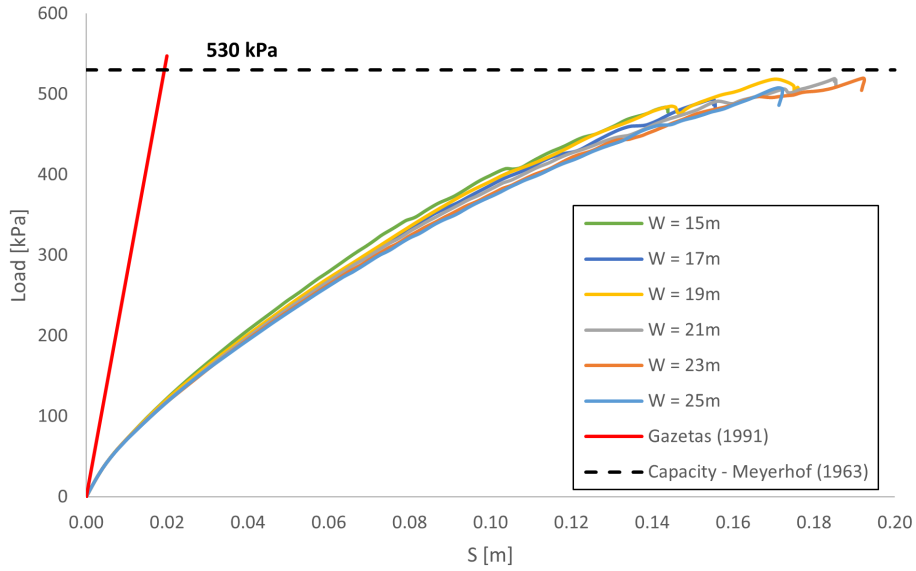


Figure 5.8: PLAXIS 2D bearing capacity results for different model widths (B=2 m)

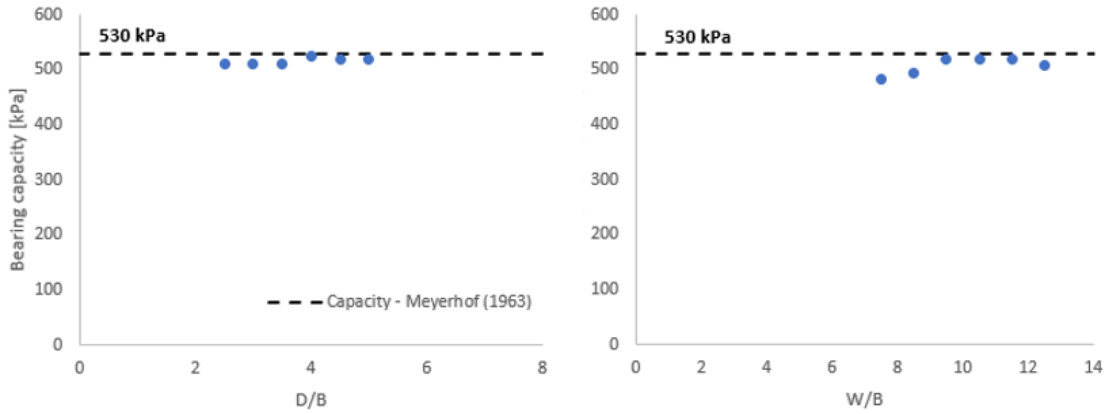


Figure 5.9: PLAXIS 2D bearing capacity for different model a) depths; b) widths (B=2 m)

Table 5.4: PLAXIS 2D bearing capacity results for different model depths and widths (Foundation width of 2 m)

Model depth (m)	PLAXIS 2D (kN/m/m)	Difference (%)	Model width (m)	PLAXIS 2D (kN/m/m)	Difference (%)
5	512	3.4	15	484	8.7
6	511	3.5	17	493	7.0
7	511	3.5	19	519	2.1
8	524	1.2	21	519	2.0
9	519	2.0	23	520	1.9
10	520	1.8	25	508	4.2

5.1.2 Clayey soil

After the parametric study performed in previous section with a homogeneous profile contains sandy soil, it is possible to assume that the same size of the numerical model is appropriate for the validation of the bearing capacity and settlements in a homogeneous clayey soil. Thus, for this model a profile with 11 meters width and 5 meters depth was selected, where the boundaries are far enough to avoid any interference in the stress-strain response. The model construction, footing and load procedures are the same as in section 5.1.1. The clayey soil was modeled using the Mohr-Coulomb constitutive model in undrained conditions. The input data about the soil parameters are shown in Table 5.5.

Usually the interface parameters could be modeled as the adjacent soil if it has a frictional behavior,

otherwise a specific material for the interface should be created by using the same properties of the adjacent soil but changing the strength parameters. For this purpose, a new material was created with the same general properties of the clay but changing the value of the cohesion to an arbitrary value of 5 kPa, in order to model the interface with a non-purely frictional behavior and the value of the angle of shearing resistance in 34°. The interface element was also set as rigid with a corresponding unit value of the strength reduction factor R_{inter}. The calculation was divided in two phases as in section 5.1.1.

Table 5.5: Clayey soil input parameters

Parameter	Name	Value
Set type	-	Soil and interfaces
Material type	-	Mohr-Coulomb
Drainage type	-	Undrained
Soil unit weight	γ $[kN/m^3]$	17.5
Initial void ratio	e_{init}	0.7
Poisson's ratio	υ'	0.4949
Shear modulus	G $[kN \cdot m^2]$	2.64E3
Undrained shear strength	$s_{u,ref}$ $[kN/m^2]$	85

Once again the central point in the footing was selected to compute the vertical displacements (S). Figure 5.10 shows the incremental values of the vertical load against the vertical displacements (S) during the analyses. The maximum reached load (446 kPa) was considered the PLAXIS 2D bearing capacity and the theoretical capacity was calculated with the relationship by Meyerhof (1963) resulting in 437 kPa. The difference between Meyerhof approach and PLAXIS 2D analysis was 2% showing that the model size used was appropriate for the analysis. To better observe if the boundaries do not affect the results, in Figure 5.11 the total stress distribution is presented, showing that in the bottom and lateral boundaries the stresses are stabilized.

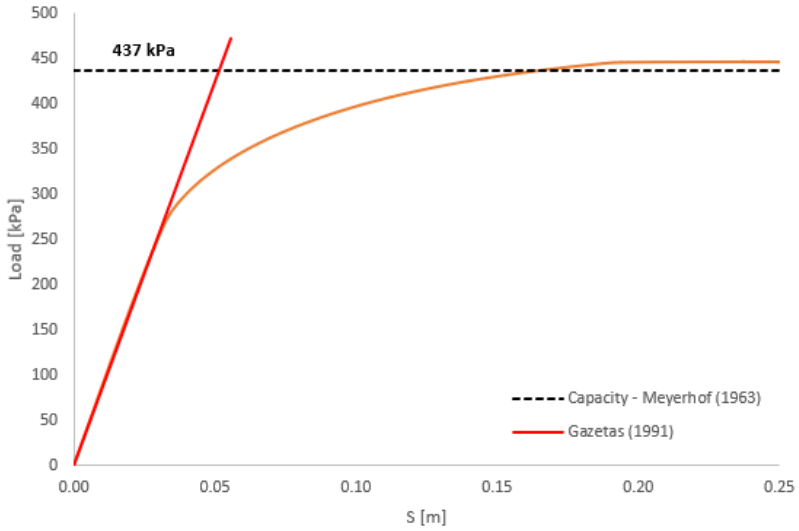


Figure 5.10: PLAXIS 2D bearing capacity results for clayey homogeneous profile

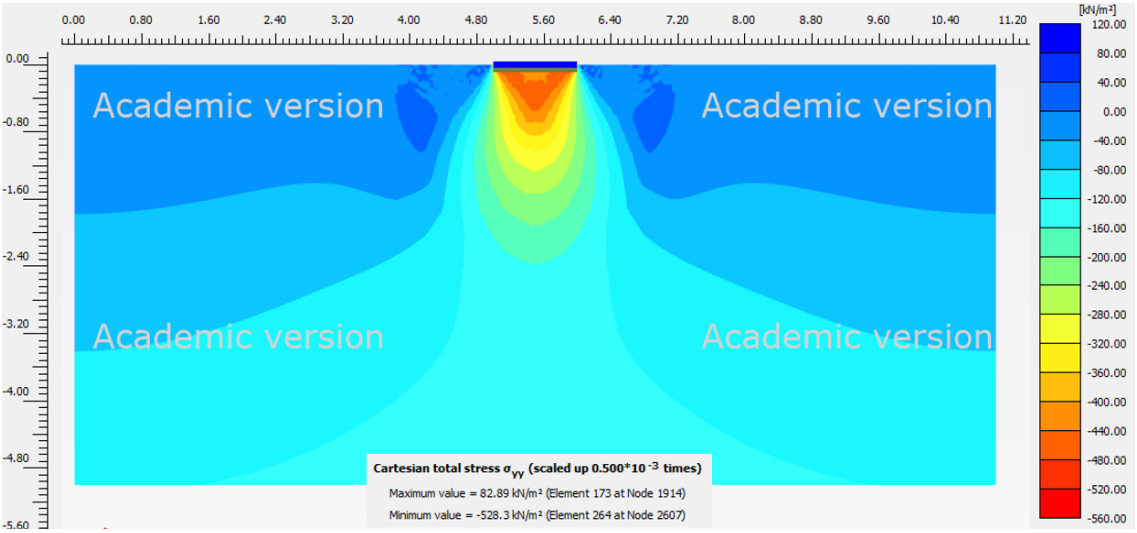


Figure 5.11: PLAXIS 2D total stress for clayey homogeneous profile

5.1.3 Layered soil profile with a liquefiable layer under a crust

This section is focused on the bearing capacity verification of a shallow footing on a two-layered deposit, with a sandy surface crust layer (Layer 1) and a liquefiable sand layer below (Layer 2).

The same properties of the sandy soil used in section 5.1.1 were used for the stiff crust. For the liquefiable layer, two cases were studied, partial liquefaction ($r_u = 0.8$) and total liquefaction ($r_u = 0.95$). Table 5.6 shows the parameters used in the second layer.

The shear strength reduction in the second layer was achieved through a degradation of the angle of shearing resistance, corresponding to a degradation of the Factor of Safety during the shaking.

The reduced angle of shearing resistance was calculated as a function of the actual angle of shearing resistance in pre-liquefaction condition, and of the excess pore pressure ratio, using the equation 5.4 suggested by Cascone and Bouckovalas (1998). The stiffness degradation was simulated through a reduction in the shear modulus, using equation 5.5 adapted to account for pore pressure build up (Kramer et al., 2016). Moreover, the liquefied layer was characterised by a null angle of dilatancy in order to represent the purely contractive behavior of the soil.

$$\phi_{deg} = tan^{-1}[(1 - r_u) \cdot tan\phi] \tag{5.4}$$

$$G_{deg} = G_0 \cdot \sqrt{\frac{\sigma'_{m0} \cdot (1 - r_u)}{p_a}} \tag{5.5}$$

Table 5.6: Liquefiable layer parameters

Parameter	$r_u = 0.8$	$r_u = 0.95$
Set type	Soil and interfaces	Soil and interfaces
Material type	Mohr-Coulomb	Mohr-Coulomb
Drainage type	Drained	Drained
γ $[kN/m^3]$	17	17
e_{init}	0.8	0.8
υ'	0.2	0.2
G $[kN \cdot m^2]$	2.52E3	1.26E3
c'_{ref} $[kN/m^2]$	0	0
ϕ' [°]	8	2

For this model a profile with 11 meters width and 5 meters of total depth was also used, being a appropriate model size as showed in section 5.1.1. Two crust thickness (H_c) were considered, 1.5 and 3.0 meters, thus four models were performed, one with 1.5 meters crust thickness and a partial liquefied second layer ($r_u = 0.8$), other one with the same crust thickness but with a totally liquefied second layer ($r_u = 0.95$), other one with 3 meters crust thickness and a partial liquefied second layer and finally one with the same crust thickness but with a totally liquefied second layer. The two considered profiles geometry are shown in Figures 5.12 and 5.1.

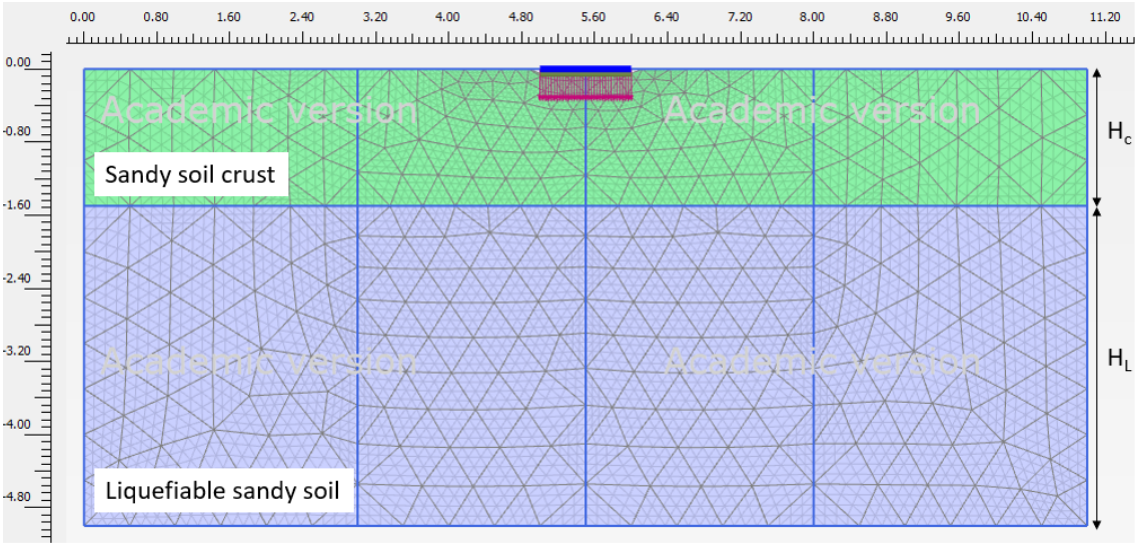


Figure 5.12: Numerical model of layered soil profile (Crust thickness of 1.5 meters)

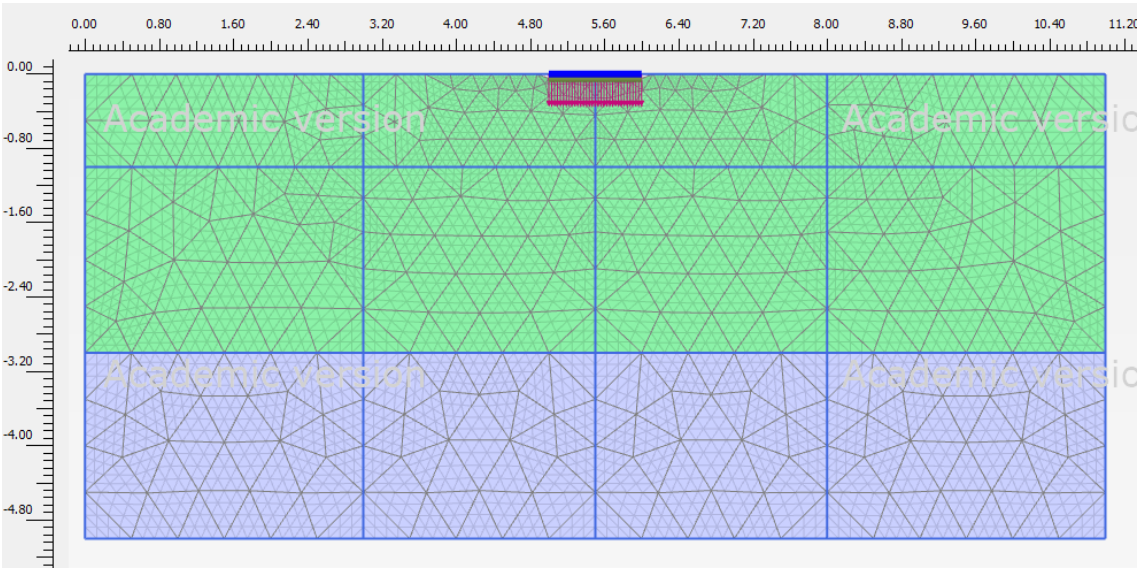


Figure 5.13: Numerical model of layered soil profile (Crust thickness of 3 meters)

A strip footing with one meter width was modeled in the surface, being considered rigid, massless and with a rough interface in order not to allow sliding. The same properties in Table 5.1 were used in the footing element. A displacement in the vertical direction was imposed until failure and the maximum load reached was considered the numerical bearing capacity. The calculation was divided in two phases as in section 5.1.1.

Validation of results

A central point in the footing was selected to compute the vertical displacements (S) in this point. Figure 5.14 shows the incremental values of the vertical load against the vertical displacements (S) during the analyses for the different models configuration.

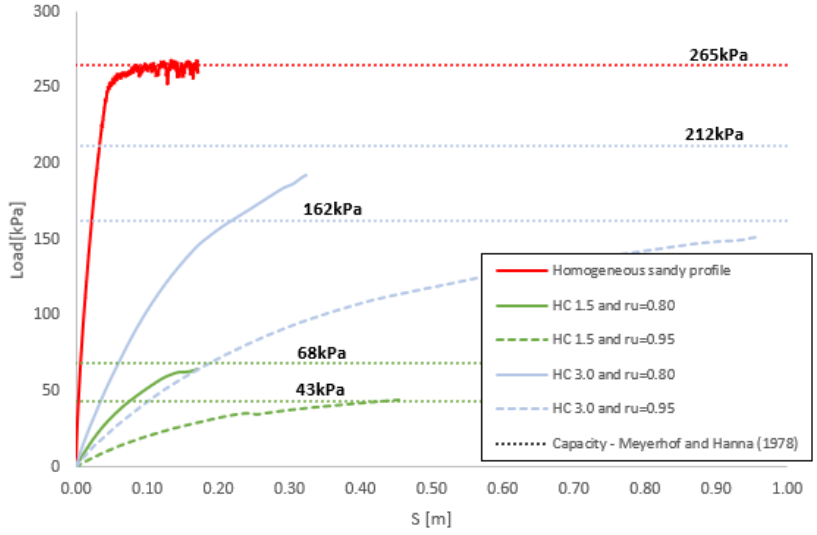


Figure 5.14: PLAXIS 2D bearing capacity results for different layered profiles

The maximum reached load was considered the PLAXIS 2D bearing capacity and the theoretical capacity was calculated with the relationship by Meyerhof and Hanna (1978) in Equation 5.6, where q_b and q_t are defined in Equations 5.7 and 5.8, respectively. Subscript (1) indicate the top soil layer properties and (2) the bottom soil layer ones. B is the foundation width, L is the foundation length and D_f is the foundation depth. c_a denotes the adhesive force along aa' and bb' in Figure 5.15 which depends on the unit or apparent cohesion of the soils c, γ the effective unit weight of the soil material and k_s is the passive earth pressure coefficient. The theoretical bearing capacity factors for a shallow horizontal strip foundation under a vertical load (N_q, N_c and N_γ) depend mainly on the angle of internal friction or shearing resistance ϕ and λ_a, λ_s, λ_{cs}, λ_{qs} and $\lambda_{\gamma s}$ are shape factors.

Table 5.7 shows the values found using PLAXIS 2D with the corresponding error when compared with the theoretical bearing capacity. The difference between Meyerhof and Hanna approach and PLAXIS 2D analyses was always less than 10%. The vertical displacements (S) were higher when a totally liquefied second layer ($r_u = 0.95$) was modeled instead a partially liquefied layer ($r_u = 0.80$).

To better observe if the boundaries do not affect the results, in Figures 5.16, 5.17, 5.18 and 5.19 are presented the total stress distribution, showing that in the bottom and lateral boundaries the stresses are stabilized.

$$q_u = q_b + \left(1 + \frac{B}{L}\right)\left(\frac{2c_a H}{B}\right)\lambda_a + \left(1 + \frac{B}{L}\right)\gamma_1 H^2\left(1 + \frac{2D_f}{H}\right)\left(\frac{k_s tan\phi_1}{B}\right)\lambda_s - \gamma_1 H \leq q_t \quad (5.6)$$

$$q_b = c_2 N_{c(2)}\lambda_{cs(2)} + \gamma_1(D_f + H)N_{q(2)}\lambda_{qs(2)} + \frac{B}{2}\gamma_2 N_{\gamma(2)}\lambda_{\gamma s(2)} \quad (5.7)$$

$$q_t = c_1 N_{c(1)}\lambda_{cs(1)} + \gamma_1 D_f N_{q(1)}\lambda_{qs(1)} + \frac{B}{2}\gamma_1 N_{\gamma(1)}\lambda_{\gamma s(1)} \quad (5.8)$$

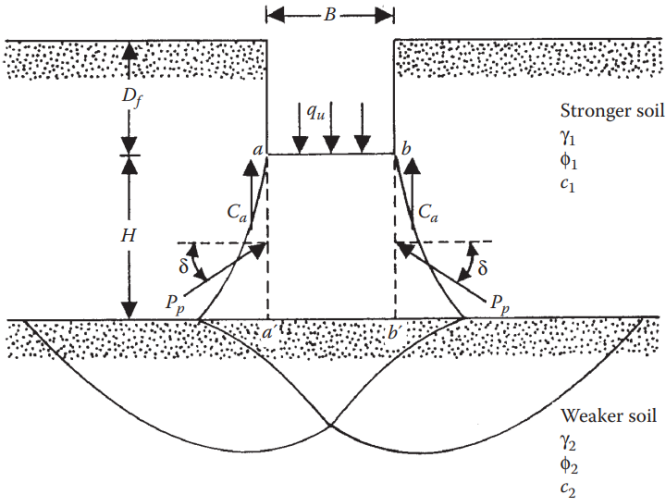


Figure 5.15: Rough continuous foundation on layered soil - stronger over weaker (Das, 2014)

Table 5.7: PLAXIS 2D bearing capacity results for different model depths and widths

H_c (m)	r_u	Theoretical (kN/m/m)	PLAXIS 2D (kN/m/m)	Difference (%)
1.5	0.80	68	65	4.4
1.5	0.95	43	44	2.3
3.0	0.80	212	192	9.4
3.0	0.95	162	152	6.2

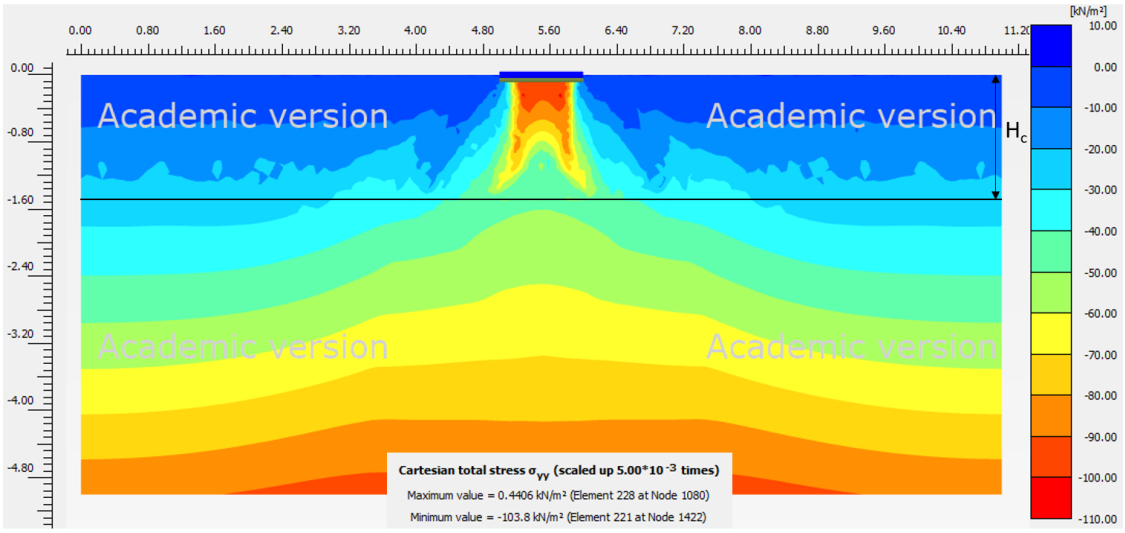


Figure 5.16: PLAXIS 2D total stress for layered profile ($H_c = 1.5$ and $r_u = 0.8$)

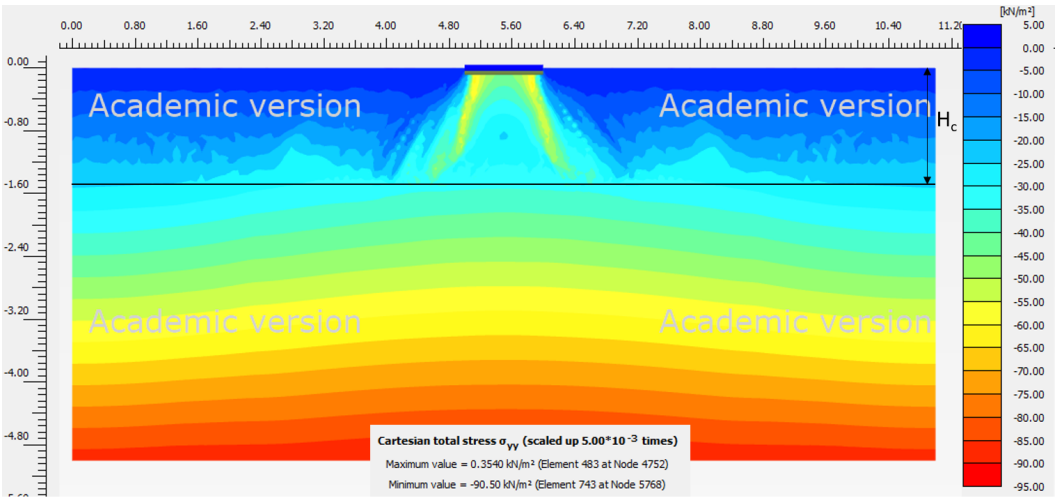


Figure 5.17: PLAXIS 2D total stress for layered profile ($H_c = 1.5$ and $r_u = 0.95$)

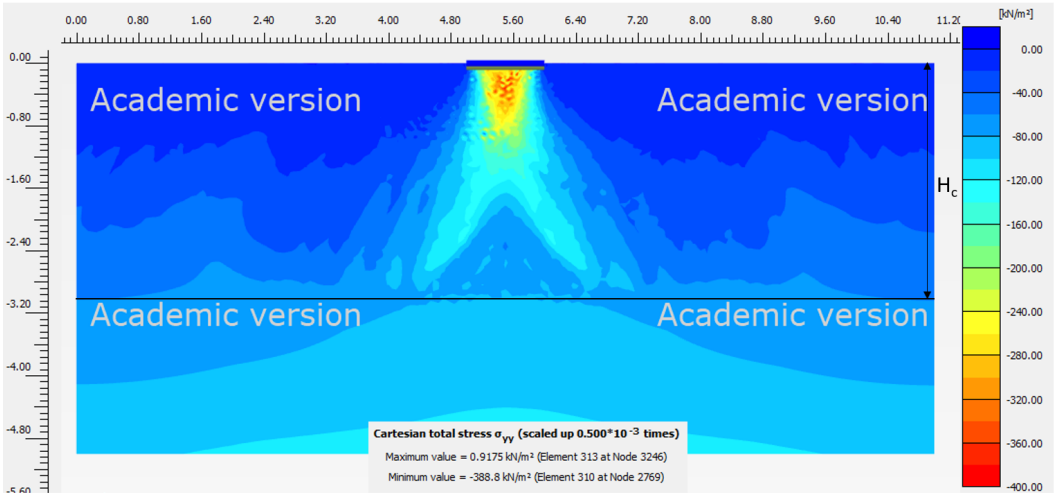


Figure 5.18: PLAXIS 2D total stress for layered profile ($H_c = 3.0$ and $r_u = 0.8$)

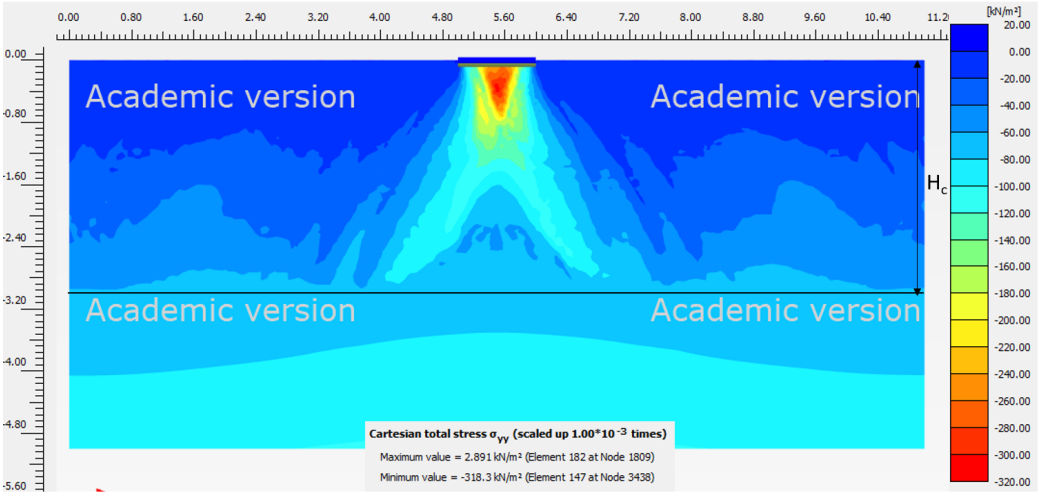


Figure 5.19: PLAXIS 2D total stress for layered profile ($H_c = 3.0$ and $r_u = 0.95$)

5.1.4 Conclusions

Appropriate model size was selected based on a parametric study in a homogeneous sandy profile, where width (W) and depth (D) of the model were varied to obtain the ultimate bearing capacity from numerical simulations and compare them with analytical solutions. When a shallow foundation of one meter width was modeled the appropriate model size was 11 meters width and 5 meters depth, while when a two meters width foundation was modeled the appropriate model size was 21 meters width and 9 meters depth, almost the double size. The selected model size was useful to also validate the bearing capacity in a homogeneous clayey profile and in a layered profile with a liquefiable sand layer. The properties of the liquefied sand in the layered profiles were calculated using some equations to reduce the strength (ϕ) and stiffness (G) simplifying the problem. Some

analyses should be performed using a constitutive model that be able to generate the excess pore pressure build-up under an earthquake load.

All the numerical results using the appropriate model size showed a good agreement with the analytical estimation values based on Meyerhof (1963) for homogeneous profiles and on Meyerhof and Hanna (1978) for layered profiles.

The results of layered profiles showed that the bearing capacity is decreased when a presence of the partially liquefied sand and even more when it is totally liquefied. Also the bearing capacity is more reduced when the crust have the lower thickness. Regarding the settlements, as expected, they are higher when the bearing capacity is lower, that is when the crust is thinner and when the second sand layer is totally liquefied.

5.2 Moment loading

The ultimate moment capacity represents the maximum moment that the foundation can experience immediately before a failure and numerical simulations are a good approach to account the soil-structure interaction effects through moment-rotation curves to catch the complexity of the phenomena. This section presents the validation of the numerical model through the comparison with the analytical simplified solution by Deng et al. (2014). As in previous section, first, sandy and clayey homogeneous soil profiles were used, and then some profiles with two layers were analyzed.

5.2.1 Sandy soil

Model construction

For this study was also used a plane strain numerical model and the water table was also neglected. The finite element mesh was refined in the region closer to the footing and gradually coarsened towards the left and right boundaries to provide a better discretization in the area of interest, a 'very fine' element distribution was selected. The lateral boundaries were normally fixed, the base model boundary was considered as rigid in order to simulate a stiff rock below then it was fully fixed; and the surface boundary was not fixed to simulate the free-field condition. The model size validated in previous section was used, 31 m width and 10 m depth. The considered numerical model is shown in Figure 5.20.

Footing and load

A strip footing with one meter width was modeled in the surface as a 'plate' (Figure 5.20). It was considered rigid, massless and with a rough interface in order not to allow sliding. The same list of input parameters for the plate element in Table 5.1 was used.

A point concentrated vertical load (N_{app}) was applied in the middle of the footing and it was set as a fraction of the analytical bearing capacity calculated from Meyerhof (1963) solution through three different factors of safety selected (1.5, 3.0 and 20.0). Additionally, a moment was added in the same point and it was set as the analytical moment capacity calculated from Deng et al. (2014) solution. If the applied moment was not high enough for reaching the soil collapse, the analysis was re-run with an increased moment until no additional moment could be tolerated, resulting in collapse.

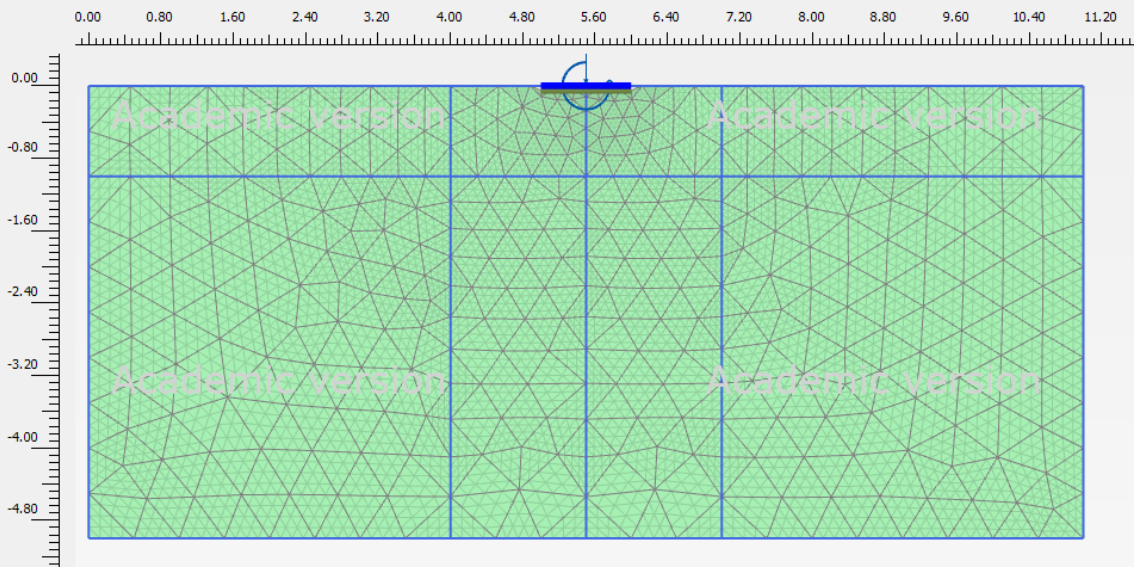


Figure 5.20: Numerical model of sandy soil profile for moment capacity analyses

Soil models

The sandy soil was modeled using the Mohr-Coulomb constitutive model in drained conditions. The input data about the soil parameters are the same in Table 5.2. An interface element under the foundation with the adjacent soil properties was added to model the soil-footing interaction, it was set as rigid with a corresponding unit value of the strength reduction factor R_{inter}.

Staged construction

The calculation was divided in three phases:

- Initial phase: The calculation type in this phase is 'K_0 procedure', where initial effective stresses, pore pressures and state parameters are generated. The plate element, interface, point load and moment were not activated in this phase.

- Phase 1: The calculation type in this phase is 'Plastic' where the elastoplastic drained or undrained analysis is performed. The plate element, interface and point load were activated in this phase and the option 'use line search' in numerical control parameters was activated.

The moment was not activated in this phase.

- Phase 2: The calculation type in this phase is 'Dynamic' where the analysis is performed in time domain. The plate element, interface and line load were kept in this phase, and the moment was activated. Dynamic calculation allows a gradual process of deformation under the footing avoiding an instability in the response,thus the moment, was applied step-by-step. The time step was one second and the moment step was 0.1, thus the total dynamic time interval was set equal to ten times the moment value.

Validation of results

Three points were selected to compute the vertical displacements (S), the central and the two external points in the foundation. Figure 5.21 shows the moment-rotation response of the footing for each factor of safety. The incremental values of the foundation rotation were calculated for each step as the difference between the incremental vertical displacements (S) registered in the two external points of the foundation divided by the foundation width (one meter). The incremental moment for each step was calculated multiplying the moment applied in the analysis by the ratio between the step number and the total number of steps.

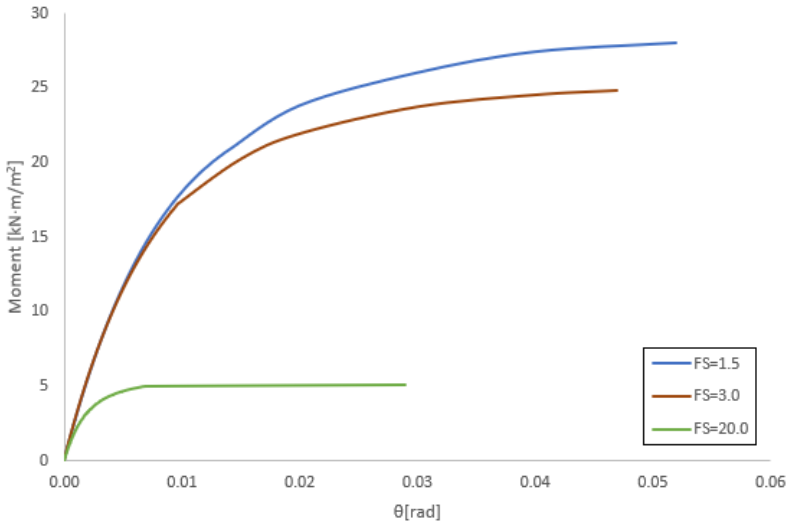


Figure 5.21: Moment-rotation response of a strip footing on a sandy homogeneous profile.

The maximum applied moment found for reaching the soil collapse was considered the PLAXIS 2D moment capacity and the theoretical capacity was calculated with the relationship proposed by Deng et al. (2014) in Equation 5.9 where B is the footing width, A_c is the critical contact area and A is the entire footing area. N_{app} was calculated as the ratio of the bearing capacity to the factor of safety. A detailed description about the estimation of the rocking moment capacity can be found in Deng et al. (2014).

$$M_{c_foot} = \frac{N_{app} \cdot B}{2} \cdot \left(1 - \frac{A_c}{A}\right) \tag{5.9}$$

Table 5.8 shows the values found using PLAXIS 2D with the corresponding error when compared with the theoretical moment capacity. The difference between Deng et al. (2014) approach and PLAXIS 2D analyses was always less than 15%.

Table 5.8: PLAXIS 2D moment capacity on sandy soil for different factors of safety (FS)

FS (m)	N_{app} (kN/m)	Moment capacity (Theoretical) (kN·m/m^2)	Moment capacity (PLAXIS 2D) (kN·m/m^2)	Difference (%)
1.5	176	29	28	3.4
3.0	88	29	25	13.8
20.0	13	6	5	15.0

5.2.2 Clayey soil

For this model was also selected a profile with 11 meters width and 5 meters depth, where the boundaries are far enough to avoid any interference in the stress-strain response. The model construction, footing and load procedures are the same as in section 5.2.1.

The clayey soil was modeled using the Mohr-Coulomb constitutive model in undrained conditions. The input data about the soil parameters are the same in Table 5.5. Usually the interface parameters could be modeled as the adjacent soil if it has a frictional behavior, otherwise a specific material for the interface should be created by using the same properties of the adjacent soil but changing the strength parameters. For this purpose, a new material was created with the same general properties of the clay but changing the value of the cohesion to an arbitrary value of 5 kPa, in order to model the interface with a non-purely frictional behavior and the value of the angle of shearing resistance in 34°. The interface element was also set as rigid with a corresponding unit value of the strength reduction factor R_{inter}. The calculation was also divided in three phases as in section 5.2.1.

One again the central point and the two external points in the footing were selected to compute the vertical displacements (S). Figure 5.22 shows the moment-rotation response of the footing for each factor of safety. The maximum applied moment found for reaching the soil collapse was considered the PLAXIS 2D bearing capacity and the theoretical capacity was calculated with the relationship by Deng et al. (2014) in Equation 5.9. Table 5.9 shows the values found using PLAXIS 2D with the

corresponding error when compared with the theoretical moment capacity. The difference between Deng et al. (2014) approach and PLAXIS 2D analysis was 17%.

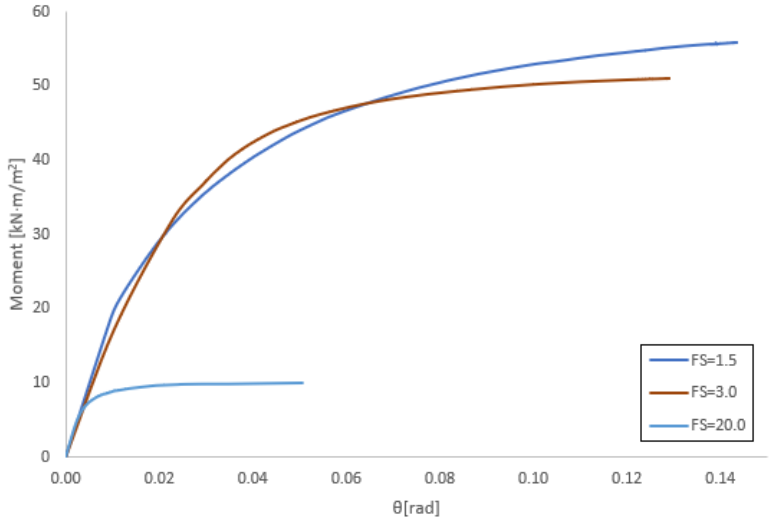


Figure 5.22: Moment-rotation response of a strip footing on a clayey homogeneous profile

Table 5.9: PLAXIS 2D moment capacity on clayey soil for different factors of safety (FS)

FS (m)	N_{app} (kN/m)	Moment capacity (Theoretical) (kN·m/m^2)	Moment capacity (PLAXIS 2D) (kN·m/m^2)	Difference (%)
1.5	291	48	56	16.7
3.0	145	48	51	6.3
20.0	21	10	10	0.0

5.2.3 Layered soil profile

This section is focused on the moment capacity verification of a shallow footing on a two-layered deposit, with a sandy surface crust layer (Layer 1) and a liquefiable sand layer below (Layer 2).

The same properties of the sandy soil used in section 5.1.1 was used for the stiff crust. For the liquefiable layer, two cases were studied, partial liquefaction ($r_u = 0.8$) and total liquefaction ($r_u = 0.95$) as in section 5.1.3. Table 5.6 shows the parameters used in the second layer.

For this model was also used a profile with 11 meters width and 5 meters of total depth, being a appropriate model size as showed in section 5.1.1. Two crust thicknesses H_c were considered, 1.5 and 3.0 meters, thus four profiles were analyzed, one with 1.5 meters crust thickness and a partial liquefied second layer ($r_u = 0.8$), other one with the same crust thickness but with a totally

liquefied second layer ($r_u = 0.95$), other one with 3 meters crust thickness and a partial liquefied second layer and finally one with the same crust thickness but with a totally liquefied second layer. The two considered geometries of the profiles are shown in Figures 5.23 and 5.24.

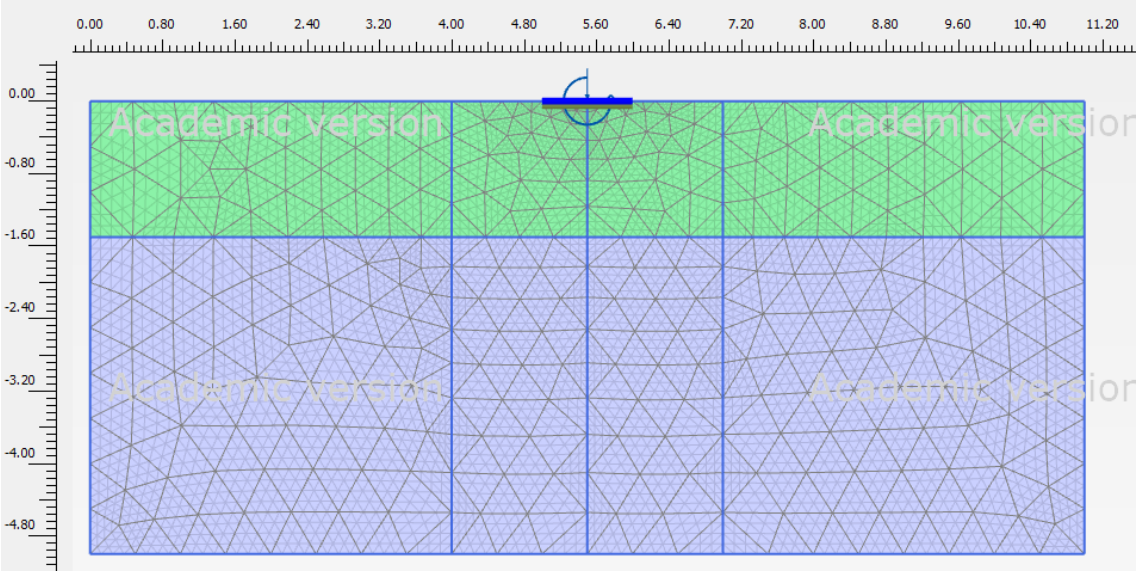


Figure 5.23: Numerical model to estimate moment capacity of a layered soil profile (Crust thickness of 1.5 meters)

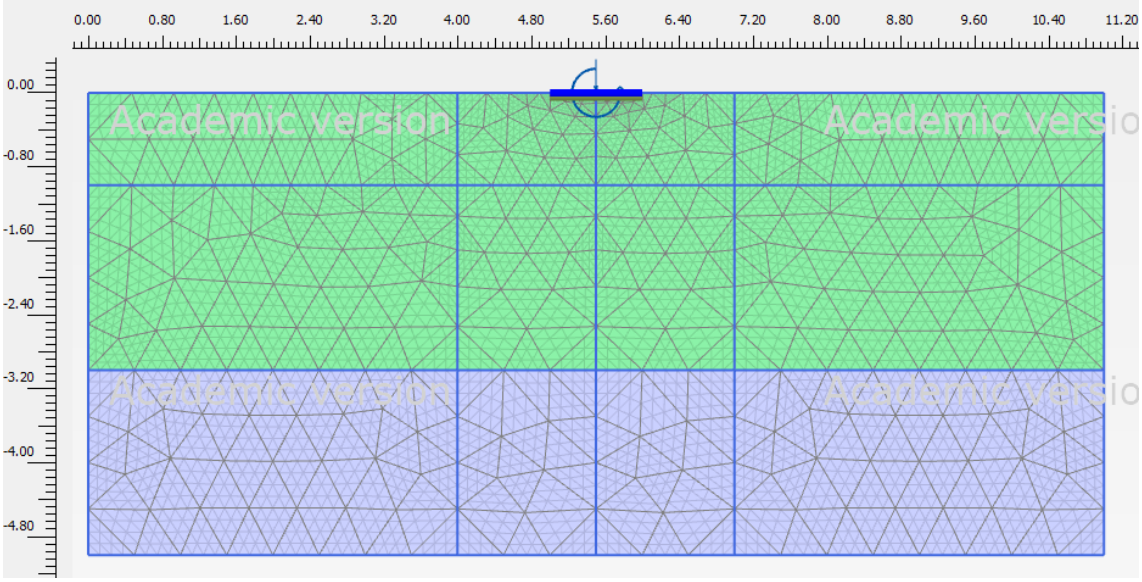


Figure 5.24: Numerical model to estimate moment capacity of layered soil profile (Crust thickness of 3 meters)

A strip footing with one meter width was modeled in the surface, being considered rigid, massless and with a rough interface in order not to allow sliding. The same properties in Table 5.1 were

used in the footing element. A point concentrated vertical load was applied in the middle of the footing and set as a fraction of the analytical bearing capacity calculated from Meyerhof and Hanna (1978) solution through three different factors of safety selected (1.5, 3.0 and 20.0). Additionally, a moment was added in the same point and set as the analytical moment capacity calculated from Deng et al. (2014) solution in Equation 5.9. If the applied moment was not high enough for reaching the soil collapse, the analysis was re-run with an increased moment until no additional moment could be tolerated, resulting in collapse.

Validation of results

Three points were selected to compute the vertical displacements (S), the central and the two external points in the foundation. Figure 5.25 shows the moment-rotation response of the footing for each factor of safety for the profile with 1.5 meters crust thickness and a partial liquefied second layer ($r_u = 0.8$), Figure 5.26 for the profile with 1.5 meters crust thickness and a totally liquefied second layer ($r_u = 0.95$), Figure 5.27 for the profile with 3 meters crust thickness and a partial liquefied second layer and finally Figure 5.28 for the profile with 3 meters crust thickness but with a totally liquefied second layer.

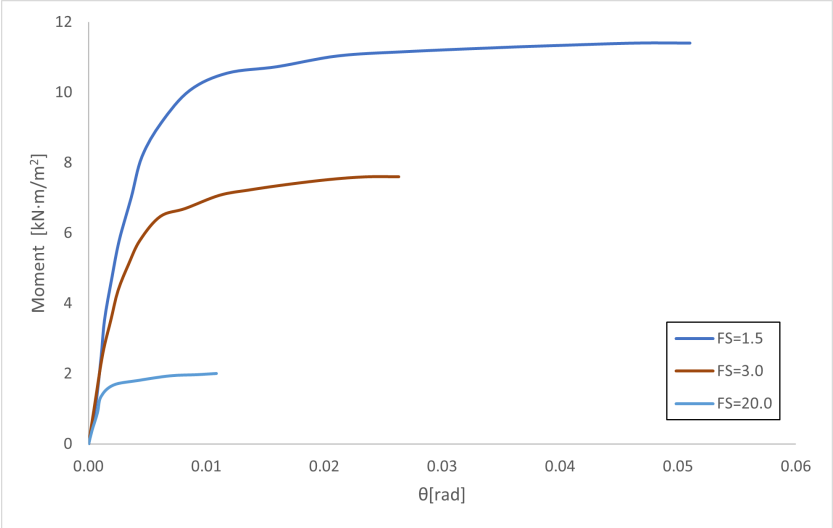


Figure 5.25: Moment-rotation response of a strip footing on a layered profile ($H_c = 1.5$ and $r_u = 0.8$)

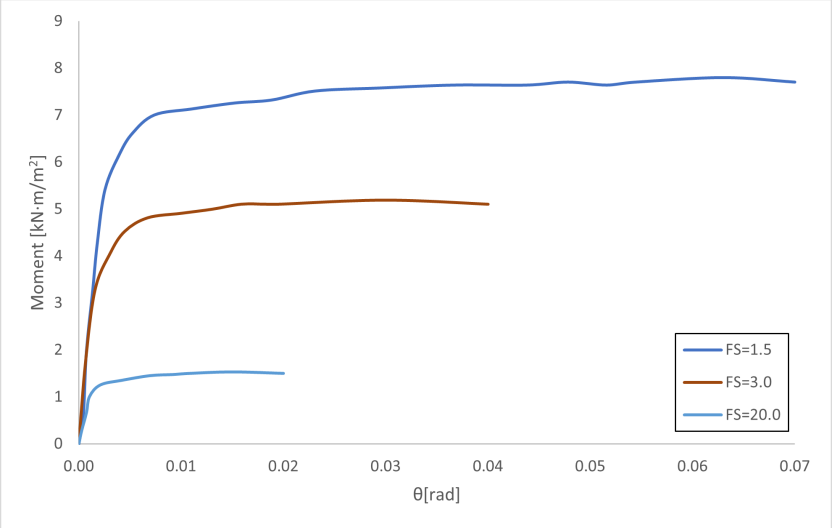


Figure 5.26: Moment-rotation response of a strip footing on a layered profile ($H_c = 1.5$ and $r_u = 0.95$)

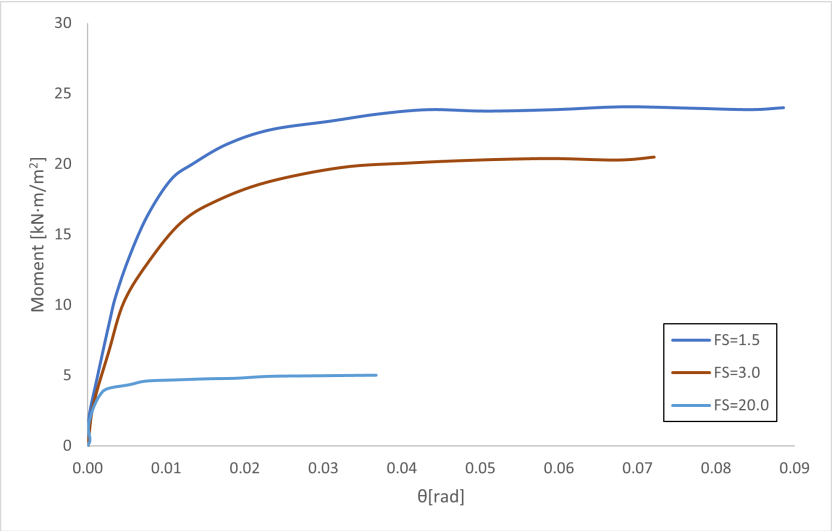


Figure 5.27: Moment-rotation response of a strip footing on a layered profile ($H_c = 3.0$ and $r_u = 0.8$)

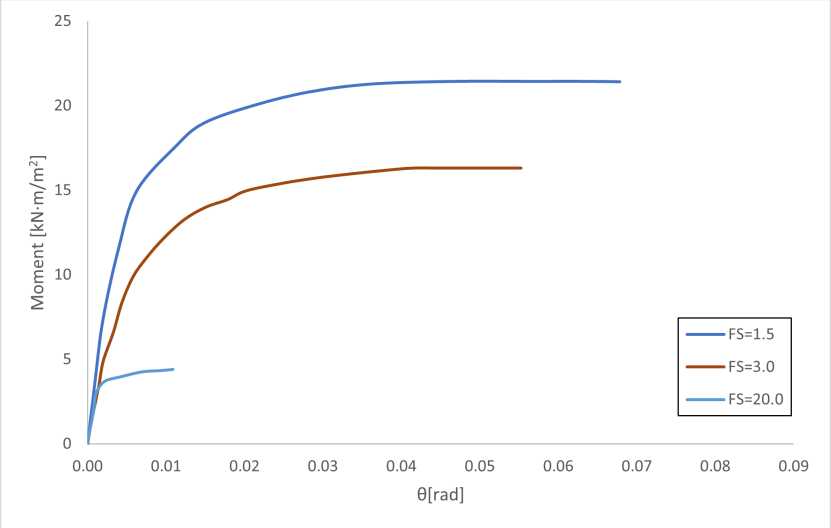


Figure 5.28: Moment-rotation response of a strip footing on a layered profile ($H_c = 3.0$ and $r_u = 0.95$)

The maximum applied moment found for reaching the soil collapse was considered the PLAXIS 2D moment capacity and the theoretical capacity was calculated with the relationship by Deng et al. (2014) in Equation 5.9. Table 5.10 shows the values found using PLAXIS 2D with the corresponding error when compared with the theoretical moment capacity. The difference between Deng et al. (2014) approach and PLAXIS 2D analyses was less than 20% in most the cases, however, when the moment capacity is so small, the error calculated was greater. The footing moment rotation was higher when a partially liquefied second layer ($r_u = 0.95$) was modeled instead a totally liquefied layer ($r_u = 0.80$), because the N_{app} applied in totally liquefied layer cases is smaller. Figure 5.29 presents the moment capacity normalized by the vertical load applied against the different factor of safety simulated. When the factor of safety was 1.5 and 3 the M/N values were almost the same even when the crust thickness H_c and r_u were variables, while when the factor of safety was 20 the M/N varied between 0.47 and 0.7, being less when H_c is higher and r_u is lower and high when H_c is lower and r_u is higher. Since A_c/A (see Equation 5.9) will always decrease with increasing factor of safety (FS), then M/N increased when FS was increased. The rate of increase was more significant for the weaker liquefiable layer ($r_u = 0.9$) and thinner crust ($H_C = 1.5$) since the effective width decreases with increasing FS, thus the influence of the liquefiable layer decreases.

Table 5.10: PLAXIS 2D moment capacity results for different layered profiles and FS

FS	H_c (m)	r_u	N_{app} (kN/m)	Moment capacity (Theoretical) (kN·m/m^2)	Moment capacity (PLAXIS 2D) (kN·m/m^2)	Difference (%)
1.5	1.5	0.80	45.241	13.313	11.4	14.4

3.0	1.5	0.80	22.621	8.011	7.6	5.1
20.0	1.5	0.80	3.393	1.505	2.0	32.9
1.5	1.5	0.95	28.646	9.623	7.7	20.0
3.0	1.5	0.95	14.323	5.502	5.1	7.3
20.0	1.5	0.95	2.148	0.978	1.5	53.4
1.5	3.0	0.80	141.435	19.153	24.0	25.3
3.0	3.0	0.80	70.717	17.127	20.5	19.7
20.0	3.0	0.80	10.608	4.241	5.0	17.9
1.5	3.0	0.95	107.735	19.639	21.4	9.0
3.0	3.0	0.95	53.867	14.800	16.3	10.1
20.0	3.0	0.95	8.080	3.336	4.4	31.9

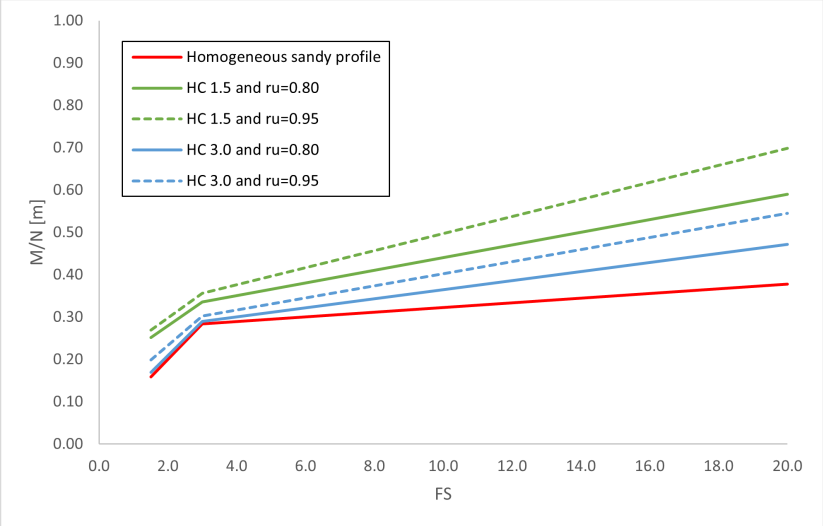


Figure 5.29: M/N vs Factor of safety for the different profiles configuration from PLAXIS 2D analysis

5.2.4 Conclusions

This section presented the validation of the moment capacity from a numerical model through the comparison with analytical simplified solution by Deng et al. (2014). All the numerical results in homogeneous profiles showed a good agreement with the analytical moment capacity estimation values based on Deng et al. (2014). The numerical results in layered profiles also showed a good agreement with the analytical ones, however, when the moment capacity was so small, the error calculated was greater.

The results of layered profiles also showed that the moment capacity is decreased when a presence

of the partially liquefied sand and even more when it is totally liquefied. Also the moment capacity is more reduced when the crust is thinner.

Regarding the settlements, when the crust was smaller, they were higher when the moment capacity and point load were lower, that is when the second layer was totally liquefied. However, when the crust was bigger, the settlements were higher when the moment capacity and point load were bigger, that is when the second layer was partially liquefied. From these results, it is clear that the moment-rotation response is highly influenced by the combination of the point concentrated vertical load, the moment and the properties of the soil profile. This study provided a useful reference to start more complex analyses.

Chapter 6

Procedure to estimate differential settlements of buildings with isolated footings

Diverse parametric studies to investigate the influence of different conditions on settlements have been developed in the last decades but none have analyzed structures with isolated footings. The pore pressure variation and stress distribution under a mat foundation is different to isolated footings, therefore a sensitivity analysis to investigate the influence of different soil conditions and building configurations on liquefaction-induced differential settlements was performed as part of this work. The commercial software, PLAXIS 2D (Bentley, 2020) was used to perform the analyses.

This section outlines the steps followed to create the numerical model to estimate differential settlements of buildings with isolated footings. The models presented in this section were considered the benchmark models that provided a reference point for investigating the key parameters that influence the building performance.

6.1 Model construction

The soil profile consisted of a top layer of 2 m thick clay (L1), a 4 m thick liquefiable sand (L2) and a 14 m thick clay on the bottom (L3). The ground water table was set at 2 m. As shown in Figure 6.1 the soil profile was 20 m deep and the total model width was 10 times the building width (B), sufficiently large to capture free-field conditions, avoid wave reflections and reduce the influence of the lateral boundaries on the response of the footings (see section 5). Three different buildings were modeled, one with 1-bay (with two columns), one with 2-bays (with three columns)

and finally one with 4-bays (with five columns), called as NF2, NF3 and NF5, respectively.

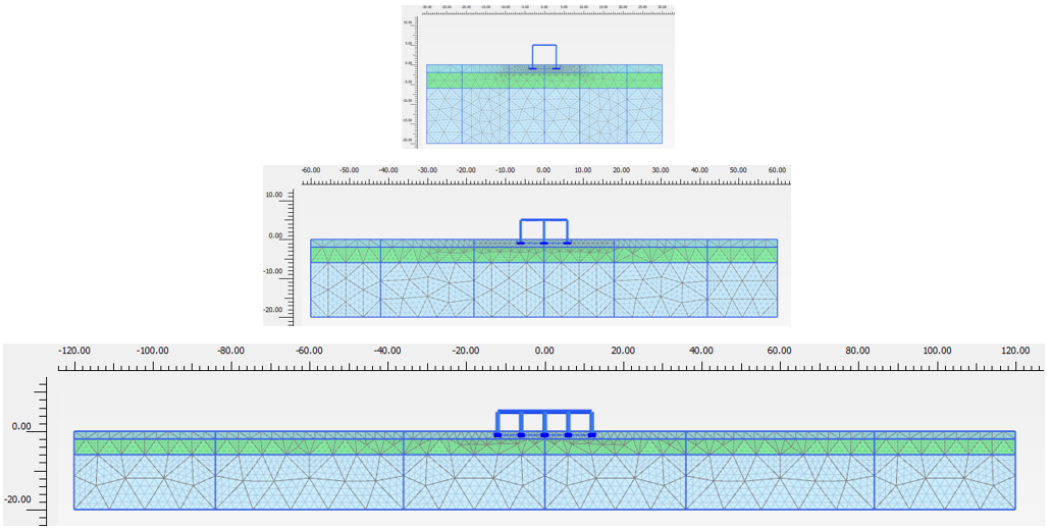


Figure 6.1: Numerical model with isolated footings for 1-bays, 2-bays and 4-bays buildings

The finite element sizes were defined using the automated meshing algorithm selecting a 'Fine' mesh. Additionally, mesh refinement was adopted below the building to provide a better discretization in the area of interest. The lateral boundaries were tied together and the bottom boundary was defined as a compliant base, also referred to as absorbing base (Mejia and Dawson, 2006).

Prior to the dynamic loading phase, soil layers were modeled using the Hardening Soil (HS) constitutive model for the definition of initial stress states and the subsequent structural loading phases. The soil model for the liquefiable layer was switched to the PM4Sand constitutive model when the dynamic loading phase started (See section 2.1.6).

The parameters defining the HS model for the soil layers are listed in Table 6.1. For the sandy layer, the void ratio (e_0) was calculated from the maximum void ratio (e_{max}), the minimum void ratio (e_{min}) and the relative density (D_R) as presented in Table 6.1. The maximum void ratio (e_{max})and the minimum void ratio (e_{min}) were always considered as 0.8 and 0.5, respectively, to keep the default values from PM4Sand constitutive model. The specific gravity (G_s) was always considered as 2.65. The relative density (D_R) for the benchmark model was considered as 50%. The shear modulus (G_{max}) was calculate from the normalised shear modulus coefficient (G_O), the atmosphere pressure (p_{atm}), and the effective confining pressure (p') in the middle of the layer (Equation 2.19). The shear modulus coefficient G_O was estimated from the relative density (Equations 2.21 and 2.17). For the liquefiable layer was also assigned the additional PM4Sand contraction rate parameter, $h_{po} = 0.25$ (Boulanger and Ziotopolou, 2017). The contraction rate parameter was calibrated by performing numerical element tests using the subroutines provided by

the authors of the PM4Sand model and adjusting the parameter to obtain a cyclic resistance ratio (CRR) of 0.126 for 15 cycles (15 cycles represent an earthquake with a magnitude of 7.5). The CRR value was estimated based on the relative density (Equations 2.10 and 2.18). The secondary set of parameters of the PM4Sand constitutive model were kept default.

Rayleigh damping was set at 2% at 0.5 Hz and 10 Hz to mitigate numerical instability (see section 4.5.2). The type of calculation used in PLAXIS was a dynamic analysis with consolidation.

Table 6.1: Input parameters of the HS model used in the parametric analysis

Parameter	L1	L2	L3
H $[m]$	2.0	4.0	14.0
γ_{unsat} $[kN/m^3]$	15.6	$\frac{G_s \cdot \gamma_w}{1+e_0}$	20.2
γ_{sat} $[kN/m^3]$	19.6	$\frac{(G_s+e_0)\cdot\gamma_w}{1+e_0}$	20.2
e_0	0.70	$\frac{e_{max}-D_R}{e_{max}-e_{min}}$	0.60
$E_{50}^{ref} = E_{oed}^{ref}$ $[kN/m^2]$	$108x10^3$	$2 \cdot G_{max} \cdot (1+\nu)$	$540x10^3$
E_{ur}^{ref} $[kN/m^2]$	$324x10^3$	$3 \cdot E_{50}^{ref}$	$1620x10^3$
ν	0.35	0.30	0.35
m	1.0	0.5	1.0
c_{ref} $[kN/m^2]$	40	0	200
ϕ	0	33	0
k $[m/s]$	$1x10^{-7}$	$1x10^{-5}$	$1x10^{-9}$

The height of the structure was 6 m and the bay length was 6 m, resulting in a total building width of 6 m, 12 m and 24 m for NF2, NF3 and NF5 models, respectively. The beams and columns of the building were 0.45 m × 0.45 m. The foundation was located at a depth (d_f) of 1 m. The footings were 2 m length (b_f). A distributed load of 53.3 kN/m was applied in the beams and no self-weight or load was added to the columns and foundation elements. The structural elements were modeled as 'Plate' elements, which can only simulate elastic behavior. They were modeled with the provided dimensions and a Young's modulus of 28 GPa. The secant-to-yield stiffness of the beams and columns was modeled according to the proposal of Haselton et al. (2016), which reduces the gross stiffness to simulate the effect of cracking and accounts for the axial force level. The secant-to-yield stiffness of the members considered was 50% of their gross stiffness. The interface between the base of the foundation elements and surrounding soil was fixed. Large deformation/P-Delta analysis was not considered. Figure 6.2 shows the stress state before the ground motion.

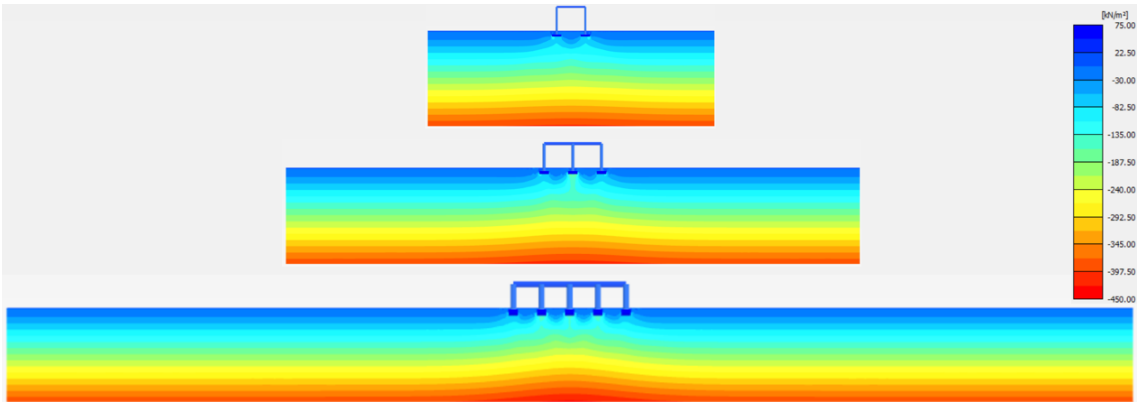


Figure 6.2: Stresses state before the ground motion

Additionally, three buildings with the same properties were modeled but the same contact pressure below the footings was simulated. Buildings with two footings already have the same contact pressure with the soil then only buildings with three and five footings were simulated again. To model this condition was applied a distributed load in the beams to generate a contact pressure of 80 kPa below the central column, then additional point loads were applied in the top of the other columns to obtain the same contact pressure below them. Figure 6.3 shows the stress state before the ground motion when the contact pressure was the same in all the footings.

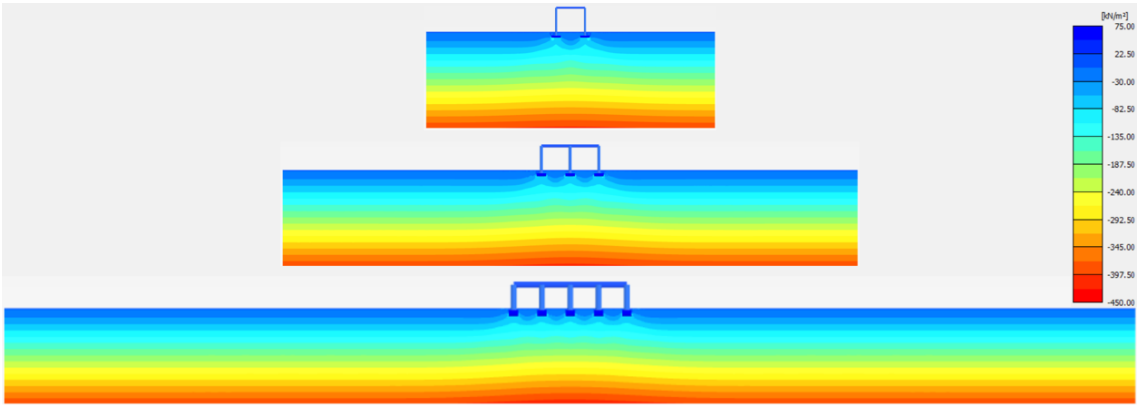


Figure 6.3: Stresses state before the ground motion for the same contact pressure in all the footings

Ground motion 6 in Table 4.3 (GM1), ground motion 1 in Table 4.3 (GM2) and ground motion 1 in Table 4.2 (GM3) were used in this study. These motions were entered as a horizontal displacement in the bottom boundary. In Figure 6.4 was plotted the Cumulative absolute velocity (CAV) of the three different ground motions to observe that their intensities and duration are so different.

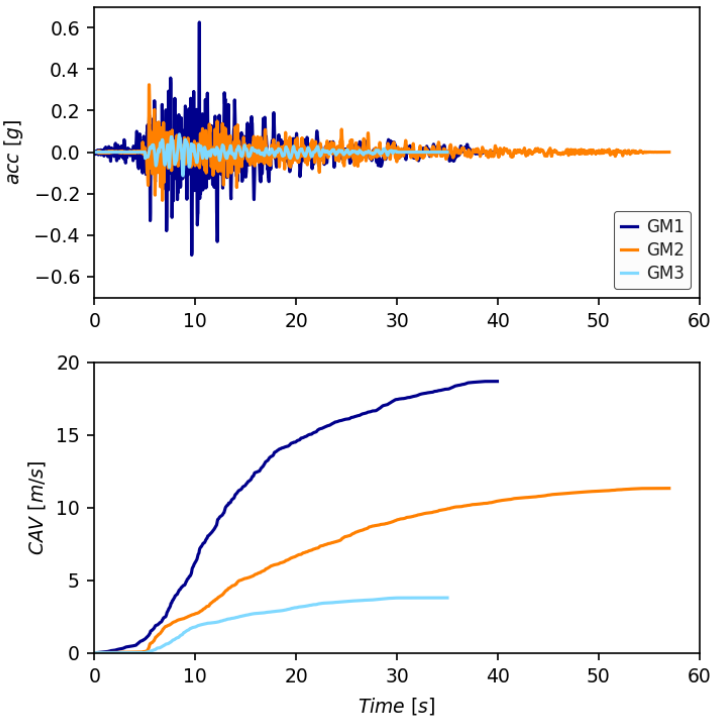


Figure 6.4: Ground motions used in the parametric analysis: a) Acceleration time series; b) Cumulative absolute velocity (CAV)

6.2 Results

In this section the results of the numerical analyses performed for the 3 ground motions are presented for the three benchmark models (NF2, NF3, NF5). Also, the results for the three additional models with the same contact pressure below the footings are analyzed. In the following figures the dots represent the numerical results and the lines represent the settlements estimated using the Bray and Macedo (2017) approach (see Section 2.3.3). Additionally, the results were also compared in terms of tilt and maximum angular distortion. Below, it will be briefly explained how the values presented in the figures containing the results were found.

Numerical settlements

Figure 6.5 shows the settlements in the end of the ground motion for the NF5 benchmark model using the GM1. In this case a maximum settlement of 0.237 m occurred in the central footing. The average settlement was calculated by summing the settlements in all the footings and then dividing by the number of footings. For this example, the average settlement was calculated by summing the five settlements (0.728 m) and then dividing by 5, resulting in 0.146 m. Thus, the triangle in the figures containing the settlements results represent the maximum settlement, and

the circles the average settlement.

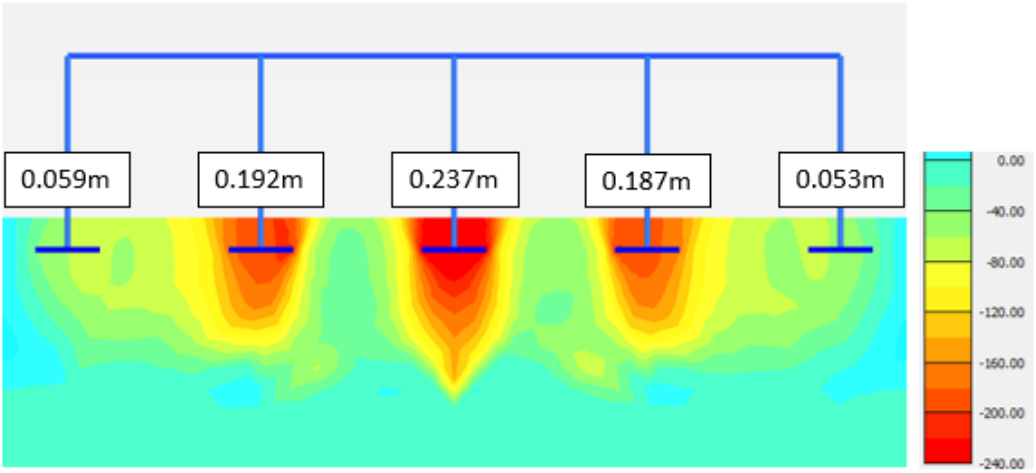


Figure 6.5: Settlements after the ground motion GM1 for benchmark models NF5

The global tilt was calculated as the differential settlement between the external footings divided by the distance between this two footings. For this example, the global tilt was calculated by subtracting the two external settlements (0.006 m) and dividing by 24 m, resulting in $2.5x10^{-4}$. Experience has shown that the damage to the superstructure is related among others to the angular distortion (β), more than to the values of the maximum settlement $Sett_{max}$ (Flora et al., 2018). For this reason the maximum angular distortion (β_{max}) was included in the results. Angular distortion (β) is a slope between two points, defined as the differential settlement between these points and the distance between them (Kim et al., 2015). The maximum value of β is for two points that are not necessarily the extremities of the foundation. Figure 6.6 shows the graphical definition of the maximum angular distortion (β_{max}).

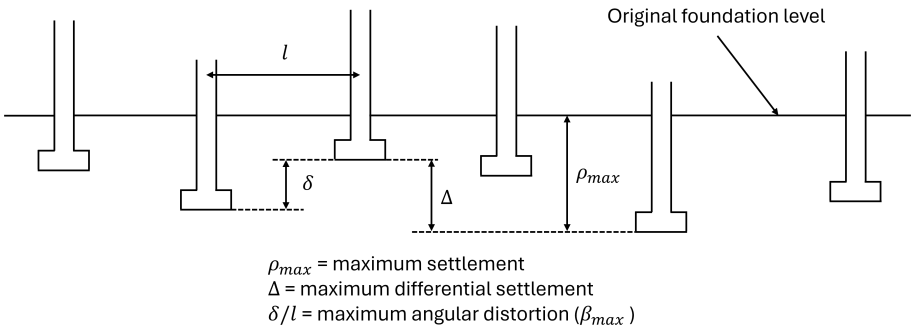


Figure 6.6: Definition of angular distortion

Bray and Macedo (2017) settlements

This simplified approach was developed for structures with mat foundation, but in this work was also used to estimate the settlement in each footing by entering each foundation contact pressure (Q) separately in the Equation 2.30. Continuing with the same example, Figure 6.7a shows the distributed load applied to the building in the numerical analysis and the stresses state before the ground motion. Figure 6.7b shows the equivalent building if this one had a mat foundation.

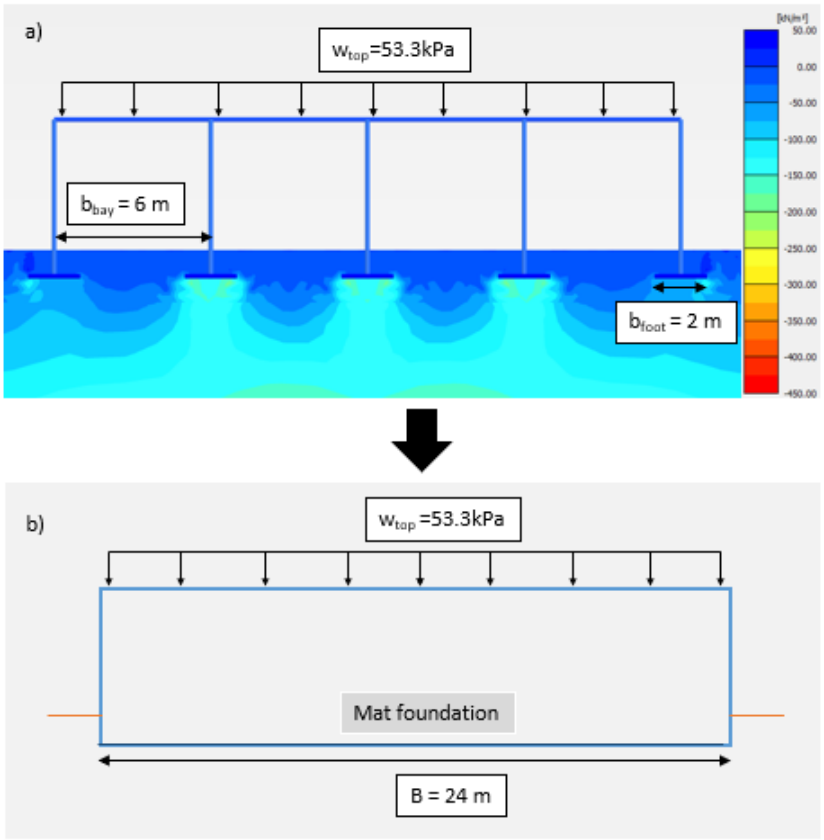


Figure 6.7: a) Initial stresses state for benchmark model NF5; b)Equivalent building with mat foundation

To calculate the settlement as if the building had a mat foundation ("Bray mat"), the contact pressure at the base of the building was considered the same load distributed at the top ($Q = w_{top}$).

To calculate the average settlement with Bray and Macedo (2017) approach ("Bray av."), first the settlement in each footing was calculated. For that, the contact pressure at the base of the footings was necessary. For the external footings the contact pressure was estimated using the Equation 6.1 and for the internal footing the Equation 6.2.

$$Q_{ext} = \frac{w_{top} \cdot b_{bay}}{2 \cdot b_{foot}} \tag{6.1}$$

$$Q_{int} = \frac{w_{top} \cdot b_{bay}}{b_{foot}} \tag{6.2}$$

Thus, the solid lines in the figures containing the results represent the settlements considering that the structure had a mat foundation, and the dotted lines the average of the settlements considering the structure with isolated footings.

Figure 6.8 shows the settlements from numerical simulations. The most evident behavior is that the ground motion with greatest Cumulative absolute velocity (CAV), GM1, caused higher settlements. For the GM2 and GM3, the settlements were similar for the three types of buildings (NF1, NF2, NF3). For GM1 the maximum settlement increased when the number of footings increased and the average settlement increased when the building had three footings but decreased when five footings were simulated. This can be explained by the fact that when the structure has more footings, the differential settlements become greater, resulting in a lower average value of settlements compared to the maximum value.

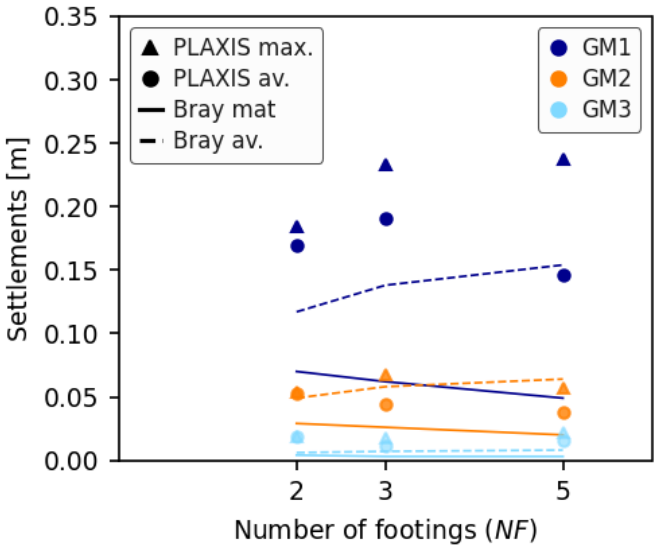


Figure 6.8: Numerical maximum and average settlements compared with Bray and Macedo (2017) approach for the benchmark models

When the Bray and Macedo (2017) approach was used considering a building with mat foundation, the settlements decreased because the contact pressure is the same for all the buildings but the total width increases, generating less settlement. Otherwise, when the approach was used considering

the original building with isolated footings, the settlements increased with the number of footings because the contact pressure in the external and internal footings is always the same independent of the number of footings, so having more footings the average of the settlements increased.

Figure 6.9 shows the maximum global tilt from numerical simulations. Once again,the most evident behavior is that ground motion GM1 caused higher tilt, particularly noticeable for the building with two footings. For GM3, the tilt was similar for the three types of buildings (NF1, NF2, NF3). For GM1 the tilt decreased when the number of footings increased and for GM2 the tilt was higher when three footings were simulated. Because tilt is calculated just based on the settlements of the external footings, it becomes challenging to discern a clear trend in the results.

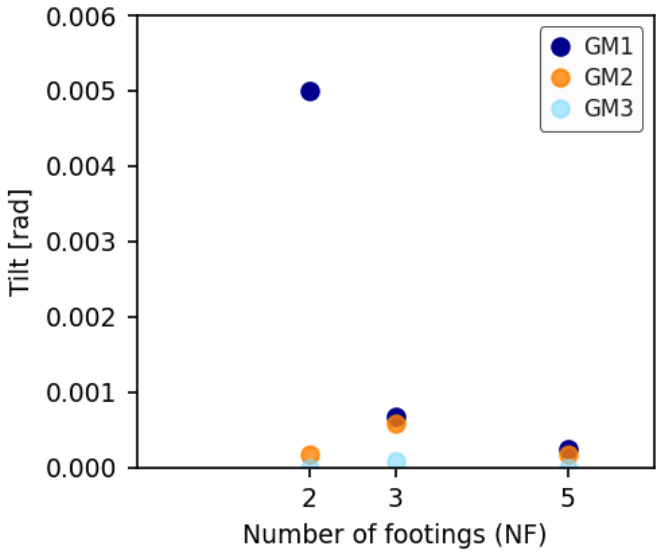


Figure 6.9: Numerical maximum tilt for the benchmark models

Figure 6.10 shows the maximum angular distortion from numerical simulations. Once again,the most evident behavior is that ground motion GM1 caused higher tilt, particularly noticeable for the buildings with three and five footings. For building with two footings, only the ground motion GM1 generated an angular distortion. GM1 and GM2 generated the same angular distortion for buildings with three and five footings. Notably, when the GM1 was used, the angular distortion increased when the number of footings increased.

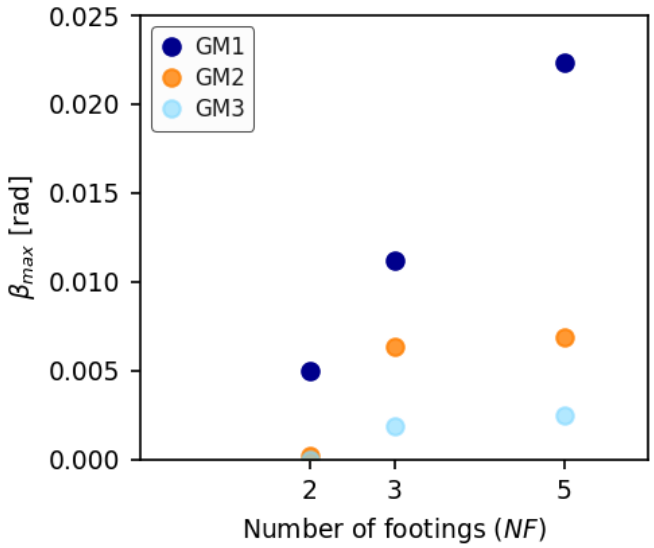


Figure 6.10: Numerical maximum angular distortion for the benchmark models

Figures 6.11 to 6.13 depict the time series derived from the numerical simulations utilizing the three distinct ground motions. Figure 6.11 shows the pore pressure ratio equal to one, indicating soil liquefaction in all cases. Time series of settlements shows how the settlements in the external footings decreased with the increase of the number of footings, while the settlement in the central footing increased. It can also be observed that the maximum settlement in the three types of structures is quite similar. The time series confirm that the angular distortion increases with the number of footings, while the tilt decreases. Figure 6.12 and Figure 6.13, for GM2 and GM3 respectively, show the same trends.

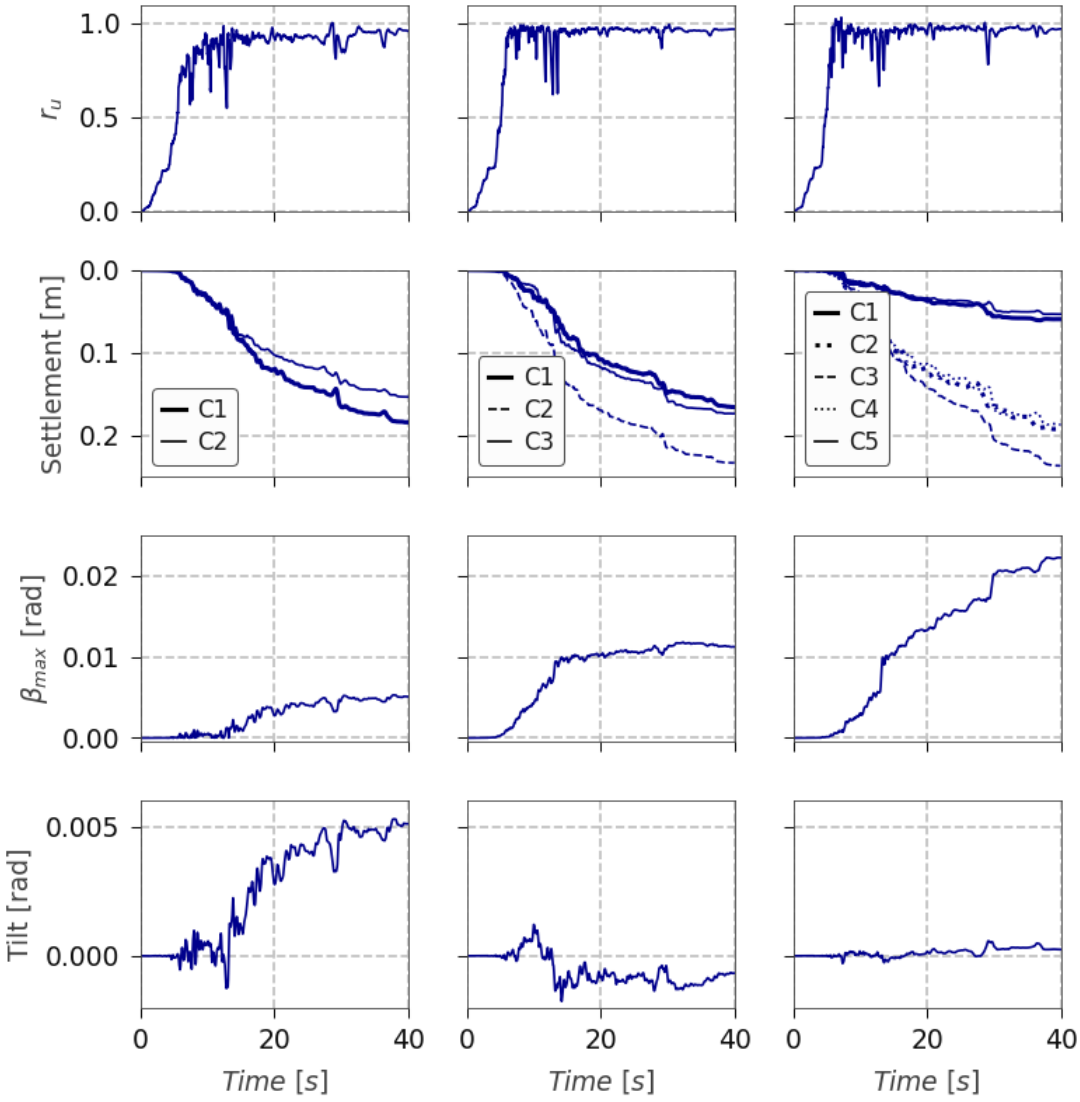


Figure 6.11: Time series for GM1 for the benchmark models

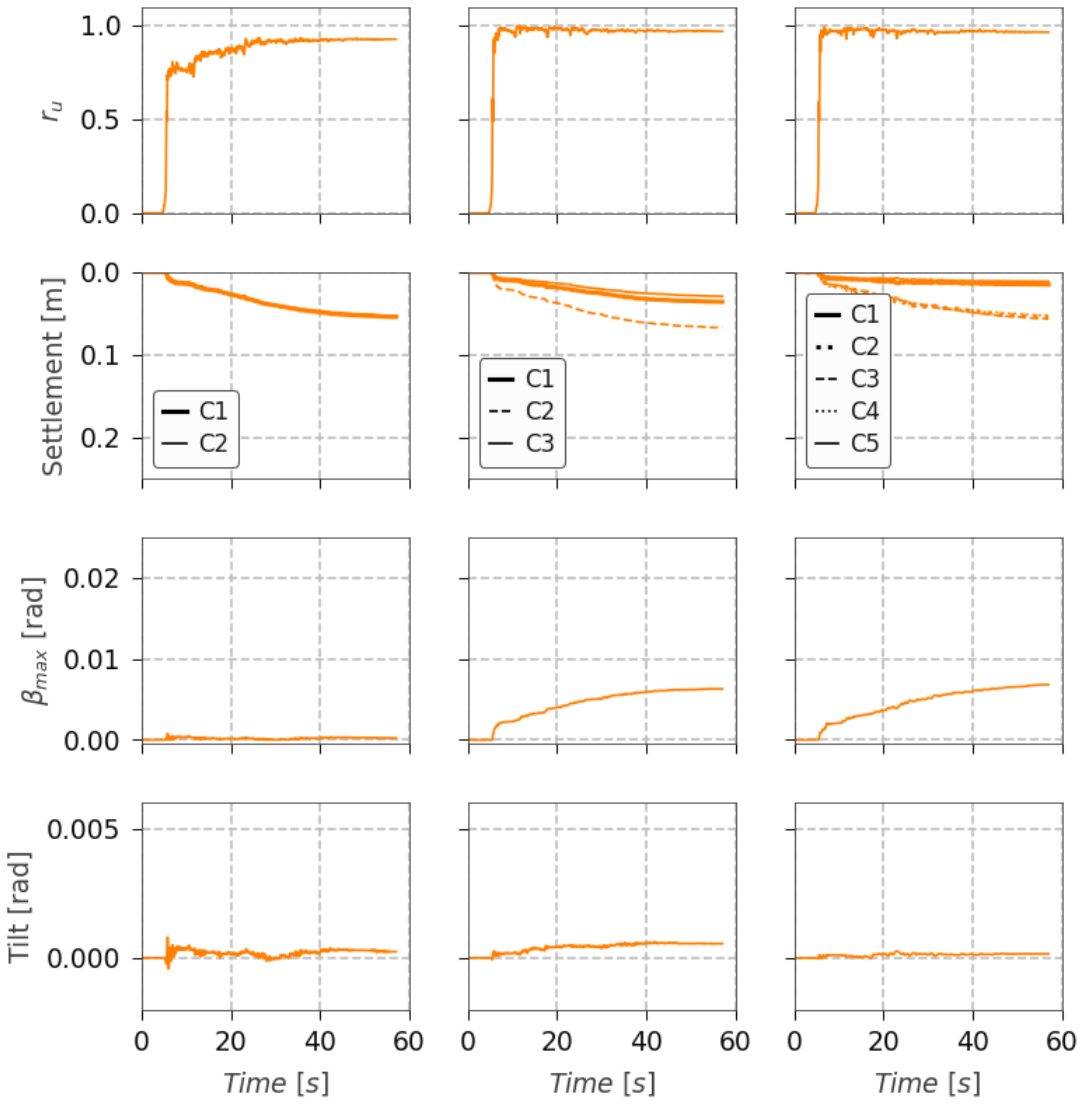


Figure 6.12: Time series for GM2 for the benchmark models

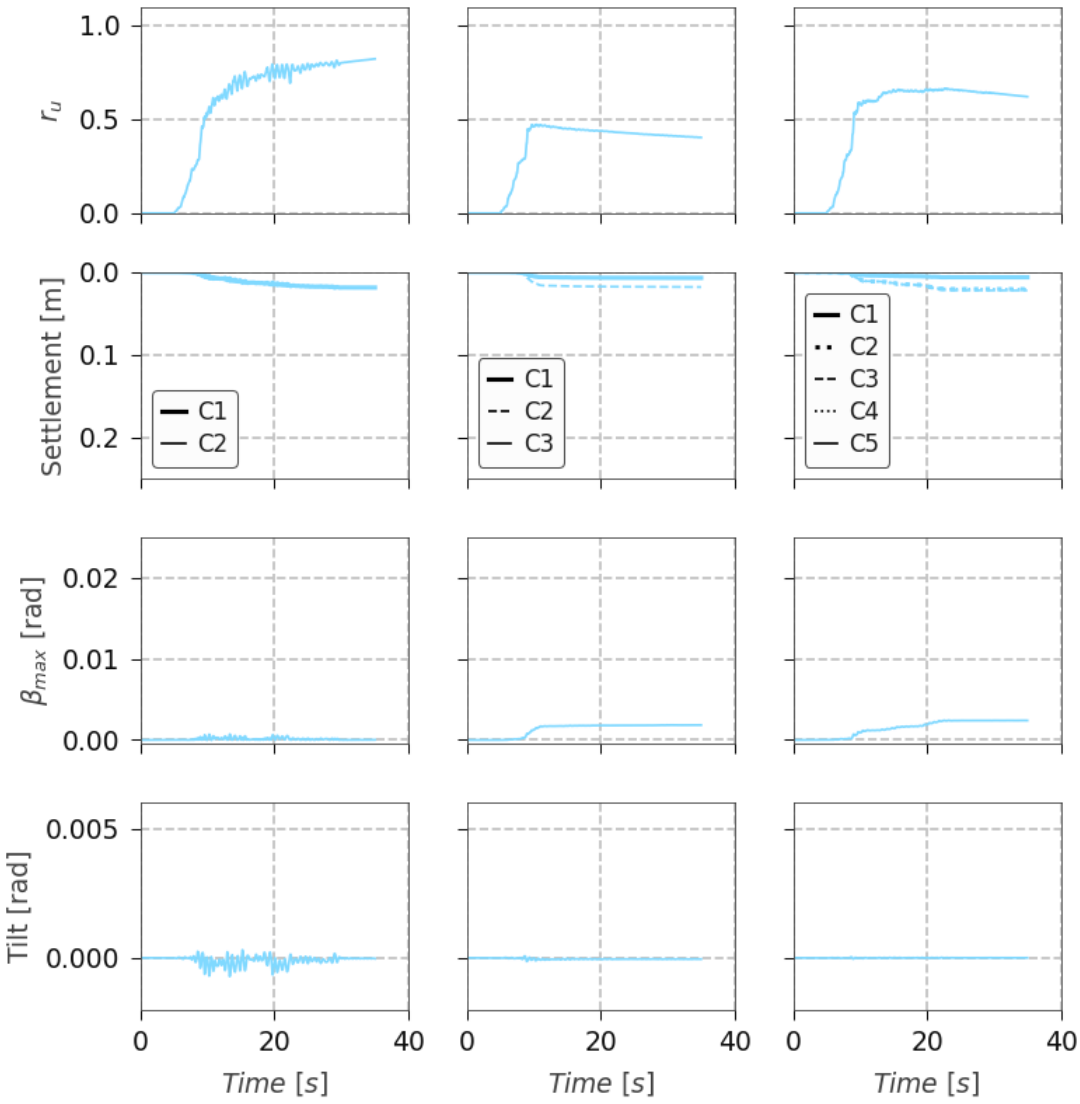


Figure 6.13: Time series for GM3 for the benchmark models

Even though in reality no structure has the same contact pressure in all footings, this case was simulated to observe whether the trends in the results are clearer. Buildings with two footings already have the same contact pressure with the soil then only buildings with three and five footings were simulated again. Figure 6.14 shows the settlements from numerical simulations when the buildings were modeled with the same contact pressure in all the footings. Observing these results, it is evident that settlements decreased as the number of footings increased. Adjacent footings increasing the bearing capacity by providing additional overburden pressure, which may be the key mechanism reducing settlement, although other more complex mechanisms could also be contributing.

When the Bray and Macedo (2017) approach was used considering a building with mat foundation,

the settlements decreased because the contact pressure is the same for all the buildings but the total width increase, generating less settlement. Otherwise, when the approach was used considering the original building with isolated footings, the settlements kept constants because the contact pressure and width of all the buildings are the same.

Figure 6.15 shows the maximum global tilt from numerical simulations. For GM2 and GM3, the tilt was similar for the three types of buildings (NF1, NF2, NF3). For GM1 the tilt decreased when the number of footings increased.

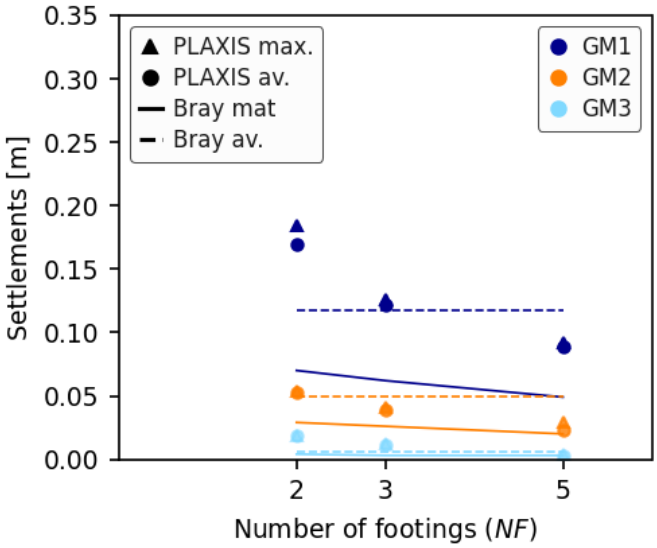


Figure 6.14: Numerical maximum and average settlements compared with Bray and Macedo (2017) approach for the same contact pressure in all the footings

Figure 6.16 shows the maximum angular distortion from numerical simulations. GM1 and GM2 generated similar angular distortion for all types of buildings. Notably, when the GM1 was used, the angular distortion decreased when the number of footings increased.

Figures 6.17 to 6.19 depict the time series derived from the numerical simulations utilizing the three distinct ground motions and modeling the same contact pressure in all the footings. Figure 6.11 shows again the pore pressure ratio equal to one, indicating soil liquefaction in all cases. Time series of settlements show how settlements decreased with the number of footings, primarily because the total width of the structure increases with the number of footings. Angular distortion and tilt also decreased when the settlements decreased. Figure 6.18 and Figure 6.19, for GM2 and GM3 respectively, show the same trends.

As the footings are very far apart their behavior tends towards a single footing. As all footings are equal in terms of load, size and supporting soil, the footings had the same movement and therefore

there would be no load redistribution. Thus, the angular distortion and tilt are minimal.

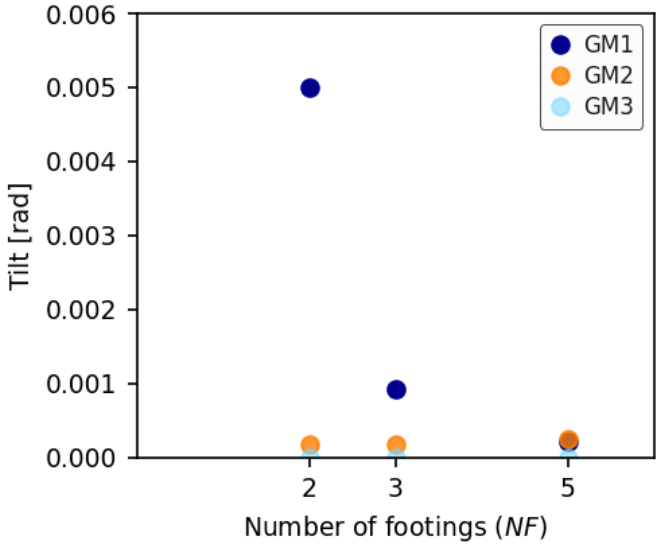


Figure 6.15: Numerical maximum tilt for the same contact pressure in all the footings

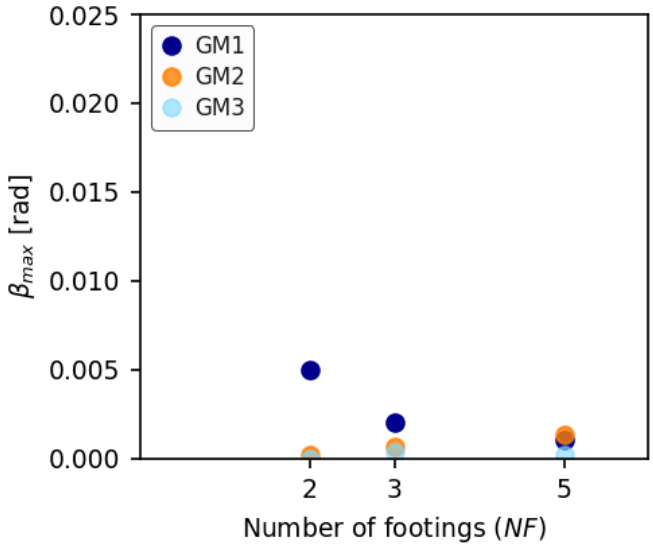


Figure 6.16: Numerical maximum angular distortion for the same contact pressure in all the footings

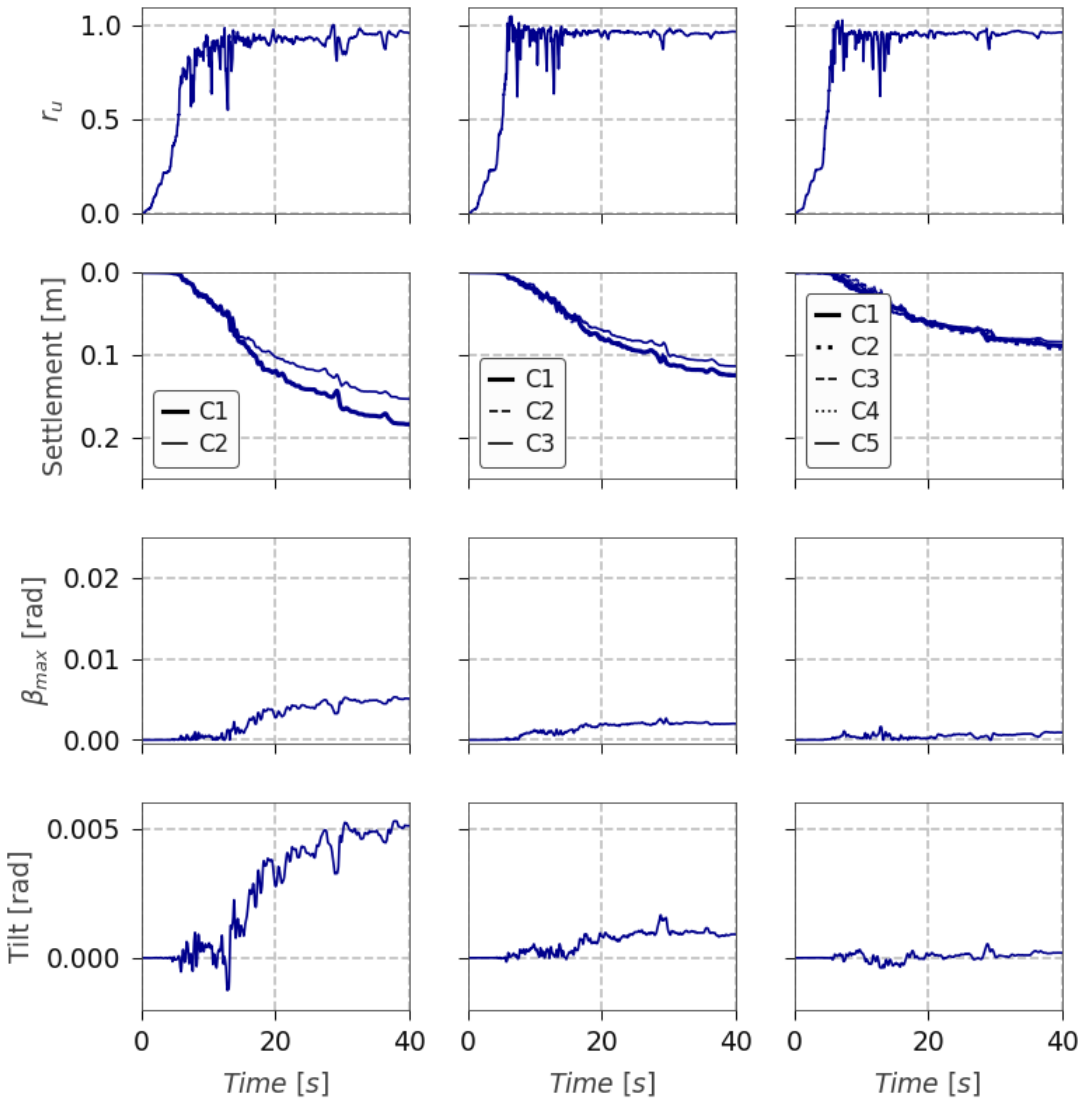


Figure 6.17: Time series for GM1 for the same contact pressure in all the footings

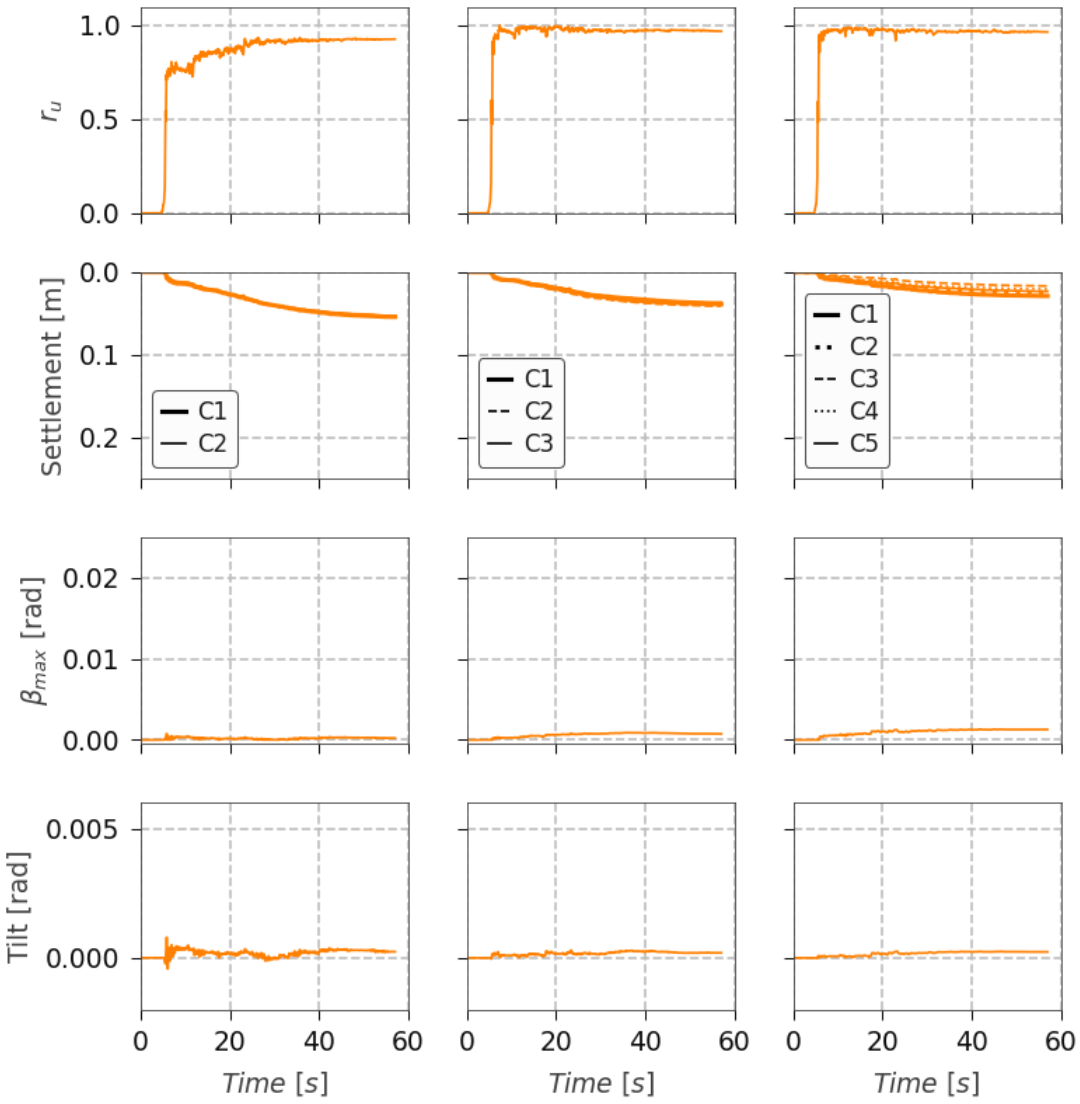


Figure 6.18: Time series for GM2 for the same contact pressure in all the footings

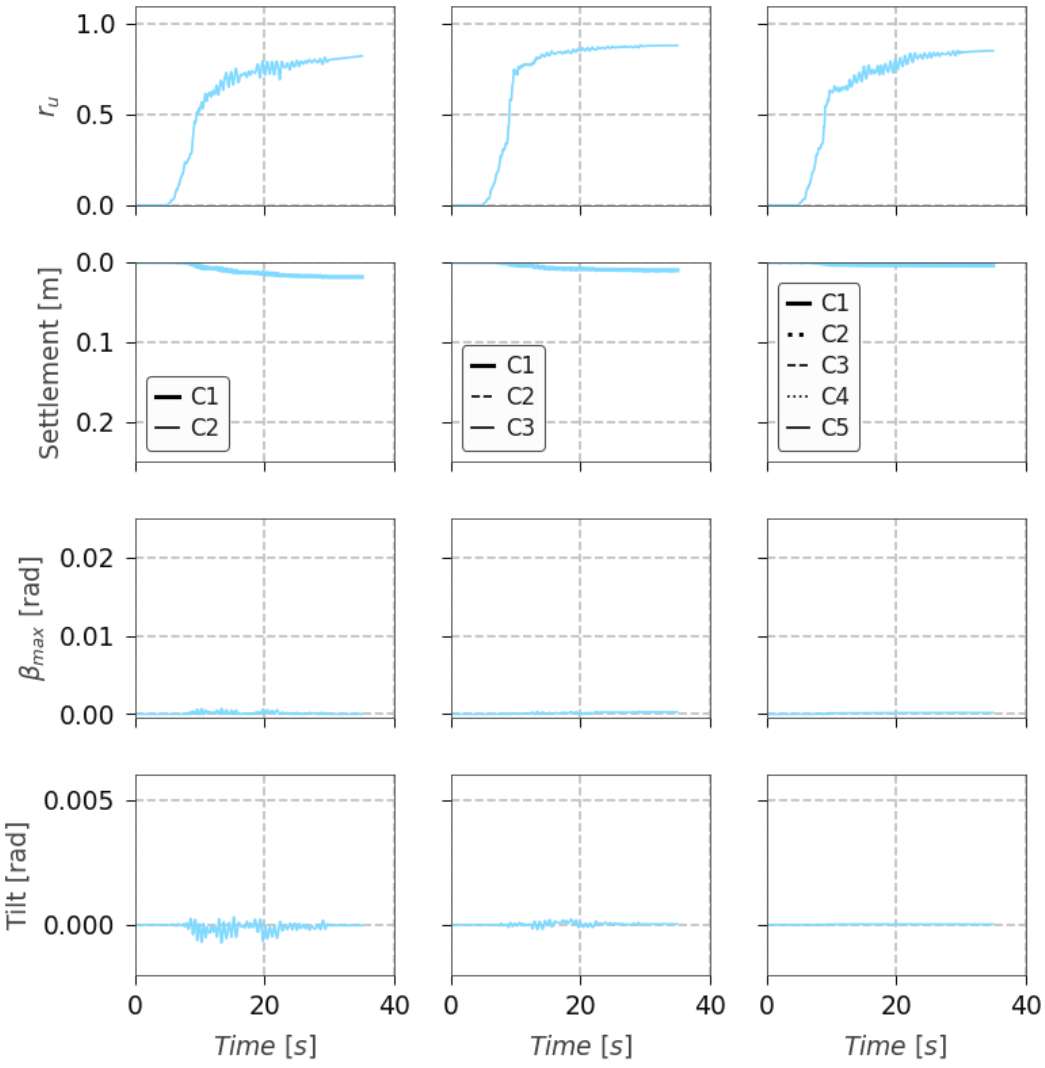


Figure 6.19: Time series for GM3 for the same contact pressure in all the footings

6.3 Conclusions

This study provides the first key insights for extending the existing methods considering more complex systems such as buildings on shallow isolated footings. The numerical models presented in this section allowed to observe the difference between total settlements and differential settlements when buildings with two, three and five footings are used. The results showed the importance of considering the number of footings in the settlements of a building. Settlements in the external footings decreased with the increase of the number of footings, while the settlement in the central footing increased. It was also observed that the maximum settlement in the three types of structures (NF2, NF3, NF5) is quite similar. The angular distortion increases with the number of footings, while the tilt decreases.

Chapter 7

Key parameters controlling liquefaction-induced differential settlements for buildings with isolated footings

In the previous section, was outlined the procedure to numerically simulate differential settlements of building with two (NF2), three (NF3) and five isolated footings (NF5). In this chapter, the study will be extended by systematically varying several parameters in the soil profile and building configuration. Therefore, a parametric set of nonlinear dynamic SSI effective stress 2D numerical analyses was performed to identify the key parameters controlling liquefaction-induced settlement for buildings with isolated footings and compare the results in terms of settlement of the footings with Bray and Macedo (2017) approach. Residual tilt and maximum angular distortion were also analyzed.

7.1 Overview

The parameters considered for the sensitivity analysis are listed in Table 7.1. The groundwater table was always set at the base of the non-liquefiable crust layer and the same boundary conditions, ground motions and damping properties as the benchmark model were used. In total, 81 different models will be analyzed. A Python script was developed to automate the execution of the numerous numerical models required for this parametric analysis, the complete code can be found in Appendix A.

Table 7.1: Parameters for sensitivity analysis

Parameter	Description	Baseline	variations	
H_C $[m]$	Non-liquefiable layer thickness	2	1	4
D_R [%]	Liquefiable layer relative density	50	35	65
H_L $[m]$	Liquefiable layer thickness	4	2	8
w_{top} $[kPa]$	Beam load	53	27	80
b_{foot} $[m]$	Footing width	2	1	3
H $[m]$	Structure height	6	3	12
d_f $[m]$	Foundation embedment depth	1	0.5	2
b_{bay} $[m]$	Bay length	6	3	12
EI_{ratio}	EI_{beam}/EI_{column}	1	0.1	10

To identify the soil profile characteristics that influence on the settlements, the thickness of the liquefiable layer (H_L) was varied from 2 to 8 m, and its relative density (D_R) from 35% to 65%. Also, the depth of the liquefiable layer was altered by varying the thickness of the non-liquefiable crust layer (H_C) from 1 to 4 m. To identify the influence of the structure configuration on the settlements, the beam load (w_{top}) was varied from 27 kPa to 80 kPa with footing widths (b_{foot}) ranging from 1 m to 3 m. As footings get closer, their stress bulbs can overlap, and the pore water cannot flow as easily to and from underneath them. To quantify this adjacent footing effects, the bay length was varied from 3 m to 12 m. Figure 7.1 presents an example of a building with three footings and the parameters varied within the structure.

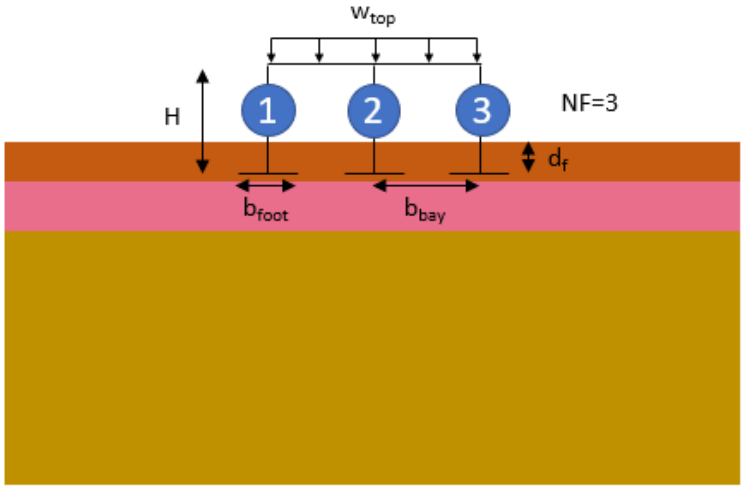


Figure 7.1: Building parameters in sensitivity analysis

7.2 Results

In this section the results of parametric analyses performed for the 3 ground motions are presented. Equally as in the results of the previous chapter, in the following figures the dots represent the numerical results and the lines represent the settlements estimated using the Bray and Macedo (2017) approach (see Section 2.3.3). Because buildings near liquefaction-induced bearing collapse exhibit a significant increase in settlement, the authors suggest that, for low bearing capacity factors of safety, evaluating settlements with this approach may not be applicable. Thus, cases where the factor of safety was less than one were highlighted in the settlement figures with an "x". Additionally, the results were also compared in terms of tilt and maximum angular distortion. First, the results when the soil parameters were varied are presented, followed by the results when the building parameters and configurations were varied.

7.2.1 Soil parameters

The results for the variation of the non-liquefiable layer thickness (H_C), liquefiable layer relative density (D_R) and liquefiable layer thickness (H_L) are presented in this section.

Non-liquefiable layer thickness (H_C)

Figures 7.2 to 7.7 shows the results of the models with varying H_C. When the H_C was increased, settlements decreased, indicating that a deeper liquefiable layer generate less settlements. When the Bray and Macedo (2017) approach was used, the settlements also decreased but were less influenced by H_C. It is important to highlight that the bearing capacity factors of safety are less than one when H_C was equal to 1 m, thus the estimation using this approach is not applicable. Notably, for GM1 the estimation was very low when the structure was considered with mat foundation. Angular distortion and tilt did not show a clear trend in the results.

Figure 7.5 shows the time series derived from the numerical simulations using GM1. The pore pressure ratio is always equal to one, indicating soil liquefaction in all cases. Time series of settlements confirmed that the settlements were higher when H_C was equal to 1 m. The angular distortion had the same behavior for the building NF2 and NF5 being maximum when H_C was equal to 2 m, but when NF3 was simulated, β_{max} was higher for H_C equal to 1 m. Figure 7.6 and Figure 7.7, for GM2 and GM3 respectively, show the same trends for the settlements. Liquefaction did not occur when GM3 was applied.

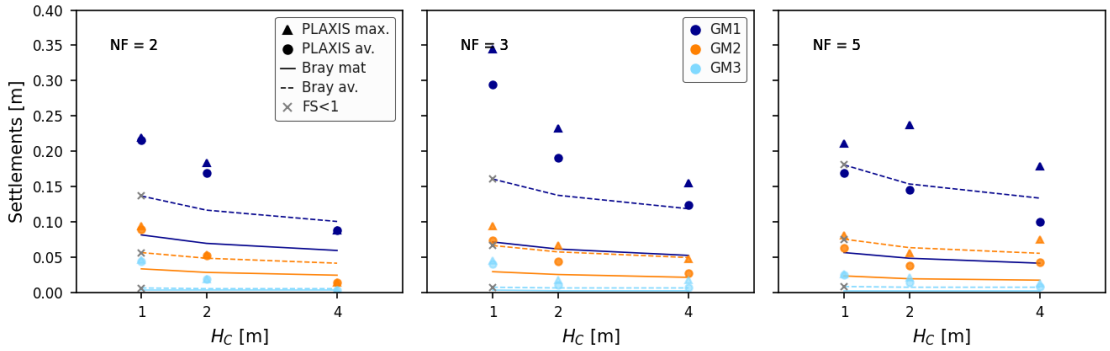


Figure 7.2: Numerical maximum and average settlements compared with Bray and Macedo (2017) approach for H_C variation

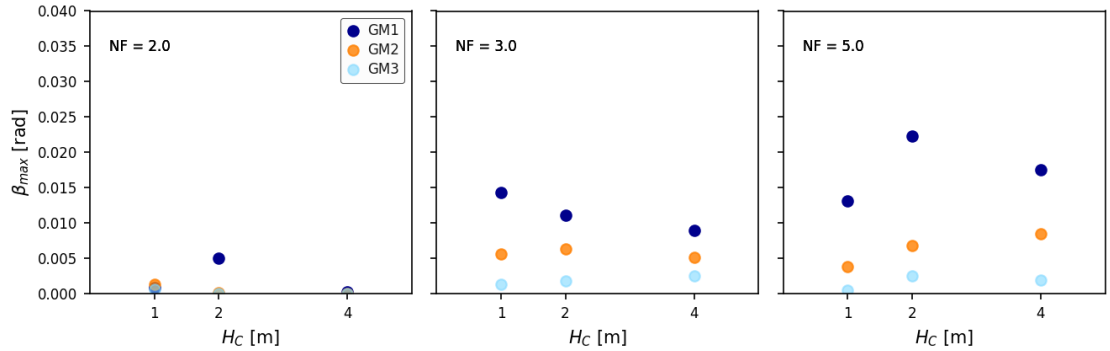


Figure 7.3: Numerical maximum angular distortion for H_C variation

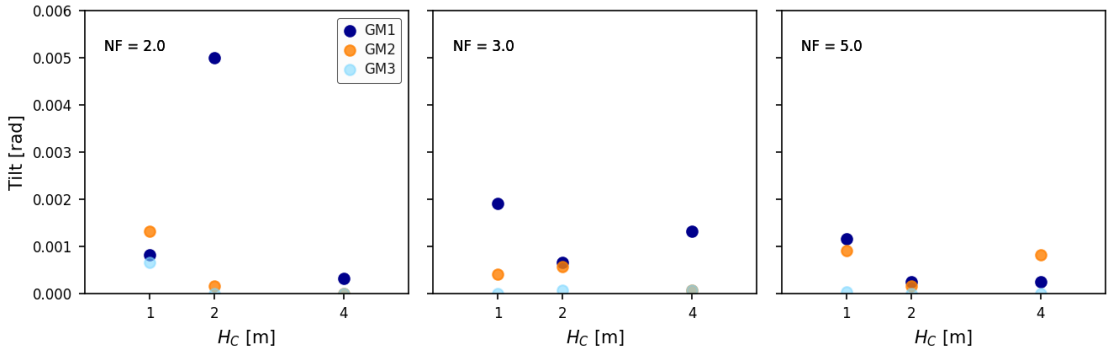


Figure 7.4: Numerical maximum tilt for H_C variation

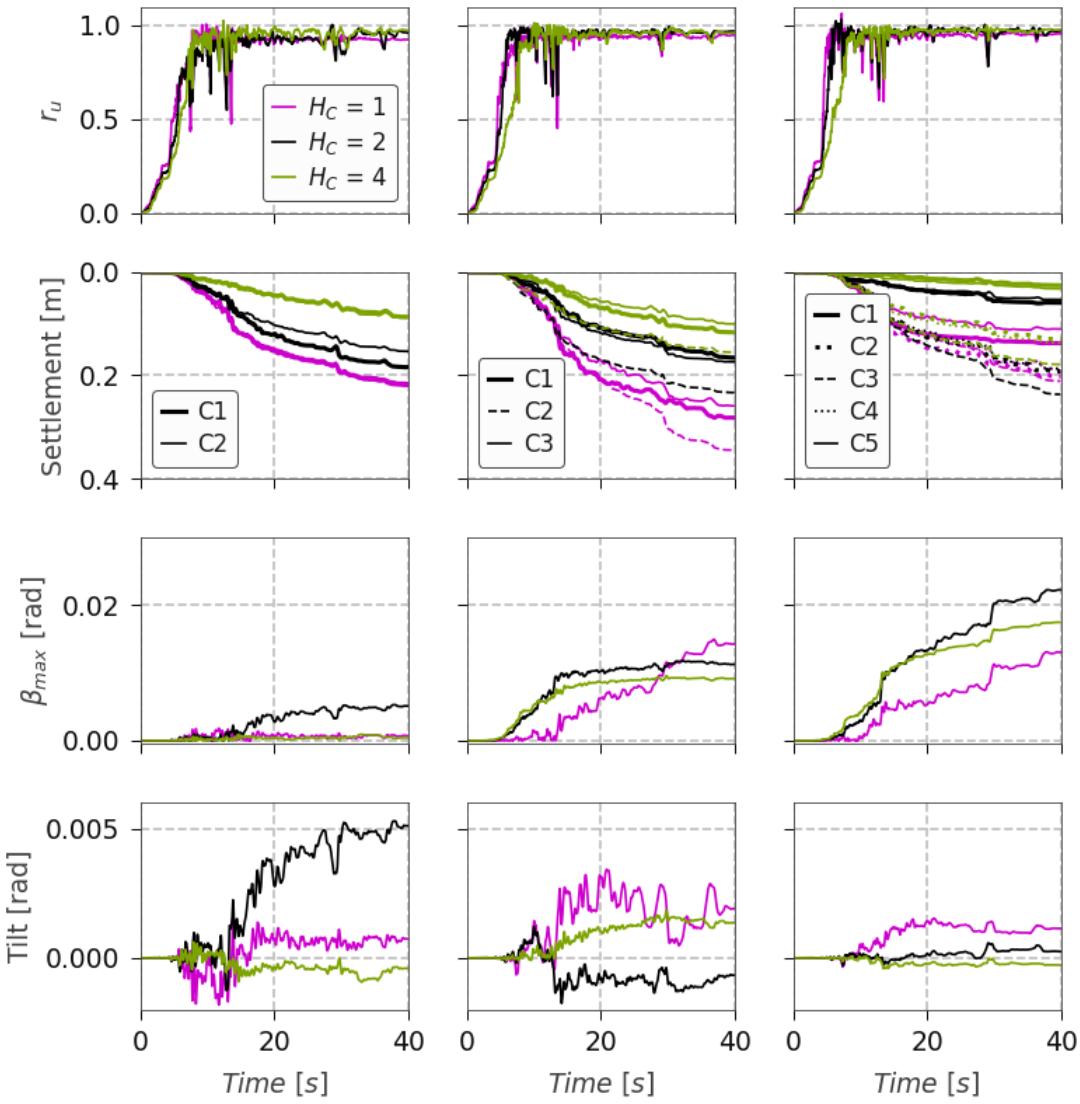


Figure 7.5: Time series for GM1 for H_C variation

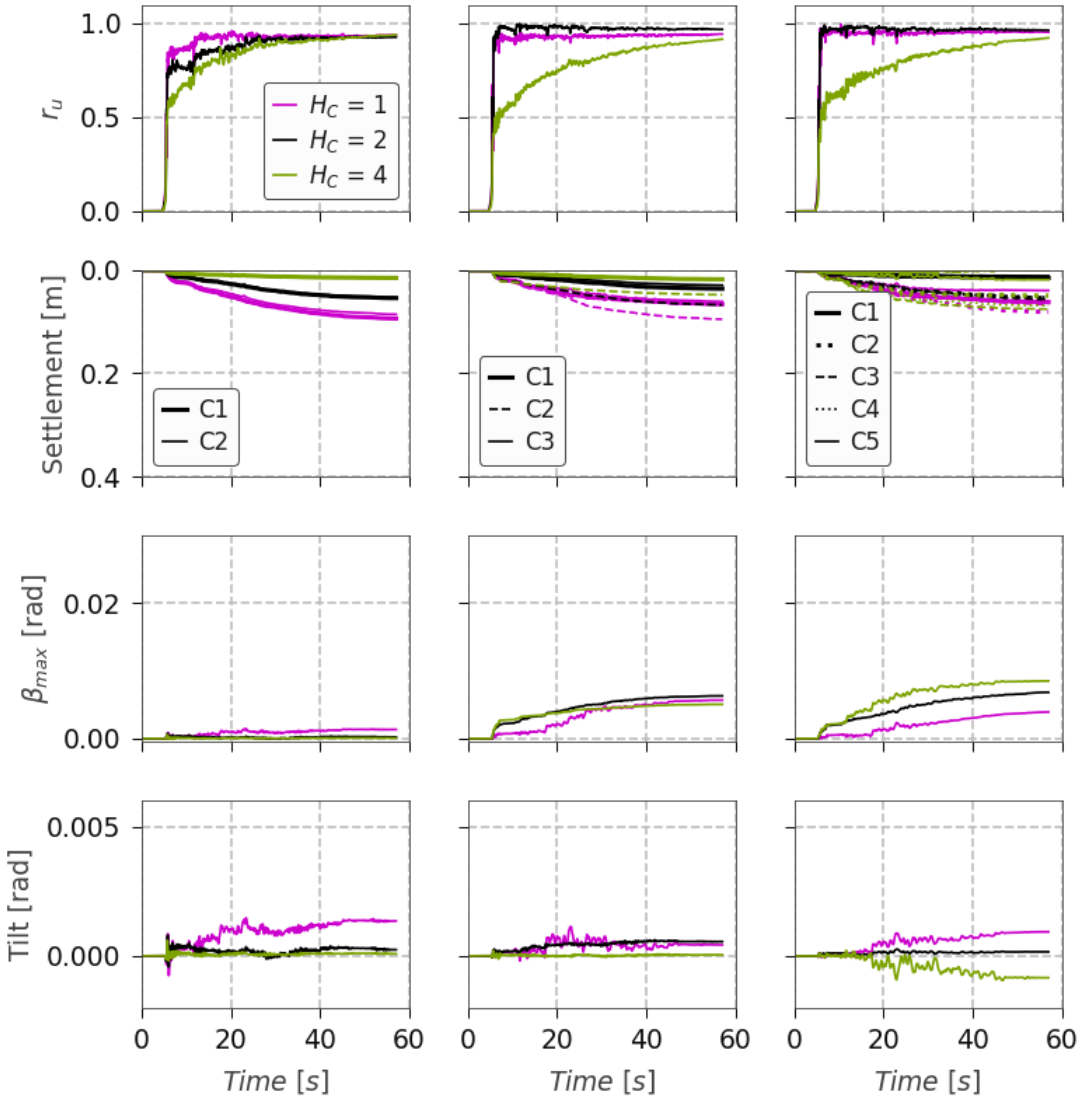


Figure 7.6: Time series for GM2 for H_C variation

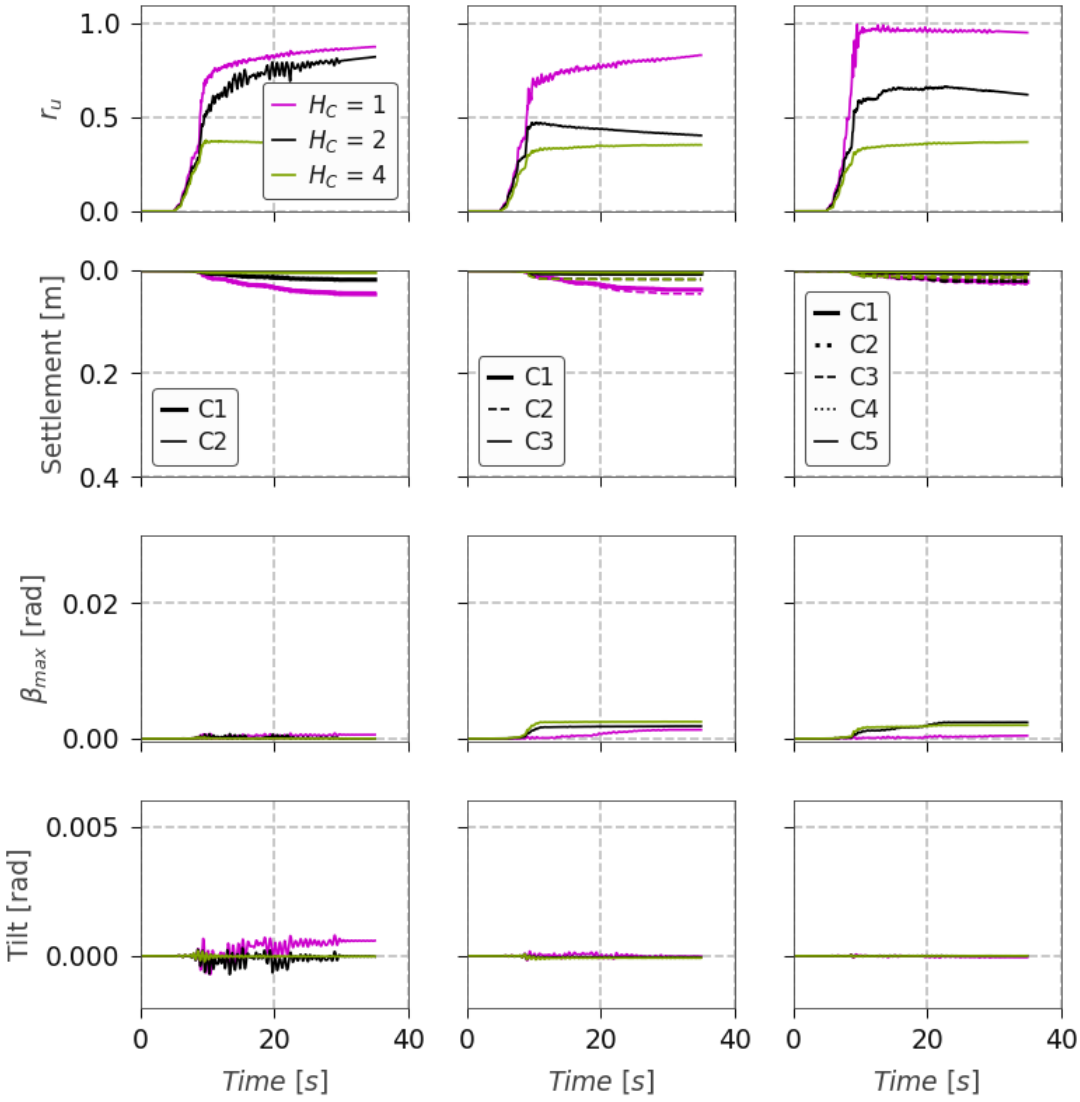


Figure 7.7: Time series for GM3 for H_C variation

Relative density (D_R)

Figures 7.8 to 7.13 shows the results of the models with varying D_R. When the D_R was increased, settlements decreased, indicating that a denser liquefiable layers generate less settlements. When the Bray and Macedo (2017) approach was used, the settlements also decreased when the D_R was increased and particularly when isolated footings were considered, the values estimated were similar with average PLAXIS 2D settlements. Once again, for GM1 the estimation was very low when the structure was considered with mat foundation. For GM2 and GM3 the tilt resulted similar and low. For GM1 and NF5 the tilt was also similar and low for all the density values. For NF3 the tilt decreased when D_R was increased and for NF2 the tilt was higher when D_R was equal to 50%. Angular distortion decreased when the D_R was increased for NF3 and NF5 but when D_R

was 35% for NF2, the behavior was different.

Figure 7.11 shows the time series derived from the numerical simulations using GM1. The pore pressure ratio is always equal to one, indicating soil liquefaction in all cases. Time series of settlements confirmed that the settlements were lower when D_R was equal to 65%. The angular distortion and tilt was also lower when D_R was equal to 65%. Figure 7.12 and Figure 7.13, for GM2 and GM3 respectively, show the same trends for the settlements. Liquefaction did not occur when GM3 was applied and D_R of 50% and 65% were simulated.

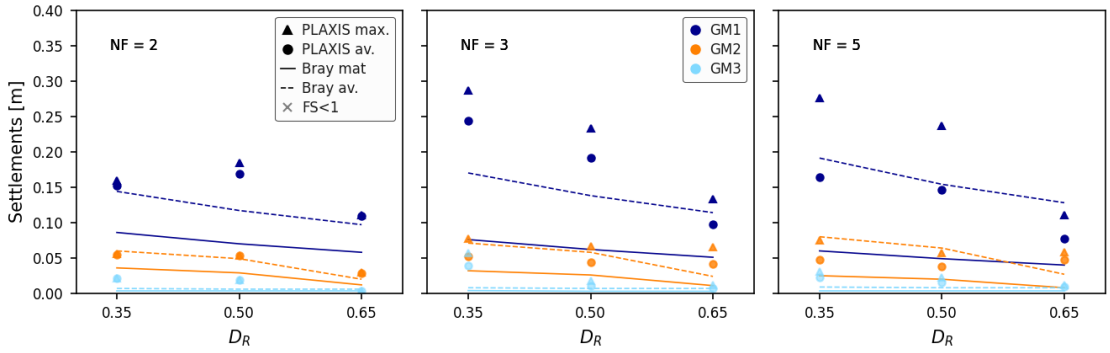


Figure 7.8: Numerical maximum and average settlements compared with Bray and Macedo (2017) approach for D_R variation

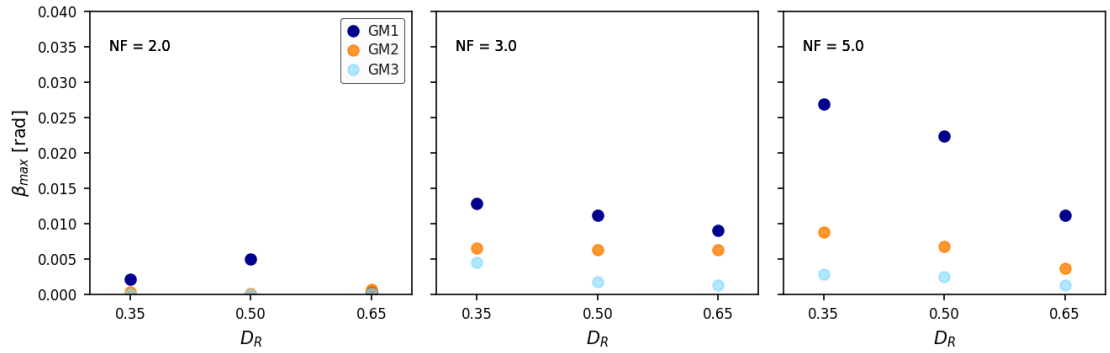


Figure 7.9: Numerical maximum angular distortion for D_R variation

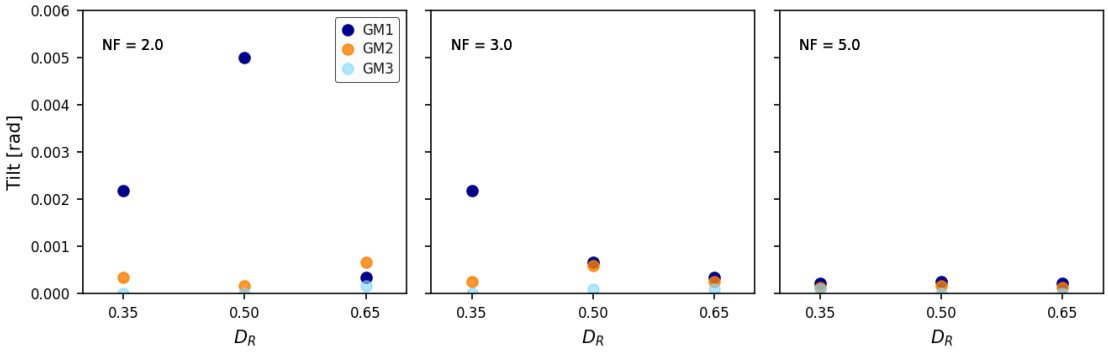


Figure 7.10: Numerical maximum tilt for D_R variation

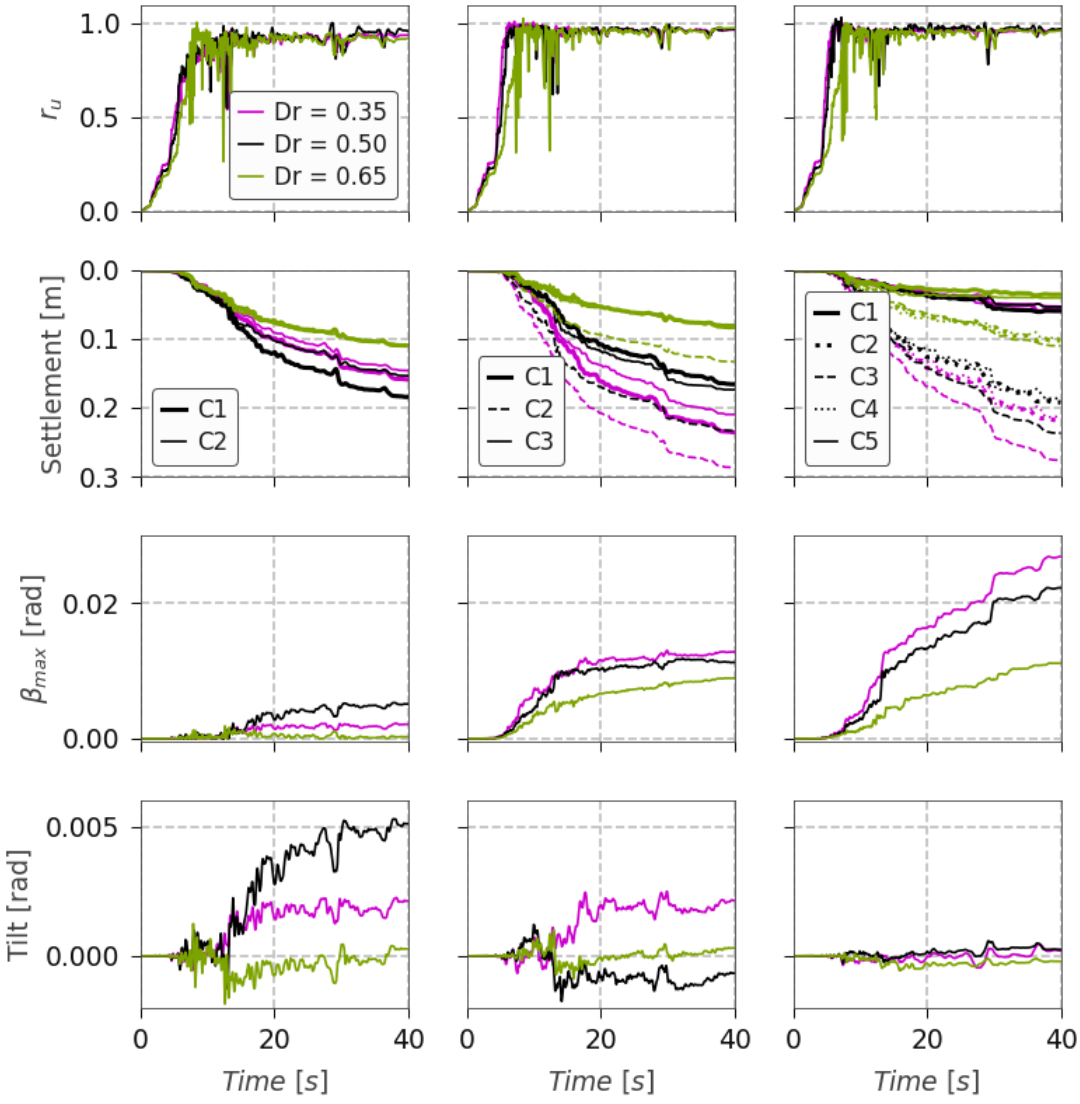


Figure 7.11: Time series for GM1 for D_R variation

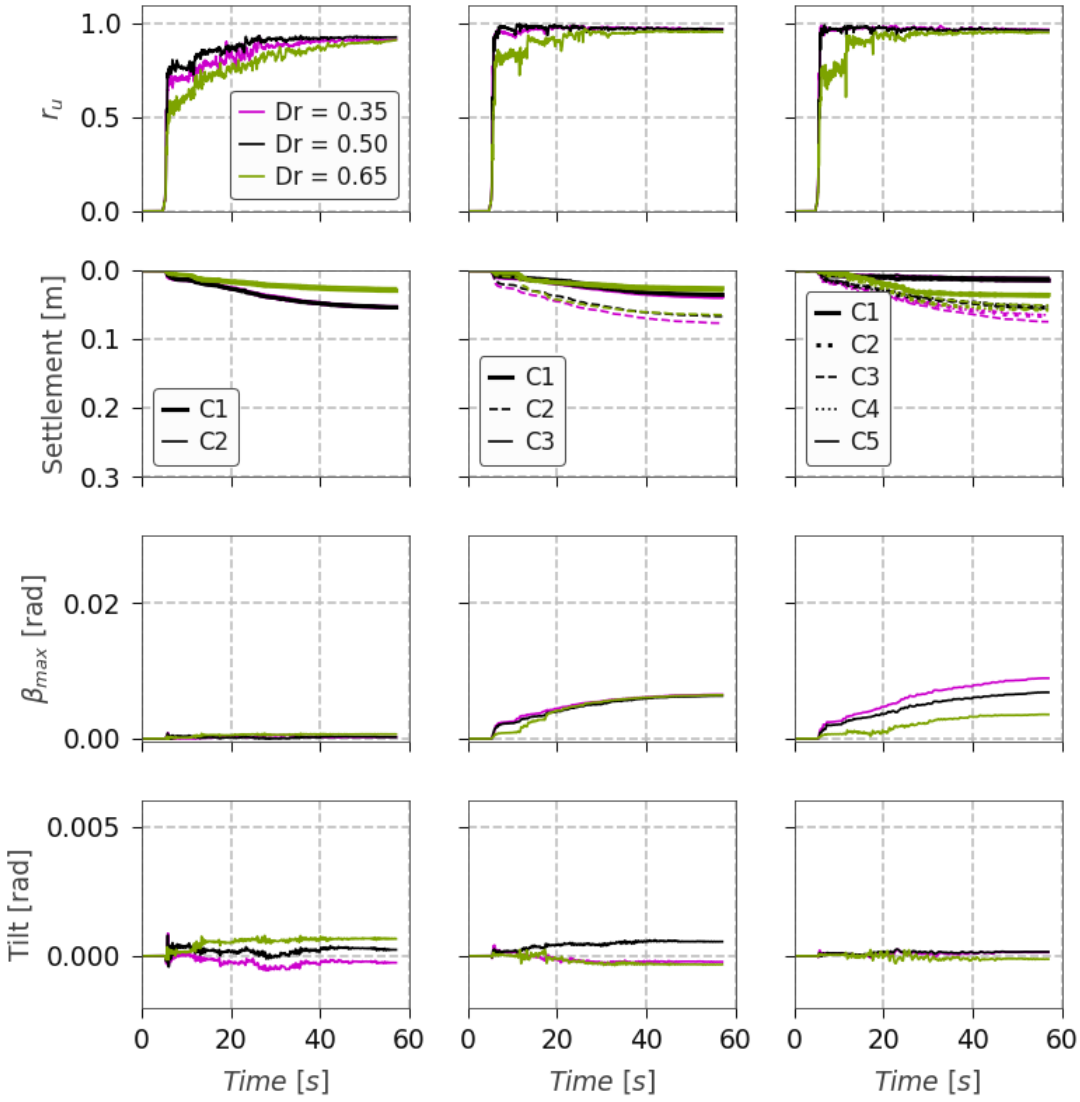


Figure 7.12: Time series for GM2 for D_R variation

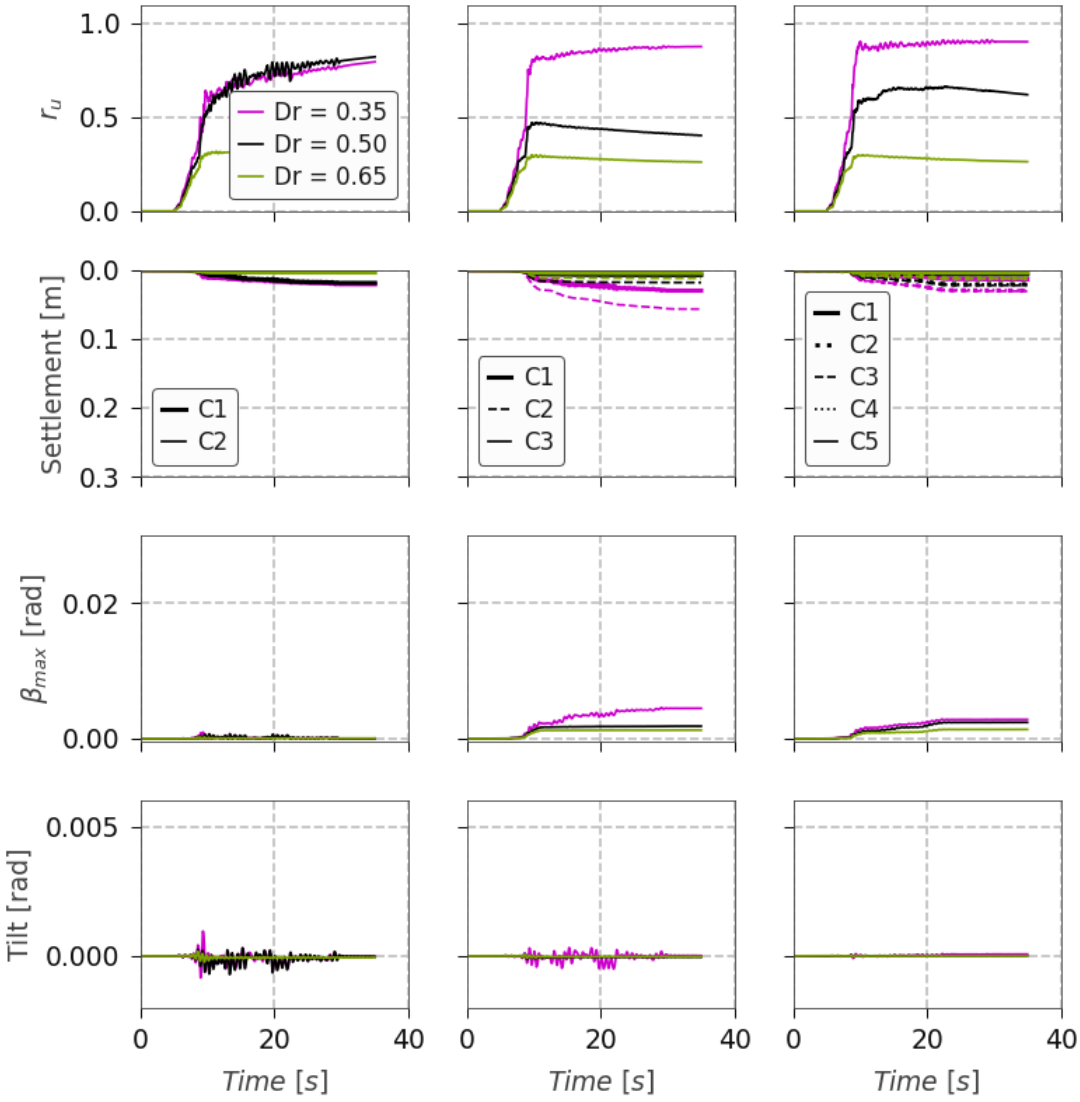


Figure 7.13: Time series for GM3 for D_R variation

Liquefiable layer thickness (H_L)

Figures 7.14 to 7.19 shows the results of the models with varying H_L. When the H_L was increased, settlements also increased, indicating that liquefiable layer with greater thickness generate more settlements. When the Bray and Macedo (2017) approach was used, the settlements also increased when the H_L was increased and notably when the structure with mat foundation was considered , the estimation was very low, while when isolated footings were considered, the values estimated were similar with average PLAXIS 2D settlements, particularly for NF5. Angular distortion and tilt do not appear to be greatly affected by H_L, except for NF2 and GM1 where the model with H_L equal to 4 m provided the greatest tilt.

Figure 7.17 shows the time series derived from the numerical simulations using GM1. The pore pressure ratio is always equal to one, indicating soil liquefaction in all cases. Time series of settlements confirmed that the settlements were higher when H_L was equal to 8 m. Figure 7.18 and Figure 7.19, for GM2 and GM3 respectively, show the same trends for the settlements. Liquefaction did not occur in most the cases when GM3 was applied, liquefaction only occurred when H_L of 8 m and NF5 was simulated.

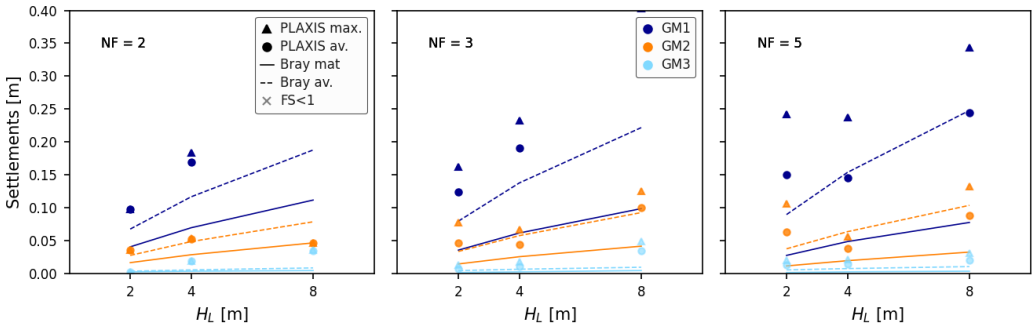


Figure 7.14: Numerical maximum and average settlements compared with Bray and Macedo (2017) approach for H_L variation

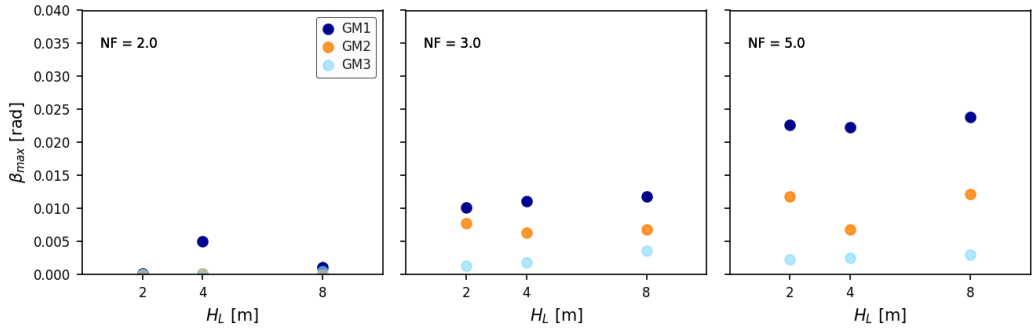


Figure 7.15: Numerical maximum angular distortion for H_L variation

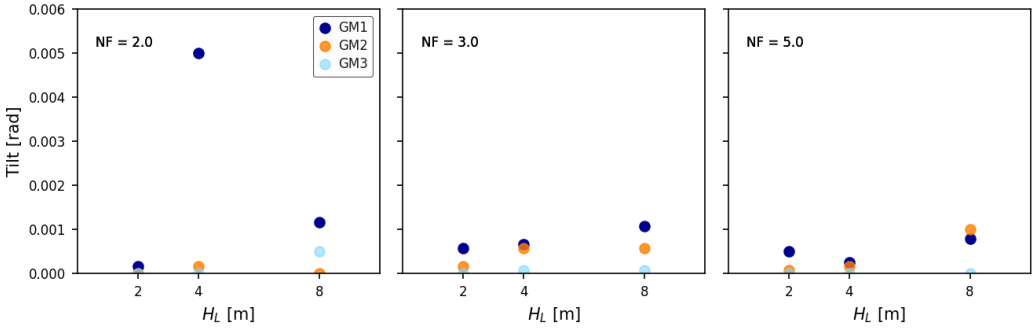


Figure 7.16: Numerical maximum tilt for H_L variation

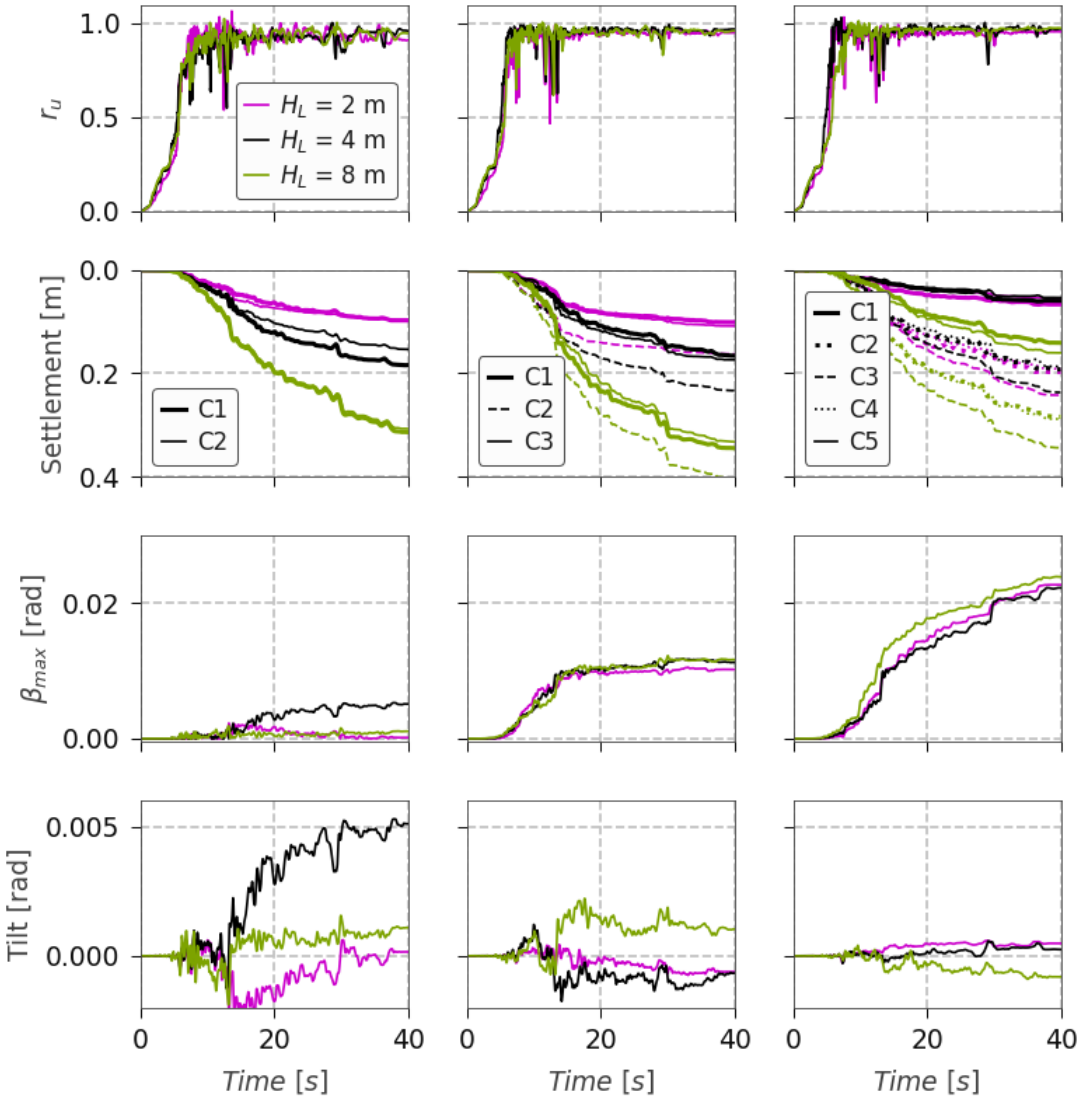


Figure 7.17: Time series for GM1 for H_L variation

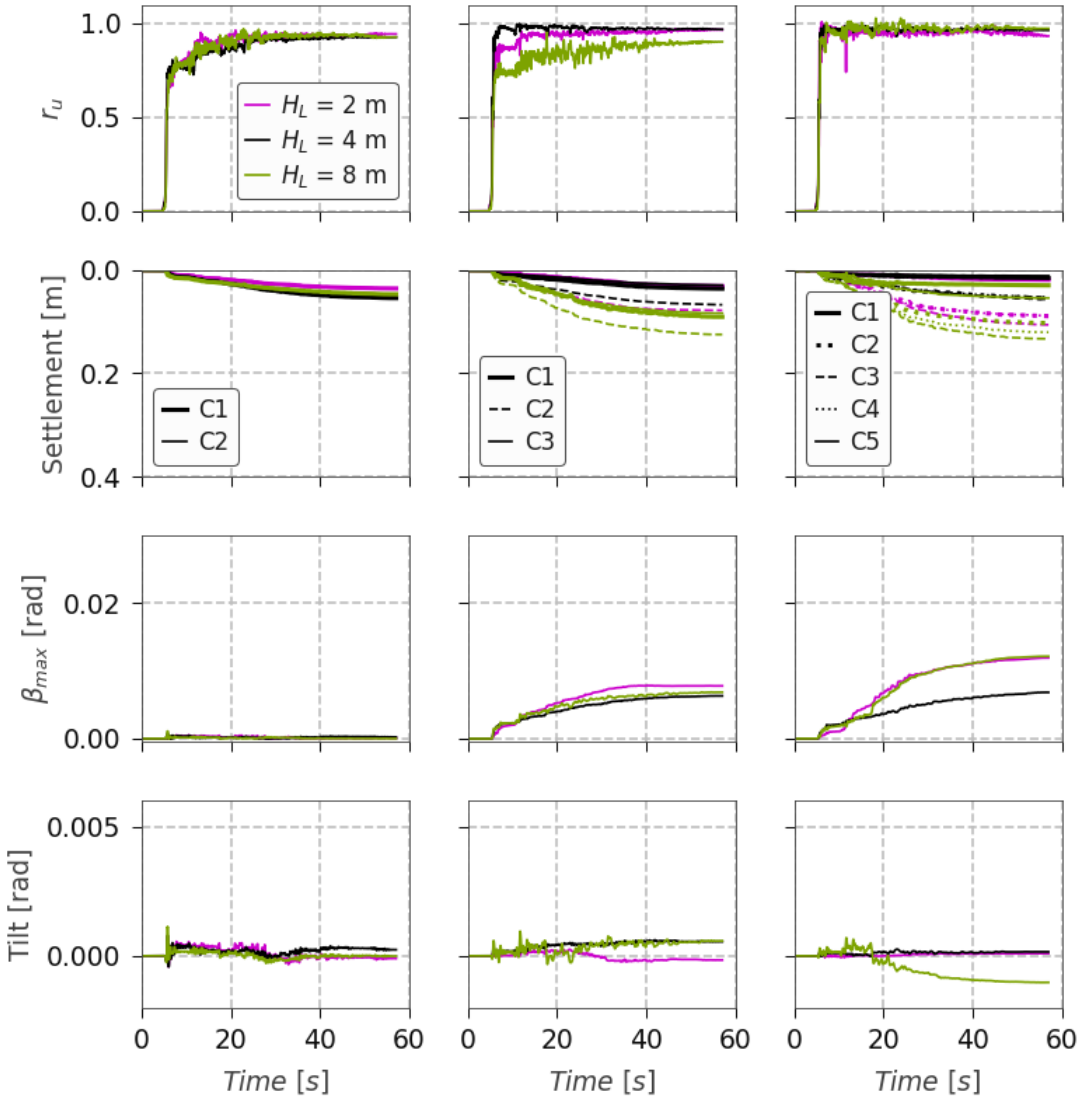


Figure 7.18: Time series for GM2 for H_L variation

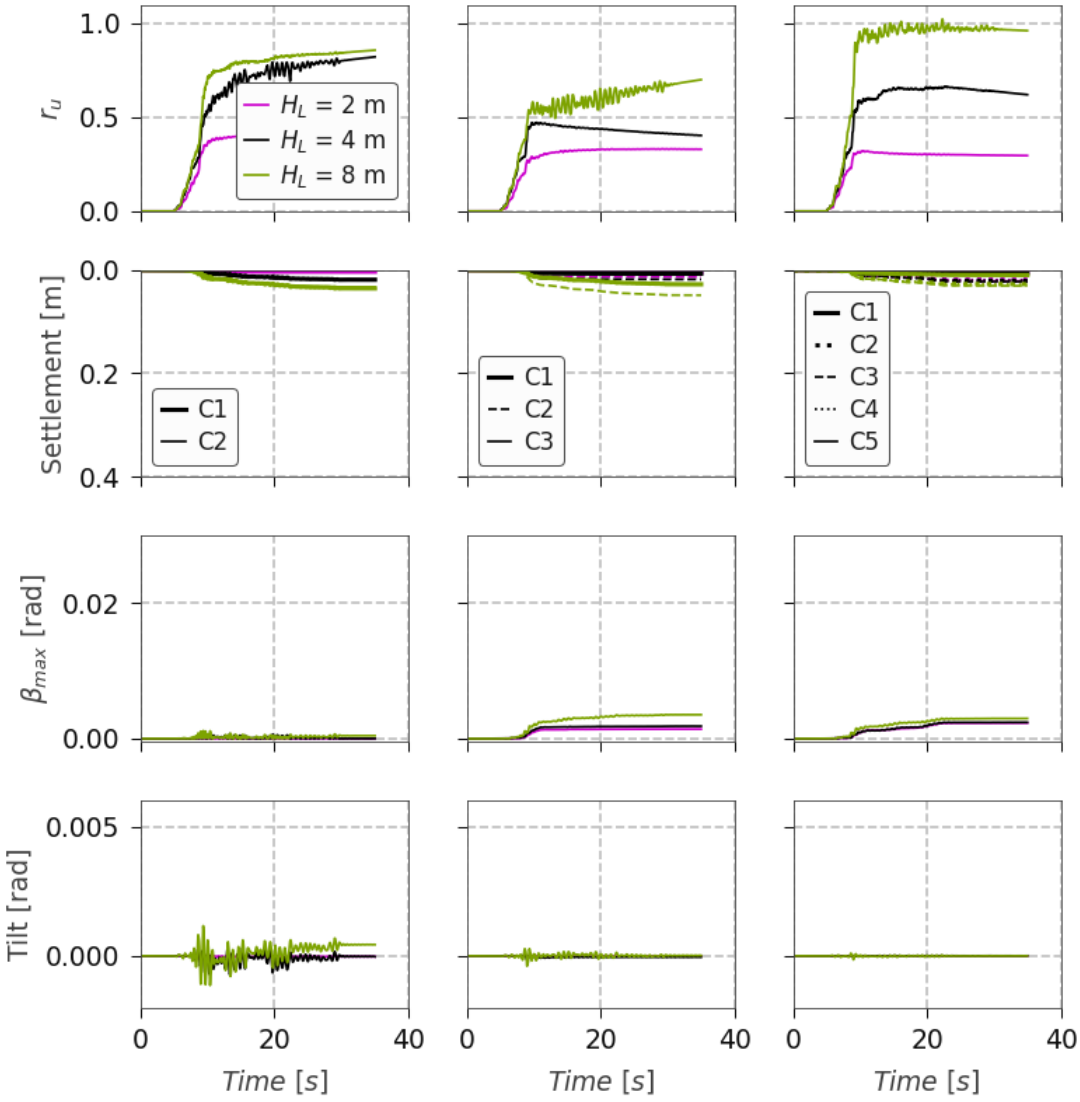


Figure 7.19: Time series for GM3 for H_L variation

7.2.2 Building parameters

The results for the variation of the beam load (w_{top}), footing width (b_{foot}), structure height (H), foundation embedment depth(d_f), bay length (b_{bay}) and EI ratio (EI_{beam}/EI_{column}) are presented in this section.

Beam load (w_{top})

Figures 7.20 to 7.25 shows the results of the models with varying w_{top}. When w_{top} was increased, settlements increased, indicating that the greater footing contact pressure generated the greater settlements. When the Bray and Macedo (2017) approach was used, the settlements also increased. This estimation was particularly good when a building with isolated footings ("Bray av.") was con-

sidered but the settlements were very low when the structure was considered with mat foundation. It is important to highlight that the bearing capacity factors of safety are less than one when w_{top} was equal to 80 kPa, for models NF3 and NF5 using GM1 and GM2, thus the estimation using this approach is not applicable. Angular distortion increased in most of the cases when w_{top} was increased and tilt did not show a clear trend in the results.

Figure 7.23 shows the time series derived from the numerical simulations using GM1. The pore pressure ratio is always equal to one, indicating soil liquefaction in all cases. Time series of settlements confirmed that the settlements were higher when w_{top} was equal to 80 kPa. The settlements of the external footings decreased when the number of footings was increased. The angular distortion also increased when the number of footings was increased and was higher for w_{top} equal to 80 kPa for NF3 and NF5, while it was higher for w_{top} equal to 53 kPa for NF2. The same behavior was observed in tilt time series. Figure 7.24 and Figure 7.25, for GM2 and GM3 respectively, show the same trends for the settlements. Liquefaction did not occur in most the cases when GM3 was applied.

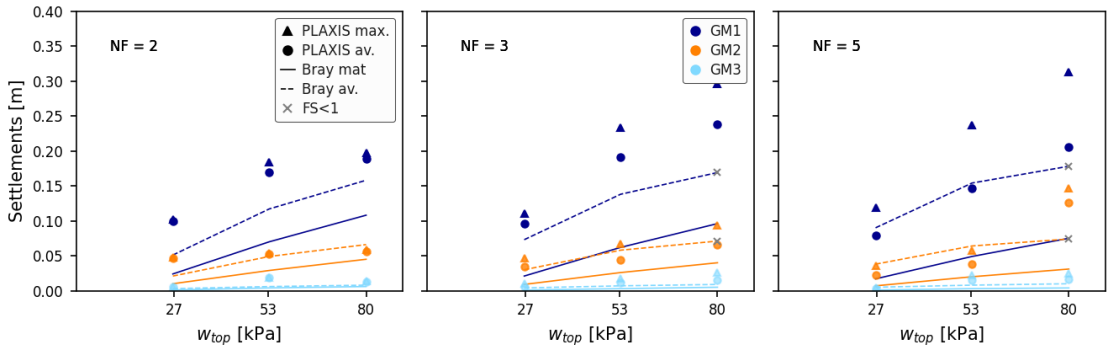


Figure 7.20: Numerical maximum and average settlements compared with Bray and Macedo (2017) approach for w_{top} variation

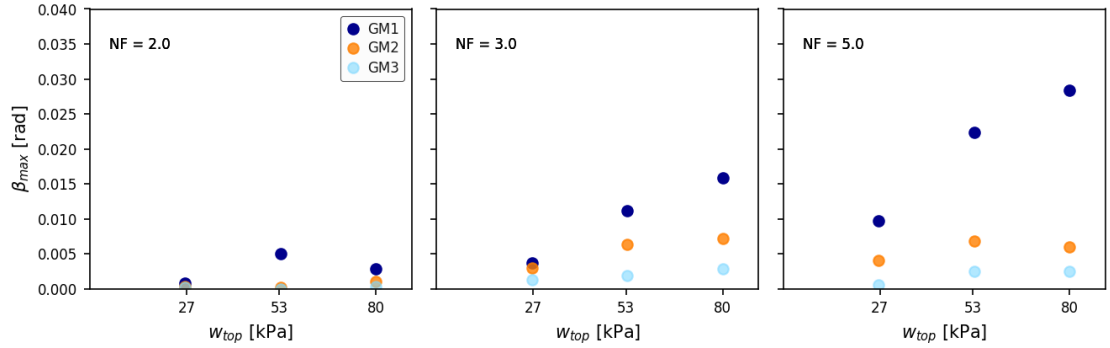


Figure 7.21: Numerical maximum angular distortion for w_{top} variation

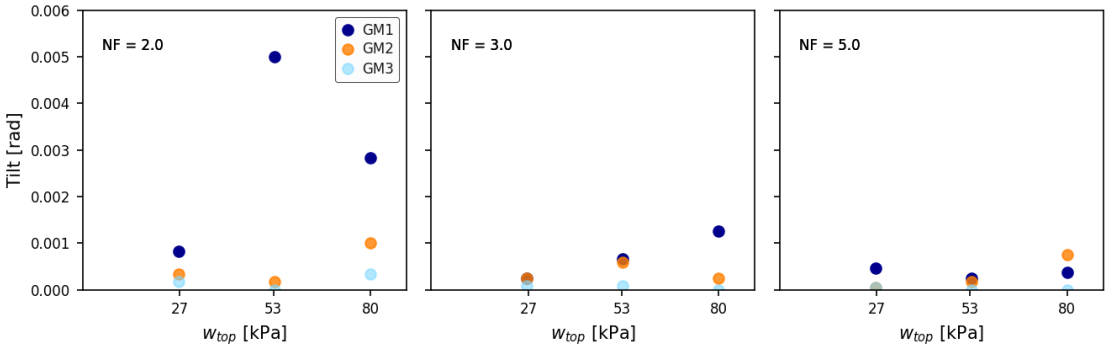


Figure 7.22: Numerical maximum tilt for w_{top} variation

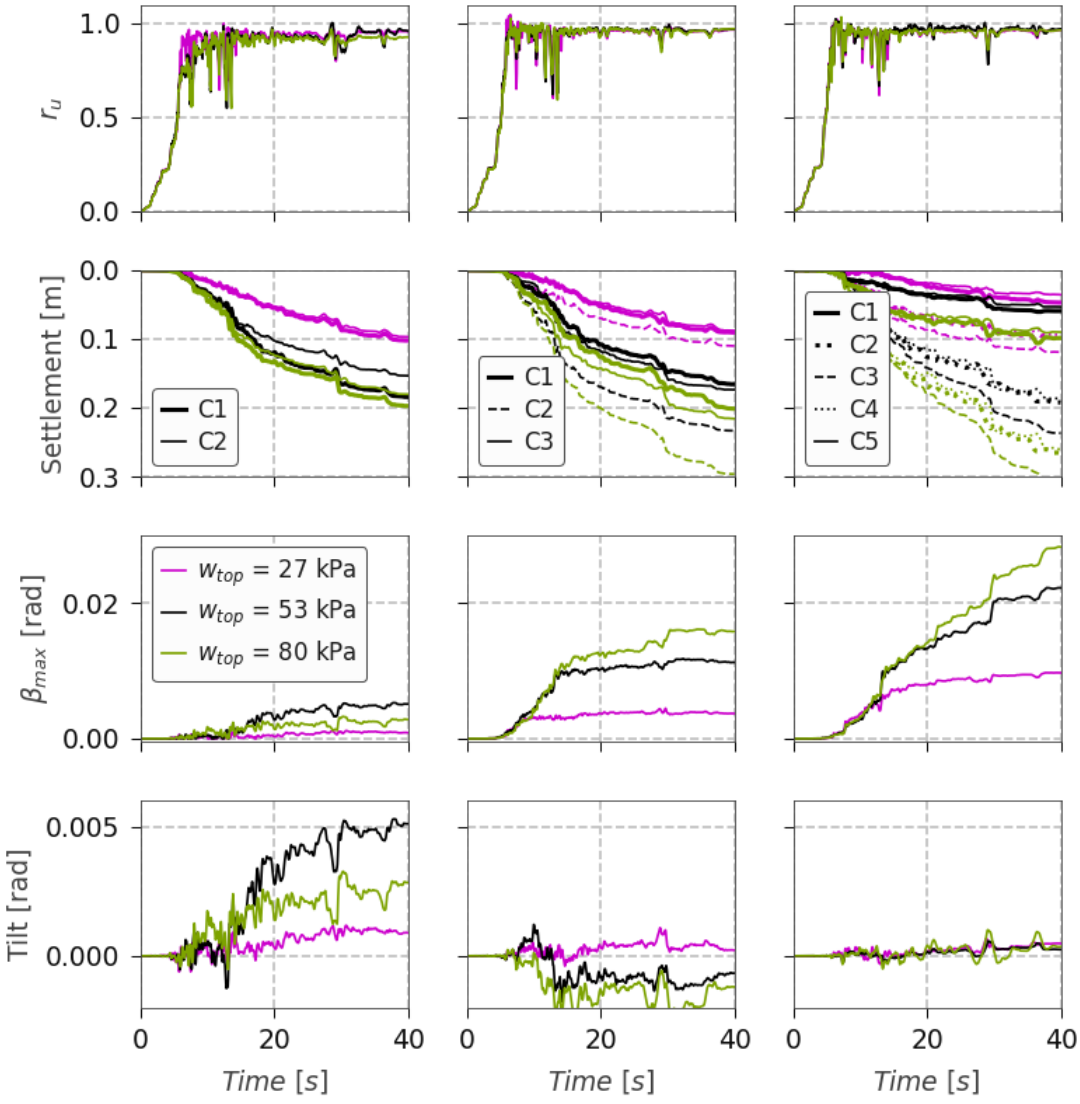


Figure 7.23: Time series for GM1 for w_{top} variation

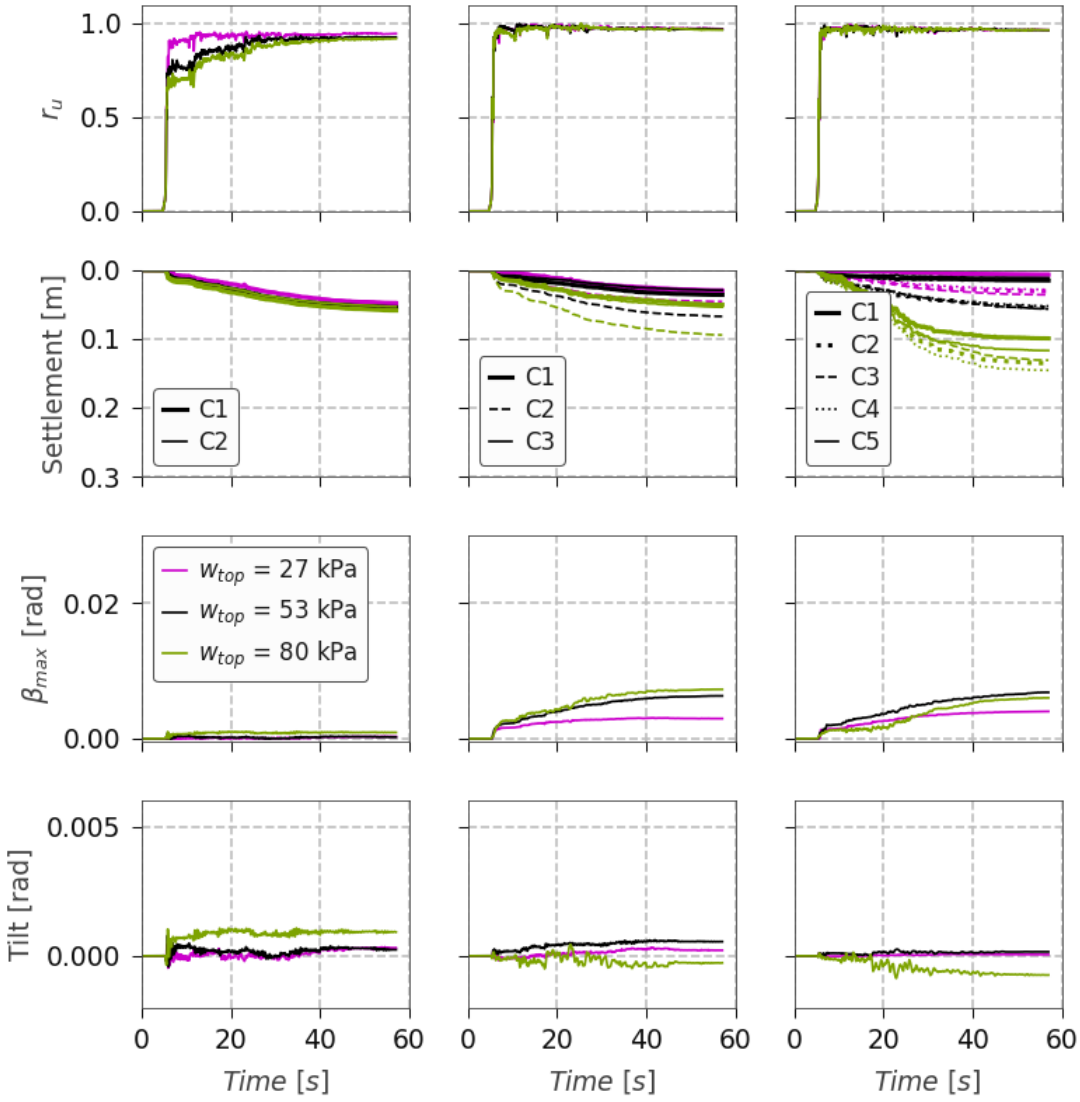


Figure 7.24: Time series for GM2 for w_{top} variation

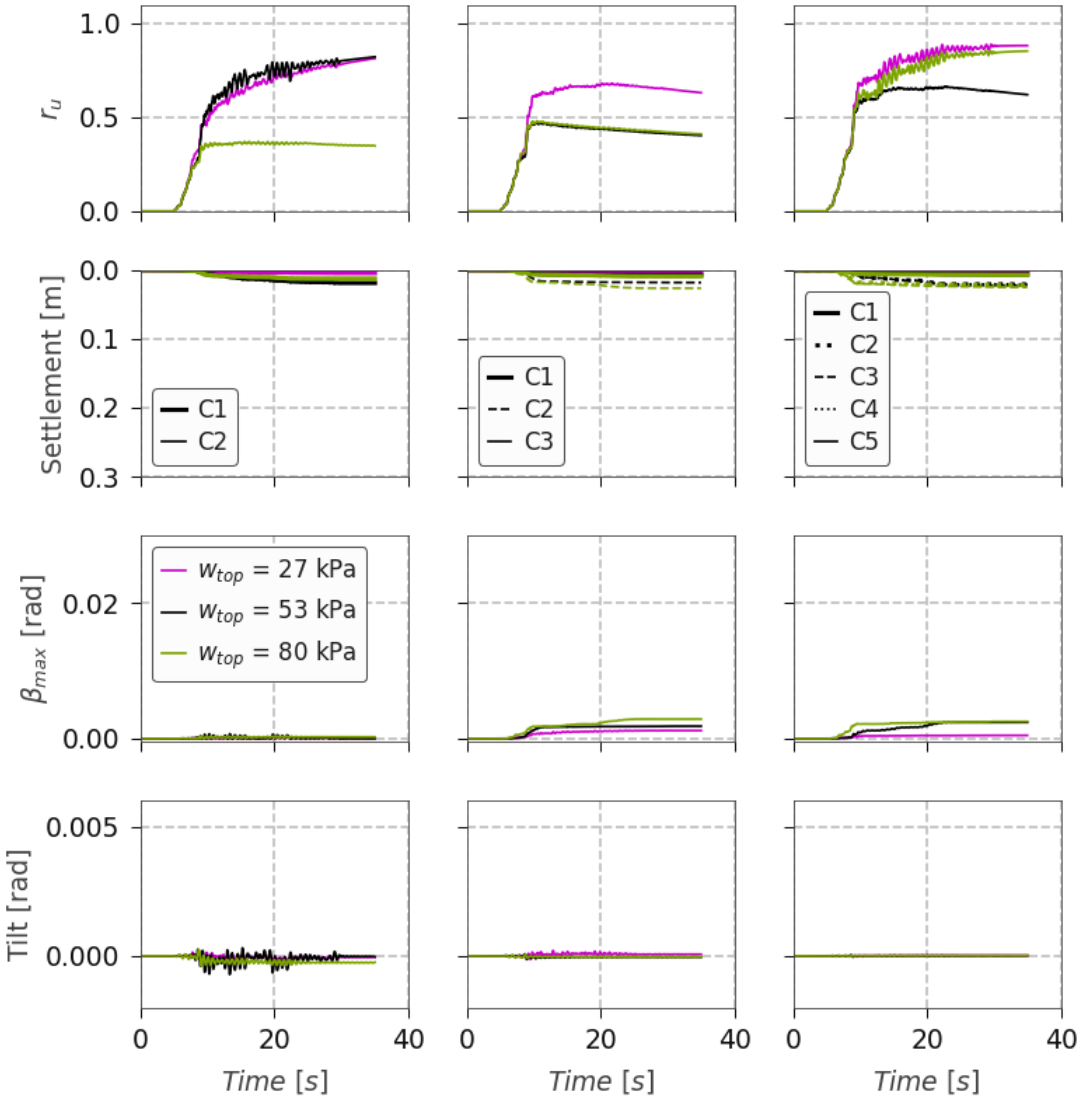


Figure 7.25: Time series for GM3 for w_{top} variation

Footing width (b_{foot})

Figures 7.26 to 7.32 shows the results of the models with varying b_{foot}. When b_{foot} was increased, settlements increased, indicating that a greatest footing contact distance generates more settlements. Normally, in structures with mat foundations, settlements decrease with increasing structure width. However, in this case, an attempt was made to simulate the same contact pressure on the external footings. To achieve this, as shown in Figure 7.29 the beam load on the top of the building had to be increased when the width of the footing was increased, explaining the increase in settlements with increasing footing width. When the Bray and Macedo (2017) approach was used considering a building with isolated footings, the settlements slightly decreased, because the width in this approach has little effect on the settlement (see section 2.3.3). On the other hand, when a mat foundation was considered, the settlements increased when the b_{foot} was increased, because the total width of the structure did not change and the contact pressure was increased. Even though there was a tendency to increase, the values were much lower than those found in the numerical models. Angular distortion increased and tilt decreased in most of the cases when b_{foot} was increased.

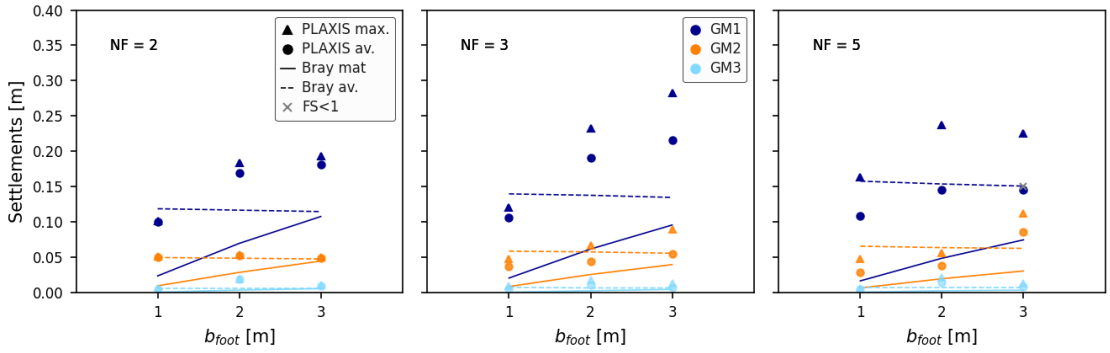


Figure 7.26: Numerical maximum and average settlements compared with Bray and Macedo (2017) approach for b_{foot} variation

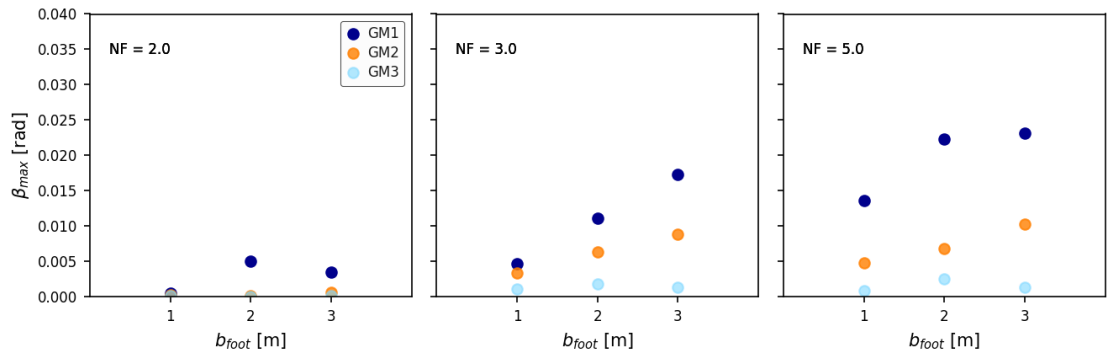


Figure 7.27: Numerical maximum angular distortion for b_{foot} variation

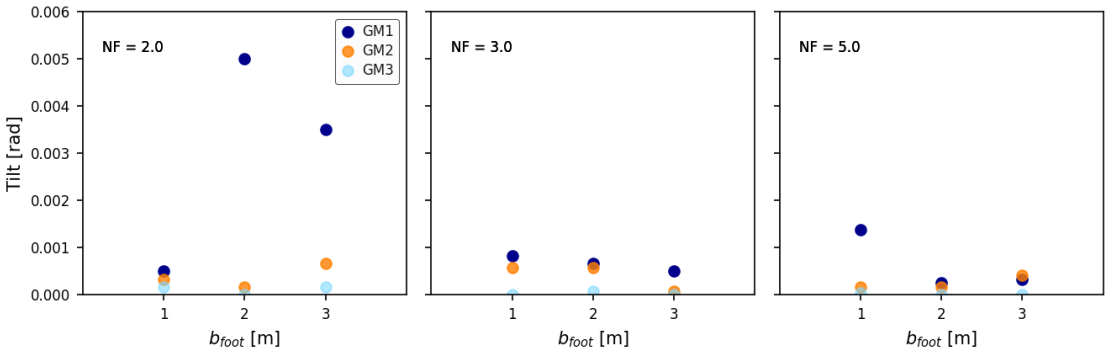


Figure 7.28: Numerical maximum tilt for b_{foot} variation

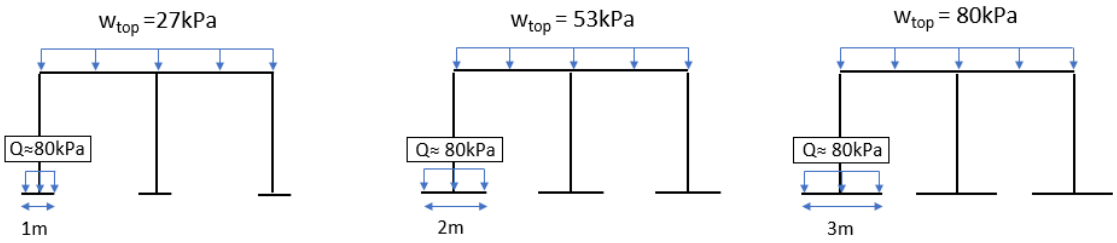


Figure 7.29: Beam load w_{top} for models with different b_{foot}

Figure 7.30 shows the time series derived from the numerical simulations using GM1. The pore pressure ratio is always equal to one, indicating soil liquefaction in all cases. Time series of settlements confirmed that the settlements were higher when b_{foot} was equal to 3 m. The settlements of the external footings decreased when the number of footings was increased and for NF5 the settlement values were very similar. The angular distortion also increased when the number of footings was increased and was higher for b_{foot} equal to 2 m and 3 m, with very similar values. The same behavior was observed in tilt for NF2 while the tilt was higher for b_{foot} equal to 1 m for NF3 and NF5. Figure 7.31 and Figure 7.32, for GM2 and GM3 respectively, show the same trends for the settlements. When GM3 was applied, partial liquefaction occurred in NF2 for b_{foot} equal to 1 m and 2 m and in NF5 for b_{foot} equal to 1 m and 3 m.

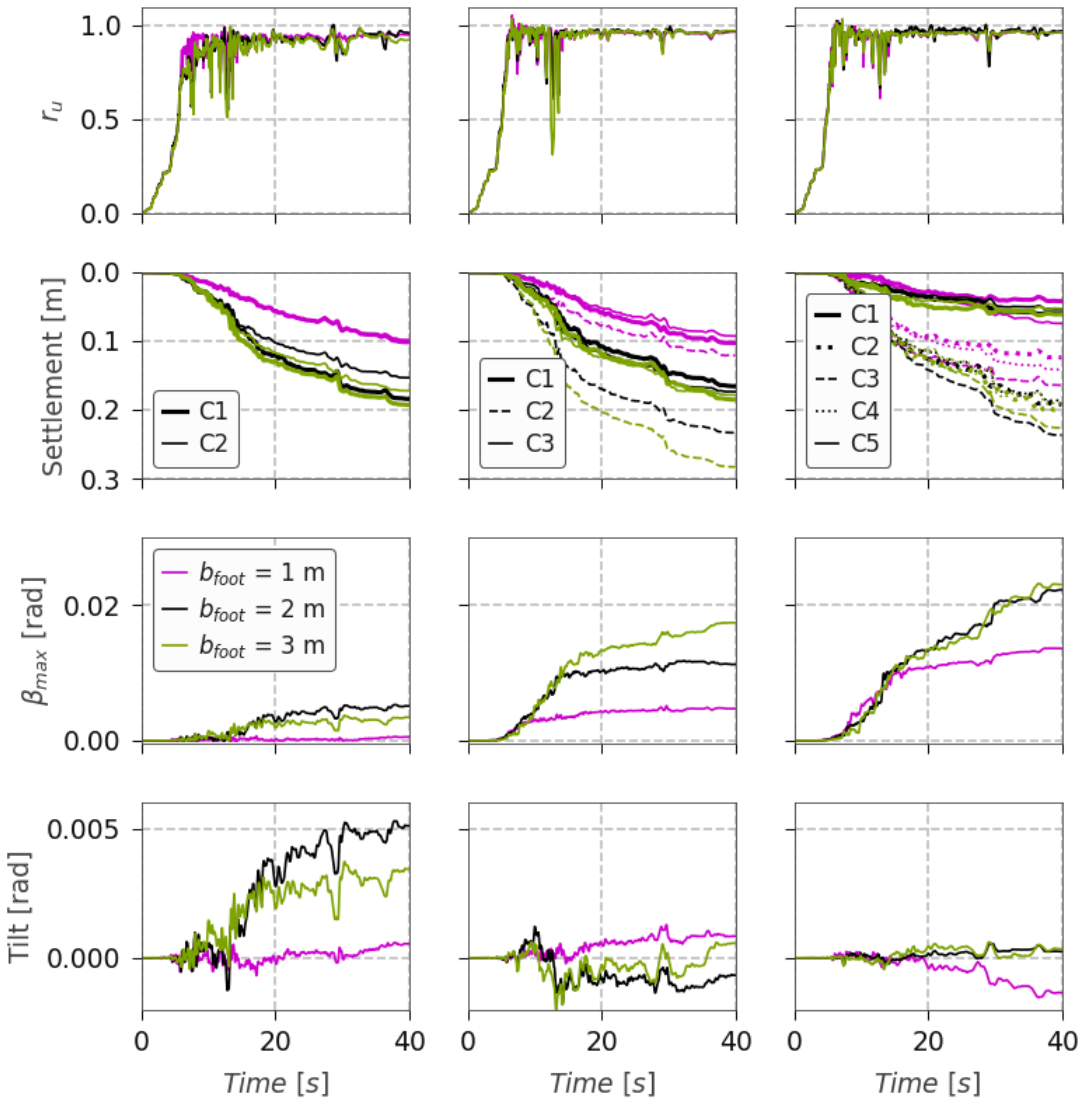


Figure 7.30: Time series for GM1 for b_{foot} variation

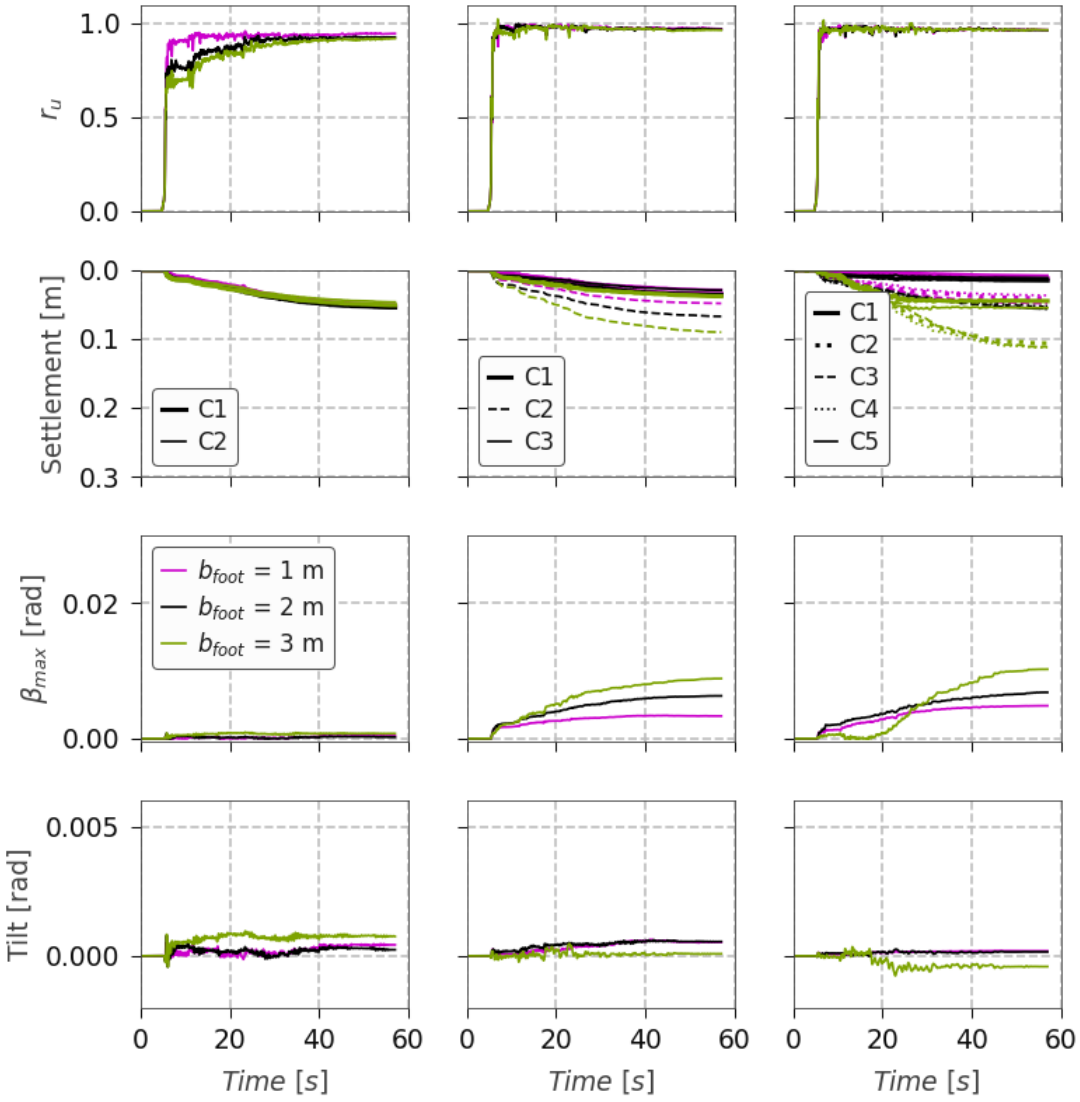


Figure 7.31: Time series for GM2 for b_{foot} variation

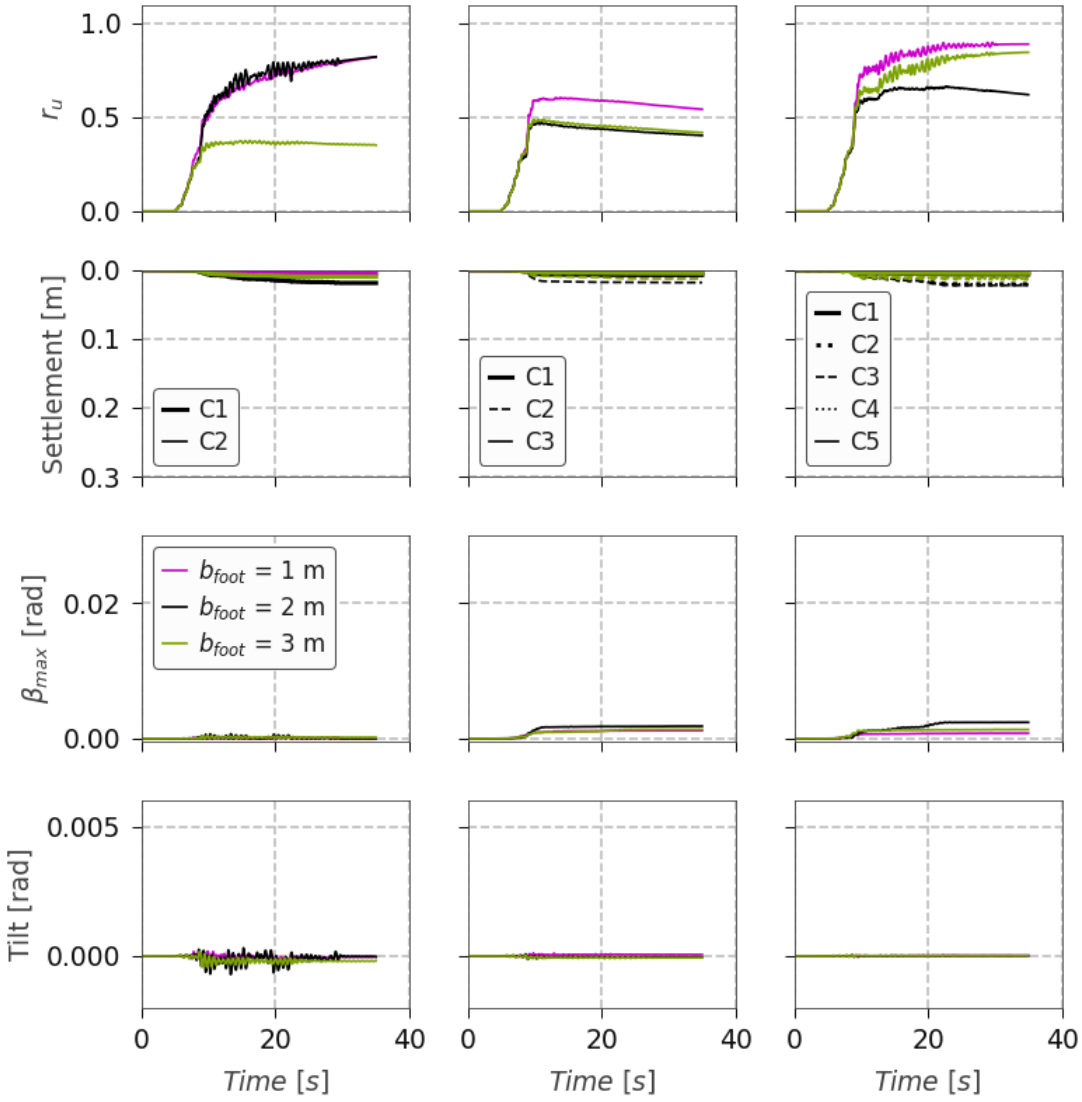


Figure 7.32: Time series for GM3 for b_{foot} variation

Structure height (H)

Figures 7.33 to 7.38 shows the results of the models with varying H. When H was increased, the settlements remained almost the same, indicating that the structure height did not greatly affect settlements. When the Bray and Macedo (2017) approach was used settlements remained also the same because this approach does not take into account the height of the structure. When a building with isolated footings was considered, the estimated settlements were similar with numerical results, particularly for NF5. On the other hand, when a mat foundation was considered, the estimated settlements were much lower than those found in the numerical models. Angular distortion and tilt decreased in most the cases when H was increased.

Figure 7.36 shows the time series derived from the numerical simulations using GM1. The pore pressure ratio is always equal to one, indicating soil liquefaction in all cases. The time series of settlements confirmed that the maximum settlements remained almost the same across different structure heights. Similarly, the settlements using different numbers of footings also remained nearly constant or slightly increased. The settlements of the external footings decreased when the number of footings was increased and the settlement values in this footings were very similar. The angular distortion increased when the number of footings was increased and was higher for H equal to 3 m. The til decreased when the number of footings was increased. Figure 7.37 and Figure 7.38, for GM2 and GM3 respectively, show the same trends for the settlements. When GM3 was applied, partial liquefaction occurred in NF2 for H equal to 3 m and 6 m and in NF5 for H equal to 3 m and 12 m.

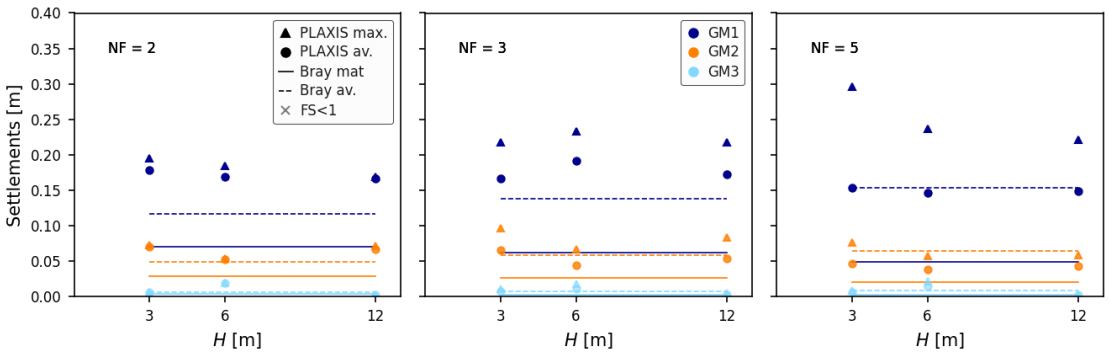


Figure 7.33: Numerical maximum and average settlements compared with Bray and Macedo (2017) approach for H variation

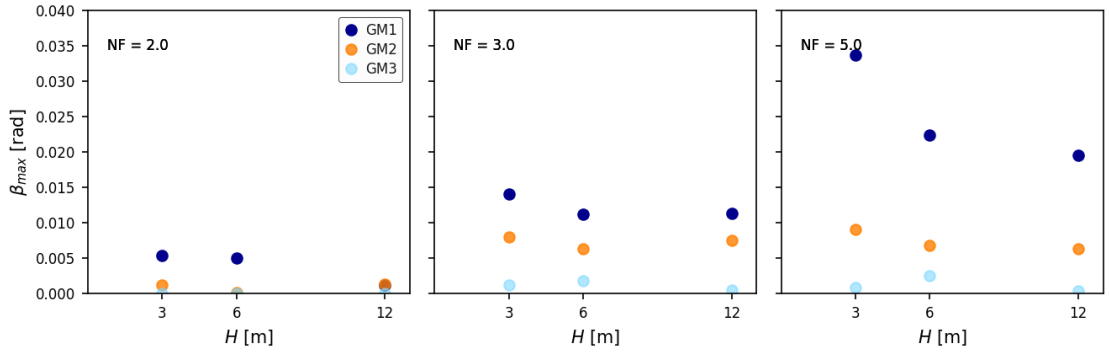


Figure 7.34: Numerical maximum angular distortion for H variation

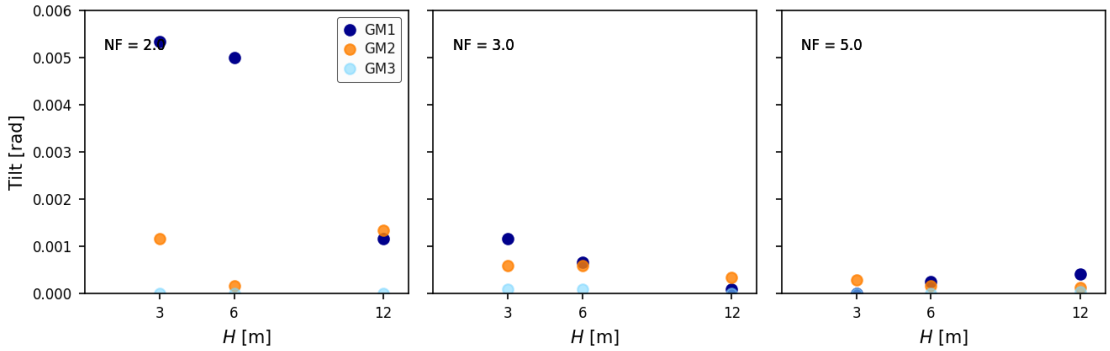


Figure 7.35: Numerical maximum tilt for H variation

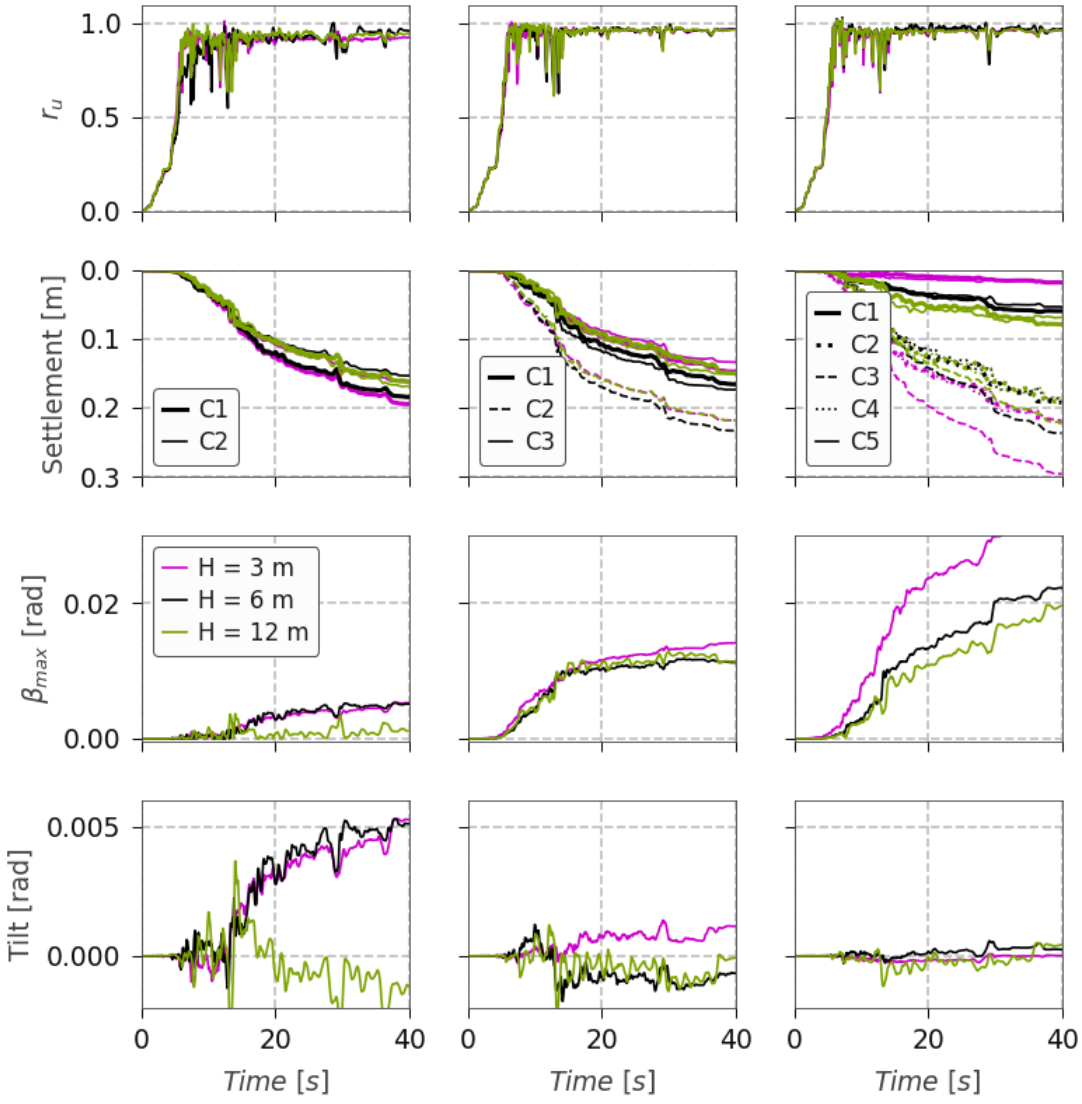


Figure 7.36: Time series for GM1 for H variation

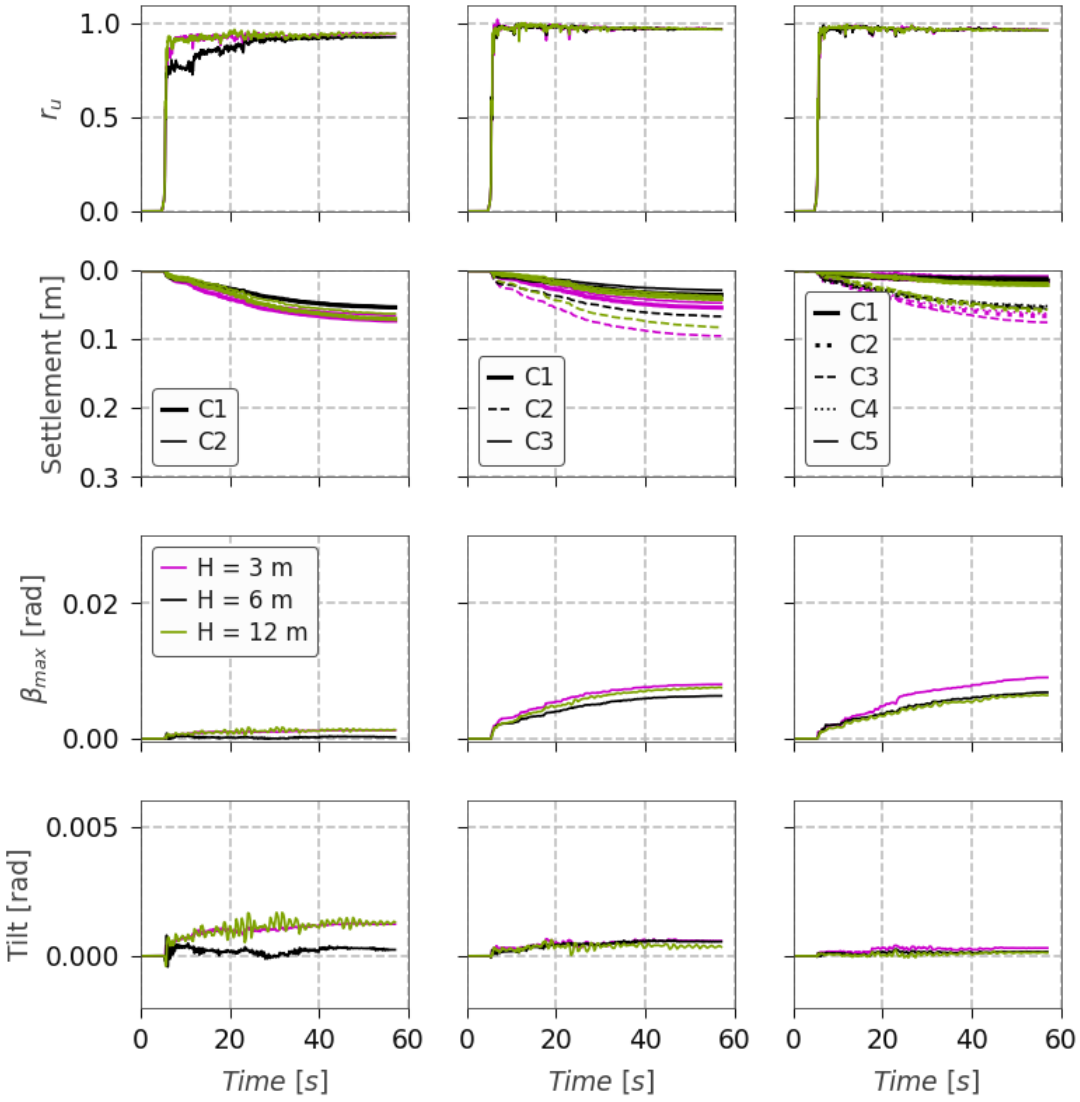


Figure 7.37: Time series for GM 2for H variation

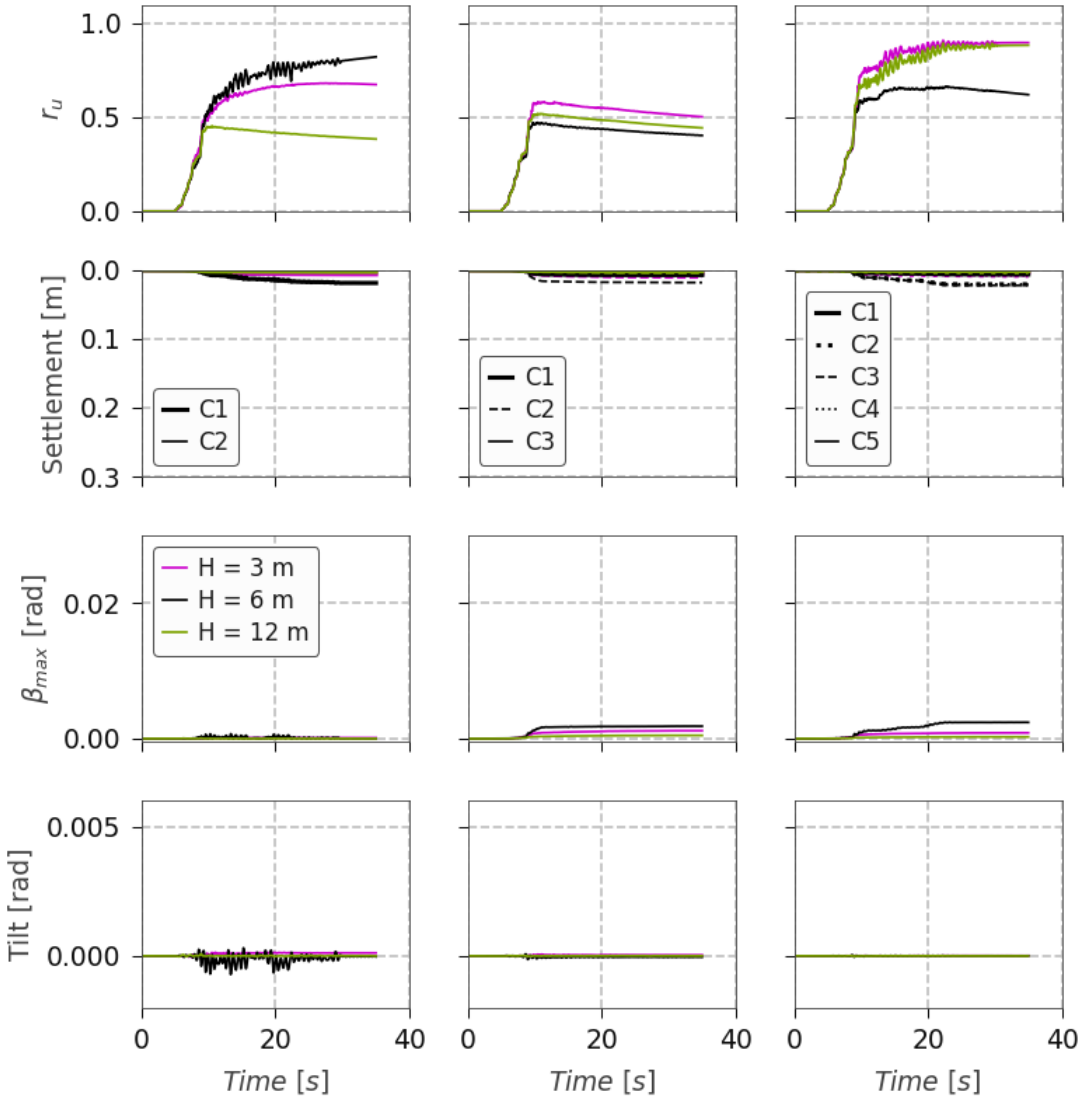


Figure 7.38: Time series for GM3 for H variation

Foundation embedment depth(d_f)

Figures 7.39 to 7.44 shows the results of the models with varying d_f. When d_f was increased, the settlements remained almost the same, less constant for NF5, indicating that the foundation embedment depth did not greatly affect settlements. When the Bray and Macedo (2017) approach was used settlements remained also the same because this approach does not take into account the foundation embedment depth. When a building with isolated footings was considered, the estimated settlements were similar with numerical results, particularly for NF5. On the other hand, when a mat foundation was considered, the estimated settlements were much lower than those found in the numerical models. It is important to highlight that the bearing capacity factors of safety are less than one when d_f was equal to 2 m for GM1 and GM2, thus the estimation using

this approach is not applicable. Angular distortion and tilt increased in most the cases when d_f was increased.

Figure 7.42 shows the time series derived from the numerical simulations using GM1. The pore pressure ratio is always equal to one, indicating soil liquefaction in all cases. The time series of settlements confirmed that the maximum settlements remained almost the same across different structure heights, less for NF5. Particularly, NF2 and NF3 showed very similar settlements for both external footings and internal footings.The settlements slightly increased when the number of footings was increased. The angular distortion increased when the number of footings was increased and was higher for d_f equal to 2 m. The tilt decreased when the number of footings was increased and was higher for d_f equal to 1 m and 2 m. Figure 7.43 and Figure 7.44, for GM2 and GM3 respectively, show the same trends for the settlements. When GM3 was applied, partial liquefaction occurred in NF2 for d_f equal to 1 m and in NF5 for d_f equal to 0.5 m and 2 m.

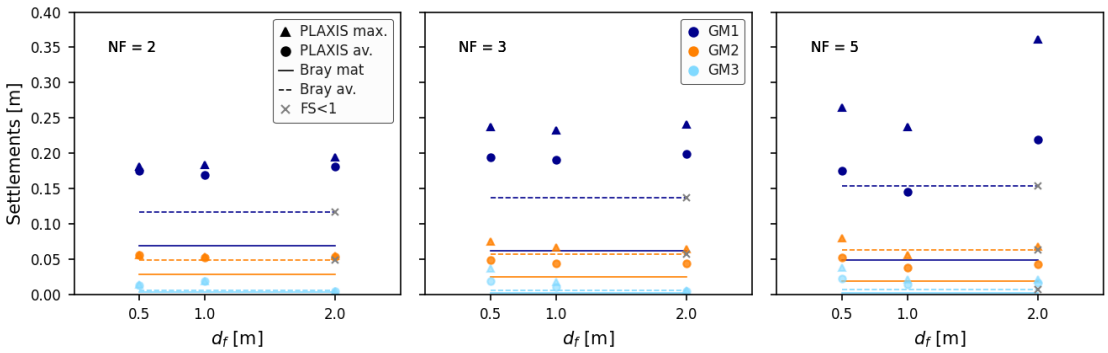


Figure 7.39: Numerical maximum and average settlements compared with Bray and Macedo (2017) approach for d_f variation

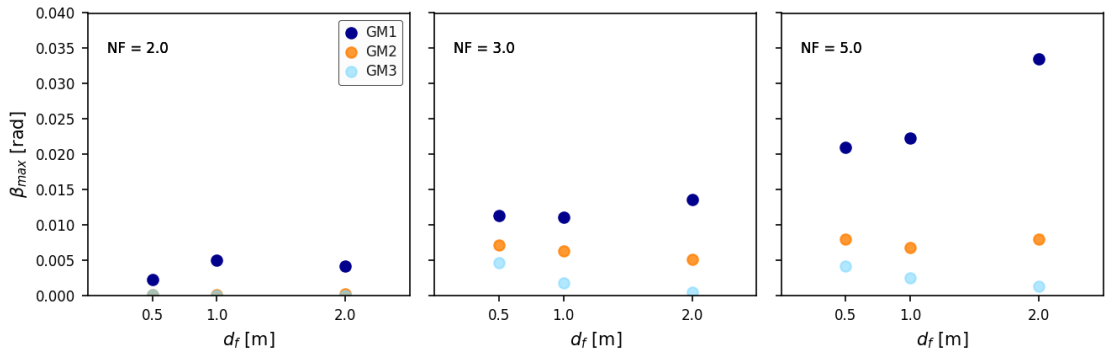


Figure 7.40: Numerical maximum angular distortion for d_f variation

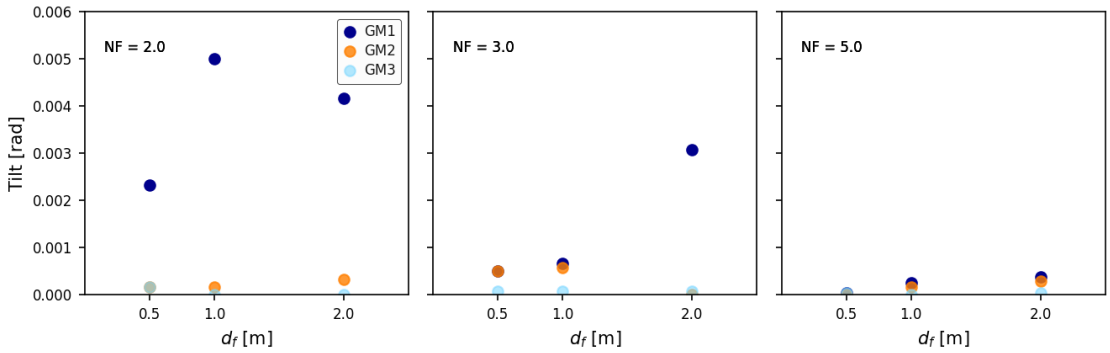


Figure 7.41: Numerical maximum tilt for d_f variation

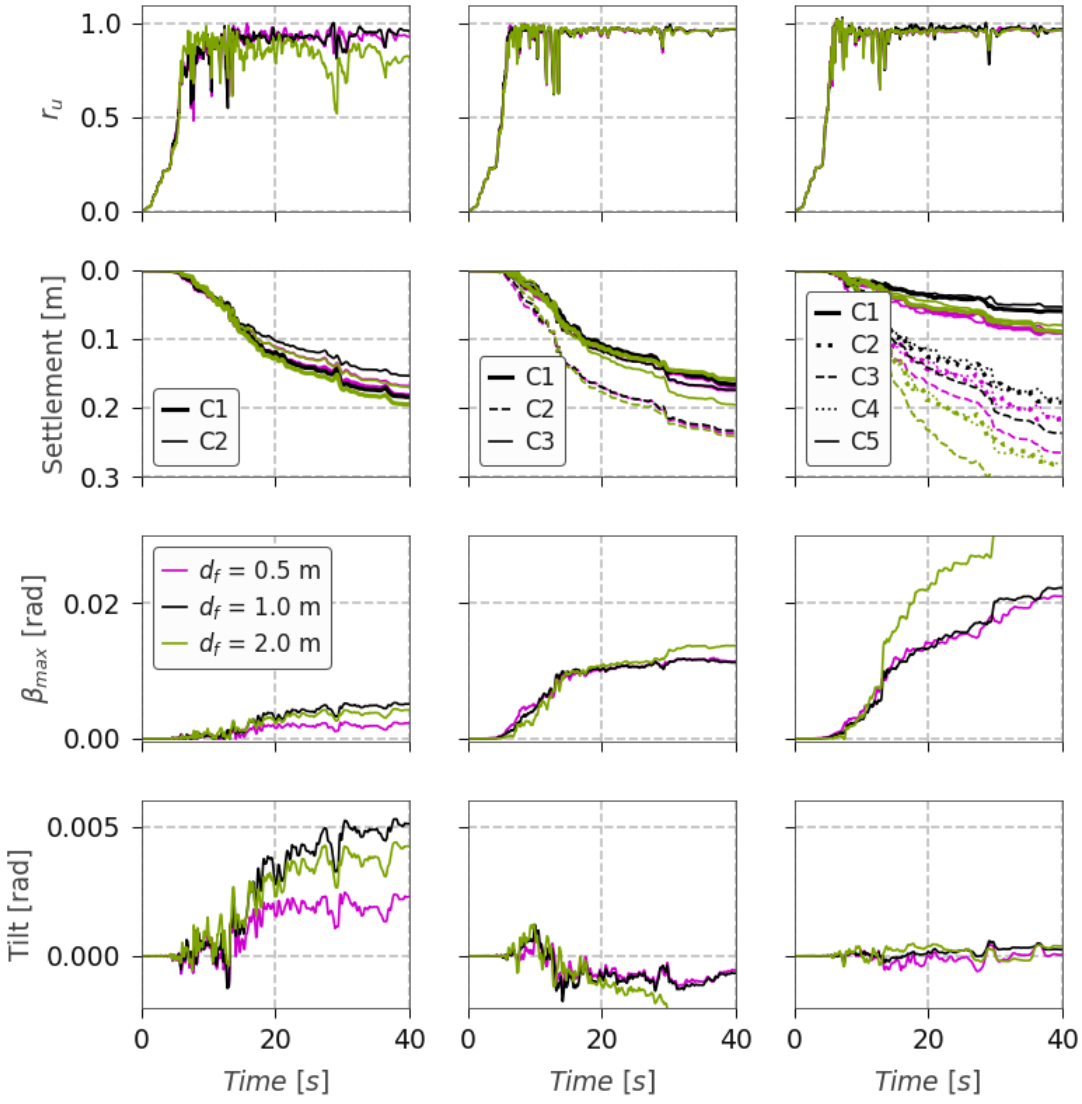


Figure 7.42: Time series for GM1 for d_f variation

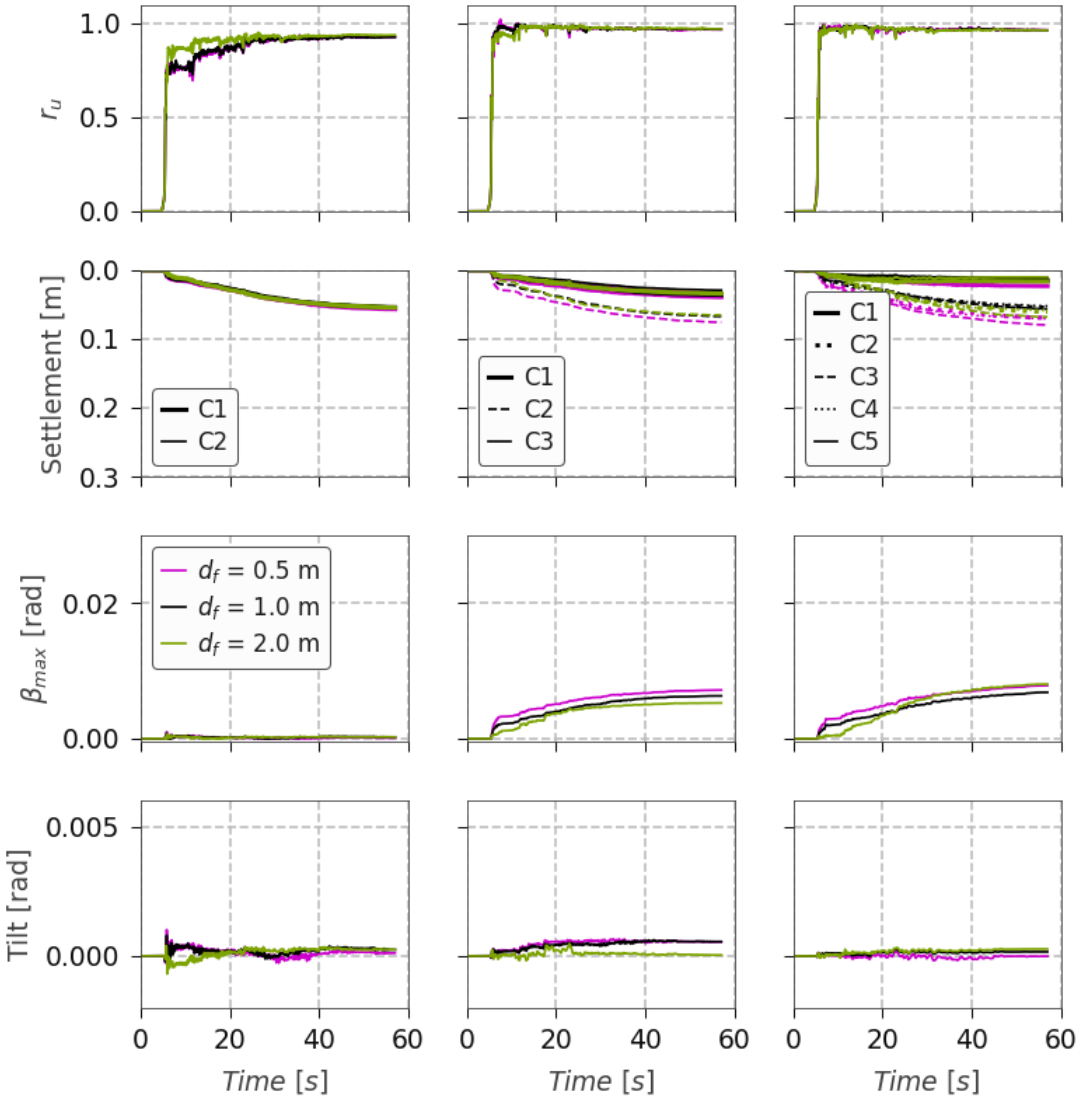


Figure 7.43: Time series for GM2 for d_f variation

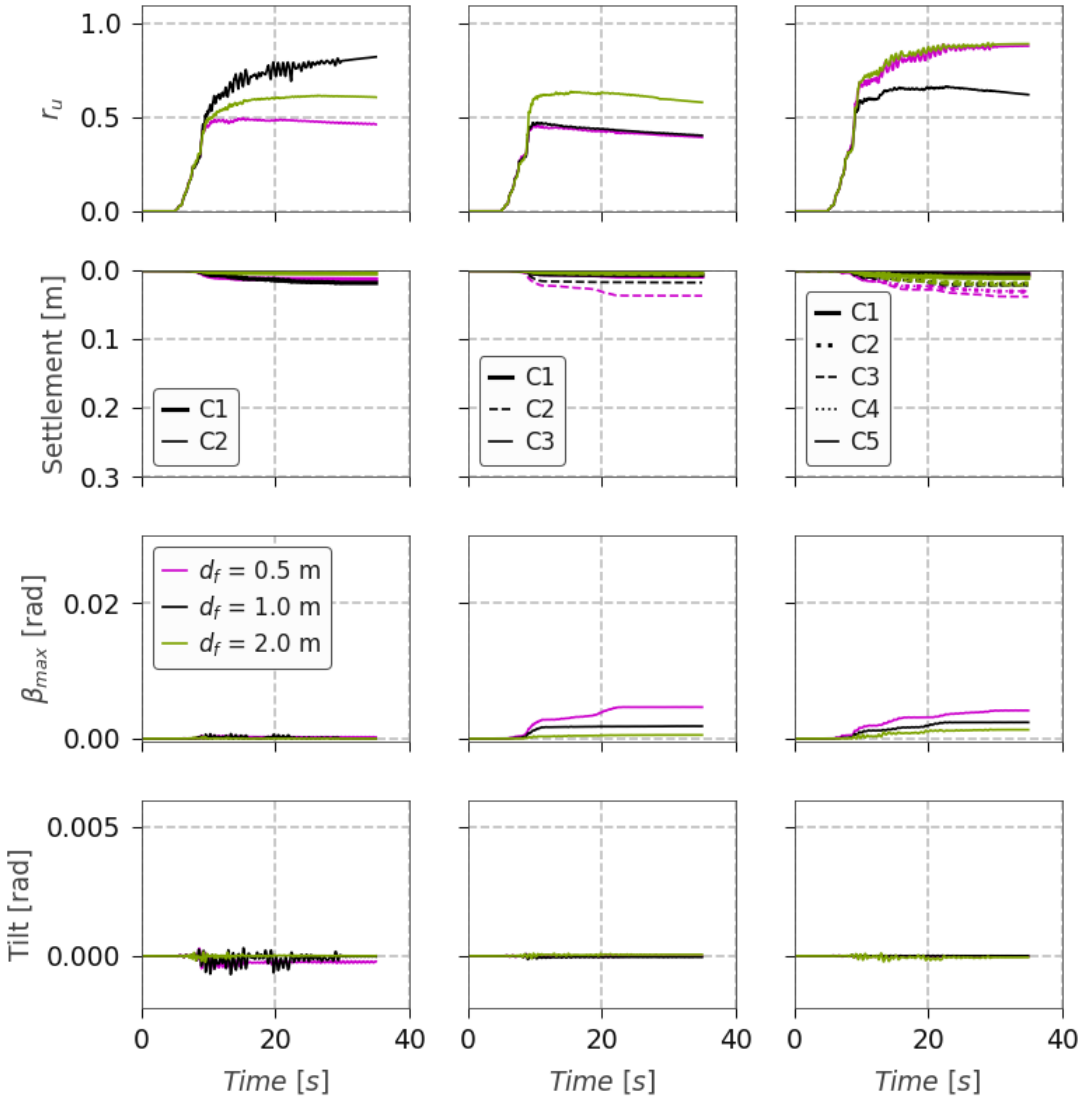


Figure 7.44: Time series for GM3 for d_f variation

Bay length (b_{bay})

Figures 7.45 to 7.51 shows the results of the models with varying b_{bay}. When b_{bay} was increased to 6 m, settlements decreased, while that when b_{bay} was increased more to 12 m, settlements remained almost the same in most cases. This indicates that equally as in structures with mat foundations, a greatest bay length generates less settlements. When the Bray and Macedo (2017) approach was used considering a building with isolated footings, the settlements remained the same, because the width and contact pressure of the footings are the same in all the cases. On the other hand, when a mat foundation was considered, the settlements decreased as b_{bay} was increased, because the beam load on top of the structure had to be decreased with the increasing bay length to achieve the same external footings contact pressure as shown in Figure 7.48. Even though there was a tendency to decrease, the values were much lower than those found in the numerical models. Angular distortion did not show a clear trend in the results and tilt decreased in most the cases when b_{bay} was increased.

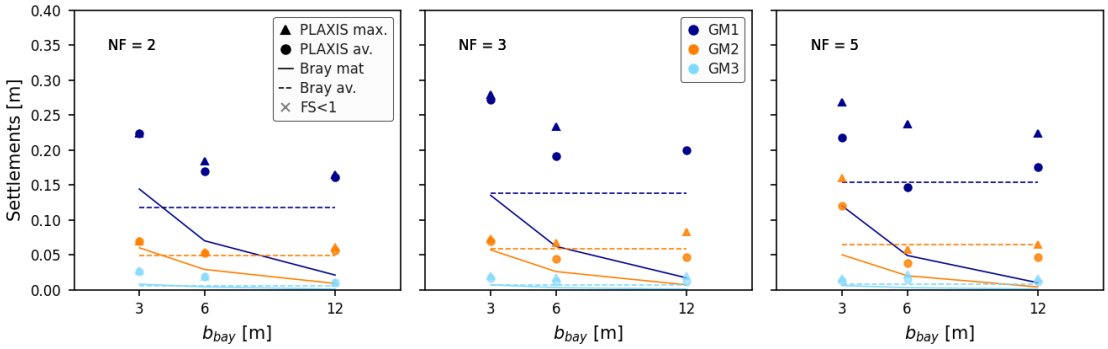


Figure 7.45: Numerical maximum and average settlements compared with Bray and Macedo (2017) approach for b_{bay} variation

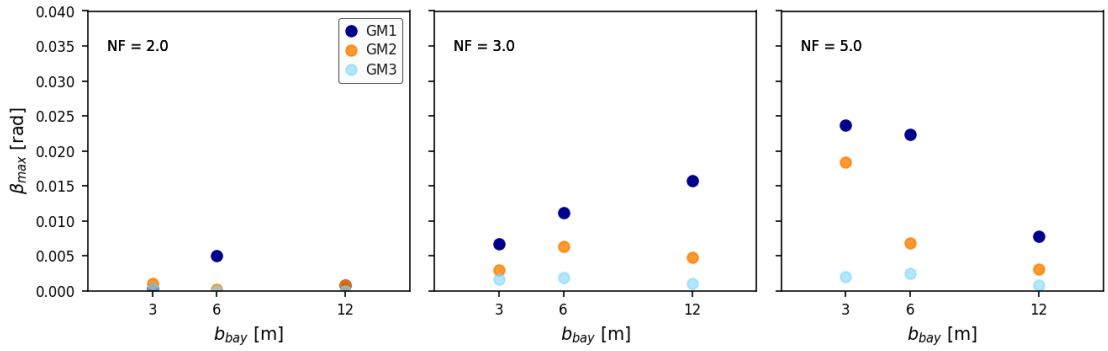


Figure 7.46: Numerical maximum angular distortion for b_{bay} variation

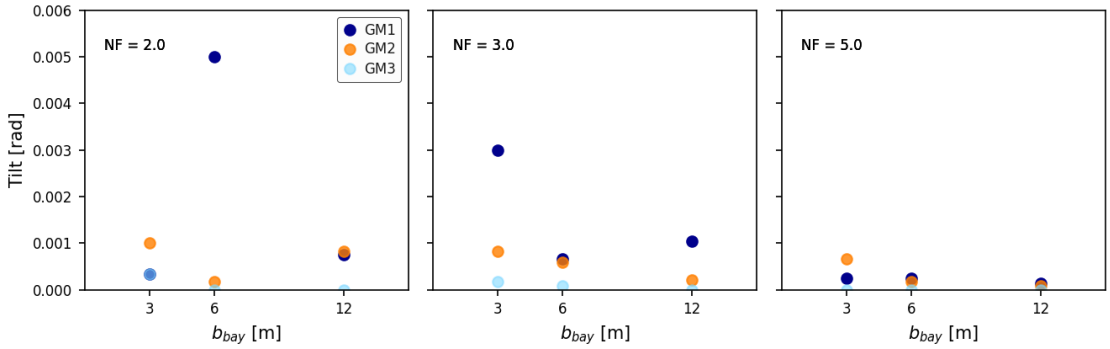


Figure 7.47: Numerical maximum tilt for b_{bay} variation

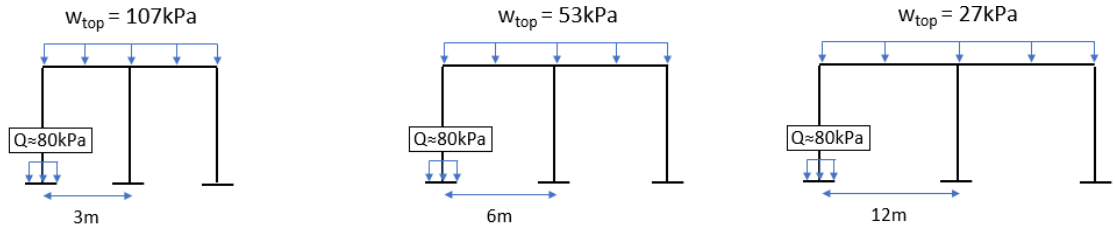


Figure 7.48: Beam load w_{top} for models with different b_{bay}

Figure 7.49 shows the time series derived from the numerical simulations using GM1. The pore pressure ratio is always equal to one, indicating soil liquefaction in all cases. Time series of settlements confirmed that the settlements were higher when b_{bay} was equal to 3 m. The angular distortion increased when the number of footings was increased and was higher for b_{bay} equal to 6 m for NF2, for b_{bay} equal to 12 m for NF3 and for b_{bay} equal to 3 m for NF5. In other words, an unclear trend was observed. On the other hand, the tilt decreased when the number of footings was increased. Figure 7.50 and Figure 7.51, for GM2 and GM3 respectively, show the same trends for the settlements. When GM3 was applied, partial liquefaction occurred in NF2 for b_{bay} equal to 3 m and 6 m and in NF3 and NF5 for b_{bay} equal to 12 m.

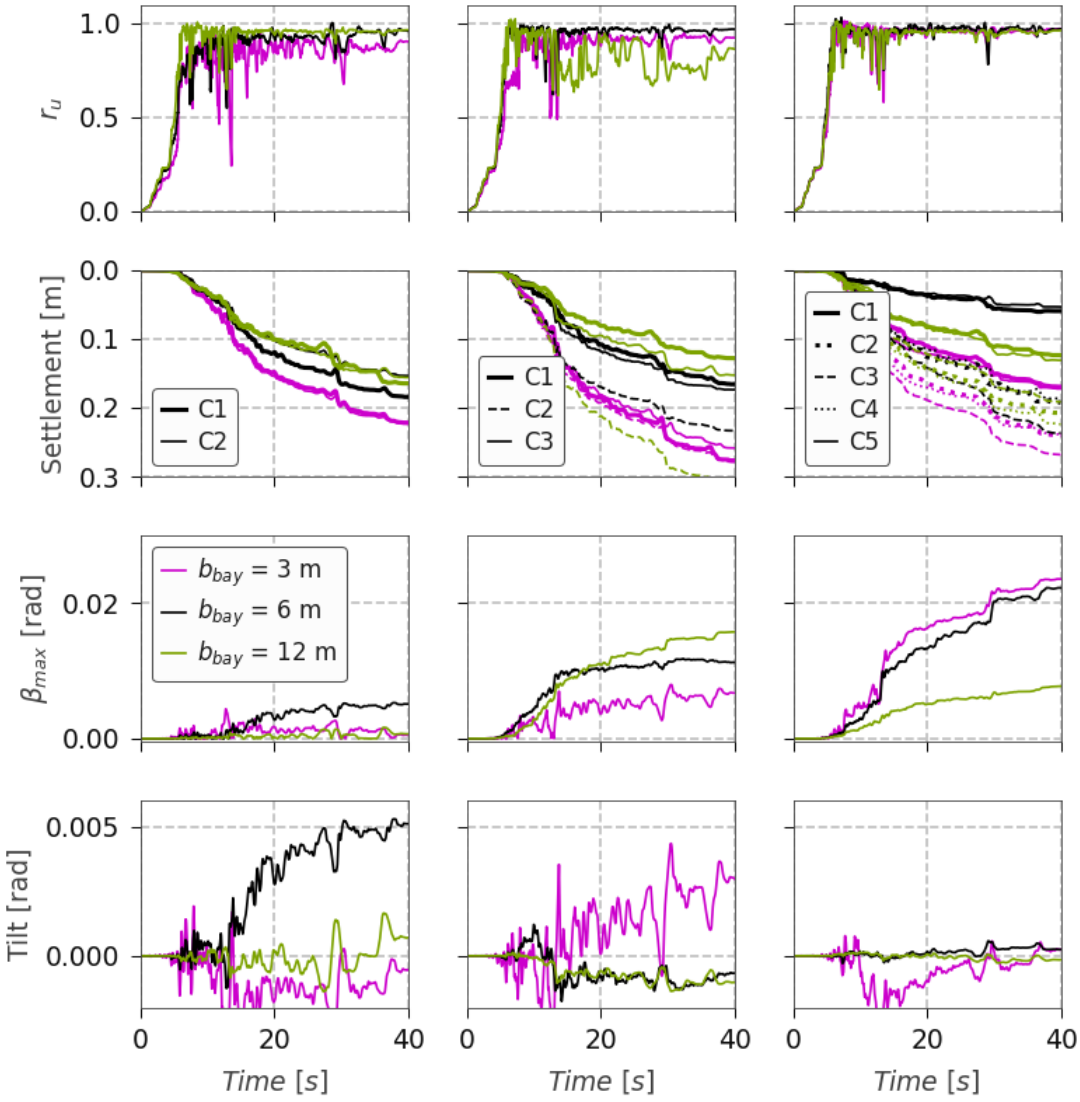


Figure 7.49: Time series for GM1 for b_{bay} variation

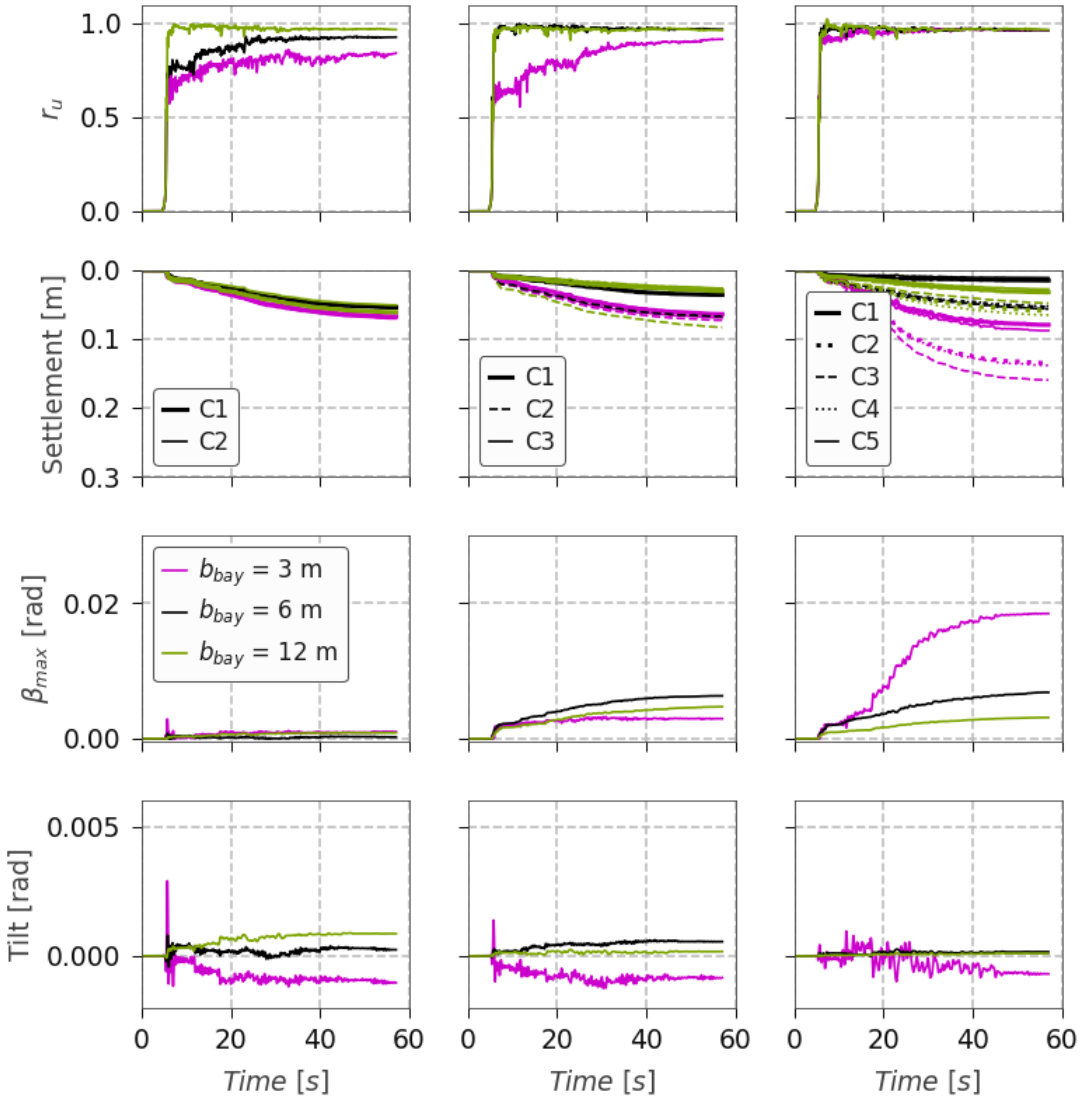


Figure 7.50: Time series for GM2 for b_{bay} variation

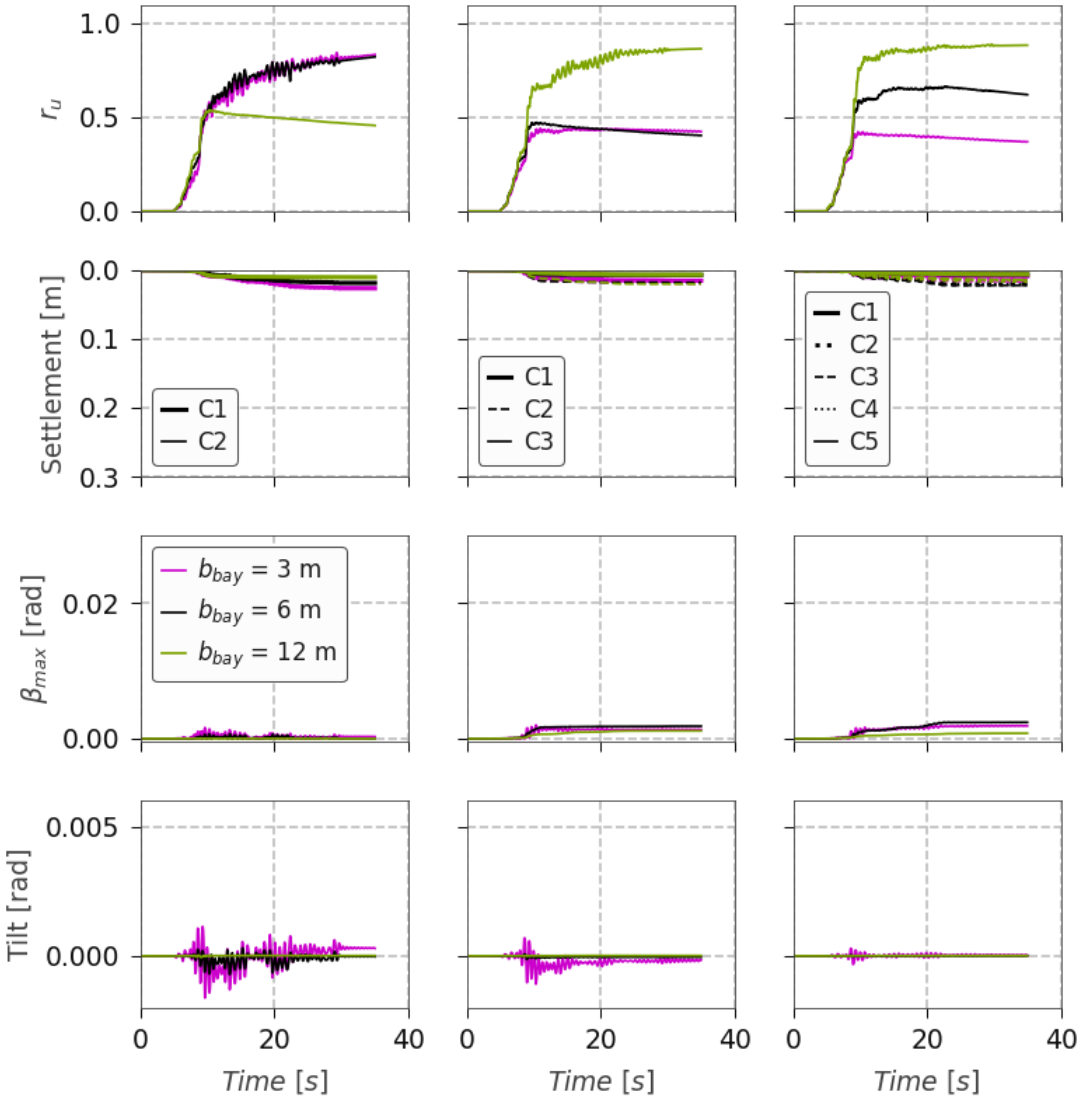


Figure 7.51: Time series for GM13 for b_{bay} variation

EI ratio (EI_{beam}/EI_{column})

Figures 7.52 to 7.57 shows the results of the models with varying EI_{ratio}. Regarding the maximum settlements, for NF2 when EI_{ratio} was increased, maximum settlements decreased, for NF3 maximum settlements remained almost constant and for NF5 maximum settlements decreased when EI_{ratio} was increased from 0.1 to 1 while remained constant when was increased more to 10. Regarding the average settlements, for NF2 when EI_{ratio} was increased, average settlements decreased (as for the maximum settlements), for NF3 average settlements remained almost constant when EI_{ratio} was increased from 0.1 to 1 while decreased when was increased more to 10, and for NF5 average settlements decreased when EI_{ratio} was increased from 0.1 to 1 while remained constant when was increased more to 10 (as for the maximum settlements). This indicates that

when EI_{ratio} was increased, the settlements remained almost the same or decreased, but never increased. When the Bray and Macedo (2017) approach was used settlements remained also the same because this approach does not take into account the EI_{ratio}. When a building with isolated footings was considered, the estimated settlements were similar with average numerical results, particularly for NF5. On the other hand, when a mat foundation was considered, the estimated settlements were much lower than those found in the numerical models. Angular distortion and tilt did not show a clear trend in the results.

Figure 7.55 shows the time series derived from the numerical simulations using GM1. The pore pressure ratio is always equal to one, indicating soil liquefaction in all cases. When the number of footings was increased, the settlements of the external footings decreased, the angular distortion increased and the til decreased. Figure 7.56 and Figure 7.57, for GM2 and GM3 respectively, show the same trends for the settlements. When GM3 was applied, partial liquefaction occurred in NF2 for EI_{ratio} equal to 1, in NF3 for EI_{ratio} equal to 0.1 and in NF5 for EI_{ratio} equal to 0.1 and 10.

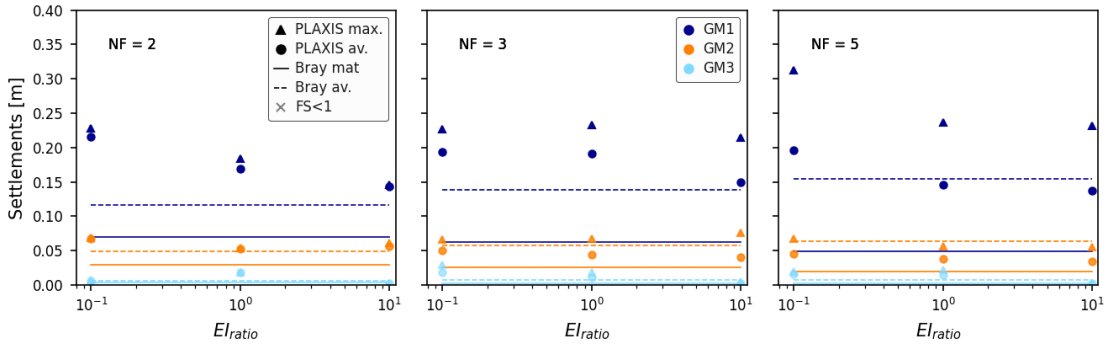


Figure 7.52: Numerical maximum and average settlements compared with Bray and Macedo (2017) approach for EI_{ratio} variation

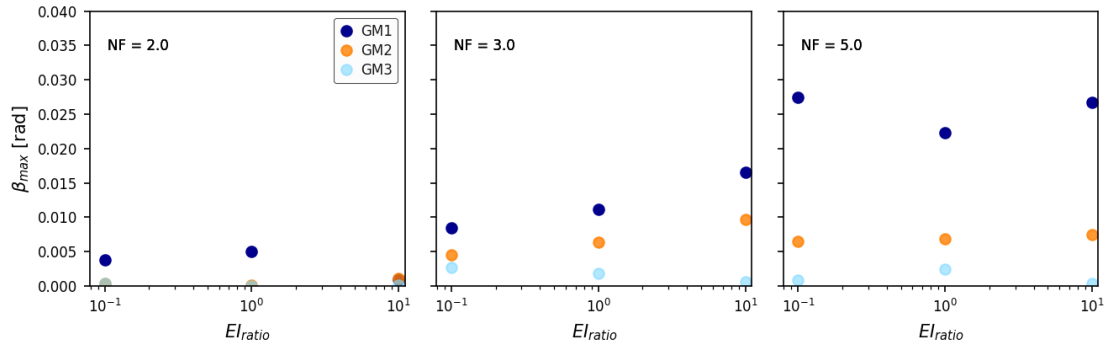


Figure 7.53: Numerical maximum angular distortion for EI_{ratio} variation

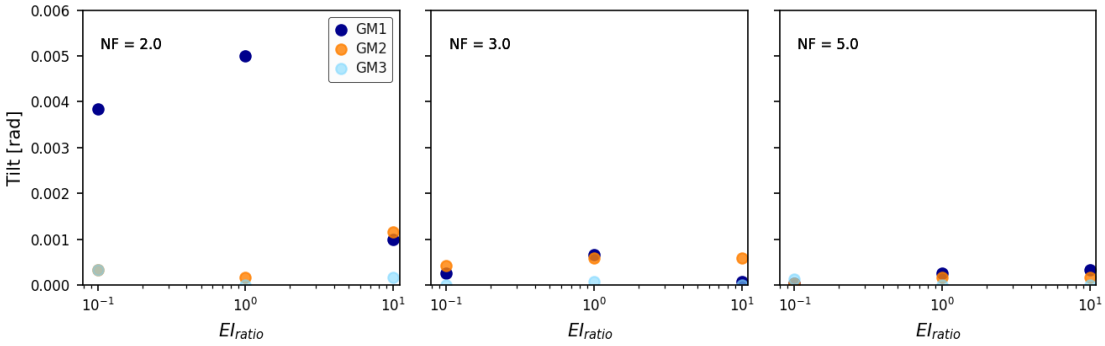


Figure 7.54: Numerical maximum tilt for EI_{ratio} variation

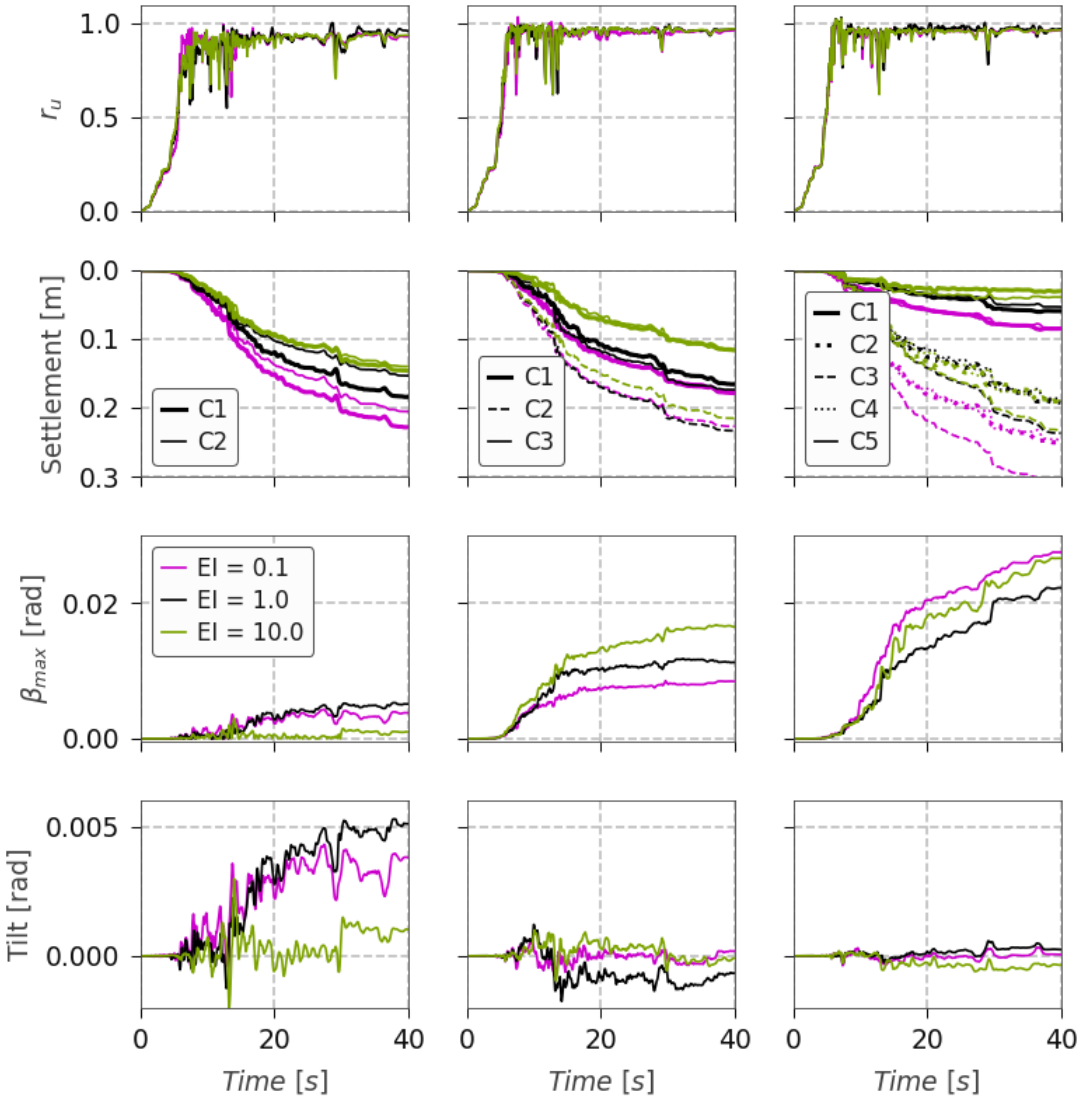


Figure 7.55: Time series for GM1 for EI_{ratio} variation

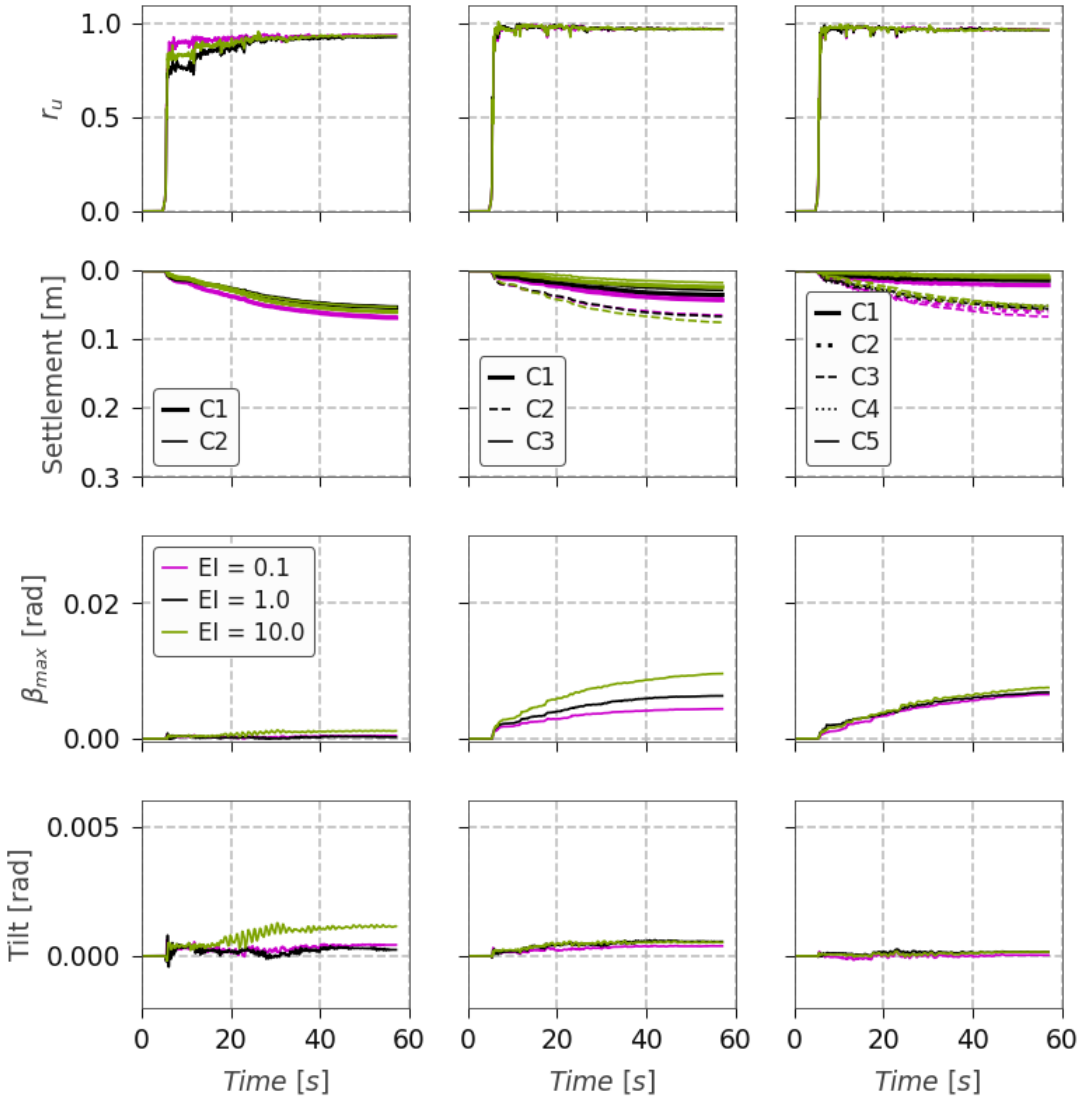


Figure 7.56: Time series for GM2 for EI_{ratio} variation

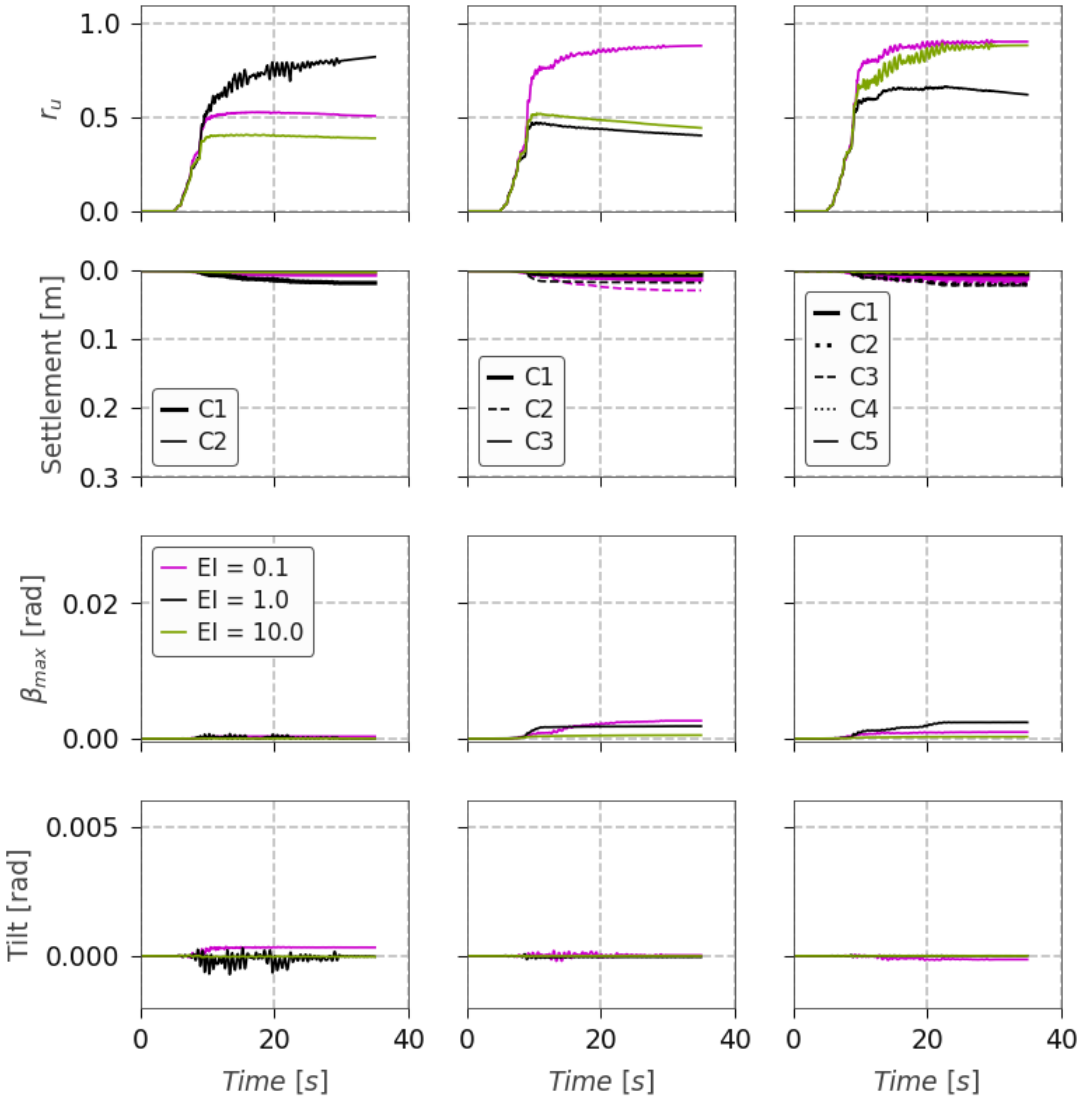


Figure 7.57: Time series for GM3 for EI_{ratio} variation

7.2.3 Summary

Figure 7.58 and Figure 7.59 show the average and maximum settlements, respectively, obtained from numerical analyses (including all the parameters in the sensitivity analysis) compared with settlement values calculated from Bray and Macedo (2017) equation considering a building with footings isolated. Some discrepancies can be observed but in general these approaches provided reasonably consistent estimates of settlement compared to the results from PLAXIS. Figure 7.60 shows the average settlements obtained from numerical analyses compared with settlement values calculated from Bray and Macedo (2017) equation considering a building with mat foundation. It is observed an underestimation when the simplified approach was used. Table 7.2 summarizes all the trends observed when the different parameters were varied. The trend in the table was

observed when the parameter indicated was increased.

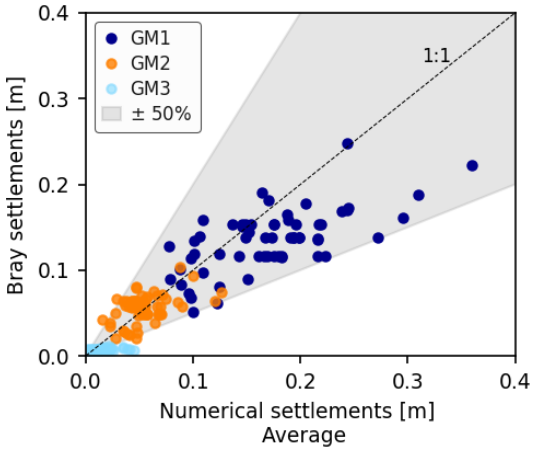


Figure 7.58: Comparison between numerical average settlements and analytical results considering isolated footings

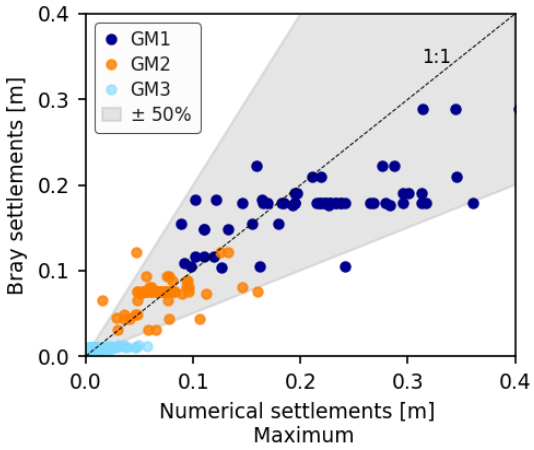


Figure 7.59: Comparison between numerical maximum settlements and analytical results considering isolated footings

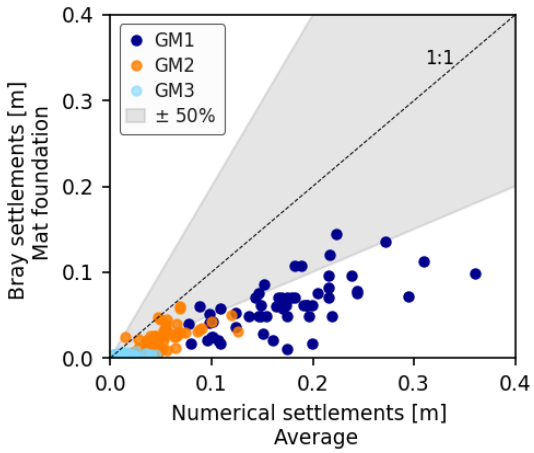


Figure 7.60: Comparison between numerical average settlements and analytical results considering mat foundation

Table 7.2 shows a summary of the trends found in the results.

Table 7.2: Summary of the trends in the results

Parameter	Settlement	Angular distortion	Tilt
H_C $[m]$	Decreased	No trend	No trend
D_R [%]	Decreased	Decreased	Decreased
H_L $[m]$	Increased	Same	Same
w_{top} $[kPa]$	Increased	Increased	No trend
b_{foot} $[m]$	Increased	Increased	Decreased
H $[m]$	Same	Decreased	Decreased
d_f $[m]$	Same	Increased	Increased
b_{bay} $[m]$	Decreased	No trend	Decreased
EI_{ratio}	Decreased	No trend	No trend

Figure 7.61 shows a tornado diagram that illustrates the influence of the considered soil, foundation and structure parameters on average settlement when NF2, NF3 and NF5 were simulated (left to right). Similarly, Figure 7.62 shows a tornado diagram that illustrates the influence on maximum settlement. The liquefiable layer thickness (H_L) and the non-liquefiable layer thickness (H_C) were the most influential parameter for NF2 and NF3 and the beam load (w_{top}) was the most influential parameter for NF5.

Figure 7.63 shows a tornado diagram that illustrates the influence on residual tilt. The liquefiable

layer thickness (H_L) and the non-liquefiable layer thickness (H_C) were the most influential parameter for NF2, the bay length (b_{bay}) and the foundation embedment depth(d_f) were the most influential parameter for NF3 and the liquefiable layer thickness (H_L) and the footing width (b_{foot}) were the most influential parameter for NF5. Similarly, Figure 7.64 shows a tornado diagram that illustrates the influence on maximum angular distortion. The liquefiable layer thickness (H_L) and the non-liquefiable layer thickness (H_C) were the most influential parameter for NF2, the footing width (b_{foot}) was the most influential parameter for NF3 and the beam load (w_{top}) and the bay length (b_{bay}) were the most influential parameter for NF5.

Figure 7.63 shows as the residual tilt decreased when the number of footings was increased while Figure 7.64 showed as the maximum angular distortion increased.

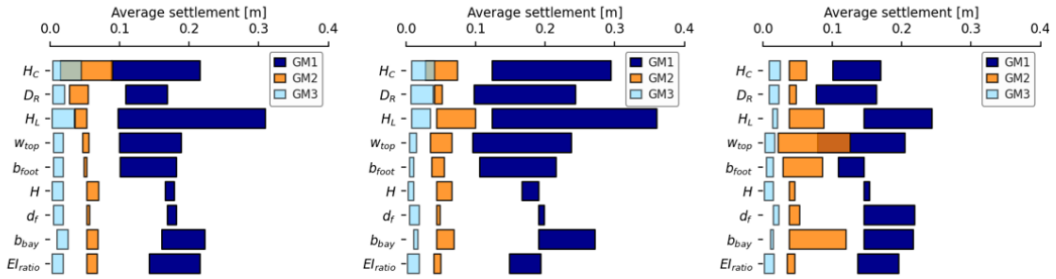


Figure 7.61: Tornado diagram for the sensitivity of average settlement for NF2, NF3 and NF5 (left to right)

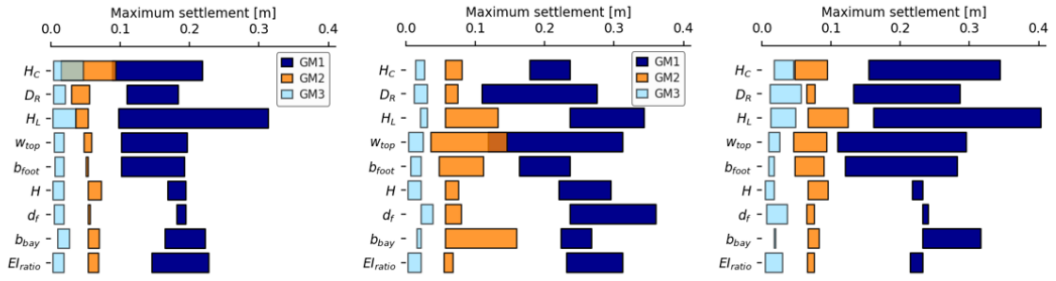


Figure 7.62: Tornado diagram for the sensitivity of maximum settlement for NF2, NF3 and NF5 (left to right)

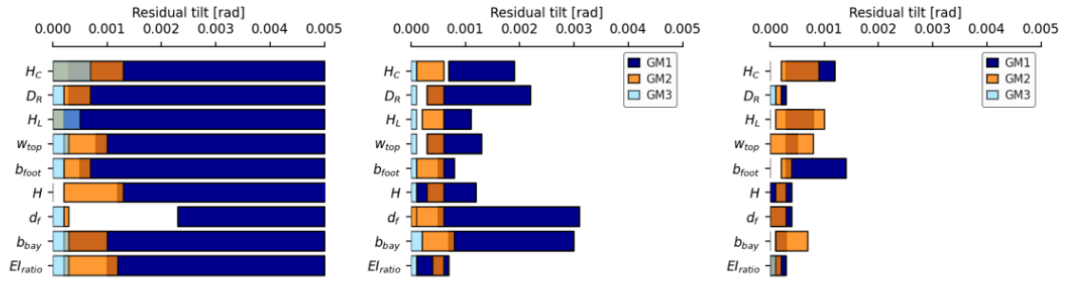


Figure 7.63: Tornado diagram for the sensitivity of residual tilt for NF2, NF3 and NF5 (left to right)

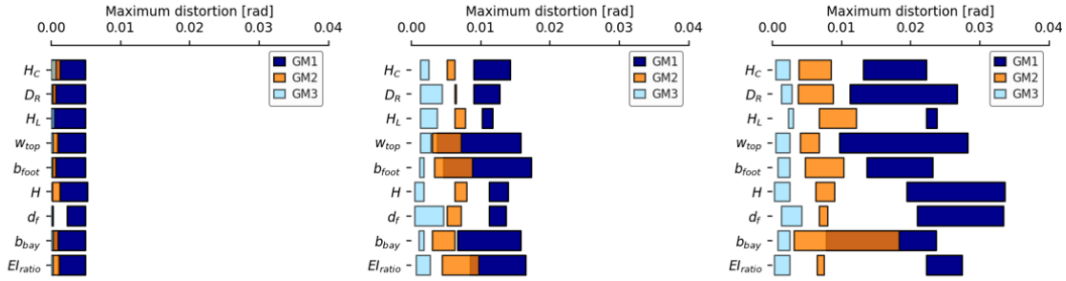


Figure 7.64: Tornado diagram for the sensitivity of maximum angular distortion for NF2, NF3 and NF5 (left to right)

7.3 Conclusions

This sensitivity analysis allowed to identify the key parameters controlling liquefaction-induced settlement for buildings with isolated footings providing the first insights for extending the existing methods considering more complex systems such as buildings on shallow isolated footings. The results also showed the importance of considering the number of footings in the settlements of a building. Because tilt is calculated just based on the settlements of the external footings, it becomes challenging to discern a clear trend in the results.

The numerical results were compared with a simplified approach that was developed for structures with mat foundation. Often, structures with isolated footings are simplified and assumed to have mat foundations to calculate liquefaction settlements. However, as seen in the results, the settlements estimated in this way are much lower compared to those provided by numerical analyses. Therefore, it is recommended that even if these approaches designed for mat foundations are utilized, settlements in each footing should be estimated individually by entering the contact pressure (Q) and width (b_{foot}) of each footing separately.

The results showed that the liquefiable layer thickness (H_L), the non-liquefiable layer thickness

(H_C) and the beam load (w_{top}) influenced more the settlements and the liquefiable layer thickness (H_L), the foundation embedment depth(d_f), the footing width (b_{foot}) and the beam load (w_{top}) influenced more the tilt and angular distortion. Clearly was observed that when the number of footings was increased, the residual tilt decreased while the maximum angular distortion increased.

Chapter 8

Case Study of a real building on a liquefiable deposit

Upon reviewing the procedure for numerically modeling structures with isolated footings and analyzing the influential soil and structure parameters, it became apparent that applying the same procedure to model a real structure was necessary. Therefore a well documented case study in Turkey was numerically modeled to analyze the differential settlements and tilt considering the soil-liquefaction-structure interaction of a real building. This case study was selected in view of the availability of sufficient data to perform the numerical model.

As described in section 2.2 different approaches can be adopted to consider soil-structure interaction (SSI) in liquefiable soils, the building-soil system can be assessed directly by modeling both soil and building in a single numerical model (a full model approach), or the building response and soil response can be completely decoupled (macro-mechanism approach). The full model approach applied in section 6 was used to model this real building in Turkey to compare the in-situ observed settlements with the numerical results. Additionally, the maximum moments in the structure elements were analyzed to show that future works can use more advanced software where the structure can be modeled as non-linear (Viana da Fonseca et al., 2023). The FLAC software was used to perform this numerical simulation.

Adapazari is the capital of Sakarya City in Turkey, which was significantly affected by the large Kocaeli earthquake of 17 August 1999, where widespread foundation damage occurred. Post-earthquake reconnaissance surveys showed that most of the buildings that suffered from ground failures were buildings with shallow raft foundations. One of these damaged buildings was the Public Education Centre (PEC) building of Adapazari and it differed from the other cases due to

its foundation type; this building was built with isolated footings. The presence of isolated footings changed the mechanisms of the damage pattern of the structure and the footings due to differential settlements. Figure 8.1 shows a photograph of the building about ten days after the earthquake.



Figure 8.1: PEC building after earthquake (Images courtesy of NISEE-PEER Library, UC Berkeley)

Image analysis of available reconnaissance photos using both the MATLAB (MATLAB, 2022) image processing toolbox and Autocad, identified settlements of 0.25-0.3 m relative to the surrounding foot path, 0-0.04 rad of foundation tilt, and 0.07-0.14 rad of residual building drift. Note that it is difficult of discerning whether the rotation was due to building drift or foundation tilt. Notably settlements of nearby buildings were between 0.20-0.90 m, but resulted in negligible structural damage since they were on raft foundations (Sancio, 2003). The PEC building was demolished and a new building is now located at the same site.

8.1 Soil conditions and input motion

Adapazari is located between Sakarya and Cark Rivers and is settled mostly on Holocene alluvial deposits, which overlie older lake bed sediments. The groundwater level is very close to the ground surface and at 1.0-3.0 m depth. The liquefiable layers are loose silty sands, sandy silts and clayey silts (silt mixtures), which are generally in the first 10 meters (Sancio, 2003; Bol et al., 2010). The normalized clean sand equivalent cone tip resistance (q_{C1Ncs}) values in these silty layers are small, in the range of 40-80, generally less than 70.

The soil profile below the PEC building was defined through CPTu, SPT and seismic (MASW) tests. The CPTu test was carried out within the Liquefact project (Lai et al., 2021) and the data of the SPT and laboratory tests and the velocity profile in the first 30 m ($V_{s,30}$) were provided

by the Sakarya Municipality. Figure 8.2 shows the CPT data and the idealized near surface soil profile at the PEC site.

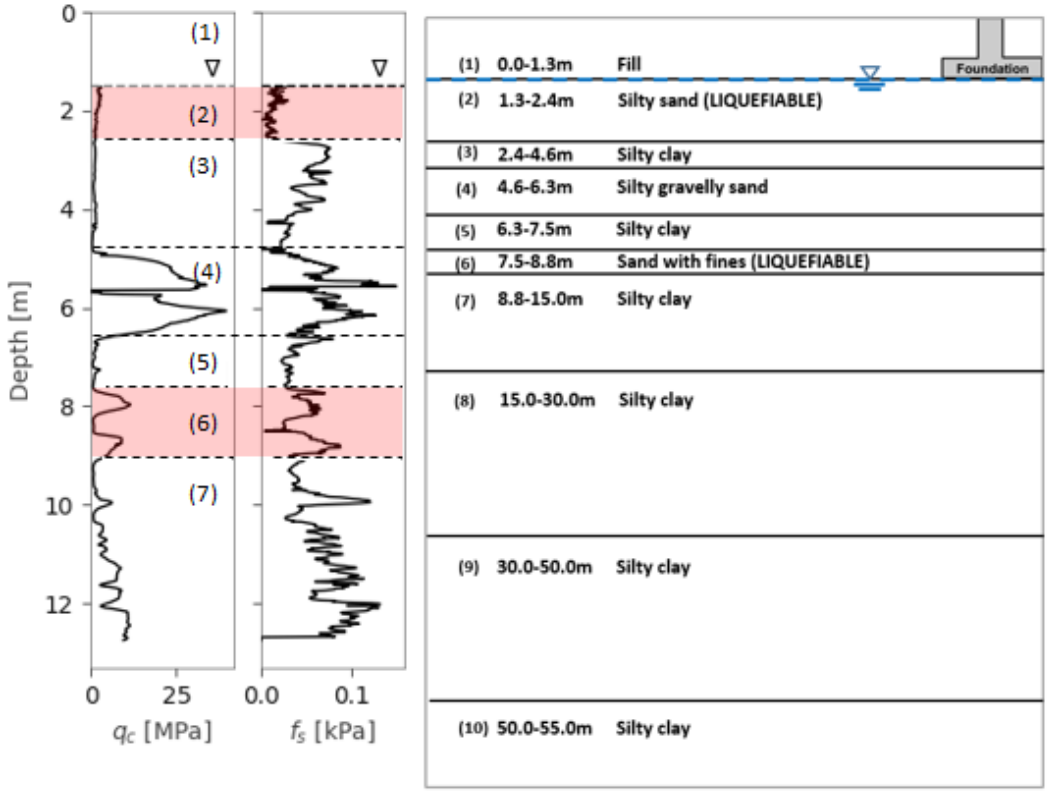


Figure 8.2: CPT data and idealized soil profile at the PEC site (Viana da Fonseca et al., 2023)

The subsoil consists of a total of ten layers from which two are considered liquefiable, one non-plastic silt just below the foundation and another sand layer at 7.5 m. The groundwater level is at 1.3 m. The shear wave velocity profile from 30 m to the bedrock at 50 m was assumed to be the same as at a 30 m depth. The soil at 50-80 m was assumed as Type C, the same at that of the SKR recording station. Figure 8.3 shows the $v_{s,30}$ profile at the PEC site based on the data provided by the Sakarya Municipality. Interpretation was then used to obtain the Vs profile between 30 m and 50 m. This is schematized in Figure 8.3. The input motion considered for the analyses was the outcrop ground motion recorded at the SKR station at around 3.6 km of the building in the EW direction and which had a PGA of 0.414 g, recorded on Type C soil (Figure 8.4).

8.2 Building and load

The PEC building was a 1970s five storey reinforced concrete building with about 200 m^2 in plan and isolated footings. In the plan view, the arrangement of the footings and the columns is shown in Figure 8.5a. The footings were located at a depth of 1.3 m and were 1.5x1.5 m^2, square in plan.

Since the software used can only simulate two-dimensional models, the comparison study is focused only on the performance of the frame corresponding to section AA' that is indicated in Figure 8.5a. Figure 8.5b presents the dimensions of the structural elements and the vertical loads corresponding to the quasi permanent load combination that are relevant for the performed seismic analyses. The floor height was 4.9 m in the first floor and the upper floors were 3.4 m in height. The beams and exterior columns of the building were 0.45x0.70 m^2 and the interior columns were 0.45x0.45 m^2. The quasi-permanent load combination was obtained from a permanent load of 6 kN/m^2 and a quasi-permanent value of the live load of 0.6 $\times$ 5 kN/m^2, according to the Turkish Earthquake Code (Code, 1975). This distributed load was then transferred to the frame by considering a tributary width of 3.2 m, giving a distributed load for the seismic load case of 28.8 kN/m for the storeys and 19.2 kN/m for the roof (just permanent load was considering for the roof load). The stiffness of the beams and columns was calculated using an assumed initial concrete stiffness of E_{cm} of 26.2 MPa and a cracked stiffness ratio of 0.5 was adopted for beams, and values between 0.35 and 0.46 for the columns depending on the axial load. The concrete design compressive strength and steel yield strength were 18 MPa and 230 MPa, respectively.

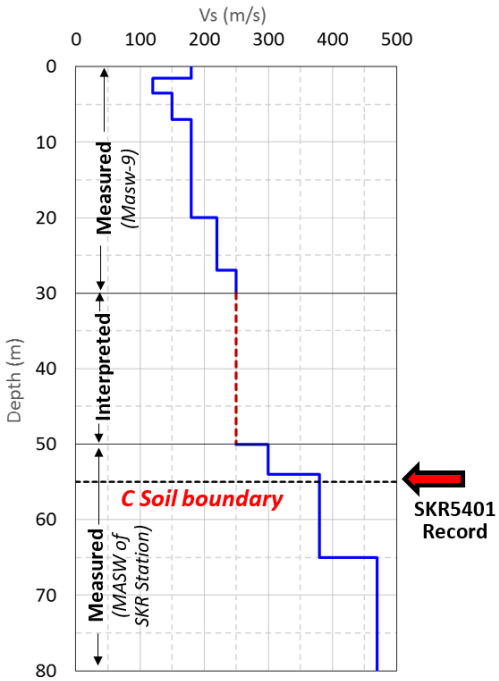


Figure 8.3: Vs profile at PEC site and considered depths (Viana da Fonseca et al., 2023)

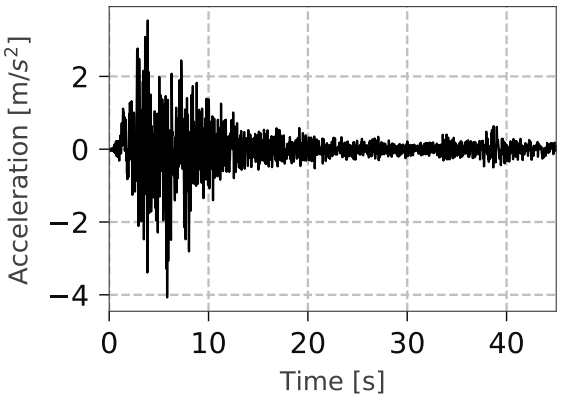


Figure 8.4: Input motion (at 55 m depth) time series (Viana da Fonseca et al., 2023)

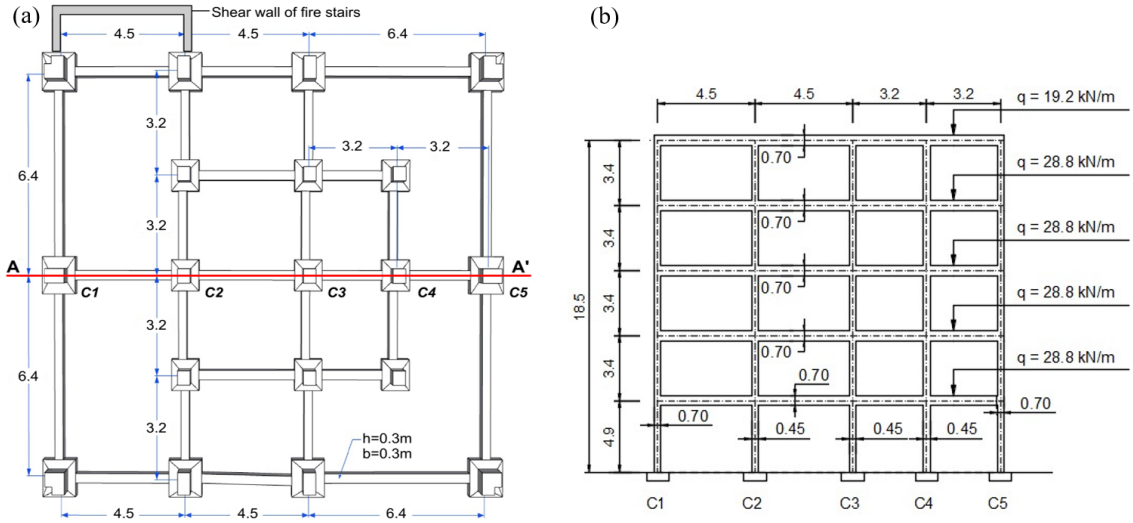


Figure 8.5: a) Plan view of the structural system; b) Frame corresponding to section AA' (Viana da Fonseca et al., 2023)

8.3 Overview of numerical model

The case study in Adapazari (Turkey) described before was numerically modeled to consider soil-liquefaction-structure interaction using the "full model" approach in the finite difference software FLAC through a nonlinear dynamic effective stress analysis.

The soil mesh was consistent with the soil profile outlined in Figure 8.6, with element sizes of approximately 0.4 m by 0.4 m near the building which were gradually coarsened to 0.7 m wide at the model edge. The total mesh was 55 m deep and 80 m wide, the lateral boundaries were tied together and the base boundary was a compliant base (absorbing) where the recorded motion was

input as a horizontal shear stress.

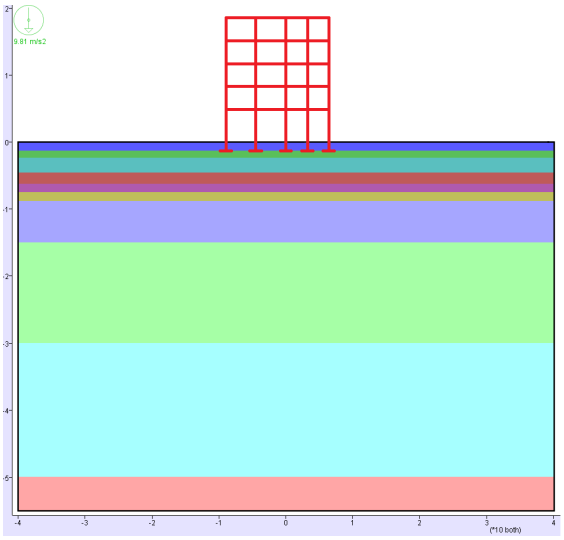


Figure 8.6: Full approach numerical model in FLAC (Viana da Fonseca et al., 2023)

The soil was modeled with only two constitutive models, Mohr-Coulomb model with "hysteretic damping" for the non-liquefiable soils and the PM4Sand model (Boulanger and Ziotopolou, 2017) for liquefiable sands (second and sixth layers). The default hysteretic damping model available in FLAC was used for the non-liquefiable layers to provide a more realistic stress-strain response. The extreme values of logarithmic strain (the values at which the tangent slope become zero), L1 and L2 parameters, were estimated as $1.7 \cdot IP^{0.5} - 3.6$ and $1.2 \cdot IP^{-0.25} + 2.25$ respectively, based on curve fitting to the modulus reduction curves from Vardanega and Bolton (2013), where IP is the plasticity index. The use of the simple Mohr-Coulomb model for the non-liquefiable layers was justified due to the amplitude of shear stresses applied to these layers in preliminary studies being less than what might result in significant strain softening and deformation. Non-liquefiable layers were modeled initially as undrained material but when the ground motion starts the ground water flow was activated allowing partial pore water pressure dissipation. Before applying the ground motion, the Mohr-Coulomb constitutive model was used in all ten layers to calculate the initial stresses in the soil profile, the parameters used are presented in Table 8.1. The strength parameters of the top 20 meters were designated via CPT of the site and laboratory tests of Sancio (2003). For the deeper layers, strength parameters were estimated by using the previous reports of the Sakarya-Municipality (2014) and considering $s_u = 0.6 \cdot \sigma'_v$. The deepest known value (at 30 m) for the ratio of undrained shear strength over vertical effective stress was 0.6. Small-strain stiffness parameters were derived from the v_s profile of the site. Secant and oedometer moduli were estimated by empirical relations proposed by Alpan (1970). An additional 1.5% Rayleigh damping was specified at 1.14 Hz and 5 Hz to mitigate numerical instability (Viana da Fonseca et al., 2023).

Table 8.1: Input parameters of the Mohr-Coulomb model

Parameter	1	2	3	4	5	6	7	8	9	10
$H\ [m]$	1.3	1.1	2.2	1.7	1.2	1.3	6.2	15.0	20.0	5.0
$\rho\ [kg/m]$	1975	1857	1786	1980	1786	1898	1908	1878	1918	2031
$G\ [MPa]$	71	38	38	134	46	97	110	108	162	325
$K\ [MPa]$	214	82	113	402	137	210	331	325	485	975
$\varphi\ [^{\circ}]$	0	33	0	36	0	33	0	0	0	-
$c\ [kPa]$	15	0	50	0	35	0	75	216	323	-
n	0.27	0.48	0.54	0.42	0.554	0.45	0.47	0.48	0.46	0.39
$k\ [m/s]$	2E-3	4E-5	9E-8	1E-5	6E-8	6E-8	2E-8	3E-9	1E-9	1E-9

The PM4Sand constitutive model (see section 2.1.6, Boulanger and Ziotopolou, 2017) was used to simulate the liquefiable soils (Layers 2 and 6) . The parameters for the upper liquefiable layer were based off the measured properties from Sancio (2003) and calibrated to best fit the hysteretic response of the cyclic simple shear test, J5-P4B and D5-P1B-3, carried out by Sancio (2003) on similar Adapazari silts at similar stress levels (Figures 8.7a and 8.7b). The lower liquefiable layer was calibrated based on the median normalized clean sand tip resistance in the liquefiable layer of 105 from the CPT. For the CPT calibration the equivalent liquefaction resistance curve adapted from Boulanger and Idriss (2016) and appendix A of Boulanger and Idriss (2014) was used for calibration to 3% single amplitude shear strain and can be seen in Figure 8.7c. The upper liquefiable layer was therefore assigned a relative density (D_R) of 43%, normalized shear modulus (G_0) of 757, contraction rate parameter (h_{p0}) of 0.325, maximum void ratio (e_{max}) of 1.2 and minimum void ratio (e_{min}) of 0.55. For The lower liquefiable layer was assigned the a D_R of 57%, G_0 of 757, h_{p0} of 0.086, e_{max} of 1.2 and e_{min} of 0.55. All other PM4Sand properties were kept at their default values for both layers.

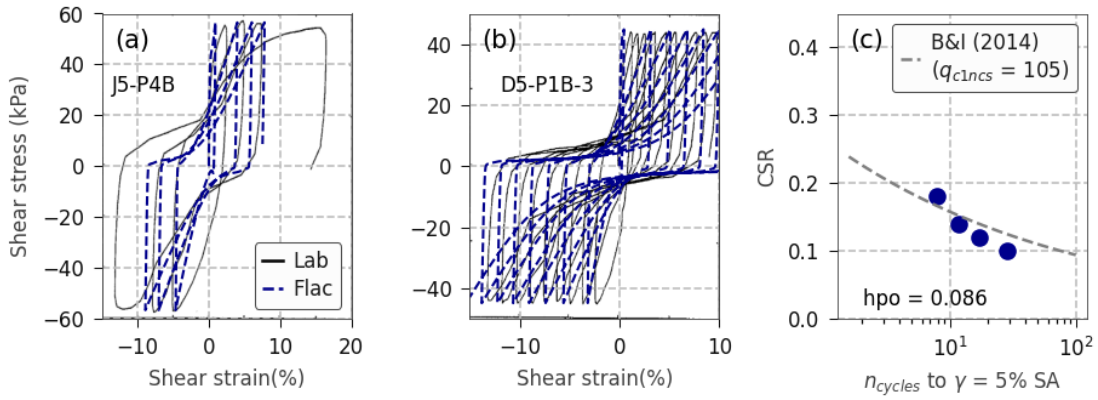


Figure 8.7: Calibration of Layer 2 PM4Sand parameters through a comparison of real and simulated CDSS test results in terms of shear stress - shear strain for a test with a CSR of: a) 0.41; b) 0.33. c) Calibration of Layer 6 PM4Sand parameters through a comparison with B&I curve (Viana da Fonseca et al., 2023)

The building elements were modeled as beam elements available in the software (Figure 8.6), which can only simulate elastic behavior. The beam and footing elements were modeled with the provided dimensions and a Young's modulus of 26.2 GPa. The secant-to-yield stiffness of the beams and columns was modeled according to the proposal of Haselton et al. (2016), which reduces the gross stiffness of a member to simulate the effect of cracking and accounts for the level of axial force. The secant-to-yield stiffness of the members is around 35%-50% of their gross stiffness, which is consistent with other proposals, e.g. see (Paulay and Priestley, 1992; EPPO, 2017). Since the FLAC software models the soil as a 2D mesh with a 1 m length of out-of-plane dimension, the foundation impedances and bearing capacity are less than what would be computed for a 3D footing using the correct footing width. While FLAC provides a spacing parameter to allow the scaling of loads and masses of structural elements, it is impossible to accurately match both the vertical and rotational stiffnesses, as well as the bearing capacity, with a single spacing value. Furthermore, the soil properties (particular frictional angle and shear modulus) are both dependent on whether the soil is loaded in plane strain on under 3D loading. Finally, it should be noted that the pore water flow could not escape in the out-of-plane direction. Given these limitations with converting a 3D model to a plane-frame superstructure on a plane-strain soil, the 1 m out-of-plane length was used unscaled, compared to the 1.5 m out-of-plane width of the foundation, reducing the bearing capacity by 22% when applying the method from Salgado (2008). The interface between the base of the footing elements and surrounding soil was fixed. However, the use of unglued interface elements was also tested in alternative analyses and there was no significant slip and no uplift. The column elements below the ground level were not attached to the soil mesh.

8.4 Results and discussion

The full effective stress 2D numerical models in FLAC software was run with nonlinear constitutive soil models and a linear elastic model for the building. Figure 8.8a shows the surface acceleration time series and Figure 8.8b the surface response spectrum where it is observed that the decrease in soil shear stiffness and resistance attenuated the higher frequencies of the input motion.

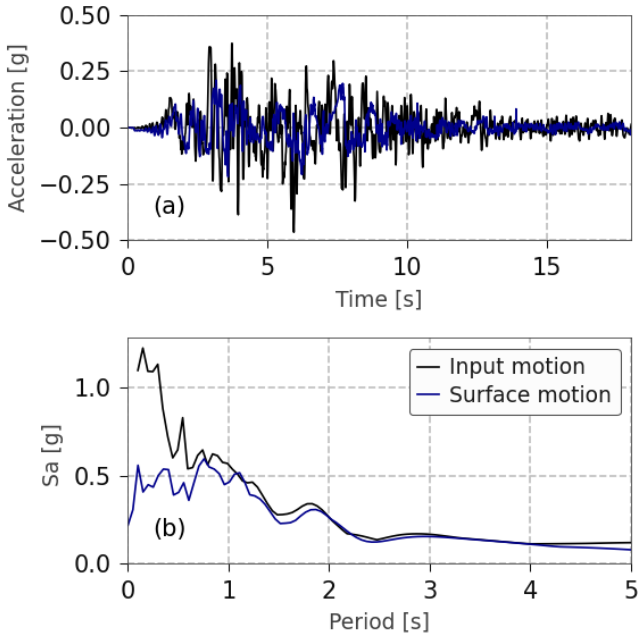


Figure 8.8: (a) Surface acceleration time series and (b) corresponding spectral acceleration (adapted from Viana da Fonseca et al., 2023)

Figure 8.9 presents several key time series. In Figure 8.9a the pore pressure ratio in the middle of the uppermost liquefiable layer for free-field conditions and under the central footing is shown. The pore pressure build up reached a state of liquefaction in the free-field, consistent with the observed soil ejecta near the building. In Figure 8.9b the shear-induced settlements below all the columns (see Figure 8.6 for numbering) are shown. Overall, the shear-induced settlement was similar but less than the observed range of 0.25-0.3 m. Additional volumetric based settlement using the method from Zhang et al. (2002) was computed as 0.06 m. When evaluating the soil profile against the ground failure chart from Ishihara (1985), ejecta-based settlement was assumed negligible. Considering the contributions from both shear-induced and volumetric settlement, the total settlement was comparable to observations.

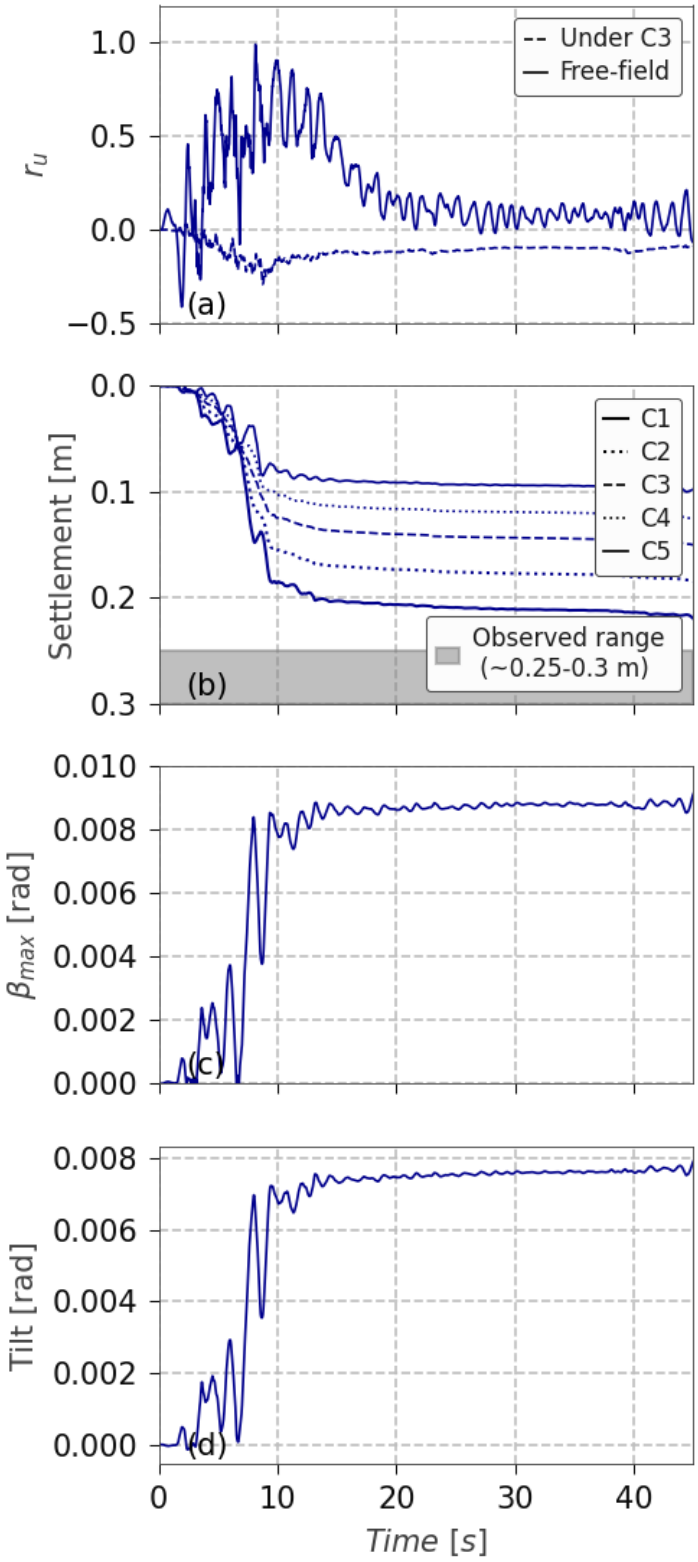


Figure 8.9: Results from numerical model: a) excess pore pressure ratio in the middle of the liquefiable layer in free-field and under central column, b) settlements at all the columns, c) maximum angular distortion, d) tilt (adapted from Viana da Fonseca et al., 2023)

In Figure 8.9c, the maximum angular distortion time series is shown, corresponding to the maximum differential settlement between C1 and C2. Finally, the global foundation tilt is shown in Figure 8.9d. The model resulted in foundation tilt value within the observed range, noting the difficulty in obtaining exact tilt values from image analysis.

The maximum moment demands in the beams (Figure 8.10) and columns (Figure 8.11) were also compared. Numerical results showed shear failures in the beams and columns of the lower storeys, while from field observations, none were reported in the beams and shear failures were reported in the lower storeys, consistent with the numerical results. Since elastic structural models do not account for the yielding of structural elements, it is recommended a nonlinear model to obtain a more reasonable estimate of overall deformation and damage.

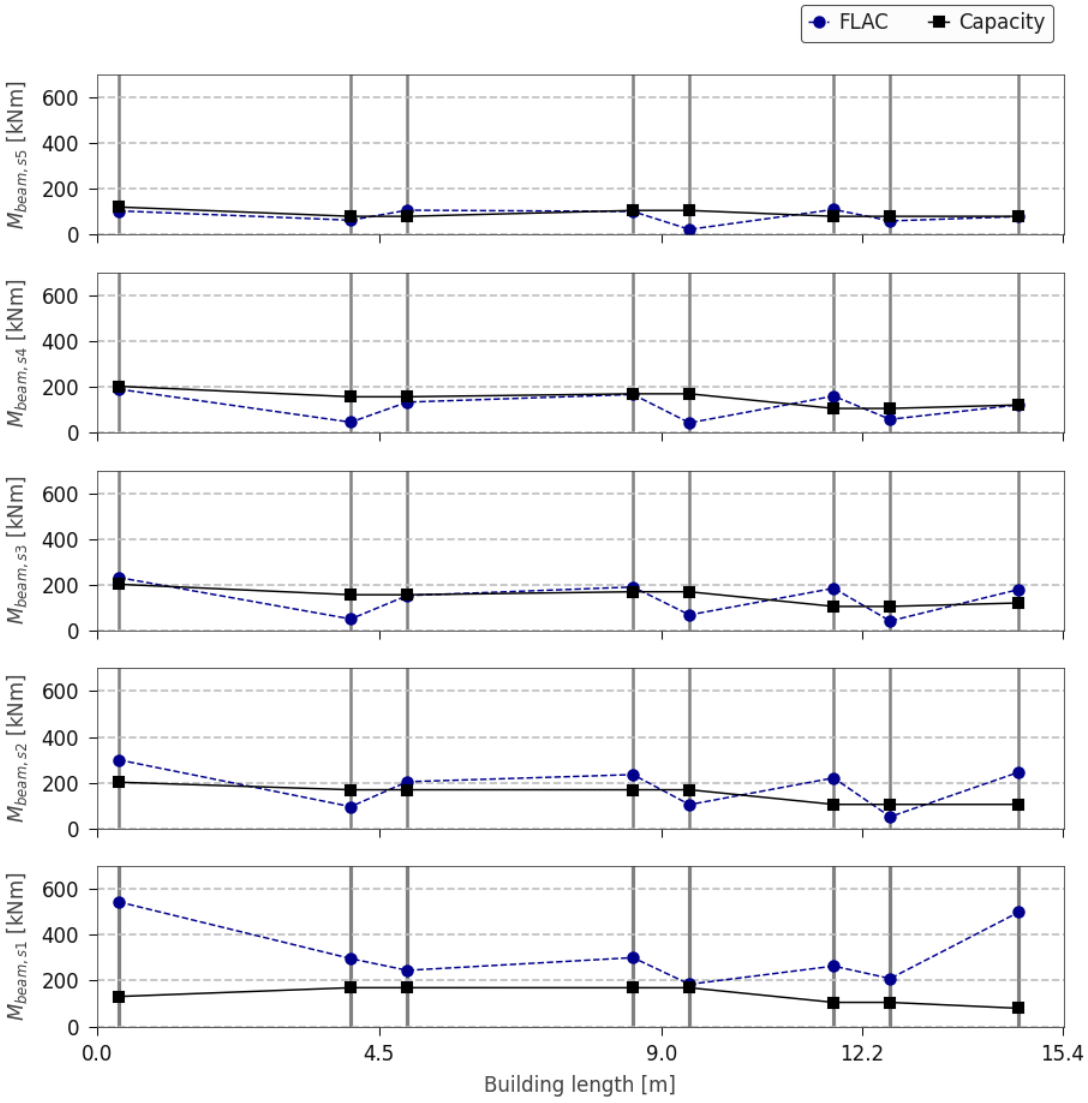


Figure 8.10: Comparison of maximum beams moment demand from FLAC full model approach (adapted from Viana da Fonseca et al., 2023)

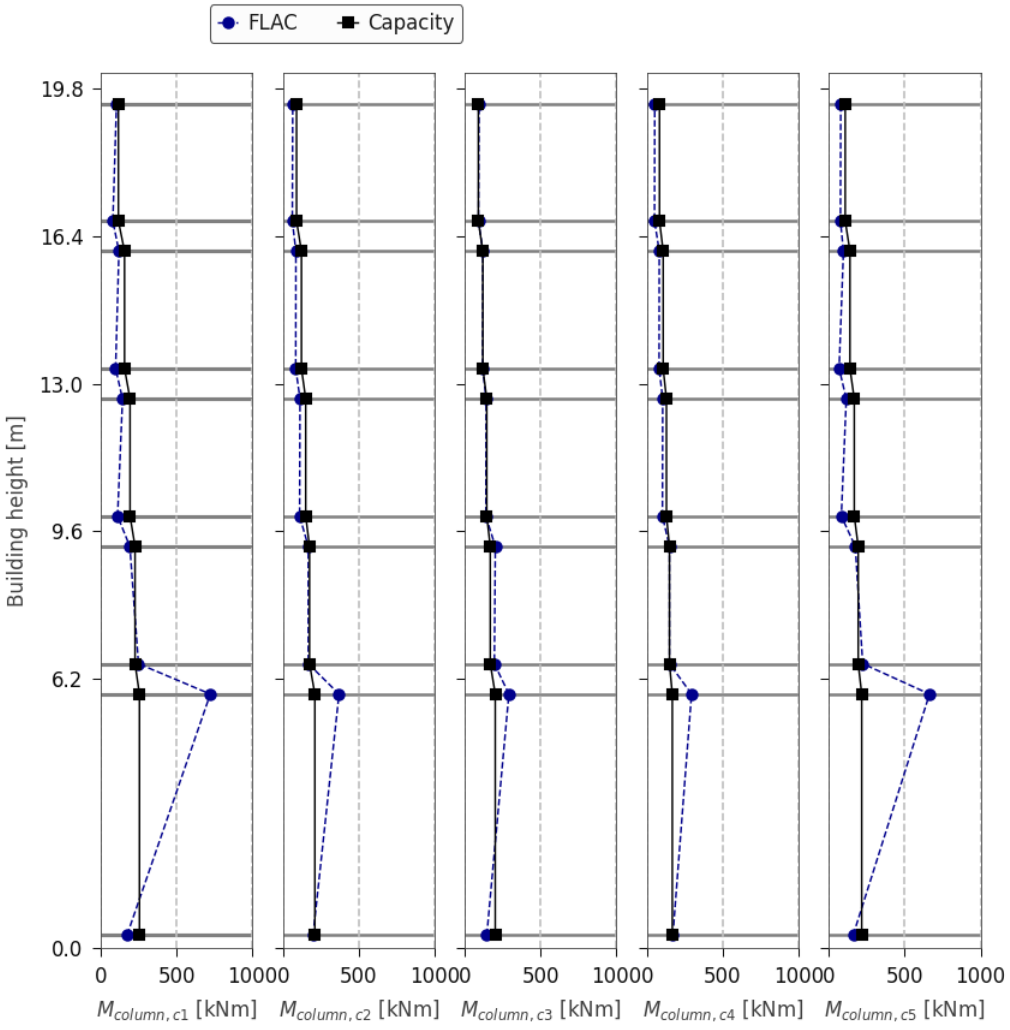


Figure 8.11: Comparison of maximum columns moment demand from FLAC full model approach (adapted from Viana da Fonseca et al., 2023)

Viana da Fonseca et al. (2023) presents the same case study numerically simulated using PLAXIS 2D and OpenSees (an open source finite element software). The findings showed that FLAC and PLAXIS 2D provide very similar results in terms of pore pressure build up, settlements and tilt. The main advantage of OpenSees model was the de-coupling of the structural analysis from the soil analysis to allow greater detail in the structural analysis that cannot be achieved with most commercial software capable of effective stress analysis. The ability of OpenSees model to provide more detailed nonlinear modeling of structural elements, and 3D foundation impedances, resulted in the model providing additional insight into the building performance compared to the full model approach (FLAC and PLAXIS 2D).

8.5 Main findings

The numerical simulation of full buildings on liquefiable soil during strong shaking is a highly demanding task for any engineer. This study presented a simulations of a case study of a building during the Adapazari 1999 earthquake to outline the key steps involved and comparative with field observations. The numerical model consisted of a full effective stress 2D numerical model of the soil domain with equivalent linear structural models to represent the building. The model was developed in the finite-difference software FLAC. While no model exactly replicated the observed outcome of the building in terms of settlement, tilt, drift, and structural damage. The uncertainty in the ground motion, building properties, soil properties (and soil heterogeneity) as well as the simplification adopted in only modeling a single frame of the building in 2D, are certainly some sources of the discrepancies.

Chapter 9

Conclusions

9.1 Final remarks

This work presented an overview of an efficient numerical procedure for simulating liquefaction-induced differential settlements in buildings with isolated footings. The geotechnical efficacy of the software and the constitutive model used was demonstrated through comparison with centrifuges and in-situ experimental results. Additionally, a well-documented case study was numerically modeled using the described procedure to analyze the differential settlements and tilt, considering the soil-liquefaction-structure interaction of a real building. The partial conclusions of each chapter are presented at the end of their respective chapters, and the most relevant findings and conclusions are summarized in this section.

It was demonstrated that PLAXIS 2D (Bentley, 2020) and FLAC (Itasca Consulting Group, Inc., 2016), two commercial software for advanced geotechnical analysis, are able to accurately predict liquefaction-induced settlements and excess pore pressure. Validation was conducted through effective stress analysis using the PM4Sand constitutive model, comparing the results with centrifuge tests performed by Dashti et al. (2010a). The settlement results showed relatively close agreement with the centrifuge tests for both simulated experiments and ground motions applied, while the pore pressures in the free-field exhibited close agreement to those under the building. These validation results were considered satisfactory for the purposes of this study.

It was also demonstrated that the two software used are capable of accurately capturing surface ground motion through site response analyses. Horizontal-to-Vertical Spectral Ratio (HVSR) curves obtained from a pilot site located in the Greater Lisbon region were used to validate the fundamental frequencies of the numerical analyses in the linear elastic domain. The results showed good agreement with the in-situ response. Generally, considering the complex geological conditions,

the several models can be considered representative, and any small differences can be attributed to the simplifications inherent in the 1D and 2D numerical analyses compared to the 3D nature of the site.

Appropriate model size was studied for capturing free-field conditions, minimizing wave reflections, and mitigating the influence of lateral boundaries on the stress-strain response of the building. The selection of the appropriate size was based on a parametric study in a homogeneous sandy profile, where width (W) and depth (D) of the model were varied to obtain the ultimate bearing capacity from numerical simulations and compare them with analytical solutions. The results showed that a model with a minimum width and depth of 10 times the width of the structure and 4 times the width of the structure, respectively, is appropriate.

From the procedure for numerically modeling structures with isolated footings, it was highlighted the importance of considering the number of footings in the settlements of a building. Settlements in the external footings decreased with the increase of the number of footings, while the settlement in the central footing increased. Additionally, the angular distortion increases with the number of footings, while the tilt decreases.

The sensitivity analysis allowed the identification of key parameters controlling liquefaction-induced settlement for buildings with isolated footings, providing initial insights for extending existing methods to consider more complex systems, such as buildings on shallow isolated footings. Typically, structures with isolated footings are simplified and assumed to have mat foundations to calculate liquefaction settlements. However, the results showed that settlements estimated in this manner are significantly lower compared to those provided by numerical analyses. Therefore, it is recommended that even if these approaches designed for mat foundations are utilized, settlements in each footing should be estimated individually by entering the contact pressure (Q) and width (b_{foot}) of each footing separately. Additionally, the results revealed that the liquefiable layer thickness (H_L), the non-liquefiable layer thickness (H_C), and the beam load (w_{top}) had more influence on settlements, while the liquefiable layer thickness (H_L), the foundation embedment depth (d_f), the footing width (b_{foot}), and the beam load (w_{top}) influenced tilt and angular distortion more significantly.

The numerical simulation of a real building in Turkey was performed using the presented procedure to estimate differential settlements. Considering the contributions from shear-induced (from numerical model) and volumetric settlement (analytical approach), the total settlement from numerical model was comparable to real observations in-situ.

9.2 Future Works

The most significant conclusions of the present work have been summarized in the previous section. However, there is still much work to be done to fully understand the differential settlements of buildings with isolated footings. This section outlines some recommendations for future research.

- Expand the range of values used in the sensitivity analysis.
- Use more advanced software where the structure can be modeled as non-linear with an acceptable computation time.
- Perform an efficient probabilistic procedure to establish a prediction equation for differential settlements of isolated footings based on the plots identified.
- Quantify the load redistribution , by performing a model with central footing having weaker soil.
- Simulate potential liquefaction mitigation strategies that could help to decrease foundation settlements. For that, modifications in the crust layer (compaction grout, cemented stabilization) and ground water level will be numerically modeled.

Bibliography

Acacio, A. A., Kobayashi, Y., Towhata, I., Bautista, R., and Ishihara, K. (2001). Subsidence of building foundation resting upon liquefied subsoil: case studies and assessment. *Soils and Foundations*, 41(6):111–128.

Ahmed, A. and Soubra, A.-H. (2014). Probabilistic analysis at the serviceability limit state of two neighboring strip footings resting on a spatially random soil. *Structural Safety*, 49:2–9.

Akbas, S. O. and Kulhawy, F. H. (2009). Reliability-based design approach for differential settlement of footings on cohesionless soils. *Journal of geotechnical and geoenvironmental engineering*, 135(12):1779–1788.

Alarcon-Guzman, A., Leonards, G., and Chameau, J. (1988). Undrained monotonic and cyclic strength of sands. *Journal of Geotechnical Engineering*, 114(10):1089–1109.

Alpan, I. (1970). The geotechnical properties of soils. *Earth-Science Reviews*, 6(1):5–49.

Andrianopoulos, K. I., Papadimitriou, A. G., and Bouckovalas, G. D. (2010). Bounding surface plasticity model for the seismic liquefaction analysis of geostructures. *Soil Dynamics and Earthquake Engineering*, 30(10):895–911.

Bakir, B. S., Sucuoglu, H., and Yilmaz, T. (2002). An overview of local site effects and the associated building damage in adapazari during the 17 august 1999 izmit earthquake. *Bulletin of the Seismological Society of America*, 92(1):509–526.

Bán, Z., Mahler, A., and Győri, E. (2017). Liquefaction assessment based on combined use of cpt and shear wave velocity measurements. In *EGU General Assembly Conference Abstracts*, page 7783.

Beaty, M. and Byrne, P. M. (1998). An effective stress model for pedicting liquefaction behaviour of sand. In *Geotechnical Earthquake Engineering and Soil Dynamics III*, pages 766–777. ASCE.

Been, K. and Jefferies, M. G. (1985). A state parameter for sands. *Géotechnique*, 35(2):99–112.

Bentley (2020). *Plaxis2D, Complete 2d Geotechnical Analysis Software Version: 21.*

Berger, J., Buckle, I., and Greene, M. (2012). The 2010 canterbury and 2011 christchurch new zealand earthquakes and the 2011 tohoku japan earthquake: Emerging research needs and opportunities. *Earthquake Engineering Research Institute, CA.*

Bertalot, D. and Brennan, A. (2015). Influence of initial stress distribution on liquefaction-induced settlement of shallow foundations. *Géotechnique*, 65(5):418–428.

Bertalot, D., Brennan, A., and Villalobos, F. (2013). Influence of bearing pressure on liquefaction-induced settlement of shallow foundations. *Géotechnique*, 63(5):391–399.

Bhatnagar, S., Kumari, S., and Sawant, V. A. (2016). Numerical analysis of earth embankment resting on liquefiable soil and remedial measures. *International Journal of Geomechanics*, 16(1):04015029.

Bird, J. F., Bommer, J. J., Crowley, H., and Pinho, R. (2006). Modelling liquefaction-induced building damage in earthquake loss estimation. *Soil Dynamics and Earthquake Engineering*, 26(1):15–30.

Bird, J. F., Crowley, H., Pinho, R., and Bommer, J. J. (2005). Assessment of building response to liquefaction-induced differential ground deformation. *Bulletin of the New Zealand society for earthquake engineering*, 38(4):215–234.

Bjerrum, L. (1963). Allowable settlement of structures. In *Proceedings of the 3rd European Conference on Soil Mechanics and Foundation Engineering, Wiesbaden, Germany*, volume 2, pages 135–137.

Bol, E., Önalp, A., Arel, E., Sert, S., and Özocak, A. (2010). Liquefaction of silts: the adapazari criteria. *Bulletin of Earthquake Engineering*, 8(4):859–873.

Bolton, M. (1986). The strength and dilatancy of sands. *Geotechnique*, 36(1):65–78.

Borozan, J., Costa, P. A., Romão, X., Quintero, J., and Da Fonseca, A. V. (2017). Numerical modelling of the dynamic response of liquefiable deposits in the presence of small scale buildings. In *COMPDYN 2017-Proceedings of the 6th International Conference on Computational Methods in Structural Dynamics and Earthquake Engineering.*

Bouckovalas, G., Psycharis, I., Gantes, C., Sextos, A., Kappos, A., and Mylonakis, F. (2018). Performance-based design of bridge piers in liquefiable sites with shallow foundation and limited ground improvement. In *Third International Conference on Performance-based Design in Earthquake Geotechnical Engineering (PBD-III)*, pages 16–19.

Bouckovalas, G. D., Tsiapas, Y. Z., Theocharis, A. I., and Chaloulos, Y. K. (2016). Ground response at liquefied sites: seismic isolation or amplification? *Soil Dynamics and Earthquake Engineering*, 91:329–339.

Boulanger, R. (2010). A sand plasticity model for earthquake engineering applications. *Report No. UCD/CGM-10/01*, 1.

Boulanger, R. and Idriss, I. (2014). Cpt and spt based liquefaction triggering procedures. *Report No. UCD/CGM.-14*, 1.

Boulanger, R., Khosravi, M., Khosravi, A., Wilson, D., Pulido, A., and Yunlong, W. (2017). Remediation of liquefaction effects for a dam using soil-cement grids: Centrifuge and numerical modeling. In *Proceedings of the 19th International Conference on Soil Mechanics and Geotechnical Engineering. Seoul, Korea*, pages 2477–2480.

Boulanger, R. and Ziotopolou, K. (2012a). Pm4sand (version 2): A sand plasticity model for earthquake engineering applications. *Report No. UCD/CGM-12/01*, 1.

Boulanger, R. and Ziotopolou, K. (2012b). Pm4sand (version 3): A sand plasticity model for earthquake engineering applications. *Report No. UCD/CGM-15/01*, 1.

Boulanger, R. and Ziotopolou, K. (2017). Pm4sand (version 3.1): A sand plasticity model for earthquake engineering applications. *Report No. UCD/CGM-17/01*, 1.

Boulanger, R. and Ziotopoulou, K. (2013). Formulation of a sand plasticity plane-strain model for earthquake engineering applications. *Soil Dynamics and Earthquake Engineering*, 53:254–267.

Boulanger, R. W. (2003). High overburden stress effects in liquefaction analyses. *Journal of geotechnical and geoenvironmental engineering*, 129(12):1071–1082.

Boulanger, R. W. and Idriss, I. (2016). Cpt-based liquefaction triggering procedure. *Journal of Geotechnical and Geoenvironmental Engineering*, 142(2):04015065.

Bray, J. D. and Macedo, J. (2017). 6th ishihara lecture: Simplified procedure for estimating liquefaction-induced building settlement. *Soil Dynamics and Earthquake Engineering*, 102:215–231.

Bray, J. D., Sancio, R. B., Durgunoglu, T., Onalp, A., Youd, T. L., Stewart, J. P., Seed, R. B., Cetin, O. K., Bol, E., Baturay, M. B., et al. (2004). Subsurface characterization at ground failure sites in adapazari, turkey. *Journal of geotechnical and geoenvironmental engineering*, 130(7):673–685.

Bullock, Z., Karimi, Z., Dashti, S., Porter, K., Liel, A., and Franke, K. (2019a). A physics-informed

semi-empirical probabilistic model for the settlement of shallow-founded structures on liquefiable ground. *Géotechnique*, 69(5):406–419.

Bullock, Z., Liel, A., Dashti, S., Karimi, Z., Porter, K., and Franke, K. (2019b). Probabilistic models for residual and peak transient tilt of mat-founded structures on liquefiable soils. *Journal of Geotechnical and Geoenvironmental Engineering*, 145(2):04018108.

Campbell, K. W. and Bozorgnia, Y. (2012). A comparison of ground motion prediction equations for arias intensity and cumulative absolute velocity developed using a consistent database and functional form. *Earthquake Spectra*, 28(3):931–941.

Carlton, B. and Tokimatsu, K. (2016). Comparison of equivalent linear and nonlinear site response analysis results and model to estimate maximum shear strain. *Earthquake Spectra*, 32(3):1867–1887.

Carvalho, J., Cabral, J., Gonçalves, R., Torres, L., and Mendes-Victor, L. (2006). Geophysical methods applied to fault characterization and earthquake potential assessment in the lower tagus valley, portugal. *Tectonophysics*, 418(3-4):277–297.

Cascone, E. and Bouckovalas, G. (1998). Seismic bearing capacity of footings on saturated sand with a clay cap. In *Proceedings of the Eleventh European Coference on Earthquake Engineering*.

CEN (2004). Eurocode 8: Design of structures for earthquake resistance - part 1: General rules, seismic actions and rules for buildings. *Brussels: European Committee for Standardization*.

Chatzigogos, C., Figini, R., Pecker, A., and Salençon, J. (2011). A macroelement formulation for shallow foundations on cohesive and frictional soils. *International Journal for Numerical and Analytical Methods in Geomechanics*, 35(8):902–931.

Chiaradonna, A., Tropeano, G., d'Onofrio, A., and Silvestri, F. (2018). Development of a simplified model for pore water pressure build-up induced by cyclic loading. *Bulletin of Earthquake Engineering*, 16(9):3627–3652.

Choffat, P. and Bensaúde, A. (1912). *Estudos sobre o sismo do Ribatejo de 23 de Abril de 1909*. Impr. nacional.

Code, T. E. (1975). Specifications for structures to be built in disaster areas, tec-75. Technical report, Turkish Ministry of Reconstruction and Resettlement.

Coduto, D. P., Kitch, W. A., and Yeung, M.-c. R. (2001). *Foundation design: principles and practices*, volume 2. Prentice Hall USA.

Coelho, P., Haigh, S., and Madabhushi, S. (2004). Centrifuge modelling of the effects of earthquake-

induced liquefaction on bridge foundations. In *Proceedings of the 11th international conference on soil dynamics and earthquake engineering*.

Cubrinovski, M., Hughes, M., Bradley, B., McCahon, I., McDonald, Y., Simpson, H., Cameron, R., Christison, M., Henderson, B., Orense, R., and O'Rourke, T. (2011). *Liquefaction impacts on pipe networks: Short Term Recovery Project No. 6 Natural Hazards Research Platform*. University of Canterbury.

Cubrinovski, M. and Ishihara, K. (1998a). Modelling of sand behaviour based on state concept. *Soils and Foundations*, 38(3):115–127.

Cubrinovski, M. and Ishihara, K. (1998b). State concept and modified elastoplasticity for sand modelling. *Soils and foundations*, 38(4):213–225.

Cubrinovski, M., Rees, S., and Bowman, E. (2010). Effects of non-plastic fines on liquefaction resistance of sandy soils. In *Earthquake engineering in europe*, pages 125–144. Springer.

Dafalias, Y. F. and Manzari, M. T. (2004). Simple plasticity sand model accounting for fabric change effects. *Journal of Engineering mechanics*, 130(6):622–634.

Daftari, A. and Kudla, W. (2014). Prediction of soil liquefaction by using ubc3d-plm model in plaxis. *International Journal of Civil and Environmental Engineering*, 8(2):106–111.

D'Appolonia, D. J., D'Appolonia, E., and Brissette, R. F. (1968). Settlement of spread footings on sand. *Journal of the Soil Mechanics and Foundations Division*, 94(3):735–760.

Darendeli, M. B. (2001). *Development of a new family of normalized modulus reduction and material damping curves*. The university of Texas at Austin.

Das, S. (2014). *Three dimensional formulation for the stress-strain-dilatancy elasto-plastic constitutive model for sand under cyclic behaviour*. University of Canterbury. Civil and Natural Resources Engineering.

Dashti, S., Bray, J., Pestana, J., Riemer, M., and Wilson, D. (2010a). Mechanisms of seismically-induced settlement of buildings with shallow foundations on liquefiable soil. *Journal of geotechnical and geoenvironmental engineering*, 136(1):151–164.

Dashti, S. and Bray, J. D. (2013). Numerical simulation of building response on liquefiable sand. *Journal of Geotechnical and Geoenvironmental Engineering*, 139(8):1235–1249.

Dashti, S., Bray, J. D., Pestana, J. M., Riemer, M., and Wilson, D. (2010b). Centrifuge testing to evaluate and mitigate liquefaction-induced building settlement mechanisms. *Journal of geotechnical and geoenvironmental engineering*, 136(7):918–929.

Davidenkov, N. N. (1938). Energy dissipation in vibrations. *Journal of Technical Physics*, 8(6):483.

Deng, L. and Kutter, B. L. (2012). Characterization of rocking shallow foundations using centrifuge model tests. *Earthquake Engineering & Structural Dynamics*, 41(5):1043–1060.

Deng, L., Kutter, B. L., and Kunnath, S. K. (2014). Seismic design of rocking shallow foundations: displacement-based methodology. *Journal of Bridge Engineering*, 19(11):04014043.

Dutta, S. C. and Roy, R. (2002). A critical review on idealization and modeling for interaction among soil–foundation–structure system. *Computers & structures*, 80(20-21):1579–1594.

EPPO (2017). Code for interventions (kanepe). Technical report, Earthquake Planning and Protection Organization of Greece, Athens, Greece.

Fema, H. (2003). Multi-hazard loss estimation methodology. *Earthquake Model/Technical Manual*.

Fenton, G. A. and Griffiths, D. (2002). Probabilistic foundation settlement on spatially random soil. *Journal of Geotechnical and Geoenvironmental Engineering*, 128(5):381–390.

Fernandes, M. M. (2020). *Analysis and design of geotechnical structures*. CRC Press.

Ferreira, C., Viana da Fonseca, A., Ramos, C., Saldanha, A. S., Amoroso, S., and Rodrigues, C. (2020). Comparative analysis of liquefaction susceptibility assessment methods based on the investigation on a pilot site in the greater lisbon area. *Bulletin of Earthquake Engineering*, 18(1):109–138.

Flora, A., Lancellotta, R., and Viggiani, C. (2018). *Foundations*, pages 364–374. Springer International Publishing, Cham.

Fotopoulou, S., Karafagka, S., and Pitilakis, K. (2018). Vulnerability assessment of low-code reinforced concrete frame buildings subjected to liquefaction-induced differential displacements. *Soil Dynamics and Earthquake Engineering*, 110:173–184.

Gazetas, G. (1991). Foundation vibrations. In *Foundation engineering handbook*, pages 553–593. Springer.

Gomez-Martinez, F., Millen, M. D., Costa, P. A., and Romao, X. (2020). Estimation of the potential relevance of differential settlements in earthquake-induced liquefaction damage assessment. *Engineering Structures*, 211:110232.

Gómez-Martínez, F., Millen, M. D., Costa, P. A., Romão, X., and da Fonseca, A. V. (2018). Potential relevance of differential settlements in earthquake-induced liquefaction damage assessment. In *16th European Conference on Earthquake Engineering*.

Groholski, D. R., Hashash, Y., Musgrove, M., Harmon, J., and Kim, B. (2015). Evaluation of 1-d non-linear site response analysis using a general quadratic/hyperbolic strength-controlled constitutive model. In *6th international conference on earthquake geotechnical engineering*, pages 1–4.

Hardin, B. O. and Drnevich, V. P. (1972). Shear modulus and damping in soils: design equations and curves. *Journal of the Soil mechanics and Foundations Division*, 98(7):667–692.

Haselton, C. B., Liel, A. B., Taylor-Lange, S. C., and Deierlein, G. G. (2016). Calibration of model to simulate response of reinforced concrete beam-columns to collapse. *ACI Structural Journal*, 113(6).

Hashash, Y. and Musgrove, M. and Harmon, J. and Groholski, D. and Phillips, C. and Park, D. (2016). *DEEPSOIL 6.1, UserManual*. University of Illinois at Urbana-Champaign.

Hausler, E. A. (2002). *Influence of ground improvement on settlement and liquefaction: A study based on field case history evidence and dynamic geotechnical centrifuge tests*. University of California, Berkeley.

Idriss, I. and Sun, J. (1992). Shake91–a computer program for conducting equivalent linear seismic response analysis of horizontally layered soils. *User's guide. University of California. Davis*.

Idriss, R. and Boulanger, I. (2008). Soil liquefaction during earthquakes, monograph mno-12. *Earthquake Engineering Research Institute, Oakland, California*.

Ishihara, K. (1985). Stability of natural deposits during earthquakes. *Proc. of 11th ICSMFE, 1985*, 1:321–376.

Ishihara, K. (1993). Liquefaction and flow failure during earthquakes. *Geotechnique*, 43(3):351–451.

Ishihara, K., Acacio, A. A., and Towhata, I. (1993). Liquefaction-induced ground damage in dagupan in the july 16, 1990 luzon earthquake. *Soils and Foundations*, 33(1):133–154.

Ishihara, K. and Cubrinovski, M. (2005). Characteristics of ground motion in liquefied deposits during earthquakes. *Journal of Earthquake Engineering*, 9(spec01):1–15.

Itasca Consulting Group, Inc. (2016). *FLAC — Fast Lagrangian Analysis of Continua, v8.0.452*. Minneapolis: Itasca.

Iwasaki, T. (1978). A practical method for assessing soil liquefaction potential based on case studies at various sites in japan. In *Proc. Second Int. Conf. Microzonation Safer Construction Research Application, 1978*, volume 2, pages 885–896.

Jefferies, M. and Been, K. (2015). *Soil liquefaction: a critical state approach*. CRC press.

Karamitros, D. K., Bouckovalas, G. D., and Chaloulos, Y. K. (2013a). A: Seismic settlements of shallow foundations on liquefiable soil with a clay crust. *Soil Dynamics and Earthquake Engineering*, 46:64–76.

Karamitros, D. K., Bouckovalas, G. D., and Chaloulos, Y. K. (2013b). B: Insight into the seismic liquefaction performance of shallow foundations. *Journal of Geotechnical and Geoenvironmental Engineering*, 139(4):599–607.

Karatzia, X., Mylonakis, G., and Bouckovalas, G. (2017). 3d dynamic impedances of surface footings on liquefiable soil: equivalent linear approach. In *16th World Conference on Earthquake Engineering WCEE*.

Karatzia, X., Mylonakis, G., and Bouckovalas, G. (2019). Seismic isolation of surface foundations exploiting the properties of natural liquefiable soil. *Soil Dynamics and Earthquake Engineering*, 121:233–251.

Karimi, Z. and Dashti, S. (2017). Ground motion intensity measures to evaluate ii: the performance of shallow-founded structures on liquefiable ground. *Earthquake Spectra*, 33(1):277–298.

Kaynia, A. (2012). Quiver_site–numerical code for nonlinear seismic site response analyses. *Norwegian Geotechnical Institute, Oslo, Norway*.

Kayser, M. and Gajan, S. (2014). Application of probabilistic methods to characterize soil variability and their effects on bearing capacity and settlement of shallow foundations: state of the art. *International Journal of Geotechnical Engineering*, 8(4):352–364.

Kim, T.-H., Kim, K.-H., and Choi, Y.-C. (2015). Assessment of angular distortion of structures adjacent to a road embankment site. *Measurement*, 74:268–277.

Kokusho, T. (2021). Energy-based liquefaction evaluation for induced strain and surface settlement—evaluation steps and case studies—. *Soil Dynamics and Earthquake Engineering*, 143:106552.

Konrad, J.-M. (1988). Interpretation of flat plate dilatometer tests in sands in terms of the state parameter. *Geotechnique*, 38(2):263–277.

Kottke, A. (2018). Python package repository: Pysra - site response analysis toolkit for python v0.2.1. pypi.

Kramer, S. and Elgamal, A. (2001). Modeling soil liquefaction hazards for performance-based earthquake engineering. Technical report, PEER Report 2001/13.

Kramer, S., Hartvigsen, A., Sideras, S., and Ozener, P. (2011). Site response modeling in liquefiable soil deposits. In *4th IASPEI/IAEE international symposium: effects of surface geology on seismic motion*, page 13.

Kramer, S., Sideras, S., and Greenfield, M. (2016). The timing of liquefaction and its utility in liquefaction hazard evaluation. *Soil Dynamics and Earthquake Engineering*, 91:133–146.

Kramer, S. L. (1996). *Geotechnical earthquake engineering*. Pearson Education India.

Kramer, S. L. and Holtz, R. D. (1991). *Soil improvement and foundation remediation with emphasis on seismic hazards*. National Science Foundation.

Kramer, S. L. and Wang, C.-H. (2015). Empirical model for estimation of the residual strength of liquefied soil. *Journal of Geotechnical and Geoenvironmental Engineering*, 141(9):04015038.

Ku, C.-S., Juang, C. H., Chang, C.-W., and Ching, J. (2012). Probabilistic version of the robertson and wride method for liquefaction evaluation: development and application. *Canadian Geotechnical Journal*, 49(1):27–44.

Lai, C. G., Bozzoni, F., Conca, D., Famà, A., Özcebe, A., Zuccolo, E., Meisina, C., Bonì, R., Bordoni, M., Cosentini, R., et al. (2021). Technical guidelines for the assessment of earthquake induced liquefaction hazard at urban scale. *Bulletin of Earthquake Engineering*, 19(10):4013–4057.

Lai, C. G., Meisina, C., Bozzoni, F., Conca, D., Famà, A., Özcebe, A. G., Zuccolo, E., Bonì, R., Poggi, V., Cosentini, R. M., Fonseca, A. V. D., Ferreira, C., Coelho, C., Coelho, J., Quintero, J., Rios, S., Millen, M., Cordeiro, D., Oztoprak, S., Bozbey, I., Oser, C., Sargin, S., Aysal, N., Ozcep, F., Kubilay, M., Ulj, K., Maček, M., Oblak, A., Petrovič, D., Kosič, M., Smolar, J., Kuder, S., and Logar, J. (2019). Deliverable d2.7: Methodology for assessment of earthquake-induced risk of soil liquefaction at the four european testing sites (microzonation). Technical report, LIQUEFACT Project, Horizon 2020 European Union funding for Research & Innovation Project ID: 700748 (www.liquefat.eu).

Liu, L. and Dobry, R. (1997). Seismic response of shallow foundation on liquefiable sand. *Journal of geotechnical and geoenvironmental engineering*, 123(6):557–567.

Loukidis, D. and Salgado, R. (2011). Effect of relative density and stress level on the bearing capacity of footings on sand. *Géotechnique*, 61(2):107–119.

Lu, C. (2017). A simplified calculation method for liquefaction-induced settlement of shallow foundation. *Journal of Earthquake Engineering*, 21(8):1385–1405.

Luque, R. and Bray, J. (2015). Dynamic analysis of a shallow-founded building in christchurch during the canterbury earthquake sequence. In *Proceedings of the 6th International Conference on Earthquake Geotechnical Engineering (ICEGE), Christchurch, New Zealand*, pages 2–4.

Luque, R. and Bray, J. D. (2017). Dynamic analyses of two buildings founded on liquefiable soils during the canterbury earthquake sequence. *Journal of Geotechnical and Geoenvironmental Engineering*, 143(9):04017067.

Manupella, G., Ferreira, A., Diniz, J., Callapez, P., Ribeiro, M., Pais, J., Rebêlo, L., Cabral, J., Moniz, C., Baptista, R., et al. (2011). Notícia explicativa da carta geológica 34-b, loures, 1: 50.000. *Laboratório Nacional De Energia E Geologia, Lisboa*, 57.

MATLAB (2022). *version 7.10.0 (R2022a)*. The MathWorks Inc., Natick, Massachusetts.

Maurer, B. W., Green, R. A., Cubrinovski, M., and Bradley, B. A. (2014). Evaluation of the liquefaction potential index for assessing liquefaction hazard in christchurch, new zealand. *Journal of Geotechnical and Geoenvironmental Engineering*, 140(7):04014032.

McGann, C. R. and Arduino, P. (2015). Numerical assessment of the influence of foundation pinning, deck resistance, and 3d site geometry on the response of bridge foundations to demands of liquefaction-induced lateral soil deformation. *Soil Dynamics and Earthquake Engineering*, 79:379–390.

Mejia, L. and Dawson, E. (2006). Earthquake deconvolution for flac. In *4th International FLAC symposium on numerical modeling in geomechanics*, pages 04–10.

Meslem, A., Iversen, H., Iranpour, K., and Lang, D. (2021). A computational platform to assess liquefaction-induced loss at critical infrastructures scale. *Bulletin of Earthquake Engineering*, 19(10):4083–4114.

Meslem, A., Iversen, H., Kaschwich, T., Iranpour, K., and Drange, L. (2019). Deliverable d6.6: Liquefact software – technical manual and application. Technical report, LIQUEFACT Project, Horizon 2020 European Union funding for Research & Innovation Project ID: 700748 (www.liquefat.eu).

Meyerhof, G. and Hanna, A. (1978). Ultimate bearing capacity of foundations on layered soils under inclined load. *Canadian Geotechnical Journal*, 15(4):565–572.

Meyerhof, G. G. (1963). Some recent research on the bearing capacity of foundations. *Canadian geotechnical journal*, 1(1):16–26.

Millen, M. (2019). Python package repository: eqsig - a python package for seismic signal processing

v1.0.0. pypi.

Millen, M., da Fonseca, A. V., and Romão, X. (2018). Preliminary displacement-based assessment procedure for buildings on liquified soil. In *16th European Conference on Earthquake Engineering*.

Millen, M., Rios, S., Quintero, J., and da Fonseca, A. V. (2020). Prediction of time of liquefaction using kinetic and strain energy. *Soil Dynamics and Earthquake Engineering*, 128:105898.

Millen, M., Viana da Fonseca, A., Quintero, J., Ferreira, C., Oztoprak, S., Oser, C., Bozbey, I., Aysal, N., Kosič, M., and Logar, J. (2021). Site classification using equivalent soil profiles for building-liquefaction interaction. *Bulletin of Earthquake Engineering*, 19(10):3987–4012.

Molina-Gómez, F., Ferreira, C., Ramos, C., and Viana da Fonseca, A. (2020). Performance of gel-push sampling in liquefiable soils. *Géotechnique Letters*, 10(2):256–261.

Moss, R., Seed, R. B., Kayen, R. E., Stewart, J. P., Der Kiureghian, A., and Cetin, K. O. (2006). Cpt-based probabilistic and deterministic assessment of in situ seismic soil liquefaction potential. *Journal of Geotechnical and Geoenvironmental Engineering*, 132(8):1032–1051.

Mousavi, S. A., Bastami, M., and Zahrai, S. M. (2016). Large-scale seismic isolation through regulated liquefaction: a feasibility study. *Earthquake Engineering and Engineering Vibration*, 15(4):579–595.

Negulescu, C. and Foerster, E. (2010). Parametric studies and quantitative assessment of the vulnerability of a rc frame building exposed to differential settlements. *Natural Hazards and Earth System Sciences*, 10(9):1781–1792.

Paolella, L., Spacagna, R. L., Chiaro, G., and Modoni, G. (2021). A simplified vulnerability model for the extensive liquefaction risk assessment of buildings. *Bulletin of Earthquake Engineering*, 19(10):3933–3961.

Paulay, T. and Priestley, M. N. (1992). *Seismic design of reinforced concrete and masonry buildings*, volume 768. Wiley New York.

Pecker, A. and Pender, M. (2000). Earthquake resistant design of foundations: new construction. In *ISRM International Symposium*. OnePetro.

Petalas, A. and Galavi, V. (2013). Plaxis liquefaction model ubc3d-plm. *Plaxis Report*.

Pyke, R. M. (1979). Nonlinear soil models for irregular cyclic loadings. *Journal of the Geotechnical Engineering Division*, 105(6):715–726.

Quintero, J., Gomes, R. C., Rios, S., Ferreira, C., and da Fonseca, A. V. (2023). Liquefaction

assessment based on numerical simulations and simplified methods: A deep soil deposit case study in the greater lisbon. *Soil Dynamics and Earthquake Engineering*, 169:107866.

Quintero, J., Saldanha, S., Millen, M., Fonseca, A. V. d., Sargin, S., Oztoprak, S., and Kelesoglu, M. (2018). Investigation into the settlement of a case study building on liquefiable soil in adapazari, turkey. In *Geotechnical Earthquake Engineering and Soil Dynamics V: Liquefaction Triggering, Consequences, and Mitigation*, pages 321–336. American Society of Civil Engineers Reston, VA.

Ramirez, J., Barrero, A. R., Chen, L., Dashti, S., Ghofrani, A., Taiebat, M., and Arduino, P. (2018). Site response in a layered liquefiable deposit: evaluation of different numerical tools and methodologies with centrifuge experimental results. *Journal of Geotechnical and Geoenvironmental Engineering*, 144(10):04018073.

Ramos, A. (2011). *Instabilities in Sands*. University of los Andes, Bogota.

Ramos, C. P. F. C. (2021). *Cyclic liquefaction susceptibility of soils from field and laboratory tests. Methodologies and critical analyses*. University of Porto.

Robertson, P. (2009). Performance based earthquake design using the cpt. *Proc. IS-Tokyo*, pages 3–20.

Robertson, P. (2015). Comparing cpt and v s liquefaction triggering methods. *Journal of Geotechnical and Geoenvironmental Engineering*, 141(9):04015037.

Sakarya-Municipality (2014). Adapazari kent merkezi 1/1000 Ölçekli revizyon uygulama İmar planına esas jeolojik-jeoteknik etüt raporu. Technical report, Sakarya Municipality.

Salgado, R. (2008). *The engineering of foundations*. McGraw-Hill Europe.

Sancio, R., Bray, J., Stewart, J., Youd, T., Durgunoğlu, H., Önalp, A., Seed, R., Christensen, C., Baturay, M., and Karadayılar, T. (2002). Correlation between ground failure and soil conditions in adapazari, turkey. *Soil Dynamics and Earthquake Engineering*, 22(9-12):1093–1102.

Sancio, R. B. (2003). *Ground failure and building performance in Adapazari, Turkey*. University of California, Berkeley.

Schneider, H. R., Romer, B., and Weishaupt, R. (2015). Probabilistic assessment of total and differential settlements due to spatial soil variability. *International Journal of Geotechnical Engineering*, 9(1):61–66.

Seed, H., Idriss, I., Makdisi, F., and Banerjee, N. (1975). Representation of irregular stress time

histories by equivalent uniform stress series in liquefaction analyses, report no. eerc 75-29. *Earthquake Engineering Res. Ctr., UC-Berkeley, CA*.

Seed, H. B. and Idriss, I. M. (1971). Simplified procedure for evaluating soil liquefaction potential. *Journal of the Soil Mechanics and Foundations division*, 97(9):1249–1273.

Seed, R. B., Cetin, K. O., Moss, R. E., Kammerer, A. M., Wu, J., Pestana, J. M., Riemer, M. F., Sancio, R. B., Bray, J. D., Kayen, R. E., et al. (2003). Recent advances in soil liquefaction engineering: a unified and consistent framework. In *Proceedings of the 26th Annual ASCE Los Angeles Geotechnical Spring Seminar: Long Beach, CA*.

Shahir, H. and Pack, A. (2009). Variation of permeability during liquefaction and its effects on seismic response of saturated sand deposits. In *8th International Congress on Civil Engineering*.

Somma, F. (2018). *Estimation of Lateral Spreading Induced Damage on Shallow Foundations in Framed Structures*. University of Naples Federico II.

Souliotis, C. and Gerolymos, N. (2016). Seismic effective stress analysis of quay wall in liquefiable soil: The case history of kobe. *GEOMATE Journal*, 10(20):1770–1775.

Stuedlein, A. W. and Bong, T. (2017). Effect of spatial variability on static and liquefaction-induced differential settlements. In *Geo-Risk 2017*, pages 31–51.

Terzaghi, K., Peck, R. B., and Mesri, G. (1996). *Soil mechanics in engineering practice*. John Wiley & Sons.

Tokimatsu, K., Hino, K., Suzuki, H., Suzuki, Y., and TC203, I. T. C. (2017). Liquefaction-induced settlement and tilting of buildings with spread foundation based on field observation and laboratory experiments. In *Proceedings of the 3rd international conference on performance-based design in earthquake geotechnical engineering*.

Vardanega, P. J. and Bolton, M. D. (2013). Stiffness of clays and silts: Normalizing shear modulus and shear strain. *Journal of Geotechnical and Geoenvironmental Engineering*, 139(9):1575–1589.

Verdugo, R. (1992). *Characterization of sandy soil behavior under large deformation*. PhD thesis, University of Tokyo.

Verdugo, R. and Ishihara, K. (1996). The steady state of sandy soils. *Soils and foundations*, 36(2):81–91.

Vesić, A. S. (1973). Analysis of ultimate loads of shallow foundations. *Journal of the Soil Mechanics and Foundations Division*, 99(1):45–73.

Viana da Fonseca, A., Millen, M., Gómez-Martinez, F., Romão, X., Quintero, J., Gómez, F., Costa, P., Rios, S., Kosik, M., Dolsek, M., Logar, J., Oztoprak, S., Bozbey, I., Kelesoglu, K., Ozcep, F., Flora, A., Rasulo, A., Modoni, G., and Croce, P. (2017). Deliverable d3.1: State of the art review of numerical modelling strategies to simulate liquefaction-induced structural damage and of uncertain/random factors on the behaviour of liquefiable soils. Technical report, LIQUEFACT Project, Horizon 2020 European Union funding for Research & Innovation Project ID: 700748 (www.liquefat.eu).

Viana da Fonseca, A., Millen, M., Quintero, J., Sargin, S., Rios, S., Romão, X., Pereira, N., Panico, F., Oztoprak, S., and Kelesoglu, M. K. (2023). Macromechanism approach for vulnerability assessment of buildings on shallow foundations in liquefied soils. *Journal of Geotechnical and Geoenvironmental Engineering*, 149(3):04023003.

Viana da Fonseca, A., Millen, M., Romão, X., Quintero, J., Rios, S., Cristiana, F., Fabrizio, P., Azeredo, C., Pereira, N., Logar, J., Oblak, A., Dolsek, M., Kosik, M., Kuder, S., Logar, M., Oztoprak, S., Kelesoglu, K., Sargin, S., Oser, C., Bozbey, I., Flora, A., Billota, E., Prota, A., Di Ludovico, M., Chiaradonna, A., Modoni, G., Paolella, L., Spacagna, R., Lai, C., Shinde, S., and F, B. (2018). Deliverable d3.2: Methodology for the liquefaction fragility analysis of critical structures and infrastructures: description and case studies. Technical report, LIQUEFACT Project, Horizon 2020 European Union funding for Research & Innovation Project ID: 700748 (www.liquefat.eu).

Viana da Fonseca, A., Ramos, C., and Cubrinovski, M. (2016). Session report: Liquefaction assessment. In B, L., HE, A.-M., and R, K., editors, *Geotechnical and Geophysical Site Characterisation 5*, volume 1, pages 217–232. NRC Research Press Ottawa, Canada.

Viggiani, C. (1993). *Fondazioni*. Cooperativa Universitaria Editrice Napoletana.

Vilhar, G., Brinkgreve, R., and Zampich, L. (2018a). Plaxis the pm4sand model 2018.

Vilhar, G., Laera, A., Foria, F., Gupta, A., and Brinkgreve, R. B. (2018b). Implementation, validation, and application of pm4sand model in plaxis. In *Geotechnical Earthquake Engineering and Soil Dynamics V*, pages 200–211. American Society of Civil Engineers Reston, VA.

Vis, G.-J., Kasse, C., and Vandenberghe, J. (2008). Late pleistocene and holocene palaeogeography of the lower tagus valley (portugal): effects of relative sea level, valley morphology and sediment supply. *Quaternary Science Reviews*, 27(17-18):1682–1709.

Wotherspoon, L. M., Orense, R. P., Green, R. A., Bradley, B. A., Cox, B. R., and Wood, C. M. (2015). Assessment of liquefaction evaluation procedures and severity index frameworks at christchurch strong motion stations. *Soil Dynamics and Earthquake Engineering*, 79:335–346.

Yang, Z., Lu, J., and Elgamal, A. (2008). Opensees soil models and solid-fluid fully coupled elements. *User's Manual. Ver*, 1:27.

Yoshimi, Y. and Tokimatsu, K. (1977). Settlement of buildings on saturated sand during earthquakes. *Soils and Foundations*, 17(1):23–38.

Yoshimine, M. and Ishihara, K. (1998). Flow potential of sand during liquefaction. *Soils and foundations*, 38(3):189–198.

Youd, T. L. and Idriss, I. M. (2001). Liquefaction resistance of soils: summary report from the 1996 nceer and 1998 nceer/nsf workshops on evaluation of liquefaction resistance of soils. *Journal of geotechnical and geoenvironmental engineering*, 127(4):297–313.

Zbyszewski, G. and Assunção, C. (1965). Notícia explicativa da folha 30-d, alenquer da carta geológica de portugal na escala 1: 50 000. *Lisboa: Serviços Geológicos de Portugal*, 104.

Zbyszewski, G. and Veiga Ferreira, O. (1968). Notícia explicativa da folha 31-c, coruche da carta geológica de portugal na escala 1: 50 000. *Lisboa: Serviços Geológicos de Portugal*.

Zbyszewski, G. and Veiga Ferreira, O. d. (1969). Notícia explicativa da folha 35-a, santo estevão da carta geológica de portugal na escala de 1: 50 000. *Lisboa: Serviços Geológicos de Portugal*.

Zhang, G., Robertson, P., and Brachman, R. W. (2002). Estimating liquefaction-induced ground settlements from cpt for level ground. *Canadian Geotechnical Journal*, 39(5):1168–1180.

Zhang, G., Robertson, P. K., and Brachman, R. (2004). Estimating liquefaction-induced lateral displacements using the standard penetration test or cone penetration test. *Journal of Geotechnical and Geoenvironmental Engineering*, 130(8):861–871.

Ziotopoulou, K. and Montgomery, J. (2017). Numerical modeling of earthquake-induced liquefaction effects on shallow foundations. In *Proceedings of 16th world conference on earthquake engineering*.

Appendix A

```
from plxscripting.easy import *

import numpy as np

from plx_scripts.tools.loader import load_input_motion

from sfsimodels import files as sfsi_files

import liquepy as lq

import os

import datetime

def run(_password):

total_depth = 20

acc_fnames = ["T2_2475_6.txt", "T2_975_1.txt", "T1_475_1.txt"]

sps = np.arange(1, 28)

nfs = [2]

bs_foot = [2]

qu_s = [80]

widths = [6]

depths_foot = [1]

hs_str = [6]

EI_ratio=1
```

```
E_str=28E6 #KPA

if EI_ratio==1:

E_col=E_str

elif EI_ratio==0.1:

E_col = E_str*10

else:

E_col = E_str/10

damp_freqs = (0.5, 10)

damp_ratio = 0.02

alpha, beta = calc_rayleigh_damping_params(f1=damp_freqs[0], f2=damp_freqs[1], d=damp_ratio)

for j, acc_fname in enumerate(acc_fnames):

for rr, n_foot in enumerate(nfs):

for ww, width in enumerate(widths):

for pp, depth_foot in enumerate(depths_foot):

for oo, height_str in enumerate(hs_str):

for nn, width_foot in enumerate(bs_foot):

for ss, sp in enumerate([4,7]):

for qq, qu in enumerate(qu_s):

if acc_fname==”T2_2475_6.txt”:

n_motion=1

elif acc_fname ==”T2_975_1.txt”:

n_motion=2

else:

n_motion=3
```

```
ecp_path = "..._SP%i.json" %sp # path of the file containing the soil profile information

ecp_models = sfsi_files.load_json(ecp_path, custom="soil-pm4sand": lq.num.flac.PM4Sand)

soil_profile = ecp_models["soil_profiles"][1]

h_c = soil_profile.layer_depth(2)

h_liq = soil_profile.layer_height(2)

dr = soil_profile.layer(2).relative_density

gwl = h_c

s, g = new_server('localhost', plaxis_port, password=_password)

#open new project

s.new()

# model geometry

width_model = (9 * width) + width # 4.5 width for each side

depth_model = total_depth

g.SoilContour.initializerectangular(-(width_model / 2), -depth_model, (width_model / 2), 0)

g.setproperties("UnitTime", "s")

#Layer1 properties

Name_1 = "1 dense crust"

Constitutive_model_1 = 3 #Hardening Soil

Drainage_1 = "Undrained (B)"

gamma_unsat_1 = soil_profile.layer(1).unit_dry_weight/1000

gamma_sat_1 = soil_profile.layer(1).unit_sat_weight/1000

void_1 = soil_profile.layer(1).e_curr

nu_1 = soil_profile.layer(1).poissons_ratio

G_1 = soil_profile.layer(1).g_mod/1000
```

E50ref_1 = 2*G_1*(1+nu_1)

Eoedref_1 = E50ref_1

Eurref_1 = E50ref_1*3

power_1 = 1.0 #0.5 for sand and 1 for clay

cohesion_1 = soil_profile.layer(1).cohesion/1000

phi_1 = soil_profile.layer(1).phi

psi_1 = soil_profile.layer(1).dilation_angle

K0_1 = 1 - np.sin(np.radians(phi_1))

kx_1 = soil_profile.layer(1).permeability

ky_1 = soil_profile.layer(1).permeability

Layer2 properties

Name_2 = "2 liq sand"

Constitutive_model_2 = 3 # Hardening Soil

Drainage_2 = "Drained"

gamma_unsat_2 = soil_profile.layer(2).unit_dry_weight/1000

gamma_sat_2 = soil_profile.layer(2).unit_sat_weight/1000

void_2 = soil_profile.layer(2).e_curr

nu_2 = soil_profile.layer(2).poissons_ratio

G_2 = soil_profile.layer(2).g_mod/1000

E50ref_2 = 2 * G_2 * (1 + nu_2)

Eoedref_2 = E50ref_2

Eurref_2 = E50ref_2 * 3

power_2 = 0.5

cohesion_2 = soil_profile.layer(2).cohesion/1000

```
phi_2 = soil_profile.layer(2).phi

psi_2 = soil_profile.layer(2).dilation_angle

K0_2 = 1 - np.sin(np.radians(phi_2))

kx_2 = soil_profile.layer(2).permeability

ky_2 = soil_profile.layer(2).permeability

# Layer2 pm4 properties

Name_2_pm4 = "2 liq sand pm4"

DR0_2 = dr

G0_2 = soil_profile.layer(2).g0_mod

hp0_2 = soil_profile.layer(2).hp0

pA_2 = 101.3

emax_2 = soil_profile.layer(2).e_max

emin_2 = soil_profile.layer(2).e_min

nb_2 = 0.5

nd_2 = 0.1

Q_2 = 10

R_2 = 1.5

PostShake_2 = 0

# Layer3 properties

Name_3 = "3 dense sand"

Constitutive_model_3 = 3 # Hardening Soil

Drainage_3 = "Undrained (B)"

gamma_unsat_3 = soil_profile.layer(3).unit_dry_weight/1000

gamma_sat_3 = soil_profile.layer(3).unit_sat_weight/1000
```

```
void_3 = soil_profile.layer(3).e_curr

nu_3 =soil_profile.layer(3).poissons_ratio

G_3 = soil_profile.layer(3).g_mod/1000

E50ref_3 = 2 * G_3 * (1 + nu_3)

Eoedref_3 = E50ref_3

Eurref_3 = E50ref_3 * 3

power_3 = 1.0

cohesion_3 = soil_profile.layer(3).cohesion/1000

phi_3 = soil_profile.layer(3).phi

psi_3 = soil_profile.layer(3).dilation_angle

K0_3 = 1 - np.sin(np.radians(phi_3))

kx_3 = soil_profile.layer(3).permeability

ky_3 = soil_profile.layer(3).permeability

# Structure properties

D = 0.5

EA = 0.5 * E_str * width_foot * D # crack factor =0.5

EI = 0.5 * E_str * width_foot * D * D * D/12

nu = 0.2

G = EA / (D * 2*(1+nu))

w=0

D_c = 0.45

EA_c = 0.5 *

E_col * D_c * D_c # crack factor =0.5

EI_c = 0.5 * E_col * D_c * D_c * D_c * D_c/12
```

```
nu_c = 0.2

G_c = EA_c / (D_c * 2*(1+nu_c))

w_c=0

D_t = 0.45

EA_t = 0.5 * E_str * D_t * D_t # crack factor =0.5

EI_t = 0.5 * E_str * D_t * D_t * D_t * D_t/12

nu_t = 0.2

G_t = EA_t / (D_t * 2*(1+nu_t))

w_t = qu * width_foot * 2 / (width/(n_foot-1))

#initialize area

#set borehole

borehole=g.borehole(0)

#The water table was neglected

borehole.Head=-gwl

#First soil layer

g.soillayer(h_c)

g.setsoillayerlevel(borehole, 0, 0)

material = g.soilmat()

material.setproperties("MaterialName", Name_1, "SoilModel", Constitutive_model_1, DrainageType,
Drainage_1, "einit", void_1, "EurRef", Eurref_1, 0, nu_1, phi_1, cohesion_1, psi_1, 0, 0, 0, gamma_unsat_1,
gamma_sat_1, kx_1, ky_1, 1, 0, 0, 0, 0, 0, 0, void_1/(1+void_1), 0, 1, 0, 0, alpha, beta, 1.0E+015,
0, 0, 0, 0, 0, 0, power_1, 100, 0, 0.9, E50ref_1, K0_1, Eoedref_1, 0, 0, 0, 0, 0, 0, 0, 0, 0, 0, 0, 0, 0, 0,
0, 0, 0, 0, 0, 0, 0, 0, 0, 0, 0, 0, 0, 0, 0, 0, 0, 0, 0, 0, 0, 0
```

#create the second soil layer

g.soillayer(h_liq)

g.setsoillayerlevel(borehole, 1, -h_c)

set new soil material

material=g.soilmat()

#set material properties

material.setproperties("MaterialName", Name_2, "SoilModel", Constitutive_model_2, Dilatancy-CutOff, False, DrainageType, Drainage_2, "EurRef", Eurref_2, 0, nu_2, phi_2, cohesion_2, psi_2, 0, 0, 0, gamma_unsat_2, gamma_sat_2, kx_2, ky_2, 1, 0, 0, 0, 0, 0, 0, void_2/(1+void_2), 0, 1, 0, 0, alpha, beta, 1.0E+015, 0, 0, 0, 0, 0, 0, power_2, 100, 0, 0.9, E50ref_2, K0_2, Eoedref_2, 0, 0, 0, 0, 0, 0

deepth_3_layer = (h_c+h_liq)

g.setsoillayerlevel(borehole, 2, -deepth_3_layer)

set new soil material

material = g.soilmat()

set material properties

material.setproperties("MaterialName", Name_3, "SoilModel", Constitutive_model_3, DrainageType, Drainage_3, "einit", void_3, "EurRef", Eurref_3, 0, nu_3, phi_3, cohesion_3, psi_3, 0, 0, 0, gamma_unsat_3, gamma_sat_3, kx_3, ky_3, 1, 0, 0, 0, 0, 0, 0, void_3 / (1 + void_3), 0, 1, 0, 0, alpha, beta, 1.0E+015, 0, 0, 0, 0, 0, 0, power_3, 100, 0, 0.9, E50ref_3, K0_3, Eoedref_3, 0, 0, 0, 0, 0, 0

g.neginterface(g.Plates[1].Parent)

Plates right footing

g.plate((width/2)-(width_foot/2), -depth_foot, (width/2), -depth_foot)

g.Plates[2].Material = plate_material

g.neginterface(g.Plates[2].Parent)

g.plate((width/2), -depth_foot, (width/2)+(width_foot/2), -depth_foot)

g.Plates[3].Material = plate_material

g.neginterface(g.Plates[3].Parent)

columns

plate_material_col = g.platemat()

plate_material_col.setproperties("MaterialName", "columns", "Elasticity", 0, "IsIsotropic", True, "EA", EA_c, "EA2", EA_c, "EI", EI_c, "w", w_c, "nu", 0.2, "d", D_c, RayleighAlpha, 0, "Rayleigh-Beta", 0, "Gref", G_c)

g.plate(-(width / 2), -depth_foot, -(width / 2), height_str-depth_foot)

g.Plates[4].Material = plate_material_col

g.plate((width / 2), -depth_foot, (width / 2), height_str-depth_foot)

g.Plates[5].Material = plate_material_col

#beam

plate_material_beam = g.platemat()

plate_material_beam.setproperties("MaterialName", "beam", "Elasticity", 0, "IsIsotropic", True, "EA", EA_t, "EA2", EA_t, "EI", EI_t, "w", w_t, "nu", 0.2, "d", D_t, RayleighAlpha, 0, Rayleigh-Beta, 0, "Gref", G_t)

g.plate(-(width / 2), height_str-depth_foot, (width / 2), height_str-depth_foot)

g.Plates[6].Material = plate_material_beam

if n_foot==3:

g.plate(- (width_foot / 2), -depth_foot, 0, -depth_foot)

```
g.Plates[7].Material = plate_material

g.neginterface(g.Plates[7].Parent)

g.plate(0, -depth_foot, (width_foot / 2), -depth_foot)

g.Plates[8].Material = plate_material

g.neginterface(g.Plates[8].Parent)

g.plate(0, -depth_foot, 0, height_str - depth_foot)

g.Plates[9].Material = plate_material_col

elif n_foot==4:

b_bay = width/(n_foot-1)

g.plate(-(b_bay/2)-(width_foot / 2), -depth_foot, -(b_bay/2), -depth_foot)

g.Plates[7].Material = plate_material

g.neginterface(g.Plates[7].Parent)

g.plate(-(b_bay/2), -depth_foot,-(b_bay/2) + (width_foot / 2), -depth_foot)

g.Plates[8].Material = plate_material

g.neginterface(g.Plates[8].Parent)

g.plate((b_bay/2) - (width_foot / 2), -depth_foot, (b_bay/2) , -depth_foot)

g.Plates[9].Material = plate_material

g.neginterface(g.Plates[9].Parent)

g.plate((b_bay/2), -depth_foot, (b_bay/2)+(width_foot / 2), -depth_foot)

g.Plates[10].Material = plate_material

g.neginterface(g.Plates[10].Parent)

g.plate(-(b_bay / 2), -depth_foot, -(b_bay/2), height_str - depth_foot)

g.Plates[11].Material = plate_material_col

g.plate((b_bay/2), -depth_foot, (b_bay/2), height_str - depth_foot)
```

```
g.Plates[12].Material = plate_material_col

elif n_foot==5:

g.plate(- (width_foot / 2), -depth_foot, 0, -depth_foot)

g.Plates[7].Material = plate_material

g.neginterface(g.Plates[7].Parent)

g.plate(0, -depth_foot, (width_foot / 2), -depth_foot)

g.Plates[8].Material = plate_material

g.neginterface(g.Plates[8].Parent)

g.plate(0, -depth_foot, 0, height_str - depth_foot)

g.Plates[9].Material = plate_material_col

b_bay = width/(n_foot-1)

g.plate(-(b_bay)-(width_foot / 2), -depth_foot, -(b_bay), -depth_foot)

g.Plates[10].Material = plate_material

g.neginterface(g.Plates[10].Parent)

g.plate(-(b_bay), -depth_foot,-(b_bay) + (width_foot / 2), -depth_foot)

g.Plates[11].Material = plate_material

g.neginterface(g.Plates[11].Parent)

g.plate((b_bay) - (width_foot / 2), -depth_foot, (b_bay) , -depth_foot)

g.Plates[12].Material = plate_material

g.neginterface(g.Plates[12].Parent)

g.plate((b_bay), -depth_foot, (b_bay)+(width_foot / 2), -depth_foot)

g.Plates[13].Material = plate_material

g.neginterface(g.Plates[13].Parent)

g.plate(-(b_bay), -depth_foot, -(b_bay), height_str - depth_foot)
```

```
g.Plates[14].Material = plate_material_col

g.plate((b_bay), -depth_foot, (b_bay), height_str - depth_foot)

g.Plates[15].Material = plate_material_col

g.posinterface((-width_model/2, -depth_model), (width_model/2, -depth_model))

mult = g.displmultiplier()

mult.Name = "ax"

mult.Signal = "Table"

mult.DataType = "Accelerations"

path_motion = "..." + acc_fname #path of the file containing the ground motion information

accs, dt = load_input_motion(path_motion)

time = np.arange(0, ((len(accs) - 1) * dt) + dt, dt)

print("time", time[-1])

acc_list=[]

for i, acc in enumerate(accs):

acc_list.append(time[i])

acc_list.append(acc)

mult.Table = acc_list

g.linedispl((-width_model/2, -depth_model), (width_model/2, -depth_model),

Displacement_x, "Prescribed", "Displacement_y", "Free", "ux_start", 0.5)

if n_foot == 3:

g.Lines[11].LineDisplacement.LineDisplacement.Multiplierx = mult

elif n_foot==4:

g.Lines[14].LineDisplacement.LineDisplacement.Multiplierx = mult

elif n_foot==5:
```

```
g.Lines[17].LineDisplacement.LineDisplacement.Multiplierx = mult

else:

g.Lines[8].LineDisplacement.LineDisplacement.Multiplierx = mult

# Lines to refine the mesh

g.line((0, 0), (0, -depth_model)) #line 4

g.line((-1.5*width, 0), (-1.5*width, -depth_model))

g.line((1.5 * width, 0), (1.5 * width, -depth_model))

g.line((-3.5 * width, 0), (-3.5 * width, -depth_model))

g.line((3.5 * width, 0), (3.5 * width, -depth_model))

g.line((-0.5*width - 0.5*width_foot, 0), (-0.5*width - 0.5*width_foot, -depth_foot))

g.line((-0.5*width - 0.5*width_foot, -depth_foot), (0.5*width + 0.5*width_foot, -depth_foot))

g.line((0.5*width + 0.5*width_foot, -depth_foot), (0.5*width + 0.5*width_foot, 0))

#create the mesh

g.gotomesh()

# g.soilpolygon=((0,5),(width_model,5),(width_model,deepth_2_layer),(0,deepth_2_layer))

#refine the mesh

if h_c ¡= depth_foot:

g.soilpolygons[2].CoarsenessFactor = 0.25

g.soilpolygons[3].CoarsenessFactor = 0.25

g.soilpolygons[4].CoarsenessFactor = 0.25

g.soilpolygons[5].CoarsenessFactor = 0.25

g.soilpolygons[6].CoarsenessFactor = 0.25

g.soilpolygons[7].CoarsenessFactor = 0.25

if n_foot==5:
```

g.soilpolygons[8].CoarsenessFactor = 0.25

g.soilpolygons[9].CoarsenessFactor = 0.25

else:

g.soilpolygons[0].CoarsenessFactor = 0.25

g.soilpolygons[1].CoarsenessFactor = 0.25

g.soilpolygons[2].CoarsenessFactor = 0.25

g.soilpolygons[3].CoarsenessFactor = 0.25

if n_foot == 5:

g.soilpolygons[4].CoarsenessFactor = 0.25

g.soilpolygons[5].CoarsenessFactor = 0.25

g.soilpolygons[10].CoarsenessFactor = 0.25

g.soilpolygons[11].CoarsenessFactor = 0.25

else:

g.soilpolygons[8].CoarsenessFactor = 0.25

g.soilpolygons[9].CoarsenessFactor = 0.25

if n_foot==3:

g.Line_11_Line_12_1.CoarsenessFactor = 1

g.Line_11_Line_12_2.CoarsenessFactor = 1

g.Line_11_Line_12_3.CoarsenessFactor = 1

g.Line_11_Line_12_4.CoarsenessFactor = 1

g.Line_11_Line_12_5.CoarsenessFactor = 1

g.Line_11_Line_12_6.CoarsenessFactor = 1

elif n_foot==4:

g.Line_14_Line_15_1.CoarsenessFactor = 1

g.Line_14_Line_15_2.CoarsenessFactor = 1

g.Line_14_Line_15_3.CoarsenessFactor = 1

g.Line_14_Line_15_4.CoarsenessFactor = 1

g.Line_14_Line_15_5.CoarsenessFactor = 1

g.Line_14_Line_15_6.CoarsenessFactor = 1

elif n_foot==5:

g.Line_17_Line_18_1.CoarsenessFactor = 1

g.Line_17_Line_18_2.CoarsenessFactor = 1

g.Line_17_Line_18_3.CoarsenessFactor = 1

g.Line_17_Line_18_4.CoarsenessFactor = 1

g.Line_17_Line_18_5.CoarsenessFactor = 1

g.Line_17_Line_18_6.CoarsenessFactor = 1

else:

g.Line_8_Line_9_1.CoarsenessFactor = 1

g.Line_8_Line_9_2.CoarsenessFactor = 1

g.Line_8_Line_9_3.CoarsenessFactor = 1

g.Line_8_Line_9_4.CoarsenessFactor = 1

g.Line_8_Line_9_5.CoarsenessFactor = 1

g.Line_8_Line_9_6.CoarsenessFactor = 1

#generate the mesh

g.mesh(0.04)

#chose one point in the middle of the structure

output_port=g.selectmeshpoints()

s_o, g_o = new_server ('localhost', output_port, password=_password)

```
#displacements

g_o.addcurvepoint('node', (-(width/2), -depth_foot)) #node 1

g_o.addcurvepoint('node', ((width / 2), -depth_foot)) #node 2

g_o.addcurvepoint('node', (-(width / 2), 0)) #node 3

g_o.addcurvepoint('node', ((width / 2), 0)) #node 4

g_o.addcurvepoint('node', (-(width / 2) - (width_foot / 2), -depth_foot)) #node 5

g_o.addcurvepoint('node', (-(width / 2) + (width_foot / 2), -depth_foot)) #node 6

g_o.addcurvepoint('node', ((width / 2) - (width_foot / 2), -depth_foot)) #node 7

g_o.addcurvepoint('node', ((width / 2) + (width_foot / 2), -depth_foot)) #node 8

g_o.addcurvepoint('node', (-(width / 2), height_str-depth_foot)) #node 9

g_o.addcurvepoint('node', ((width / 2), height_str-depth_foot)) #node 10

#accelerations

g_o.addcurvepoint('node', (3.5*width, 0)) #node 11

g_o.addcurvepoint('node', (-3.5 * width, 0)) #node 12

#pore pressures

g_o.addcurvepoint('node', (3.5 * width, -h_c-(h_liq/2))) #node 13

g_o.addcurvepoint('stresspoint', (3.5 * width, -h_c - (h_liq / 2)))

g_o.addcurvepoint('node', (3.5 * width, -h_c - 0.2)) #node 14

g_o.addcurvepoint('stresspoint', (3.5 * width, -h_c - 0.2))

g_o.addcurvepoint('node', (3.5 * width, -h_c - h_liq + 0.2)) #node 15

g_o.addcurvepoint('stresspoint', (3.5 * width, -h_c - h_liq + 0.2))

g_o.addcurvepoint('stresspoint', (-3.5 * width, -h_c - (h_liq / 2)))

g_o.addcurvepoint('stresspoint', (-3.5 * width, -h_c - 0.2))

g_o.addcurvepoint('stresspoint', (-3.5 * width, -h_c - h_liq + 0.2))
```

```
g_o.addcurvepoint('stresspoint', (1.5 * width, -h_c - (h_liq / 2)))

g_o.addcurvepoint('stresspoint', (1.5 * width, -h_c - 0.2))

g_o.addcurvepoint('stresspoint', (1.5 * width, -h_c - h_liq + 0.2))

g_o.addcurvepoint('node', (-(width/2),-h_c-(h_liq/2))) #node 16

g_o.addcurvepoint('stresspoint', (-(width / 2), -h_c - (h_liq / 2)))

g_o.addcurvepoint('node', (-(width / 2), -h_c - 0.2)) #node 17

g_o.addcurvepoint('stresspoint', (-(width / 2), -h_c - 0.2))

g_o.addcurvepoint('node', (-(width / 2), -h_c - h_liq + 0.2)) #node 18

g_o.addcurvepoint('stresspoint', (-(width / 2), -h_c - h_liq + 0.2))

g_o.addcurvepoint('node', (0, -h_c - (h_liq / 2))) #node 19

g_o.addcurvepoint('stresspoint', (0, -h_c - (h_liq / 2)))

g_o.addcurvepoint('node', (0, -h_c - 0.2)) #node 20

g_o.addcurvepoint('stresspoint', (0, -h_c - 0.2))

g_o.addcurvepoint('node', (0, -h_c - h_liq + 0.2)) #node 21

g_o.addcurvepoint('stresspoint', (0, -h_c - h_liq + 0.2))

g_o.addcurvepoint('node', ((width / 2), -h_c-(h_liq/2))) #node 22

g_o.addcurvepoint('stresspoint', ((width / 2), -h_c - (h_liq / 2)))

g_o.addcurvepoint('node', ((width / 2), -h_c - 0.2)) #node 23

g_o.addcurvepoint('stresspoint', ((width / 2), -h_c - 0.2))

g_o.addcurvepoint('node', ((width / 2), -h_c - h_liq + 0.2)) #node 24

g_o.addcurvepoint('stresspoint', ((width / 2), -h_c - h_liq + 0.2))

if n_foot==3:

g_o.addcurvepoint('node', (0, -depth_foot)) #node 25

g_o.addcurvepoint('node', (0, 0))
```

```
g_o.addcurvepoint('node', (0 - (width_foot / 2), -depth_foot))

g_o.addcurvepoint('node', (0 + (width_foot / 2), -depth_foot))

g_o.addcurvepoint('node', (0, height_str - depth_foot))

elif n_foot==4:

g_o.addcurvepoint('node', (-(b_bay / 2), -depth_foot)) #node 25

g_o.addcurvepoint('node', (-(b_bay / 2), 0)) #node 26

g_o.addcurvepoint('node', (-(b_bay / 2) - (width_foot / 2), -depth_foot)) #node 27

g_o.addcurvepoint('node', (-(b_bay / 2) + (width_foot / 2), -depth_foot)) #node 28

g_o.addcurvepoint('node', (-(b_bay / 2), height_str - depth_foot)) #node 29

g_o.addcurvepoint('node', ((b_bay / 2), -depth_foot)) #node 30

g_o.addcurvepoint('node', ((b_bay / 2), 0))

g_o.addcurvepoint('node', ((b_bay / 2) - (width_foot / 2), -depth_foot))

g_o.addcurvepoint('node', ((b_bay / 2) + (width_foot / 2), -depth_foot))

g_o.addcurvepoint('node', ((b_bay / 2), height_str - depth_foot))

g_o.addcurvepoint('stresspoint', (-(b_bay / 2), -h_c - (h_liq / 2)))

g_o.addcurvepoint('stresspoint', (-(b_bay / 2), -h_c - 0.2))

g_o.addcurvepoint('stresspoint', (-(b_bay / 2), -h_c - h_liq + 0.2))

g_o.addcurvepoint('stresspoint', ((b_bay / 2), -h_c - (h_liq / 2)))

g_o.addcurvepoint('stresspoint', ((b_bay / 2), -h_c - 0.2))

g_o.addcurvepoint('stresspoint', ((b_bay / 2), -h_c - h_liq + 0.2))

elif n_foot==5:

g_o.addcurvepoint('node', (0, -depth_foot)) #node 25

g_o.addcurvepoint('node', (0, 0)) #node 26

g_o.addcurvepoint('node', (0 - (width_foot / 2), -depth_foot)) #node 27
```

```
g_o.addcurvepoint('node', (0 + (width_foot / 2), -depth_foot)) #node 28

g_o.addcurvepoint('node', (0, height_str - depth_foot)) #node 29

g_o.addcurvepoint('node', (-(b_bay), -depth_foot)) #node 30

g_o.addcurvepoint('node', (-(b_bay), 0)) #node 31

g_o.addcurvepoint('node', (-(b_bay) - (width_foot / 2), -depth_foot)) #node 32

g_o.addcurvepoint('node', (-(b_bay) + (width_foot / 2), -depth_foot)) #node 33

g_o.addcurvepoint('node', (-(b_bay), height_str - depth_foot)) #node 34

g_o.addcurvepoint('node', ((b_bay), -depth_foot)) #node 35

g_o.addcurvepoint('node', ((b_bay), 0))

g_o.addcurvepoint('node', ((b_bay) - (width_foot / 2), -depth_foot))

g_o.addcurvepoint('node', ((b_bay) + (width_foot / 2), -depth_foot))

g_o.addcurvepoint('node', ((b_bay), height_str - depth_foot))

g_o.addcurvepoint('stresspoint', (-(b_bay), -h_c - (h_liq / 2)))

g_o.addcurvepoint('stresspoint', (-(b_bay), -h_c - 0.2))

g_o.addcurvepoint('stresspoint', (-(b_bay), -h_c - h_liq + 0.2))

g_o.addcurvepoint('stresspoint', ((b_bay), -h_c - (h_liq / 2)))

g_o.addcurvepoint('stresspoint', ((b_bay), -h_c - 0.2))

g_o.addcurvepoint('stresspoint', ((b_bay), -h_c - h_liq + 0.2))

g_o.update()

g.gotostages()

phase1 = g.phase(g.Phases[0])

phase1.Deform.UseDefaultIterationParams = True

g.set(phase1.Deform.ResetDisplacementsToZero, True)

phase2 = g.phase(g.Phases[1])
```

```
phase2.Deform.UseDefaultIterationParams = True

g.set(phase2.Deform.ResetDisplacementsToZero, True)

phase3 = g.phase(g.Phases[2])

phase3.Deform.UseDefaultIterationParams = True

phase4 = g.phase(g.phases[3])

# change type of the

phase4.DeformCalcType = "Consolidation"

phase4.Deform.LoadingType = "Minimum excess pore pressure"

phase4.Deform.Loading.PStop = 1

phase4.Deform.UseDefaultIterationParams = True

phase5 = g.phase(g.phases[4])

# change type of the

phase5.DeformCalcType = "Plastic"

phase5.Deform.UseDefaultIterationParams = True

phase6 = g.phase(g.phases[5])

phase6.DeformCalcType = "Dynamic with consolidation"

if n_motion == 2:

phase6.Deform.TimeIntervalSeconds = 57.02

else:

phase6.Deform.TimeIntervalSeconds= time[-1]

# phase6.Deform.TimeIntervalSeconds = 0.1

g.set(phase6.Deform.ResetDisplacementsToZero, True)

g.set(phase6.Deform.ResetStateVariables, True)

g.set(phase6.Deform.ResetTime, True)
```

```
phase6.Deform.UseDefaultIterationParams = False

phase6.Deform.MaxSteps = int(time[-1]/0.02)

# _deactivate(Soil_1_4)

# Phase_1

if h_c ¡= depth_foot:

g.Soils[3].Active[phase1] = False

g.Soils[4].Active[phase1] = False

g.Soils[5].Active[phase1] = False

g.Soils[6].Active[phase1] = False

if n_foot==5:

g.Soils[7].Active[phase1] = False

g.Soils[8].Active[phase1] = False

else:

g.Soils[0].Active[phase1] = False

g.Soils[1].Active[phase1] = False

g.Soils[2].Active[phase1] = False

g.Soils[3].Active[phase1] = False

if n_foot == 5:

g.Soils[4].Active[phase1] = False

g.Soils[5].Active[phase1] = False

#structure

g.Plates[0].Active[phase2] = True

g.Plates[1].Active[phase2] = True

g.Plates[2].Active[phase2] = True
```

g.Plates[3].Active[phase2] = True

g.Plates[4].Active[phase2] = True

g.Plates[5].Active[phase2] = True

g.Plates[6].Active[phase2] = True

g.Plates[7].Active[phase2] = True

g.Plates[8].Active[phase2] = True

if n_foot==3:

g.Plates[9].Active[phase2] = True

g.Plates[10].Active[phase2] = True

g.Plates[11].Active[phase2] = True

g.Plates[12].Active[phase2] = True

g.Plates[13].Active[phase2] = True

elif n_foot==4:

g.Plates[9].Active[phase2] = True

g.Plates[10].Active[phase2] = True

g.Plates[11].Active[phase2] = True

g.Plates[12].Active[phase2] = True

g.Plates[13].Active[phase2] = True

g.Plates[14].Active[phase2] = True

g.Plates[15].Active[phase2] = True

g.Plates[16].Active[phase2] = True

g.Plates[17].Active[phase2] = True

g.Plates[18].Active[phase2] = True

elif n_foot==5:

g.Plates[9].Active[phase2] = True

g.Plates[10].Active[phase2] = True

g.Plates[11].Active[phase2] = True

g.Plates[12].Active[phase2] = True

g.Plates[13].Active[phase2] = True

g.Plates[14].Active[phase2] = True

g.Plates[15].Active[phase2] = True

g.Plates[16].Active[phase2] = True

g.Plates[17].Active[phase2] = True

g.Plates[18].Active[phase2] = True

g.Plates[19].Active[phase2] = True

g.Plates[20].Active[phase2] = True

g.Plates[21].Active[phase2] = True

g.Plates[22].Active[phase2] = True

g.Plates[23].Active[phase2] = True

if h_c ¡= depth_foot:

g.Soils[3].Active[phase3] = True

g.Soils[4].Active[phase3] = True

g.Soils[5].Active[phase3] = True

g.Soils[6].Active[phase3] = True

if n_foot==5:

g.Soils[7].Active[phase3] = True

g.Soils[8].Active[phase3] = True

else:

g.Soils[0].Active[phase3] = True

g.Soils[1].Active[phase3] = True

g.Soils[2].Active[phase3] = True

g.Soils[3].Active[phase3] = True

if n_foot == 5:

g.Soils[4].Active[phase3] = True

g.Soils[5].Active[phase3] = True

g.dynamics.Active[g.InitialPhase] = False

g.dynamics.Active[g.phases[6]] = True

g.set(g.Deformations.BoundaryXMin, g.phases[6], 'Free')

g.set(g.Deformations.BoundaryXMax, g.phases[6], 'Free')

g.set(g.Dynamics.BoundaryXMin, g.phases[6], 'Tied degrees of freedom')

g.set(g.Dynamics.BoundaryXMax, g.phases[6], 'Tied degrees of freedom')

g.set(g.Dynamics.BoundaryYMin, g.phases[6], 'Compliant base')

g.setmaterial(g.Soil_2, g.phases[5], material2_2)

g.activate(g.LineDisplacement_1, g.phases[6])

g.activate(g.DynLineDisplacement_1, g.phases[6])

def getphasevalue (plxobject, phase):

return plxobject[phase]

g.calculate()

output_port = g.view(phase6)

s_o, g_o = new_server('localhost', output_port, password=_password)

utot = g_o.getcurveresults(g_o.Curvepoints.Nodes.value[0], g_o.phases[6], g_o.ResultTypes.Soil.Uy)

g_o.update()

folder_dir = PLAXIS_RESULTS + "SP%i/N%i_BF%i/Q%i_B%i/DF%i_H%i/" %(sp, n_foot, width_foot, qu, width, depth_foot, height_str)

if not os.path.exists(folder_dir):

os.makedirs(folder_dir)

g.save(folder_dir + "GM%i" %n_motion)

def calc_rayleigh_damping_params(f1, f2, d):

w1 = 2 * np.pi * f1

w2 = 2 * np.pi * f2

beta = 2 * (((w1 * d) - (w2 * d)) / ((w1 ** 2) - (w2 ** 2)))

alpha = beta * w1 * w2

return alpha, beta

def create_phases_name_map(phases):

result = {}

for phase in phases[:]:

result[phase.Name.value] = phase

return result

if __name__ == '__main__':

_password = ' '

PLAXIS_RESULTS = "..." # path where the files of the PLAXIS 2D model will be saved

plaxis_port=10000

run(_password)